Optimal H_2 Control Design of Active Front-end Integrating Grid Model Identification

by Kang Li, MSc

Thesis submitted to The University of Nottingham
for the degree of Doctor of Philosophy, Aug 2021

The University of Nottingham

Contents

List of Figures

Abstract

Small-signal stability and dynamic performance are of great concern for AC power grids with high penetration of power converters. The interactions between these converters may lead to performance degradation or even system instability and failure at certain conditions. To deal with such problems, global modelling and integrated control are proposed. However, because of the highly integration of power grids in commercial industry environment, the lack of information about parameters and methods of the embedded converters, impedes the development of global models for system analysis and control design.

To fill the gap, this research investigated the utility of system identification techniques to estimate a state space model of the unknown power grid, and proposed an approach to incorporate it into the design of local converters. Hence interactions between the grid and the to be designed converters could be taken into account and issues mitigated.

Specifically in this research, the proposed method is applied to the control design of a grid-connected active front end (AFE). In a notional system, a voltage source inverter (VSI) is included to emulate the unknown grid and supplies power to an AFE feeding a constant power load (CPL). Firstly, a state space model of the grid is identified through perturbation and response test at the point of common coupling (PCC) in a specially designed experiment. It is then combined with the open loop model of the AFE to build a global model of the grid-AFE system. The plant for the control design will then be not only represented by the AFE's dynamics, but will also include that of the identified grid at the PCC. Implementation of the identification experiment involved and mathematical manipulations used to merge the two subsystem models are presented in detail.

The global model is utilized to synthesize a state feedback controller, denoted as 'optimal H_2 controller' in this thesis for the AFE by the use of a structured H_2 algorithm, which optimizes the dynamic performance of AFE while intrinsically ensuring stability of the grid-AFE system.

Effectiveness and advantages of the proposed control design method is validated by simulations

and experiments. The grid-AFE system performance when the AFE adopts the optimal H_2 controller or best-tuned proportional-integral (PI) controllers is compared. The use of optimal H_2 controller outperforms with faster dynamic response and greater stability margin the PI based solution. Scalability of the proposed method in more complex power grids and its robustness against system parameters drifting are also discussed.

Acknowledgements

At the beginning, I wish to thank Prof. Wheeler Patrick for giving me the opportunity to do my PhD in Power Electronics Machines and Control (PEMC) research group at the University of Nottingham. I also want to show my great gratitude to Prof. Pericle Zanchetta, a great and kind professor who supported me a lot in my research and life in Nottingham.

Especially, I want to thank Dr. Andrea Formentini who gave me great guidance on my research and papers throughout my PhD period. I sincerely appreciate and admire his kindness in encouraging me and expertise in our research field.

I want to thank Dr. David Dewar, Dr. Luca Rovere, Dr. Sabino.Pipolo, Dr. Zhuang Wen, and Mr. Jingwen Xue for their valuable advice in my research and daily life. My thanks also go to all the staff and fellow students in PEMC. It is a great honor and pleasure to work with all of you in UK in the last five years.

I want to express my gratitude and love to my parents and senior sister for their love and support in my life.

At last, I want to thank the China Scholarship Council (CSC) who financially supported my study in UK.

Chapter 1

Introduction

1.1 Background

Power electronics embedded networks are being adopted in an increasing number of modern applications, ranging from more-electric and all electric aircraft [1–3], electric ships [4, 5], renewable energy and distributed generation [6], microgrid [7] and smart grid [8]. In these systems, different distribution subsystems (AC and DC) and voltage levels coexist, and power converters have the central role in connecting them with high reliability and high power density [9]. However, interactions between those sources and loads built upon locally optimized converters designed not taking into account the external influence of the system in which they are operating, may lead to performance degradation or even system instability and failure at certain operating conditions [10–18].

A considerable amount of research has been recently published in the fields of AC grid modelling, control design and stability analysis [19–21]. Stability of a grid-connected converter during weak grid conditions can be guaranteed if the ratio of the grid impedance to the converter impedance satisfies the Nyquist stability criterion [11]. Aiming to address AC microgrid stability under high penetration of converter-interfaced loads, active compensation techniques are investigated to actively reshape the source impedance of the interfacing inverter [19, 22]. Active damping signals sourced from a VSI's output capacitor currents are filtered and injected into its voltage and current control loops in order to make its reshaped output impedance satisfy the Nyquist admittance ratio criterion [11, 23] when feeding converter-fed loads. The capacitor current is scaled by a gain and processed by a low pass filter stage to filter the high-frequency contents and to provide internal model dynamics within a specified frequency-range. The active damping loops map the frequency modes of the output voltage to the closed loop system to provide damping capabilities by increasing the damping of poorly damped modes associated with high penetration

of converter-interfaced loads. This technique, however, introduces a new compensation loop and demands extra attention on tuning of its control gains. Similarly, an impedance controller which established a control link between q-axis voltage and q-axis current reference is proposed in [24]. It reshapes the q-axis impedance of grid-connected inverters into a positive resistance to relieve the instability concerns caused by its PLL (Phase-Locked Loop). Nevertheless, it makes the current control more sensitive to grid voltage disturbances which in turn introduces an additional concern related to instability. Those endeavour for ensuring sufficient stability margin in the local design of a power converter, failing to consider dynamic characteristics of other systems connected to the same source grid, sometimes leads to a conservative design and compromises the converter's own dynamic performance [25].

In fact, this issue could be well tackled by designing the power converters' controllers and analysing system stability based on a global model of the grid [26–29]. To deal with the stability issues of an aircraft electrical power system, the dq modelling approach is applied to derive individual power system component models and to constitute the corresponding generalized power system global model, as a powerful and flexible stability analysis tool in [26]. In [30], based on the generalized state space averaging method, a modular approach to build a global model of a multi-converter DC power system is proposed, to simplify the analysis and reduce the simulation time required for such complex systems.

However, such global models are often not available in practice as they are all based on a full knowledge of every part in the system. In modern industrial applications, embedded grids are usually comprised of different power converters sourced from different vendors. Information of commercial products, such as control strategy and filters topology, are usually not accessible, making it difficult in achieving a global power grid model. It is therefore desirable to employ estimation techniques to identify a model of the unknown subsystems, mostly in the form of impedance seen from a point of interest within the grid.

Apart from system modelling and stability analysis, harmonic penetration studies, transient analysis, and passive harmonic filter design would all benefit from an accurate knowledge of the impedance of the power system [31]. Additionally, it can provide significant improvements to the design and operation of active filters [32], particularly if the impedance can be monitored in real time.

Methodologies and practical implementation of grid impedance measurement have gained substantial interest among the scientific community in the past two decades [33–54]. In the model identification of grids, usually there is very little data available, but, even with adequate documentation the complexity and dynamic nature of the grids may prohibit a reliable estimation of the impedance. Measurement of the impedance is also very difficult because the power supply and

loads may contain harmonic sources; signals of significant or measurable levels have to be injected across the whole frequency range of interest while not disturbing the normal operation of the grid. Therefore, accurate and fast measurement of grid impedance is still an appealing research topic.

1.2 Motivations and objectives

1.2.1 Motivations of the research

The proliferation of power electronic systems and distributed generation in modern power networks has raised important issues regarding effects that inter-connected converters systems can have on performance and stability of the whole grid. Interactions between the locally optimized converters may lead to performance degradation or even system instability and failure. Therefore, interactions at each interface must be properly managed in the component design and system assembling. Otherwise, even though each system component is properly designed for stand-alone operation, the entire system could still result in an unacceptable performance degradation or instability [55].

So far, design of power converters is mostly implemented individually and locally, based on the their open loop models. Their impedances is actively shaped so that the impedance ratio to the power grid, on which the to be designed converter will be attached, meets the Nyquist impedance ratio criterion. However, parametric models of the grid did not take part in their modelling or control tuning process. This approach usually leads to an unnecessarily conservative control design [19, 24].

In order to address these issues, adaptive control design methods for power converters based on real-time grid model estimation are proposed to ensure the system stability when they are working with a varying grid [56–58]. The methods are based on impedance-based stability criterion and non-parametric model identification of the grid. However, in a converter-dense grid, impedance at PCC can be complex. The non-parametric grid models and their approximations adopted in these approaches can be limiting. Since the way of integrating a parametric estimated grid model had not been reported before this research, accurate and complete representations of grid characteristics were taken into the controller synthesis of local power converters.

1.2.2 Objectives of the research

Hence in this thesis, a globally optimized local converter control tuning method, which is based on a state space model identification of the unknown grid seen from the converter at its point of common coupling (PCC), is presented. The mathematical technique of integrating a parametric estimation of the grid into a system global model is presented. The plant for the control design

will then be not only represented by the local converter dynamics, but will also include that of the identified grid at the PCC. Then the H_2 control algorithm is applied to synthesise an optimal H_2 controller. The gains matrix of the state feedback controller is imposed by a specified constraint on its structure. Then the gains which are supposed to be multiplied by the states of the unknown grid are forced to zero. Hence the implementation of the optimal H_2 control does not rely on the measurement of state variables the estimated grid model.

The proposed control method is applied on an active front end (AFE) converter in this research, which is powered by an AC power grid. With the proposed control strategy, current and voltage interactions between the grid and the AFE is mitigated effectively during system transients. In addition, the stability of the system is reliably guaranteed by the proposed control design method. It is also scalable and flexible to fit for design tasks in more complex power grids.

1.2.3   Steps to deliver the goal of optimal H_2 control design

Key aim of this research is to propose a control design approach for the design of grid-connected active front-ends. To deliver this goal, the procedures below should be followed.

- Employ the active-front end converter as an excitation source to inject current perturbations into the to be estimated grid.

- Collect voltage and current response at the PCC.

- Process the voltage and current data to fit them for identification, e.g. remove outliers and filtering the data with a low-pass filter.

- Estimate a state space model for the grid by the prediction error minimization method based on the voltages and currents.

- Formulate a global system model by merging the estimated grid model and open loop model of the active front-end.

- Synthesize an optimal H_2 controller based on the global model and the structured H_2 algorithm.

The procedures listed above clearly present the roadmap of prosed control design method and details of these steps will be described in later chapters.

1.3   Summary of contributions and dissertation outline

An AC system comprised of a voltage source inverter (VSI) feeding an active front-end (AFE), in what is regarded a very generic system configuration, is considered in this research. In effect, it
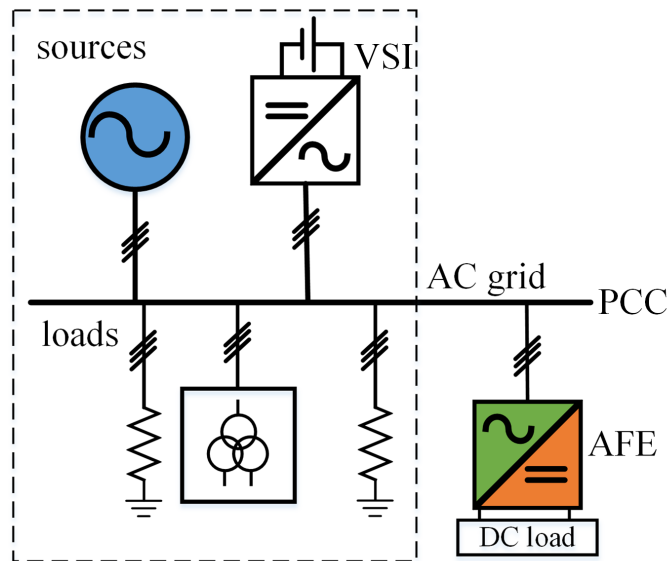
Figure 1.1: Electrical AC subsystem under investigation

could represent many applications, for example, an uninterruptable power supply feeding an active load in a building, or an AC subsystem within a microgrid as shown in Fig.1.1.

In this research work, a new method to tune the control of a grid-connected converter in such an AC system is deployed. Actually it is valid for any more complex systems. A parametric grid dynamic model as seen at converter PCC is firstly identified. Subsequently it is merged with the converter's internal model in order to obtain a global dynamic representation of the interconnected system considered. Finally, the latter is used to synthesise a controller for the converter that intrinsically has kept in consideration dynamic interactions between the grid and the converter itself. Compared to other works, the proposed approach results in a systematic tuning procedure that guarantees a stable controller of which performances are selected through the tuning of few parameters.

Prior to this research, impedance of the peripheral system only serves as a benchmark in predicting the system stability, and rarely takes part in the control design process of a local converter. Stability and performance of the converter-based power network is mainly guaranteed through individually and elaborately designed subsystems. Lack of consideration about the interface interactions impedes a globally optimal design from a system level. In addition, passive filters in large volume may also be needed to mitigate the interactions. Although considerable work on the adaptive control based on grid impedance identification has been published, especially for the design of grid-connected inverters, none of the those takes parametric models of grid as part of the control plant. Hence, the capacity in improving the converter dynamic performance while ensuring

system stability is limited.

Aiming to make some achievements on this issue, an optimal power converter control design method is proposed in this research. The main contributions and novelty of this work can be summarized in two main points. At first, a mathematical procedure for incorporating an identified parametric model of an unknown grid into building a global model of the grid-converter system is developed. Therefore, interactions between the to be designed converter and the unknown grid could be handled through proper control design. Second, advantages of the proposed optimal control design method compared to traditional PI-based control methods are verified by simulations and experiments. Controllers synthesized by these two different methods are compared in terms of dynamic performance and robustness against parameters drifting of passive components. The results confirmed the superiority of the proposed optimal control design method.

It is also worth to point out that most papers about grid-connected power converters control design focus on the grid-connected inverters, of which the q-q axis impedance exhibits negative impedance behaviour as a result of current injection and grid synchronization [59–61]. When the negative impedance interfaces with an inductive grid, it results in a source of instability. Differently this thesis focuses on the design of load-interfaced converters exhibiting negative impedance behaviour in its d-d axis impedance due to constant power consuming. For both grid-connected inverters and load-interfaced converters, the negative impedance will create a 180° phase difference with respect to the grid impedance in the low frequency range [62]. If at the same frequency, impedance magnitude of the inverter is smaller than the grid, or that of the load converter is smaller than the grid, instability occurs.

Organization of the thesis and a chapter by chapter overview are given below.

Chapter 2 reviews literatures about grid impedance measurement and adaptive control design for power converters based on grid impedance identification. In addition, the impedance-based stability criterion for three-phase AC system analysis is also introduced.

Chapter 3 presents the small signal modelling of the VSI-AFE-PLL system discussed in this research. State space models of the three subsystems are derived. It is the basis of discussions in chapters that follows. Based on the open loop models and control schemes used, either state feedback control or the PI control, analytical impedance models of the converters are derived.

Chapter 4 starts with an introduction about the H_2 optimization. Significantly, the mathematical way of integrating estimated grid parametric models into system global model derivation for the control design of AFE is presented. The controller structure specifications when applying the structured H_2 algorithm is discussed. Simulations are implemented to verify the effectiveness of the proposed control design method and advantages compared to the PI method.

Chapter 5 investigates some of the passive components' impact on the converter impedance and

further system stability. More important, performance of the optimal H_2 control design method and the traditional PI method are compared in presence of parameter drifting of these components. And utility of the proposed method in multi-converter applications is also demonstrated by simulations.

Chapter 6 presents some fundamental knowledge about the system identification and the prediction error method (PEM) used for grid model identification in this research. The identification experiment design is also discussed.

Chapter 7 presents the experimental results for validating the proposed control design method. And the controllers' experimental performances are analysed and compared with those of best tuned traditional PI controllers. Advantages of the proposed method are clearly shown through the collected experimental results.

Chapter 8 draws the conclusion.

Chapter 2

Literature review

The first section of this chapter reviews state of the art techniques used in the field of grid impedance identification/measurement. The next two sections reviews the utilities of identified/measured grid impedance from two aspects, i.e. system stability assessment and adaptive control design of power converters. In this thesis, the terms 'impedance measurement' and 'impedance identification' are not rigorously distinguished.

2.1 Grid impedance measurement

2.1.1 Overview

The characteristics of a power grid, especially its impedance, have major effects on the operation and control of grid-connected power electronic devices, such as wind and solar inverters. Ideally, the grid should behave like an ideal voltage source and the inverter should be controlled as an ideal current source to avoid any interconnect problems. In practice, however, this ideal condition never exists and the stability of the inverter-grid system requires that the ratio of the grid impedance to the inverter output impedance satisfies the Nyquist criterion [63]. One particular problem arising from impedance mismatch, that has been discussed extensively in the scientific literature is harmonic resonance between the inverter and the grid [11, 64]. Since the grid impedance varies from location to location, as well as over time, one effective solution is to adaptively change the inverter control based on the impedance of the grid it connects to. Such adaptive control of inverters, to guarantee stability under different grid conditions, requires online measurement of the grid impedance performed in real-time. Online wideband monitoring of grid impedance is also the key enabler for applications such as active filtering tuning [65], grid health analysis and islanding detection [66–69], and harmonic penetration studies [70].

The impedance measurement consists in generating a wideband perturbation controlled in both magnitude and duration for both voltage and current at the impedance measurement point. Then, advanced digital signal processing techniques can be applied on the measured voltage and current to extract impedance of the system under test.

An ideal impedance identification would complete the measurement in a very short time, allowing fast and effective detection of system variations. Even though narrowband identification methods based on injection of sine sweeps give the best impedance measurement accuracy, they are not suitable for online applications due to the very long measurement time. In contrast, wideband identification methods based on injection of a rich frequency content signal able to excite all frequencies of interest simultaneously meet the requirement of fast measurement and have been proposed in [35–52]. These methods were first proposed for dc systems [35, 36], and then extended to AC systems [37–52].

The online wideband impedance identification methods can be categorized in steady state methods and transient methods. In the steady state methods, a wideband small-signal perturbation signal is superimposed onto the steady state operating point for a certain amount of time and the impedance is extracted from the response during the perturbation [37–43, 45]. In the transient methods, usually a current impulse is injected at the impedance measuring point and the impedance is extracted from its transient response [46, 50, 51, 71, 72]. Despite the relatively longer perturbation time, steady-state methods are recently of greater interest because of the too aggressive nature of the transient methods.

The online wideband impedance identification methods can also be categorized in invasive methods [44–52, 73], which require a dedicated power hardware to perform the impedance identification task, and non-invasive methods [35–43], which use the existing power hardware in the system. Among the noninvasive solutions, methods for wideband identification of power impedances in conjunction with existing power electronics converters are quite attractive, especially in power-electronics-based AC power distribution systems [37–43]. In fact, since many of the converters connected to the AC grid have digital control and sensing, they may also be used to monitor AC power grid impedances on the top of their power conversion function. Digital network analyser techniques [35, 36] can be integrated into the converter controllers allowing them to be used as online monitors without any extra power hardware.

Impedance measurement methods can also be categorized in other different ways. For example, depending on the way of generating perturbations to be imposed on the grid, impedance measurement methods could be categorized as passive methods, realized by approaches such as capacitor bank plunge [74], chopper circuits [75, 76] and load switching [46, 77], and active methods realized by grid embedded power converters [38, 40, 51], which could deliberately control the perturbations.

Regarding the form of impedance model in demand, impedance measurement methods can be categorized as non-parametric [78] and parametric methods [41, 79].

When selecting a method for a specific practice of impedance measurement, different facets such as utility of the desired impedance model, requirement on the timeliness, tools and device available, etc. should be considered as a whole. For example, as the online measurement requires fast data analysis, its results are usually confined to non-parametric models, which needs less computation comparing to the parametric identification. Regarding the selection of impedance models type, either parametric or non-parametric, the choice depends on the intended use of the impedance models: while non-parametric models are advantageous in stability assessment, parametric models are mainly used for integrated control design.

2.1.2 Online identification

Since both the converter and the grid impedances change in real-time due to the non-stationary nature of power systems, offline grid impedance identification [37, 51, 80] followed by custom converter design are insufficient to guarantee system stability during normal operating conditions, hence it gained much less attention compared to online identification.

Online implementation of grid impedance identification is often embedded within a grid-connected converter [33, 81, 82]. The approach is based on online analysis of the grid response to a disturbance and serves for assessing in real-time the stability of the interconnected system formed by the grid-connected converter and the grid.

Online analysis of the grid response to a wide-band disturbance shall be realized by the direct discrete Fourier transform (DFT) [83] algorithm implemented inside the DSP of a grid-connected converter. The frequency domain components in the response data are extracted. In signal processing, the DFT is defined as follows:

$$G(k) = \sum_{n=0}^{2N-1} g(n)e^{-j2\pi nk/(2N)}, 0 \leqslant k \leqslant 2N - 1 \tag{2.1}$$

where $g(n)$ is a $2N$-length input sequence and $G(k)$ is its DFT. In the context of grid impedance identification, the $g(n)$ can be either the sampled waveform of current or voltage. Then the grid impedance in frequency domain is calculated by dividing the voltage and current spectra.

$$z_g(e^{jw}) = \frac{DFT(v(k))}{DFT(i(k))} = \frac{v(e^{jw})}{i(e^{jw})} \tag{2.2}$$

To increase the refresh rate of the identified grid impedance, it is desirable to begin computation of each element in $G(k)$ as soon as a new element of $g(n)$ is available from the cycle-to-cycle perturbation-response test, instead of gathering $g(n)$ completely before the full-length DFT begins

computation. The drawback is that computing the grid impedance on a sample-by-sample basis implies that the identification process should be completed before every new sample arrives, which may result in an overflow of the converter control process beyond a single timer interrupt. To avoid this problem, most research compute the full-length DFT after the full-length sequence of the response data has been gathered, and the grid impedance calculation is allocated to the time remaining in each interrupt cycle after the converter control process has been completed [81].

In this research, the three-phase AC grid impedance parametric identification is implemented offline. Since the prediction error method (PEM) used for data analysis in this research requires much more time and computation resource to complete the data fitting than the DFT, which is more suitable for SISO system non-parametric identification, it is not proper to be integrated into the converter's power conversion functionality. The basic theory of PEM algorithm will be detailed in Chapter 6. Therefore, the data analysis and parametric model estimation is implemented offline by a remote PC, while the perturbation injection and response collection experiment is carried out online. On the other hand, the optimal control design method proposed in this research is delivered by solving a numerical optimization problem after obtaining a grid impedance model. The optimization process may be trapped in a local minimum and work out a false solution. Therefore, at the current stage, extra manual inspection is required on the solutions to exclude those unsatisfactory results. Hence, it is not necessary to pursue a great timeliness of grid impedance identification.

2.1.3   MIMO system identification

Three-phase grid-connected systems are multiple-input multiple-output (MIMO) systems. All the frequency responses of such systems can be measured by applying a broadband excitation to each input and measuring responses at all outputs in turn, and cross-correlating each input and output signal combination. A good example of such a procedure is the impedance measurement in the direct-quadrature (dq) reference frame. In the dq transformation, the non stationary grid-connected system is mapped to a rotating reference frame [84,85]. The transformation reduces three (balanced) AC quantities to two DC quantities, which greatly simplifies the analysis and controller design. Moreover, using the dq reference frame, the measurements are not affected by spectral leakage from the fundamental component, which may have large amplitude. The measurement technique based on the MLBS injection (will be discussed later in this chapter) was applied in the dq domain in [86–88]. In the work, the d and q components of the inverter output impedance were obtained by separately injecting the MLBS into the d and q component of the grid reference voltage and measuring the corresponding components from the inverter output currents and voltages.

Impedance model of an AC system in the dq-frame could be represented as

$$z = \begin{bmatrix} z_{dd} & z_{dq} \\ z_{qd} & z_{qq} \end{bmatrix} \tag{2.3}$$

In the perturbation and response test, when identifying such an impedance model, usually the perturbations are injected into the d- and q-axis sequentially. Assume the perturbation in d-axis i_d is injected firstly into terminals of the to be measured MIMO system; the voltage responses it induces in d- and q-axis are v_d and v_q respectively, so that the first two impedance elements can be constructed as:

$$z_{dd} = \frac{DFT(v_d)}{DFT(i_d)}, z_{qd} = \frac{DFT(v_q)}{DFT(i_d)} \tag{2.4}$$

The perturbation in the q-axis i_q is injected subsequently. Assume the voltage responses in d- and q-axis are v_d' and v_q' respectively, then the remaining two impedance elements can be constructed as:

$$z_{dq} = \frac{DFT(v_d')}{DFT(i_q)}, z_{qq} = \frac{DFT(v_q')}{DFT(i_q)} \tag{2.5}$$

Reference [42, 89] proposed the use of orthogonal binary sequence injection, which allows simultaneously identifying d- and q- components impedance of the MIMO system under test. Therefore, the operating conditions of the system can be kept constant during the measurements, and the overall measurement time is significantly reduced.

2.1.4 Non-parametric methods

Impedance identification may be done by parametric [41, 79] and non-parametric methods [78]. Non-parametric methods are advantageous when the objective is assessing system stability, which does not require to parametrize the impedance model. Non-parametric methods are classified as impulse response methods, small-signal perturbation method and frequency response methods.

In [90,91], the grid impedance is measured by injecting sinusoidal currents into the grid, sweeping the frequency range and performing Fourier analysis at steady state using the measured current and voltage responses. Reference [92] relied on a frequency response analyser to sweep the grid impedance in a single-phase application. Using sine sweeps provides the highest possible signal-to-noise ratio (SNR) and hence the most reliable and accurate estimate of grid impedance. However, due to the non-stationary nature of power systems and the large test time associated with sequentially identifying each relevant point of a frequency response curve, frequency response methods (i.e. sine sweep methods) are not practical for real-time impedance identification.

Using broadband excitation, such as impulse or small-signal perturbations, the grid impedance can be simultaneously measured over a broad frequency range.

Impulse injection was applied in [46] to obtain the grid impedance over a wide spectral range. Moreover, small-signal perturbation such random pulse width modulation (PWM) signals, maximum length binary sequence (MLBS), and discrete-interval binary sequence (DIBS) injection were proposed in [80], [93] and [94] respectively. Their injection, by means of a three-phase grid-connected inverter and corresponding analysis, have been demonstrated in [81] for the impulse and in [43] for the MLBS in the sequence domain and [94] for the DIBS in the dq domain.

Impulse response method

Conversely, impulse response methods offer an estimation of grid impedance over a wide frequency spectrum and within a few fundamental cycles, hereby making the method insensitive to the non-stationary nature of the power system.

The simplest impulse response identification method consists of subjecting the system to an impulsive test input [46]. The salient advantage of an impulse test input is that the effects of a non-stationary grid voltage are minimized by offering a grid impedance estimation on a cycle-to-cycle basis. The main drawbacks are the potential danger of exceeding system ratings and the excitation of nonlinear system dynamics.

The impulse injection analysis assumes the AC system is stationary between two consecutive fundamental cycles. The effects of background harmonics are removed by subtracting the unperturbed system trajectory from the impulse response of the AC system, as shown in (2.6). It is essential for grid impedance identification in sequence domain as there is no stationary equilibrium point.

$$\Delta x(t) = x_p(t) - x(t) \tag{2.6}$$

$x_p(t)$ corresponds to the time domain response of the voltage or current during the fundamental cycle which has been perturbed with the impulsive test signal, and $x(t)$ corresponds to the fundamental cycle just before the perturbed cycle. So the response data collection lasts for 2 fundamental cycles. The DFT computation and impedance calculation usually consume much less time compared to the data acquisition and can be negligible. In the reference [58, 81], adaptive control for the PLL of a grid-connected inverter are proposed based on an impulse response identification of grid impedance. In order to accommodate not only the two fundamental cycles for grid impedance identification, but also to allow the control parameters adaptation transient to settle before the next cycle of perturbation is injected, the perturbation and response test will

cease for several fundamental cycles. Therefore the refresh rate of grid impedance estimation is usually about several fundamental cycles.
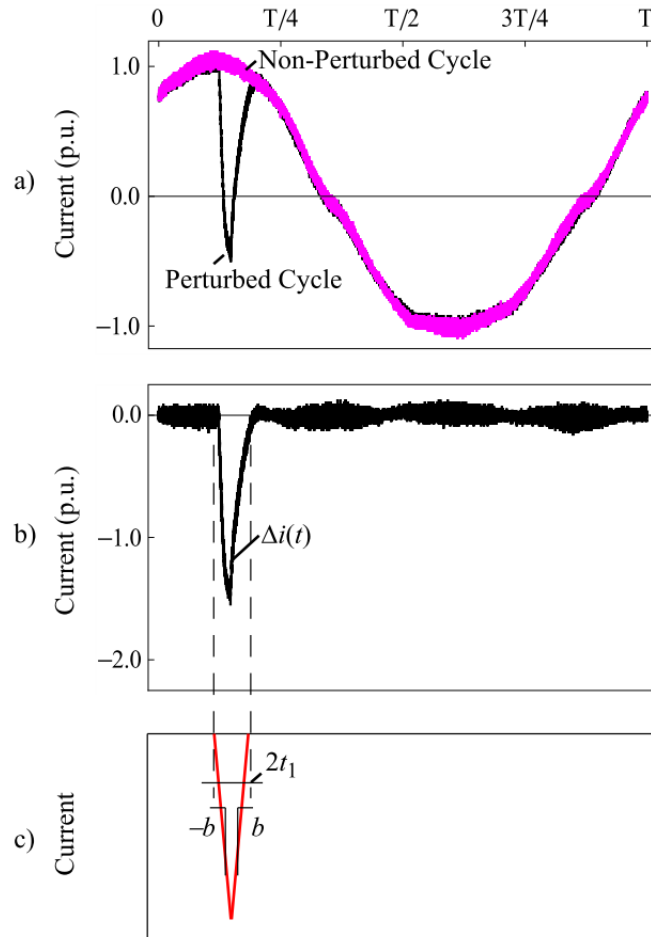
Figure 2.1: Impulse injection signal analysis: (a)perturbed and non-perturbed cycles; (b)differential signal on a cycle to cycle basis; (c)idealization of impulse injection signal

Online measurement of the grid impedance based on impulse perturbation was presented in [81]. An impulse current was injected on top of the normal output current; the resulting responses in the grid voltage were measured, and Fourier analysis was applied to extract the corresponding frequency components in both voltage and current. The grid impedance was then determined by the ratio between the perturbed voltage and current at different frequencies. The time location of the perturbation pulse along the sinusoidal trajectory determines the maximum differential cycle-to-cycle impulse amplitude that can be achieved without exceeding converter ratings. In reference [81], the pulse is located at the peak of the sinusoidal trajectory of the current and with a negative polarity. A maximum of 1.5 p.u. pulse amplitude on a cycle-to-cycle basis is achieved,

without exceeding the converter current ratings within a single perturbed cycle as shown in the Fig.2.1. In the Fig.2.1(b), $\Delta i(t)$ signifies magnitude of the current pulse injected. In the Fig.2.1(c), $2t_1$ signifies duration of the pulse perturbation and b is slope of the triangle used to simulate the pulse perturbation. In practice, the impulse signal is approximated by a triangle pulse. It is desirable to maximize the slope of the triangle pulse to increase high frequency excitation, while avoiding the possibility of exceeding converter ratings.

Small-signal perturbation method

The perturbation signal used in identification experiments can have a significant influence on the final result. To reduce the effect of noise on the impedance measurement and produce enough energy to excite the to be measured system, a signal of sufficiently large amplitude should be injected into the power system. To minimize the impact on the power system operation, the injection must be kept as small as possible. In addition, a large perturbation may drive the system far away of its equilibrium point, where linear identification methods are valid. Therefore, we have to find a trade-off between these two aspects when determining the perturbation amplitude. In practice, it is in a trial and error approach to select the amplitude being used. From the view of spectral feature, the energy of the excitation needs to be rich enough through the whole frequency range of interest. As dynamic and stability of the system are mainly decided by low frequency characteristics thereof, the low frequency content of the perturbation signal is of more importance.

The pseudo random binary sequence (PRBS), a digital approximation of white noise which is wide bandwidth in nature, is the most commonly used type of perturbation. By the use of PRBS, all frequencies of interest at the impedance measurement point can be excited at once. The amplitude of the PRBS test signal should still be limited to avoid exceeding the linearity region of the system under test. PRBS is a periodic broadband signal based on a sequence of length N. The most commonly used signals are based on maximum length binary sequences (MLBS). Such sequences exist for $N = 2^n - 1$, where n is the length of used shift register. They are popular because they can be straightforwardly generated using a shift register with exclusive or (XOR) feedback, as shown in Fig.2.2. Fig.2.3 shows the frequency spectrum of a MLBS generated using a seven-bit-length shift register ($n = 7$) by generation frequency f_{gen} of 4 kHz. The frequency resolution of a MLBS can be calculated as $f_{res} = f_{gen}/N$. The MLBS has the lowest possible peak factor among all perturbation signals, which means that the signal time-domain amplitude can be kept very small. Therefore, the sequence is well suited for sensitive systems in which normal system operation must be guaranteed during the injection. Due to the deterministic nature of the sequence, the signal can be repeated and injected precisely and the SNR can be increased by synchronous averaging of the response periods [95]. Hence, the accurate results are achieved by

using relatively small amplitude of the injection also in noisy conditions. For continuous online measurements of power systems, the low-amplitude is required to avoid decreasing the produced power quality.
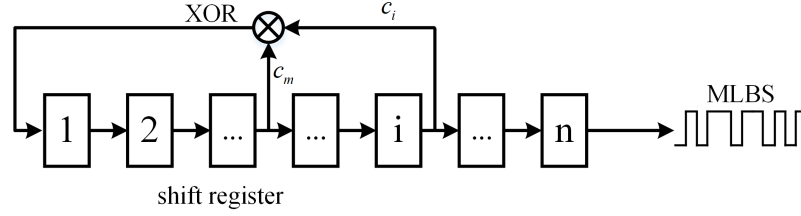
Figure 2.2: N-bit shift register with XOR feedback for MLBS generation
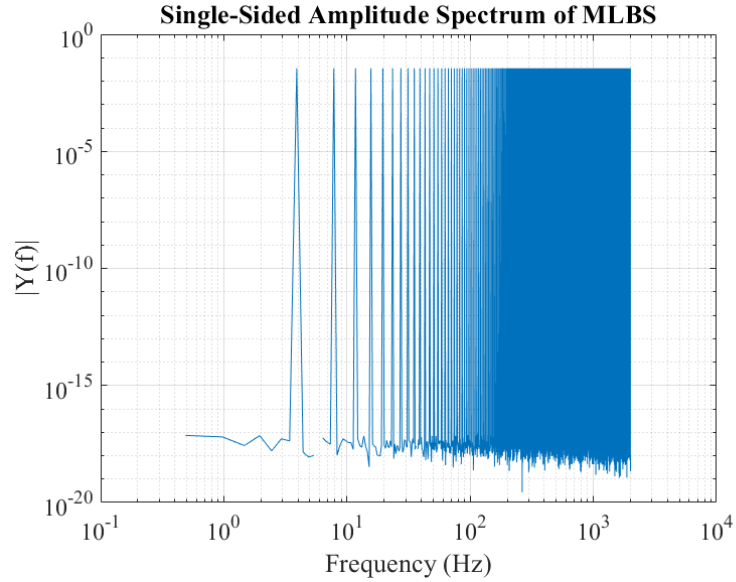
Figure 2.3: DFT of a MLBS signal

The starting point in designing the MLBS is to define the length of sequence N and the generation frequency f_{gen}. These variables define the frequency resolution f_{res} and the time required for the injection of one excitation period T_i. To avoid signal corruption caused by time aliasing [96], N should be selected such that:

$$N = 2^n - 1 \geq f_{gen}T_{st} \tag{2.7}$$

where T_{st} denotes the settling time of the system's impulse response. Thus, the duration of one excitation period (time length of injection), i.e. $T_i = \frac{N}{f_{gen}}$, should be at least as large as the length

of the system settling time. And it is equal to the the inverse of the frequency resolution f_{res} of the identified impedance.

$$T_i = \frac{1}{f_{res}} \tag{2.8}$$

As the time window is directly linked to the number of complex data points (i.e. N) of the non-parametric impedance, for a fixed sampling rate, a long enough time window should be selected in order to have enough data points to capture eventual sharp features of the identified impedance, such as lightly damped resonances. On the other hand, the time window should be chosen short enough to avoid increasing impedance calculation time. For the real-time impedance identification of power electronics based AC power systems, it is important to set the time window short enough in real-time identification in order to catch fast changing impedances for example due to load steps or system re-configuration .

The generation frequency f_{gen} must be higher than the measurable bandwidth, i.e., the upper boundary of the identifiable frequency f_{ident}

$$f_{gen} \geq f_{ident} \tag{2.9}$$

but low enough to avoid the negative effects caused by switching harmonics [97]. At the same time, according to the Nyquist–Shannon sampling theorem [98],

$$f_{sam} \geq 2 * f_{gen} \tag{2.10}$$

where f_{sam} is the sampling frequency of current and voltage response.

The DFT assumes infinite periodicity of the signal to be transformed. However, such an assumption is not practical because all the signal acquisitions are limited in time. During the acquisition, the DFT returns additional spurious frequency components around the existing harmonic content because of the discontinuities at the edges of the time window when the number of the acquired periods is not an integer. This well-known problem is called spectral leakage [99] and it is the main reason for the non-perfect harmonic cancellation. In order to minimize the effect of spectral leakage, two recommendations are made: 1) creation of Hanning window of the same length as the acquired signal and 2) ensuring periodicity of the injection in synchronism with the acquisition over an integer number of fundamental frequency cycles (integer multiples of 20 ms for 50 Hz or 2.5 ms for 400 Hz).

Discrete-interval binary sequence (DIBS) is another class of PRBS, in which the power spectrum can be specified by the user [94]. Basically, the DIBS is a sum of sinusoids with phase values that result in a binary form in the time domain. Using a conventional method to produce the sum

of sinusoids is more straightforward, but the method creates much higher peaks in the injection signal compared with the DIBS. The DIBS is a computer optimized signal, where the goal of the optimization is to force as much power as possible into the specified harmonic frequencies without increasing the signal time domain amplitude. Therefore, it is especially superior to other types of PRBS when applied in identification of a strong grid, of which the impedance is relatively low and so is its response to the perturbations. Even though the grid impedance is no longer a problem in real strong grid from stability viewpoint, accurate measurements are still required, e.g., in power line conditioner and in verifying the grid conditions. When using DIBS, the frequency resolution is weakened at the same time, but otherwise the DIBS has the same attractive properties as those of the conventional MLBS; the sequence is periodic, has a fixed time-domain amplitude and has the lowest possible crest factor. In addition to the increased SNR, the DIBS is useful in identification tasks, where the harmonics needs to be carefully defined to avoid exciting a resonance in a system or to separate actuator dynamics from those of the system.

In reference [94], a strong grid is measured using DIBS injection, and the advantages of DIBS is proved compared to the failure of MLBS. There also exist many optimized broadband excitations of non-binary form, such as multisine [100]. Compared with the DIBS, the design of multisine is much simpler. However, the multisine (and other types of non-binary sequences) consists of an infinite number of signal levels, resulting in problems if the input transducer can only cope with a small number of discrete amplitudes. In addition, the multisine usually presents large peaks on the waveform, and hence, the system under test may easily deviate away from its linear operational range.

Comparing the wideband perturbation identification with single sine sweeps, there are certain drawbacks that need to be emphasized. First, the possible nonlinearities should be carefully considered. Perturbing a system at a specific frequency may create harmonics at other frequencies, e.g., due to saturation nonlinearities. This is not an issue with sine sweeps, where the system is perturbed and analysed one frequency at a time. However, using broadband excitation and computing the frequency response simultaneously at multiple number of frequencies, the non-linearities may create distortions to the measured response. Having information of the nonlinear characteristics, the DIBS may be designed such that the energy at certain harmonic frequencies, that create nonlinearities, is suppressed.

2.1.5   Parametric methods

Parametric model identification of grid impedance is discussed in [41, 79, 101, 102]. Different from non-parametric methods, parametric identification assumes a system model type, either a transfer

function [41, 79] or a state space representation [101, 102], before the perturbation-response test. Then a vector that could parametrize such a model is numerically searched by identification algorithms, such as the least-square method and the prediction error minimization method (PEM), aiming to minimizing the error between response data collected in the perturbation-response test and predicted output by the parametric model. More detailed discussions about these two identification algorithms is included in Chapter 6. The model order is selected based on prior knowledge of the to be identified system. If it is not available, the order can be tentatively estimated by increasing it until the fitting results matches with the response well. In [79], a grid impedance is first identified with non-parametric methods and then transformed into a parametric model by the use of the least-square method fitting the non-parametric model to a polynomial function. In [101], a state space model identification method for grid impedance measuring is proposed. It is based on the PEM that numerically searches the best solution that minimizes a cost function defined by the error between predicted output and response data collected in the perturbation-response experiment.

2.1.6   Dealing with the harmonics

The harmonics included in the injection and generated by the to be identified power system should be carefully considered. To minimize the impact of these harmonics on the impedance identification, basically two methods are adopted. Firstly, a steady state compensation was implemented. The harmonics generated by the power system could be compensated by assuming it is static over the measurement period. The voltages and currents are recorded for several cycles just before the injection of the transients and then subtracting this from the subsequent transient voltage and current. However, there still could be significant discontinuities at those harmonic frequencies (fundamental, fifth, seventh, eleventh and thirteenth harmonic frequencies) due to the time varying nature of the magnitude and phase of the source harmonics voltages (i.e varying from cycle to cycle). This means that an exact cancellation will not occur, and therefore the impedance estimates at these specific frequencies will contain errors. As the frequencies at which these discontinuities occur can be easily predicted, it is possible to ignore these inaccurate measurements and interpolate between points [51]. The injected voltage transient should have a relatively high frequency resolution, which provides inter-harmonic values and thus allows for the interpolation of the system impedance at the harmonic frequencies. It requires a high frequency resolution in estimation, which can be achieved by increasing the data length and sampling duration. It means a reasonably smooth plot of impedance versus frequency can be obtained, easing the process of deriving a transfer function for the impedance.

2.1.7   Grid inductive approximation

In order to develop adaptive control laws for grid-connected converters (which will be discussed in Sec.2.3) based on grid impedance measurement, the grid impedance is usually assumed mostly inductive in the low frequency range and the non-parametric model is parametrized and approximated as an inductance:

$$z_g(s) = sL_g \tag{2.11}$$

The inductive part of the grid impedance is an underlying reason for problems of harmonic resonance between an inverter and the grid. This is a conclusion reached when it is identified that the integral and resonant current control techniques lead to a capacitive impedance behavior on the inverter side, which creates a resonance with the inductive impedance on the grid side [58] [107].

Given a non-parametric gird impedance measurement in the form as (2.2), the inductive component can be obtained by dividing the estimated grid impedance by the corresponding angular frequency where the impedance is assumed inductive.

$$L_g = \frac{I_m[z_g(e^{jw})]}{\omega} = \frac{M(\omega) \cdot sin[P(\omega)]}{\omega} \tag{2.12}$$

where ω is the angular frequency, $z_g(e^{jw})$ is the measured grid impedance, $M(\omega)$ is absolute value of the impedance magnitude and $P(\omega)$ is phase angle of the impedance. When L_g is estimated using only the imaginary component of the $z_g(e^{jw})$, the resistive component does not affect the accuracy of inductance estimation. The the inductance values are computed using the frequency components at low frequencies, where the grid is assumed to be inductive.

However in fact, the AC power distribution grid has been experiencing an increase of nonlinear, harmonic-producing loads and distributed sources interfaced via power electronic converters operating at high switching frequencies. As a result, the distribution power grid is becoming a wideband system. Therefore, adaptive control design based on a pure inductive approximation of grid impedance could not reliably ensure system stability and may fail in practice due to its inaccuracy.

2.2   Impedance-based stability criterion

The stability of a power systems is often analysed using eigenvalues, which are extracted from the system matrix 'A' of the canonical state space model representation of the system in question. This approach requires the use of full dynamic models for all the elements in the system, including physical and control parameters. As such, power network assemblers need to manage an enormous

amount of information to derive these models. On the other hand, the sharing of proprietary information from different system component vendors is not feasible, ultimately impeding the proper modelling of the system [103].

As a more practical alternative to the system full model, impedance based stability analysis has been successfully used in dc systems [55, 104], where the stability of each interface is determined using measured impedance and Nyquist stability criterion. As the impedance intrinsically models all circuit components, including physical components and control parameters, the impedance-based criterion offers a more insightful law for stability judgement. This allows for new loads or sources to be added to the system easily without knowing their internal parameters and re-modelling of the whole system to assess its impact on the system stability.
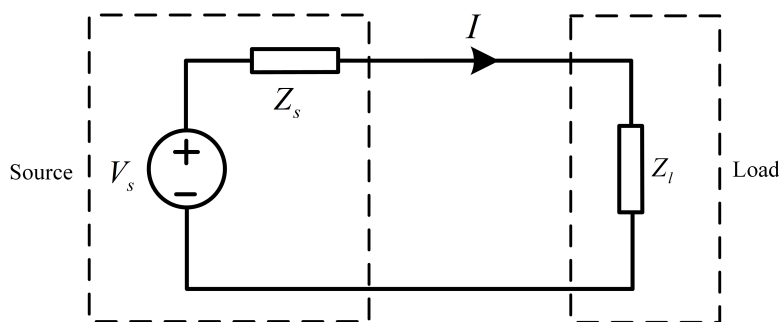
Figure 2.4: Small signal representation of a voltage source with load

The essence of the impedance-based stability criterion, first presented in [23], is to partition the system under study into a source and a load subsystem. The source subsystem is modelled by its Thevenin equivalent circuit consisting of an ideal voltage source (V_s) in series with an output impedance (Z_s), while the load subsystem is modelled by its input impedance (Z_l)(see Fig.2.4). Since almost all power electronic circuits are nonlinear, this linear representation is only valid for small-signal analysis.

With the assumed small-signal model, the current I flowing from the source to the load is

$$I(s) = \frac{V_s(s)}{Z_l(s) + Z_s(s)} \tag{2.13}$$

which can be rearranged in the following form:

$$I(s) = \frac{V_s(s)}{Z_l(s)} \frac{1}{1 + Z_s(s)/Z_l(s)} \tag{2.14}$$

For system stability analysis, it can be assumed that
(1) the source voltage is stable when unloaded and
(2) the load current is stable when powered from an ideal source

In that case, both $V_s(s)$ and $1/Z_l(s)$ are stable, such that stability of the current depends on the stability of the second term on the right-hand side of (2.14), which is

$$H(s) = \frac{1}{1 + Z_s(s)/Z_l(s)} \tag{2.15}$$

The impedance-based stability criterion is based on the observation that $H(s)$ resembles the closed loop transfer function of a negative feedback control system, where the forward gain is unity and the feedback gain is $Z_s(s)/Z_l(s)$; that is the ratio of the source output impedance to the load input impedance. By linear control theory, $H(s)$ is stable if and only if $Z_s(s)/Z_l(s)$ satisfies the Nyquist stability criterion. Regarding frequency domain, this means that the Nyquist curve of $Z_s(s)/Z_l(s)$ never encircles the $(-1, j0)$ in the complex plane [11]. Note that a critical precondition of applying the impedance-based stability criterion above is that the source should be a voltage source that is stable when unloaded.

To develop an impedance-based stability criterion for current source systems, a small-signal model for current source system is derived. Instead of using a Thevenin equivalent circuit, the current source is represented by a Norton equivalent circuit, in the form of a current source (I_s) in parallel with an output admittance (Y_s). The load is represented by its input admittance, Y_l (see Fig.2.5).
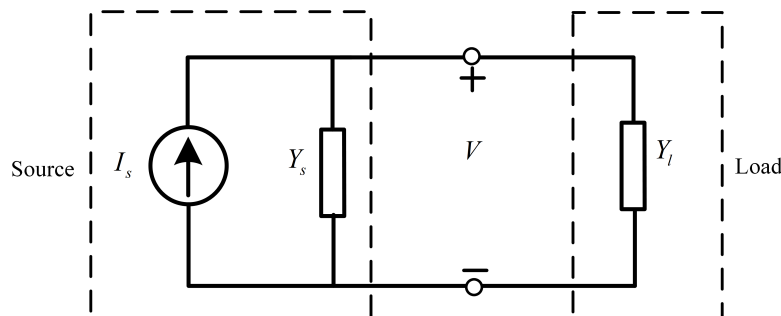
Figure 2.5: Small signal representation of a current source with load

With this small-signal representation, the voltage across the load is

$$V(s) = \frac{I_s(s)}{Y_l(s) + Y_s(s)} \tag{2.16}$$

which can be rearranged as

$$V(s) = \frac{I_s(s)}{Y_l(s)} \frac{1}{1 + Y_s(s)/Y_l(s)} \tag{2.17}$$

Similar to the voltage source case, the current source can be assumed stable when unloaded (that is, when the load is a short circuit such that its admittance is infinite), and the load is stable when powered from an ideal current source. Under these assumptions, both $I_s(s)$ and $1/Y_l(s)$ are

stable, such that the stability of $V(s)$ depends on the stability of the second term on the right-hand side of (2.17). Note that this term resembles the closed loop transfer function of a negative feedback control system where the forward gain is unity and the feedback gain is $Y_s(s)/Y_l(s)$. Therefore, a current source system is stable if and only if the ratio of the source output admittance to the load input admittance satisfies the Nyquist criterion. If the notation of impedance is used, (2.17) becomes

$$V(s) = I_s(s)Z_l(s)\frac{1}{1 + Z_l(s)/Z_s(s)} \tag{2.18}$$

Therefore, the stability of the interconnected system requires the ratio of the load input impedance to the source output impedance meet the Nyquist criterion. Apparently, this is the opposite to the condition for voltage source system. A current source should have high (ideally infinite) output impedance, while a voltage source should have low (ideally zero) output impedance in order to ensure stable operation with a wide range of loads; and a current source system is more stable when the load impedance is low, while a voltage source system is more stable when the load impedance is high.

In terms of three-phase AC systems, similar impedance stability analysis formulated in a mathematical framework based on the generalized Nyquist stability criterion, reference frame theory, and multi-variable control are set forth for stability assessment [105]. Impedance-based small-signal stability analysis for three-phase AC system is usually carried out in dq frame by transformation from stationary (abc) frame. It is due to the fact that if a three-phase AC system is modelled in abc frame, there is no dc-valued equilibrium point exists for small-signal linearisation. While in dq frame, a balanced three-phase AC system becomes two coupled dc systems. Then small-signal model of the system can be extracted using traditional linearisation methods [106].

Alternatively, in reference [107, 108], impedance modelling of three-phase AC systems is implemented in the phase domain and yields decoupled positive- and negative-sequence impedances. As a result, it enables signal-input and single-output stability analysis of balanced three-phase converter systems.

Different from impedances of dc systems, impedance of a three-phase AC system is modelled by a 2-by-2 matrix as shown in (2.19). The off-diagonal entries represent the coupling effect between d- and q-axis.

$$Z(s) = \begin{bmatrix} z_{dd}(s) & z_{dq}(s) \\ z_{qd}(s) & z_{qq}(s) \end{bmatrix} \tag{2.19}$$

Impedance of source and load are represented by (2.20) and (2.21) respectively.

$$Z_{sdq}(s) = \begin{bmatrix} z_{sdd}(s) & z_{sdq}(s) \\ z_{sqd}(s) & z_{sqq}(s) \end{bmatrix} \tag{2.20}$$

$$Z_{ldq}(s) = \begin{bmatrix} z_{ldd}(s) & z_{ldq}(s) \\ z_{lqd}(s) & z_{lqq}(s) \end{bmatrix} \tag{2.21}$$

Similar to what has been done to dc systems, balanced three-phase AC systems can be represented by a coupled system in dq domain and partitioned into source and load subsystems. In the d-axis, the small signal representation of source voltage i.e. $V_{sd}(s)$ can be represented by the sum of source impedance contribution $v_{sd}(s)$ and load impedance contribution $v_{ld}(s)$.

$$V_{sd}(s) = v_{sd}(s) + v_{ld}(s) \tag{2.22}$$

where

$$v_{sd}(s) = z_{sdd}(s)i_d(s) + z_{sdq}(s)i_q(s) \tag{2.23}$$

$$v_{ld}(s) = z_{ldd}(s)i_d(s) + z_{ldq}(s)i_q(s) \tag{2.24}$$

In the q-axis, the small signal representation of source voltage i.e. $V_{sq}(s)$ can be represented by the sum of source impedance contribution $v_{sq}(s)$ and load impedance contribution $v_{lq}(s)$.

$$V_{sq}(s) = v_{sq}(s) + v_{lq}(s) \tag{2.25}$$

where

$$v_{sq}(s) = z_{sqd}(s)i_d(s) + z_{sqq}(s)i_q(s) \tag{2.26}$$

$$v_{lq}(s) = z_{lqd}(s)i_d(s) + z_{lqq}(s)i_q(s) \tag{2.27}$$

Hence the small signal of voltage source

$$V_s(s) = \begin{bmatrix} V_{sd}(s) \\ V_{sq}(s) \end{bmatrix} = \begin{bmatrix} v_{sd}(s) + v_{ld}(s) \\ v_{sq}(s) + v_{lq}(s) \end{bmatrix} = \left(\begin{bmatrix} z_{sdd}(s) & z_{sdq}(s) \\ z_{sqd}(s) & z_{sqq}(s) \end{bmatrix} + \begin{bmatrix} z_{ldd}(s) & z_{ldq}(s) \\ z_{lqd}(s) & z_{lqq}(s) \end{bmatrix} \right) \begin{bmatrix} i_d(s) \\ i_q(s) \end{bmatrix} \tag{2.28}$$

Namely,

$$V_s(s) = (Z_{sdq}(s) + Z_{ldq}(s)) \begin{bmatrix} i_d(s) \\ i_q(s) \end{bmatrix} \tag{2.29}$$

Therefore the interface current I can be derived as (2.30).

$$I(s) = \begin{bmatrix} i_d(s) \\ i_q(s) \end{bmatrix} = \frac{V_s(s)}{Z_{ldq}(s) + Z_{sdq}(s)} = \frac{V_s(s)}{Z_{ldq}(s)} \frac{1}{1 + Z_{sdq}(s)/Z_{ldq}(s)} \tag{2.30}$$

The "minor loop gain" is defined as (2.31), which is the ratio between source and load impedances in dq frame.

$$L(s) = Z_{sdq}(s)/Z_{ldq}(s) \tag{2.31}$$

As reported in [105], the condition for balanced three-phase AC system stability can be determined by applying the generalized Nyquist stability criterion (GNC) [63] to the minor loop gain $L(s)$.

"Let $\Lambda_1(s), \Lambda_2(s)$ be the set of frequency-dependent eigenvalues of $L(s)$. These eigenvalues trace in the complex plane the characteristic loci of matrix $L(s)$ as the variable s traverses the standard Nyquist contour in the clockwise direction. Then the generalized Nyquist stability criterion can be formulated as:

Assume the multivariable system has no open loop unobservable or uncontrollable modes whose corresponding characteristic frequencies lie in the right-half plane. Then the system will be closed loop stable if and only if the net sum of anticlockwise encirclements of the critical point $(-1, 0i)$ by the set of characteristic loci of $L(s)$ is equal to the total number of right-half plane poles of $Z_{sdq}(s)$ and $Z_{ldq}(s)$." [109]

Notably, in low voltage distribution grids, simplifications can be made to neglect the cross terms of impedance matrices for the following reasons:

(1) Low voltage distribution grids are mainly resistive, i.e., $X/R < 1$ (negligible capacitive and inductive effects).

(2) Grid-connected inverters embody decoupling controls which significantly reduce the magnitude of the cross terms of their output impedance compared with the terms of the main diagonal [13].

(3) Grid-connected active reciters operate as high power factor loads and, as results, the magnitude of the cross terms of their input admittance is significantly reduced with respect to that of the terms of the main diagonal [15, 110].

Therefore, the stability analysis of a three-phase system could be implemented in two channels (d-d channel and q-q channel) sequentially in the same way with dc systems.

The guidelines for impedance shaping proposed for dc systems holds for AC systems as well [111]. A mismatch between the grid impedance and grid-connected converter impedance may cause harmonic resonance, which can lead to instability of the grid and disruption of converter operation. The stability criterion stated above indicates that the grid (or voltage source converter) should be designed to have as low output impedance as possible, and input impedance of its load as high as possible in order to operate stably under a wide range of grid conditions. The impedances, therefore, are an important characteristic for converters, and provides a simple means for characterizing and comparing different converter designs. Basically, design of converter impedance could be guided under the principle that their impedance ratio with the varying existing power grid

should meet the stability criteria.

Reference [104] proposes to keep the Nyquist plot of impedance ratio, defined as $G = Z_s/Z_l$ here, inside the unit circle on the complex plane, so that it never encircles the critical point $(-1, 0i)$, and the system is stable. This concept requires the input impedance magnitude of the load subsystem be larger than the output impedance magnitude of source system at all frequencies. Actually, it is a sufficient, but not necessary condition while it may leads to a too conservative design with bulky filters or constrained operation limits.

To exactly explore how far the achievement for system performance could reach through proper impedance shaping, phase margin (PM) and gain margin (GM) are defined as pointed out in Fig.2.6. Reference [112] proposes a possible way to define the forbidden region as shown in Fig.2.6 based on desired value of PM and GM, denoted as 'pm' and 'gm' respectively , on the complex plane where the G (Nyquist plot of the impedance ratio) should not enter. If the G does not enter the forbidden region, it is not possible for the G to encircle the $(-1, j0)$ point, which ensures the stability of the integrated system. Also, any time the G crosses the unit circle, the phase of the G will always be such that there is at least pm of phase margin. Furthermore, any time the G crosses the negative real axis, the magnitude of the G will always be such that there is at least gm of gain margin.
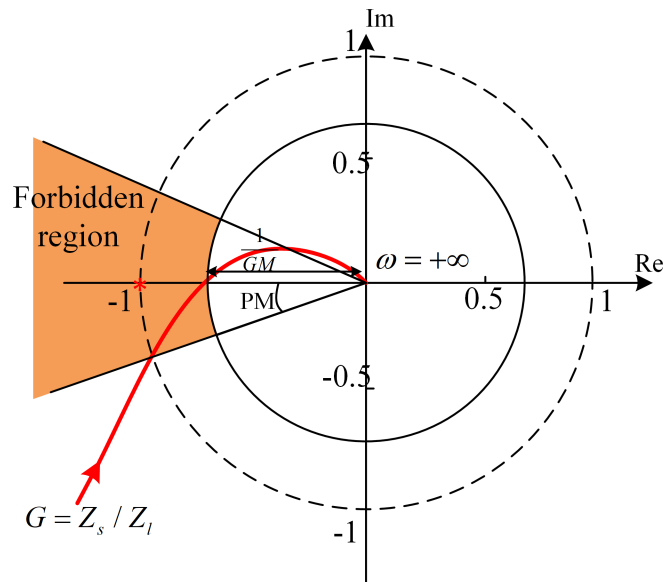
Figure 2.6: Nyquist plot of Z_s/Z_l of a stable plant with the phase margin (PM) and gain margin (GM) indicated, in this figure, PM=gm and GM=gm

The forbidden region shown in Fig.2.6 can also be transformed to load impedance (Z_l) specification in the bode plot as shown in Fig.2.7. In the frequency range where the magnitude of

the load impedance is higher than the gain limit, which is magnitude of source impedance plus the GM, there will be no restriction for the phase of load impedance ($\angle Z_l$). In the frequency range where the magnitude of the load impedance is lower than the gain limit, the $\angle Z_l$ should stay inside its valid region. Hence the sum of the difference between $\angle Z_l$ and $\angle Z_s$ plus PM will not reach $180°$, therefore ensuring stability of the system. Compare with the concept proposed in reference [104], this forbidden region concept is less conservative, which allows G to go outside the unit circle. Namely, the rule here allows the $|Z_s|$ bigger than $|Z_l|$ at some frequencies, but ensures the system stability with certain margin. Some other different forbidden region concepts were proposed [57, 113, 114], and they can be transformed to certain load impedance specifications as useful tools for companies and engineers.
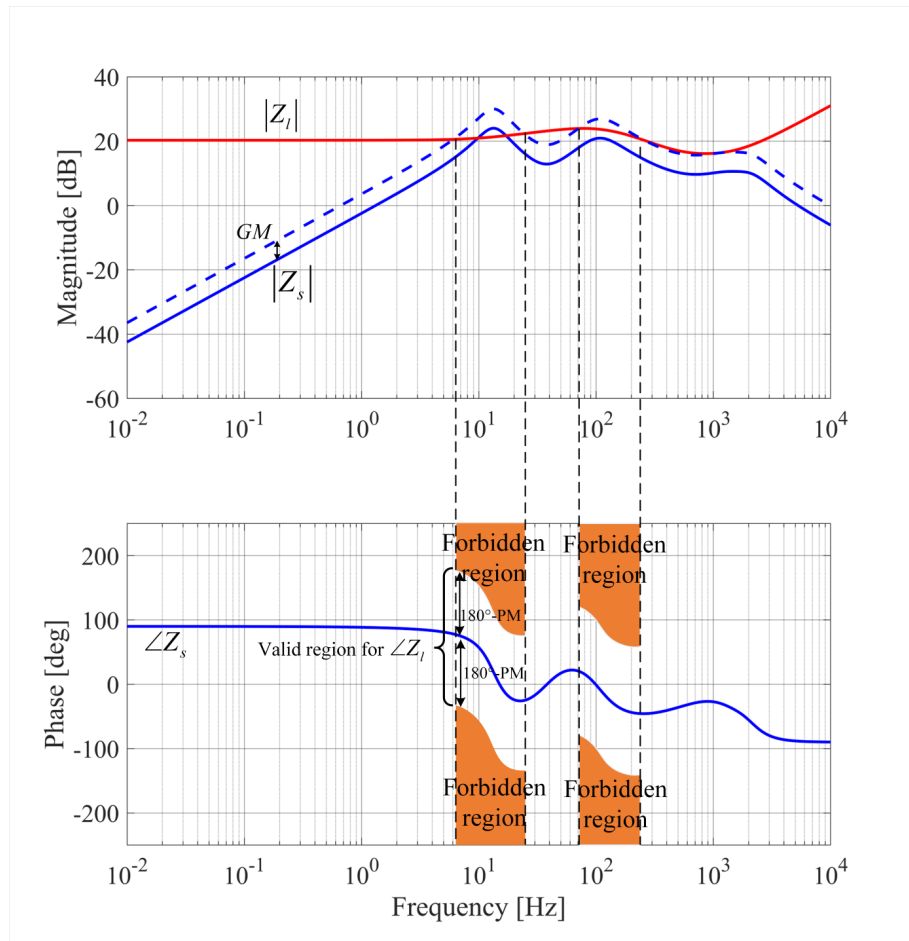
Figure 2.7: Bode plot of source impedances and load impedance specifications

2.3 Impedance-based adaptive control design

However, the pursuit of impedance shaping may come at the cost of compromising system dynamic performance. Take grid-connected inverters as an example. The grid impedance is usually assumed to be mostly inductive with a small resistance in the low frequency range. When the PLL of a grid-connected inverter has a high crossover frequency where its q-q channel impedance exhibits a negative resistance behavior [13], and the phase of the inductive grid impedance rises close to 90 degrees at low frequencies meanwhile, then their phase difference increases over 180 degrees and creates an instability concern. Hence, the PLL crossover frequency has to be set low enough to avoid the instability at the interconnection point between the grid and grid-connected inverter. However, the ability of the PLL to track changes in phase of the grid voltages weakens. Hence the crossover frequency of PLL should be selected such that the instability is avoided while a sufficient grid frequency tracking capacity is provided.

In the presence of a varying grid, the PLL bandwidth of grid-connected converters should decrease when the grid is more inductive and increase when the grid is less inductive. Since the grid condition varies over time, the grid-connected converter controllers are desired to have abilities of adapting their gains to the varying grid conditions to ensure the system stability and fast dynamic performance. Adaptive control laws based on grid impedance identification are proposed to address this issue [56, 115]. The adaptive controller, which adjusts the converter control parameters automatically based on the continuous grid impedance measurements, ensures the proper operation of the converter in varying grid conditions.

The adaptive controller has been applied to dc systems in [57] and extended to three-phase AC systems in [58]. For the adaptation, numerical stability analysis approach such as Routh-Hurwitz method is used to derive, analytically, the stable operation boundaries of the grid-converters system. Namely, the system characteristic polynomial characterised by passive component values and converter control parameters is built. The grid impedance is also included in the characteristic polynomial. Therefore, the controller gains of grid-connected converters can be adapted to the variation of the identified grid impedance in order to maintain solutions of the characteristic polynomial all have negative real parts. To simplify the analytical derivations, the grid impedance is usually assumed pure inductive at low frequencies and curve fitted to the online impedance measurements.

In reference [58], the PLL parameters of a grid-connected inverter are updated at the end of every grid impedance measurement cycle, which is integrated into the inverter current control process. The grid impedance is approximated by a pure inductance and measured through an impulse response analysis of the grid. By the adaptive control of PLL gains, the bandwidth of the

PLL is adjusted according to the variation of inductive approximation of grid, hence the harmonic resonance problem caused by connecting a weak grid and an inverter with a wide bandwidth PLL is resolved. Reference [25] extends the study from sequence domain to dq domain. It also proposed an adaptive gain-scheduling scheme for the PLL control loop of a grid-connected inverter. The internal PI controller gains (proportional gain Kp and integral gain Ki) of the PLL are automatically adjusted using the gain scheduling method based on the continuous measurements of grid impedance, to ensure the stability with a varying grid. However, the grid conditions are only classified into two status, namely mildly inductive or highly inductive. Correspondingly, only two sets of PLL gains are pre-defined to choose from in different grid conditions.

In [116,117], a method for adaptive control of grid-connected three-phase inverters is proposed. In the work, the adaptively adjusted parameters are bandwidth of the PLL and gain of the proportional grid voltage feedforward. The method adds an additional algorithm to the converter control, which measures the grid impedance during the start up, and chooses the most suitable control parameters from a preset table. The control parameters are chosen based on the generalized Nyquist criterion assessment of the grid interface, and the use of sensitivity function for ensuring sufficient stability margins. More specifically, the so-called sensitivity function is defined to quantify the distance between GNC loci and the critical point $(-1, 0i)$ in the complex plane, and to evaluate the system stability and robustness against grid disturbance. The adaptive control method calculates and compares the sensitivity function for different control parameter sets in the preset table based on the measured grid impedance and GNC loci. Consequently the parameter set which results in the biggest sensitivity function is chosen as the optimal control parameters in the specific grid condition.

Grid impedance measurement is also beneficial to the design of active filters. Reference [65] presents a control concept for grid connected converters. It is based on grid impedance measurement aiming to adapt the converters' control online to varying grid conditions and to improve the voltage quality at the converters connection point. To mitigate or compensate voltage unbalances and 5th- and 7th- voltage harmonics, a current is injected with the converter which leads to a voltage drop across the equivalent grid impedance. Once this voltage drop has the same magnitude and opposite phase in relation to the existing voltage unbalances and voltage harmonics at the converters connection point, unbalanced and harmonic voltage compensation is achieved. The grid impedance is acquired by a grid impedance analyser [90] for adapting this information to the converters control. Instead of approximating the grid impedance with an inductance, the grid impedance is measured at those several harmonics frequencies where the voltage harmonics is sought to be compensated.

Reference [69] proposed a method of fault identification and location for grid-connected convert-

ers based on grid impedance identification. The method uses CWT(Continuous Wavelet Transform) method to analyse transients associated with small disturbances imposed by the power converter and determine the net impedance back to the grid. The CWT method largely speeded up the estimation by reducing data capture time. As the different fault types and locations in the grid exhibit different impedance characteristics compared to the normal grid operation, the fast impedance identification provides the possibility of grid fault detection and distinction between fault types and locations.

In a word, to the authors' knowledge, previous research on the adaptive control design of grid-connected converters based on grid impedance identification found in literatures mainly focus on non-parametric grid model identification or its parametric approximation in the low frequency range. Since the way of integrating a parametric estimated grid model had not been reported before this research, accurate, complete and mathematical descriptions of grid characteristics were taken into the controller synthesis of grid-connected converters. Therefore, those non-parametric or parametric approximations of grid only served as a benchmark in predicting the system stability and work out relatively simple adaptive control laws.

Differently, the primary contribution of our research is that we proposed the way of integrating parametric estimations of grid into the control design of a local converter. The plant for the control design will then be not only represented by the local converter dynamics, but will also include that of the identified grid at the PCC. Hence it has a strong capacity of improving the dynamic performance of the grid-converter system while ensuring the system stability at the same time.

2.4   Conclusion

In this chapter, literatures relating to the topic of system model identification and adaptive control for power converters were reviewed. The review set up the background for this research. At first, some main aspects of system identification were discussed, including on-line and off-line identification, property of different forms of perturbations, narrow band and wide band identifications, steady state methods and transient methods, etc. Especially, details of small signal perturbation injection method and techniques used in MIMO identification which would be used in later chapter of this thesis were presented. In the next, two application directions of impedance identification, namely stability analysis and adaptive control were discussed. The procedure of stability analysis based on the information of impedance was presented. And some literature of adaptive control design of power converters based on identified models of peripheral system were reviewed. However, those research were based on either non-parametric models or relatively rough parametric

approximations of grid for the control design of local converters. Hence capacity of local power converter controllers obtained in those research were limited.

Chapter 3

Modelling of the VSI-AFE system

In this chapter, state space model representation of the system discussed in this thesis, including a voltage source inverter (VSI), an active-front end (AFE) and a phase-locked-loop (PLL), will be derived in detail. It lays theoretical foundation for control design of those power converters in the later chapters.

As a contrast to the novel state feedback control design method proposed in this thesis that will be detailed in the next chapter, PI control design for the two converters are briefly described. Based on the mathematical models derived, methods of building analytical impedance models for the two power converters i.e the VSI and AFE, with either PI or state feedback control schemes, are presented. The procedure involved is akin to way of establishing a system global model, which is the core of proposed optimal control design method. At last, system stability assessment and performance analysis tools used in this thesis such as poles' location map, and characteristic loci are introduced.

3.1   State space model of VSI and AFE

The system discussed in this research is schematized in Fig.3.1. A voltage source inverter with an LC output filter is adopted here to generate an AC grid. A constant power load (CPL) fed by an active-front end (AFE) is attached on the AC grid. An inductive input filter, capacitor output filter and PLL for AFE are included. The optimal control design method proposed in this thesis will be applied to the AFE. Constant power loads instead of other types of loads such as resistive loads or constant current loads are considered here due to the fact that constant power loads exhibit negative resistance behavior which creates more challenge for control design [13]. The effectiveness and advantages of proposed control design method could be demonstrated more convincingly if it

is applicable to constant power loads.
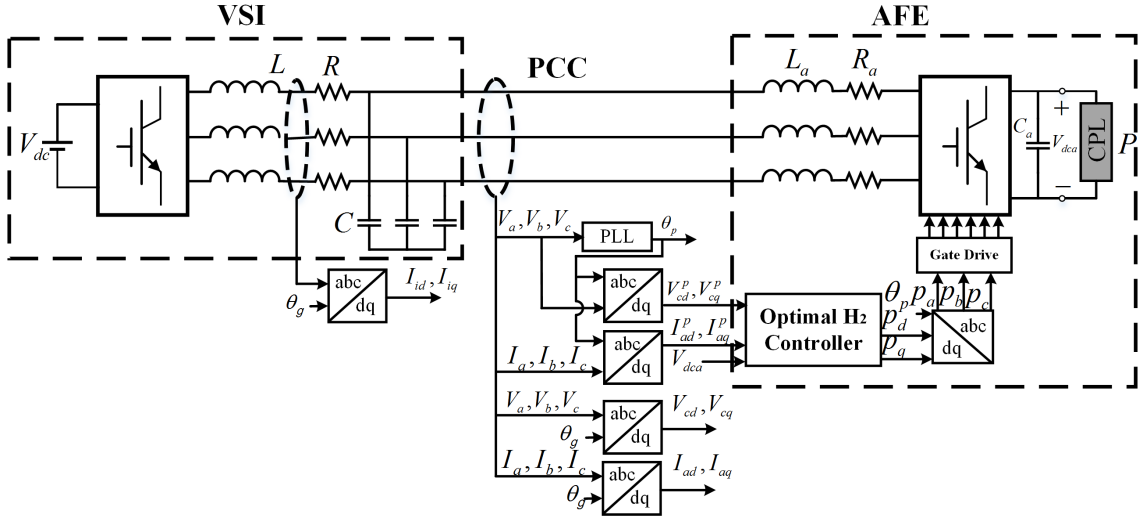
Figure 3.1: Schematic of the VSI-AFE system

3.1.1 State space model of VSI

Average model of the VSI-AFE system in the dq reference frame is shown in Fig.3.2. Its derivation is discussed in detail in [118–120].
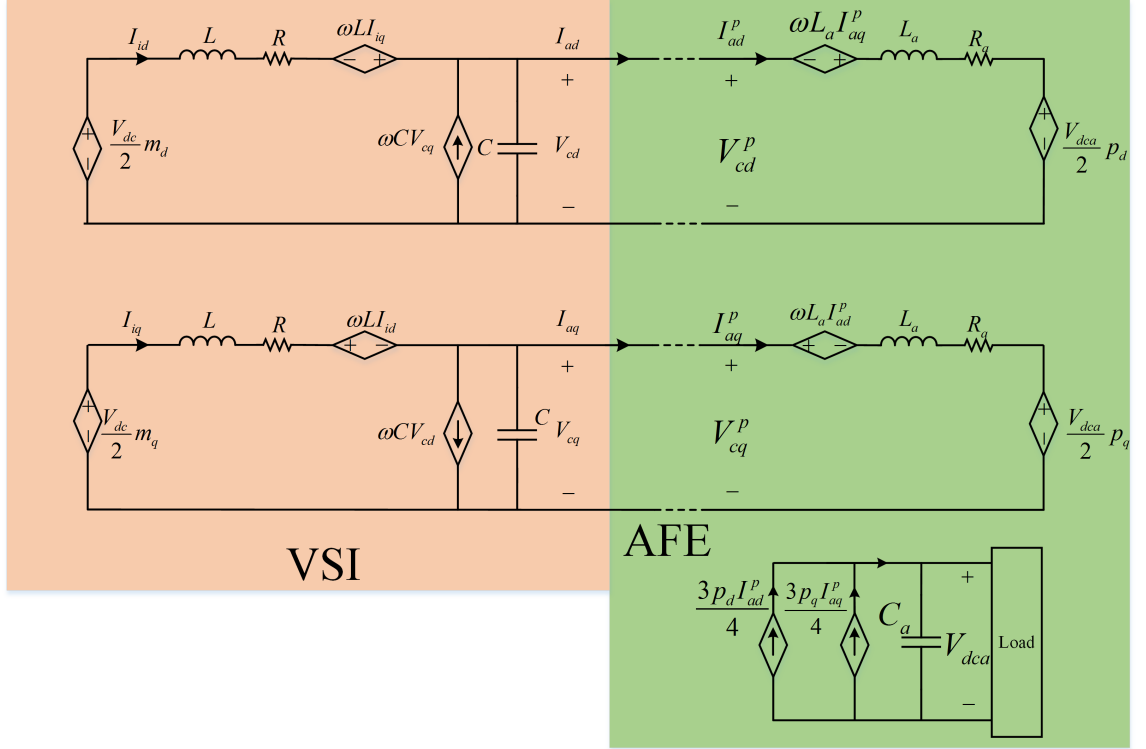
Figure 3.2: Average model of the VSI-AFE system

Based on the average model, the differential-equation representation of VSI and AFE dynamic behavior can be developed as (3.1) and (3.23) respectively.

$$\dot{V}_{cd} = \omega V_{cq} + \frac{1}{C}I_{id} - \frac{1}{C}I_{ad} \tag{3.1a}$$

$$\dot{V}_{cq} = -\omega V_{cd} + \frac{1}{C}I_{iq} - \frac{1}{C}I_{aq} \tag{3.1b}$$

$$\dot{I}_{id} = -\frac{1}{L}V_{cd} - \frac{R}{L}I_{id} + \omega I_{iq} + \frac{V_{dc}}{2L}m_d \tag{3.1c}$$

$$\dot{I}_{iq} = -\frac{1}{L}V_{cq} - \omega I_{id} - \frac{R}{L}I_{iq} + \frac{V_{dc}}{2L}m_q \tag{3.1d}$$

The terms V_{cd} and V_{cq} represent the VSI output capacitor voltages in the dq frame. I_{id} and I_{iq} represent the VSI inductor currents. I_{ad} and I_{aq} are output currents of the VSI, and apparently also the input currents of the AFE. m_d and m_q are modulation indexes of the VSI. V_{dc} is the DC source of VSI.

The state space model of VSI therefore can be derived as (3.2) with the small signal linearisation method discussed extensively in [118, 121].

$$\begin{cases} \dot{x}_{vsi} = A_{vsi}x_{vsi} + B_{vsi}u_{vsi} + G_{vsi}r_{vsi} \\ y_{vsi} = C_{vsi}x_{vsi} \end{cases} \tag{3.2}$$

The x_{vsi} is the state vector, A_{vsi} is the state matrix, B_{vsi} is the input matrix relating to control input, G_{vsi} is the interference matrix relating to the output current I_{ad}, I_{aq} and C_{vsi} is the output matrix relating to the output voltage V_{cd}, V_{cq}. In this these, quantities expressed by notation starting with lower-case letters are small variations of corresponding variables.

$$x_{vsi} = \begin{bmatrix} v_{cd} & v_{cq} & i_{id} & i_{iq} \end{bmatrix}^T \tag{3.3}$$

$$u_{vsi} = \begin{bmatrix} m_d & m_q \end{bmatrix}^T \tag{3.4}$$

$$r_{vsi} = \begin{bmatrix} i_{ad} & i_{aq} \end{bmatrix}^T \tag{3.5}$$

$$A_{vsi} = \begin{bmatrix} 0 & \omega & \frac{1}{C} & 0 \\ -\omega & 0 & 0 & \frac{1}{C} \\ -\frac{1}{L} & 0 & -\frac{R}{L} & \omega \\ 0 & -\frac{1}{L} & -\omega & -\frac{R}{L} \end{bmatrix} \tag{3.6}$$

$$B_{vsi} = \begin{bmatrix} 0 & 0 \\ 0 & 0 \\ \frac{V_{dc}}{2L} & 0 \\ 0 & \frac{V_{dc}}{2L} \end{bmatrix}, \quad G_{vsi} = \begin{bmatrix} -\frac{1}{C} & 0 \\ 0 & -\frac{1}{C} \\ 0 & 0 \\ 0 & 0 \end{bmatrix} \tag{3.7}$$

$$C_{vsi} = \begin{bmatrix} 1 & 0 & 0 & 0 \\ 0 & 1 & 0 & 0 \end{bmatrix} \tag{3.8}$$

3.1.2   State space model of PLL

PLL is an essential part of the AFE to synchronize its operation with the grid voltages. The PLL used here is a PI-SRF (PI-Synchronous reference frame) PLL as shown in Fig.3.3 [122, 123]. Its model in dq-frame is shown in Fig.3.4. k_p^p and k_i^p are proportional and integral gains of the PLL's internal PI. ω_i is output of the integrator which has the integral gain of k_i^p. ω_0 is the nominal angular frequency of grid voltages. The superscripts 'p' indicate the corresponding terms are in the PLL-dq reference frame, which is illustrated in Fig.3.5 and rotates to synchronize with the VSI output voltage angular speed ω_0 [124]. In the case of this study, $\omega_0 = 2\pi \cdot 400$ rad/s.
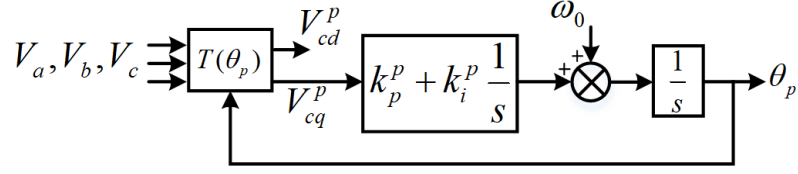
Figure 3.3: The PLL's structure used in this research
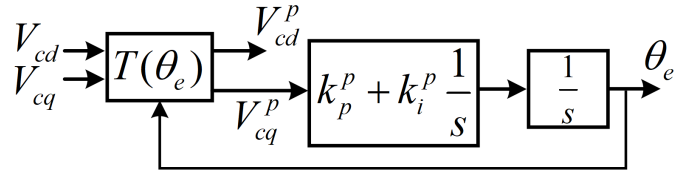
Figure 3.4: Model of the PLL in dq-frame
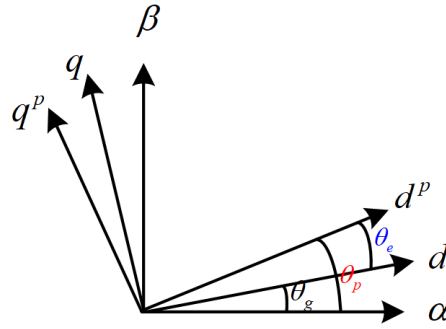
Figure 3.5: $\alpha\beta$ frame by Clarke transform, VSI-dq frame by Park transform, and PLL-dq frame estimated by PLL

Assume θ_g is real phase angle of the grid voltages and θ_p is the estimated angle by the PLL. θ_e is the difference between θ_g and θ_p, namely the angle shift between the VSI-dq frame and PLL-dq frame.

$$\theta_e = \theta_p - \theta_g \tag{3.9}$$

Apparently, transformation included in the Fig.3.4 between the VSI-dq frame and PLL-dq frame is

$$T(\theta_e) = \begin{bmatrix} cos(\theta_e) & sin(\theta_e) \\ -sin(\theta_e) & cos(\theta_e) \end{bmatrix} \tag{3.10}$$

Therefore,

$$I^p_{ad} = cos(\theta_e)I_{ad} + sin(\theta_e)I_{aq} \tag{3.11a}$$

$$I_{aq}^p = -sin(\theta_e)I_{ad} + cos(\theta_e)I_{aq} \tag{3.11b}$$

$$V_{cd}^p = cos(\theta_e)V_{cd} + sin(\theta_e)V_{cq} \tag{3.11c}$$

$$V_{cq}^p = -sin(\theta_e)V_{cd} + cos(\theta_e)V_{cq} \tag{3.11d}$$

The quantities with superscript 'p' indicate currents or voltages that are viewed in the PLL-dq reference frame. Linearise (3.11) around the system equilibrium point $\theta_e^* = 0$, $V_{cq}^* = 0$ and $I_{aq}^* = 0$, and such replacements can be derived.

$$i_{ad}^p \rightarrow i_{ad} \tag{3.12a}$$

$$i_{aq}^p \rightarrow -\tilde{\theta}_e I_{ad}^* + i_{aq} \tag{3.12b}$$

$$v_{cd}^p \rightarrow v_{cd} \tag{3.12c}$$

$$v_{cq}^p \rightarrow -\tilde{\theta}_e V_{cd}^* + v_{cq} \tag{3.12d}$$

The V_{cd}^* is the steady state value of V_{cd}.

According to the Fig.3.4, dynamics of the PLL can be modelled by (3.13)(3.14).

$$\begin{cases} \dot{\tilde{\theta}}_e = k_p^p v_{cq}^p + \omega_i = k_p^p(-\tilde{\theta}_e V_{cd}^* + v_{cq}) + \omega_i = -V_{cd}^* k_p^p \tilde{\theta}_e + k_p^p v_{cq} + \omega_i & (3.13) \\ \dot{\omega}_i = k_i^p v_{cq}^p & (3.14) \end{cases}$$

In this thesis, as part of AFE, the PLL will also be optimized by the proposed state feedback control method. Hence it is a prerequisite to transform the closed-loop differential equations of PLL in (3.13)(3.14) into its state space model representation.

According to (3.12d),

$$\dot{v}_{cq}^p = -V_{cd}^* \dot{\tilde{\theta}}_e + \dot{v}_{cq} = -V_{cd}^*(k_p^p v_{cq}^p + \omega_i) + \dot{v}_{cq} \tag{3.15}$$

$$\dot{v}_{cq}^p = -V_{cd}^* k_p^p v_{cq}^p - V_{cd}^* \omega_i + \dot{v}_{cq} \tag{3.16}$$

Based on (3.14)(3.16), state space model representation of the PLL is

$$\begin{bmatrix} \dot{v}_{cq}^p \\ \dot{\omega}_i \end{bmatrix} = \begin{bmatrix} 0 & -V_{cd}^* \\ 0 & 0 \end{bmatrix} \begin{bmatrix} v_{cq}^p \\ \omega_i \end{bmatrix} + \begin{bmatrix} -V_{cd}^* & 0 \\ 0 & 1 \end{bmatrix} \begin{bmatrix} k_p^p v_{cq}^p \\ k_i^p v_{cq}^p \end{bmatrix} + \begin{bmatrix} \dot{v}_{cq} \\ 0 \end{bmatrix} \tag{3.17}$$

In a concise form,

$$\dot{x}_p = A_p x_p + B_p u_p + r_p \tag{3.18}$$

where x_p is the state vector, u_p is the dummy input and r_p in the interference.

$$x_p = \begin{bmatrix} v_{cq}^p \\ \omega_i \end{bmatrix}, u_p = K_p x_p = \begin{bmatrix} k_p^p & 0 \\ k_i^p & 0 \end{bmatrix} \begin{bmatrix} v_{cq}^p \\ \omega_i \end{bmatrix}, r_p = \begin{bmatrix} \dot{v}_{cq} & 0 \end{bmatrix}^T \tag{3.19}$$

$$A_p = \begin{bmatrix} 0 & -V_{cd}^* \\ 0 & 0 \end{bmatrix} \tag{3.20}$$

$$B_p = \begin{bmatrix} -V_{cd}^* & 0 \\ 0 & 1 \end{bmatrix} \tag{3.21}$$

Its closed-loop representation is

$$\begin{bmatrix} \dot{v}_{cq}^p \\ \dot{\omega}_i \end{bmatrix} = \begin{bmatrix} -k_p^p V_{cd}^* & -V_{cd}^* \\ k_i^p & 0 \end{bmatrix} \begin{bmatrix} v_{cq}^p \\ \omega_i \end{bmatrix} + \begin{bmatrix} \dot{v}_{cq} \\ 0 \end{bmatrix} = (A_p + B_p K_p)x_p + r_p$$

$$= (\begin{bmatrix} 0 & -V_{cd}^* \\ 0 & 0 \end{bmatrix} + \begin{bmatrix} -V_{cd}^* & 0 \\ 0 & 1 \end{bmatrix} \begin{bmatrix} k_p^p & 0 \\ k_i^p & 0 \end{bmatrix}) \begin{bmatrix} v_{cq}^p \\ \omega_i \end{bmatrix} + \begin{bmatrix} \dot{v}_{cq} \\ 0 \end{bmatrix} \tag{3.22}$$

3.1.3 State space model of AFE

According the average model of AFE shown in the Fig.3.2, current and voltage dynamics of the AFE can be modelled by (3.23) in the PLL-dq frame.

$$\dot{I}_{ad}^p = -\frac{R_a}{L_a}I_{ad}^p + \omega I_{aq}^p - \frac{V_{dca}p_d}{2L_a} + \frac{V_{cd}^p}{L_a} \tag{3.23a}$$

$$\dot{I}_{aq}^p = -\omega I_{ad}^p - \frac{R_a}{L_a}I_{aq}^p - \frac{V_{dca}p_q}{2L_a} + \frac{V_{cq}^p}{L_a} \tag{3.23b}$$

$$\dot{V}_{dca} = \frac{3}{4C_a}(p_d I_{ad}^p + p_q I_{aq}^p) - \frac{P}{C_a V_{dca}} \tag{3.23c}$$

$$\dot{V}_{dca} = \frac{3}{4C_a}(p_d I_{ad}^p + p_q I_{aq}^p) - \frac{V_{dca}}{C_a R_l} \tag{3.23d}$$

I_{ad}^p, I_{aq}^p and V_{dca} are input filter currents and output DC-link voltage of the AFE respectively. $p_{d/q}$ are modulation indexes of the AFE. R_a, L_a represent AC filter resistance, inductance respectively while C_a is output filter capacitance. (3.23c) and (3.23d) represent the cases when AFE powers a constant power load (CPL) whose power is P and a resistive load of which the resistance is R_l respectively. In this study, the case of AFE powering a CPL will be focused on as it is more challenging for control design due to its negative resistance feature.

Since the differential equations in (3.23) governing the evolution of AFE's variables are non-linear, again the small signal linearisation method is applied to obtain the state space model of

AFE,

$$\begin{cases} \dot{x}_{afe} = A_{afe}x_{afe} + B_{afe}u_{afe} + G_{afe}r_{afe} \\ y_{afe} = C_{afe}x_{afe} \end{cases} \tag{3.24}$$

where

$$x_{afe} = \begin{bmatrix} i^p_{ad} & i^p_{aq} & v_{dca} & w_{i_{aq}} & w_{v_{dca}} \end{bmatrix}^T \tag{3.25}$$

$$y_{afe} = \begin{bmatrix} i^p_{ad} & i^p_{aq} \end{bmatrix}^T \tag{3.26}$$

$$u_{afe} = \begin{bmatrix} p_d & p_q \end{bmatrix}^T , r_{afe} = \begin{bmatrix} v^p_{cd} & v^p_{cq} \end{bmatrix}^T \tag{3.27}$$

$$A_{afe} = \begin{bmatrix} -\frac{R_a}{L_a} & \omega & -\frac{p^*_d}{2L_a} & 0 & 0 \\ -\omega & -\frac{R_a}{L_a} & -\frac{p^*_q}{2L_a} & 0 & 0 \\ \frac{3p^*_d}{4C_a} & \frac{3p^*_q}{4C_a} & \frac{P}{C_a V^{*2}_{dca}} & 0 & 0 \\ 0 & -1 & 0 & 0 & 0 \\ 0 & 0 & -1 & 0 & 0 \end{bmatrix} \tag{3.28}$$

$$B_{afe} = \begin{bmatrix} -\frac{V^*_{dca}}{2L_a} & 0 \\ 0 & -\frac{V^*_{dca}}{2L_a} \\ \frac{3I^*_{ad}}{4C_a} & 0 \\ 0 & 0 \\ 0 & 0 \end{bmatrix} , G_{afe} = \begin{bmatrix} \frac{1}{L_a} & 0 \\ 0 & \frac{1}{L_a} \\ 0 & 0 \\ 0 & 0 \\ 0 & 0 \end{bmatrix} \tag{3.29}$$

$$C_{afe} = \begin{bmatrix} 1 & 0 & 0 & 0 & 0 \\ 0 & 1 & 0 & 0 & 0 \end{bmatrix} \tag{3.30}$$

$w_{i_{aq}}$ and $w_{v_{dca}}$ are integral states used to eliminate steady state error of the regulated I_{aq} and V_{dca}. The reference value of V_{dca} is denoted as $V_{dca,ref}$. I_{aq} should be regulated to $I_{aq,ref} = 0$ to maintain a unity power factor on the AC bus. Superscripts * in (3.28) and (3.29) signify the equilibrium value of the corresponding state variables.

$$W_{v_{dca}} = \int_0^{+\infty} (V_{dca,ref} - V_{dca})dt \tag{3.31}$$

$$W_{i_{aq}} = \int_0^{+\infty} (I_{aq,ref} - I_{aq})dt \tag{3.32}$$

3.1.4 Realization of CPL in experiment

The constant power load is realized by a series combination of a controlled switch and a resistor R_l in the experiments of this research, as shown in Fig.3.6. The duty of switching varies according to instantaneous voltage sensing, as shown by (3.34), to deliver constant power P to the load in different switching periods.
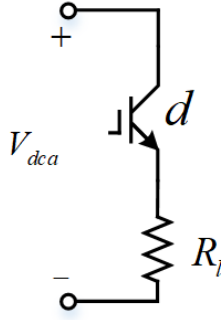
Figure 3.6: Realization of a constant power load

Assume the sampling period of dc-link voltage is T and the desired switch duty cycle in this period T is d. Hence the energy consumed in this period is

$$P \cdot T = \frac{V_{dca}^2}{R_l} \cdot dT \tag{3.33}$$

Therefore

$$d = \frac{P \cdot R_l}{V_{dca}^2} \tag{3.34}$$

The duty cycle is calculated through (3.34) every cycle with the sampled dc-link voltage V_{dca}. Particularly, in order to maintain the duty cycle to be lower than 1, a relatively small resistor R_l is used.

3.1.5 Equilibrium calculation

The state space models of VSI, AFE and PLL are derived by linearising the non-linear equations around the equilibrium point. Therefore the linear models obtained are only valid in the vicinity of this equilibrium point. As can be seen in the matrices (3.28)(3.29), some entries include equilibrium values and they need to be calculated before developing such state space models. At the equilibrium point, the system is stable and differential of all states are zero. Therefore, let left side of (3.23) be zero and solve the equations in (3.35), then the equilibrium values p_d^*, p_q^*, I_{ad}^* can be worked

out. The V_{dca}^* and V_{cd}^* are reference values of V_{dca} and V_{cd} respectively specified by engineers.

$$-\frac{R_a}{L_a}I_{ad}^* - \frac{V_{dca}^* p_d^*}{2L_a} + \frac{V_{cd}^*}{L_a} = 0 \tag{3.35a}$$

$$-\omega I_{ad}^* - \frac{V_{dca}^* p_q^*}{2L_a} = 0 \tag{3.35b}$$

$$\frac{3}{4C_a}p_d^* I_{ad}^* - \frac{P}{C_a V_{dca}^*} = 0 \tag{3.35c}$$

According to the authors' practice on the experimental rig, a higher bandwidth controller of AFE has more difficulty to start the system and built up the stationary operation point successfully. When conducting experiments on the prototype of VSI-AFE system, the AFE always starts with a relatively low bandwidth controller. After the system entered into its steady state, the controller is switched to another which is of a higher bandwidth and synthesized by the proposed optimal control design method to highlight its advantages. This procedure of controller switching helps to guarantee a smooth start of the system.

At the instant of switching, it is inevitable to incur some transient oscillations. If the transient is not properly handled, state variables may deviate too far from their equilibrium values. Then controllers designed around the equilibrium may not be able to stabilize the system any more. In order to minimize this transient, essentially to maintain the modulation indexes during the controller switching, it is required to set initial values for integral states $w_{i_{aq}}, w_{v_{dca}}$ to be their nominal values which are updated when the new controller is introduced.

According to (3.35), the nominal values of modulation index p_d and p_q do not depend on the control gains. Therefore, as long as the load condition and references (i.e. V_{dca}^* and V_{cd}^*) remain unchanged, the p_d^* and p_q^* are consistent as well. To minimize the transient, we try to keep the p_d and p_q before and after the controller switching.

For the convenience of explanation, the variables before and after the switching instant are marked with superscripts 1 and 2 respectively. The aim of integral states reset is to keep

$$\begin{bmatrix} p_d^2 \\ p_q^2 \end{bmatrix} = \begin{bmatrix} p_d^1 \\ p_q^1 \end{bmatrix} \tag{3.36}$$

Before the instant of controller switching, the system entered in steady state hence $p_d^1 = p_d^*$ and $p_q^1 = p_q^*$. However in (3.36), the real time value of modulation indexes before switching p_d^1 and p_q^1 instead of p_d^* and p_q^* are used since modulation indexes in steady state may be slightly different from the equilibrium values due to disturbances.

Meanwhile, it is reasonable to assume the physically existing variables I_{ad}, I_{aq} and V_{dca} do not change before and after controller switching, as the time interval, namely one period of control command execution, is very short.

$$\begin{bmatrix} i_{ad}^2 \\ i_{aq}^2 \\ v_{dca}^2 \end{bmatrix} = \begin{bmatrix} i_{ad}^1 \\ i_{aq}^1 \\ i_{dca}^1 \end{bmatrix} \tag{3.37}$$

According to (3.36),

$$\begin{bmatrix} p_d^2 \\ p_q^2 \end{bmatrix} = K_{afe}^2 \begin{bmatrix} i_{ad}^2 \\ i_{aq}^2 \\ v_{dca}^2 \\ w_{i_{aq}}^2 \\ w_{v_{dca}}^2 \end{bmatrix} = K_{afe}^2 \begin{bmatrix} i_{ad}^1 \\ i_{aq}^1 \\ v_{dca}^1 \\ w_{i_{aq}}^2 \\ w_{v_{dca}}^2 \end{bmatrix} = \begin{bmatrix} p_d^1 \\ p_q^1 \end{bmatrix} \tag{3.38}$$

The K_{afe}^2 signifies a general state feedback controller for AFE. It will be optimized by the proposed control design method and detailed in the next chapters. Assume its has a form shown in (3.39).

$$K_{afe}^2 = \begin{bmatrix} k_{11} & k_{12} & k_{13} & k_{14} & k_{15} \\ k_{21} & k_{22} & k_{23} & k_{24} & k_{25} \end{bmatrix} \tag{3.39}$$

So the equilibrium value of integral states $w_{i_{aq}}^2$, $w_{v_{dca}}^2$ under the new controller could be solved by

$$\begin{bmatrix} w_{i_{aq}}^2 \\ w_{v_{dca}}^2 \end{bmatrix} = \begin{bmatrix} k_{14} & k_{15} \\ k_{24} & k_{25} \end{bmatrix}^{-1} \begin{bmatrix} p_d^1 - k_{11} \cdot I_{ad}^1 - k_{12} \cdot I_{aq}^1 - k_{13} \cdot V_{dca}^1 \\ p_q^1 - k_{21} \cdot I_{ad}^1 - k_{22} \cdot I_{aq}^1 - k_{23} \cdot V_{dca}^1 \end{bmatrix} \tag{3.40}$$

At the instant when new controller is adopted, the value of integral states is reset by the equation above, and the modulation indexes could be maintained consistently and system disturbance arising from controller switching could be minimized.

3.2 PI control design for VSI and AFE

To highlight advantages of the proposed control design method, the most commonly used control design method, Proportional-Integral (PI) control for the VSI and AFE in this research is briefly discussed and will be compared within later chapters.

PI control is executed through a cascade of outer loop and inner loop. The outer loop is the voltage loop to regulate voltage output and generate the current reference for the inner loop. The

inner loop is the current loop to calculate the duty cycle of the switching device according to the difference between sensed actual value and reference value of the currents. When implement PI control in simulations and experiments, the PI output is prevented from saturation and its amplitude is confined within the range from -1 to 1. When its output generated from the proportional and integral calculation exceeds the limits, the integral calculation is stopped.

3.2.1   PI control of VSI
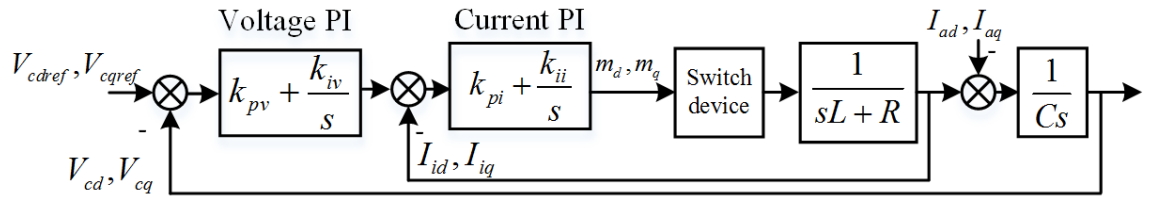
Figure 3.7: Scheme of PI VSI

The complete control loop of VSI employing PI control can be shown as Fig.3.7. According to references [125, 126], the control gains can be tuned as

$$
\begin{cases}
k_{pv} = 2C \cdot 2\pi f_v; \\
k_{iv} = C \cdot (2\pi f_v)^2; \\
k_{pi} = 2\xi L \cdot 2\pi f_i - R; \\
k_{ii} = L \cdot (2\pi f_i)^2;
\end{cases}
\tag{3.41}
$$

The k_{pv} and k_{iv} are proportional and integral gains of the voltage controller and k_{pi} and k_{ii} are those of the current controller. f_v and f_i are voltage and current bandwidths respectively. ξ is the damping factor, which is 0.707 here.

3.2.2   PI control of AFE

The PI control loop for AFE is shown in Fig.3.8. The PI gains are tuned by (3.42) according to the pole-placement approach [126].

$$
\begin{cases}
k_{pv} = 2C_a \cdot 2\pi f_v; \\
k_{iv} = C_a \cdot (2\pi f_v)^2; \\
k_{pi} = -2\xi L_a \cdot 2\pi f_i + R_a; \\
k_{ii} = -L_a \cdot (2\pi f_i)^2;
\end{cases}
\tag{3.42}
$$
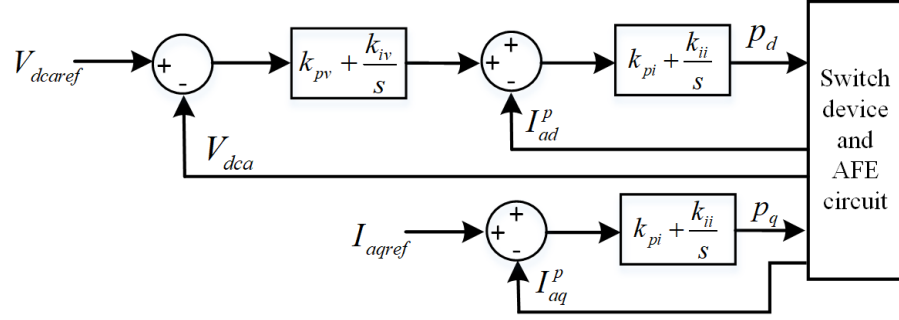
Figure 3.8: Scheme of PI AFE

3.3 Impedance of VSI and AFE

As discussed in Chapter 2, impedance is an important index in the design of a power converter. Based on the open loop models derived and control scheme described in this chapter, analytical impedance models of the VSI and AFE could be developed.

Specifically as the VSI serves as an AC grid generator of which the control is not the centre of discussion in this thesis, it is fixedly designed with PI control method. While the AFE is designed by either PI method or the proposed state feedback control method, and the performance thereof will be compared. Therefore, the impedance models to be developed here include VSI impedance model with PI control, AFE impedance model with PI control and AFE impedance with state feedback control.

The impedance models development is deemed as a pre-condition to apply the impedance ratio criterion to judge the VSI-AFE system stability. In addition, the analytical impedance models built on nominal parameters will be used as references and compared with identified impedance of the converters in later chapters, to evaluate accuracy of the identified ones.

3.3.1 Connotation of impedance model

As discussed in Chapter 2, impedance measurement of either a grid or a power converter is realized by a perturb-response test. Perturbations is created and imposed on the measurement point and voltage and current response is collected. Then frequency spectra is extracted by FFT and the impedance is calculated by dividing the voltage and current spectra. For example, two admittance entries y_{dd} and y_{qd} in the 2 by 2 admittance matrix of AFE could be obtained by injecting d-axis voltage perturbations $\tilde{v}_d$ into AFE terminals, implementing FFT on the current response $\tilde{i}_d$ and $\tilde{i}_q$ and voltage perturbation $\tilde{v}_d$, and dividing the results.

$$y_{dd}(jw) = \frac{FFT(\tilde{i}_d, w)}{FFT(\tilde{v}_d, w)} \tag{3.43}$$

$$y_{qd}(jw) = \frac{FFT(\tilde{i}_q, w)}{FFT(\tilde{v}_d, w)} \tag{3.44}$$

Sequentially q-axis voltage perturbations $\tilde{v}_q$ is injected to AFE, and the remaining two entries y_{dq} and y_{qq} are

$$y_{dq}(jw) = \frac{FFT(\tilde{i}_d, w)}{FFT(\tilde{v}_q, w)} \tag{3.45}$$

$$y_{qq}(jw) = \frac{FFT(\tilde{i}_q, w)}{FFT(\tilde{v}_q, w)} \tag{3.46}$$

The impedance of VSI is defined as the ratio from voltage response to current perturbations. For example, z_{dd} represents the ratio between d-axis voltage response $\tilde{v}_d$ and current perturbation $\tilde{i}_d$, when the current perturbation is only injected in d-axis. However, in order to reduce the time required and increase the refresh speed of impedance estimates, in the identification experiment in this research, d-axis and q-axis perturbations are injected simultaneously. It means that the small signal voltage deviation in d-axis, namely $\tilde{v}_d$, is comprised of two parts, i.e. $z_{dd}\tilde{i}_d$ and $z_{dq}\tilde{i}_q$ as shown in (3.47). Therefore, direct dividing of voltage and current spectra is no longer right. Instead, the numerical optimization method PEM is adopted to identify a MIMO impedance model of converters. The specific procedure involved will be detailed in Chapter 6.

$$\begin{bmatrix} \tilde{v}_d \\ \tilde{v}_q \end{bmatrix} = \begin{bmatrix} z_{dd} & z_{dq} \\ z_{qd} & z_{qq} \end{bmatrix} \begin{bmatrix} \tilde{i}_d \\ \tilde{i}_q \end{bmatrix} \tag{3.47}$$

Likewise, for admittance measurement of AFE, voltage perturbations are injected into its terminal, and current response is collected. Its admittance is also a 2 by 2 matrix in which the d-d axis admittance y_{dd} is defined as the ratio from d-axis current response $\tilde{i}_d$ to d-axis voltage perturbation $\tilde{v}_d$, when voltage perturbations is injected only in d-axis. However, in the identification experiment in this research, the voltage perturbations are injected into d-axis and q-axis simultaneously. Therefore, the d-axis current response $\tilde{i}_d$ will be a combination of $y_{dd}\tilde{v}_d$ and $y_{dq}\tilde{v}_q$.

$$\begin{bmatrix} \tilde{i}_d \\ \tilde{i}_q \end{bmatrix} = \begin{bmatrix} y_{dd} & y_{dq} \\ y_{qd} & y_{qq} \end{bmatrix} \begin{bmatrix} \tilde{v}_d \\ \tilde{v}_q \end{bmatrix} \tag{3.48}$$

Hence the connotation of impedance/admittance for VSI and AFE is explained by (3.47) and (3.48).

3.3.2   Analytical impedance model of closed loop VSI with PI control

In last section, connotation of the impedance/admittance model for VSI and AFE is discussed. In this section, analytical expressions of those impedance will be derived based on control schemes and open loop models. The analytical impedance/admittance models of VSI and AFE derived here will serve for validating estimated models in later chapters. These analytical models are built upon nominal values of passive components and denoted as 'nominal models' hereafter.
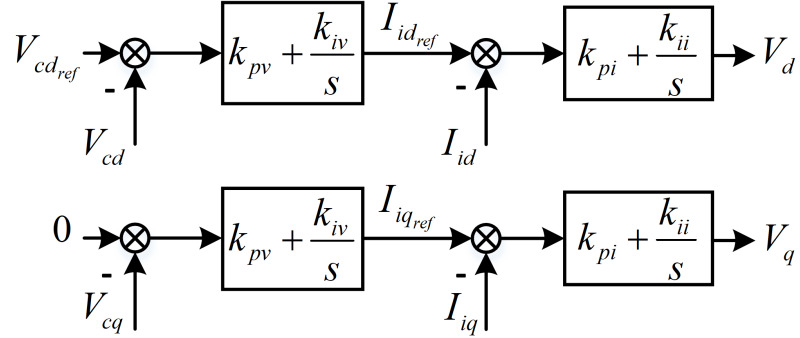
Figure 3.9: VSI's control link

In Fig.3.9, cascade PI control link of VSI is illustrated. Voltage command generated by the PI control link are denoted as V_d and V_q. Then the control link equations of VSI can be obtained as

$$\dot{V}_d = k_{pi}(\dot{I}_{id_{ref}} - \dot{I}_{id}) + k_{ii}(I_{id_{ref}} - I_{id}) \tag{3.49a}$$

$$\dot{I}_{id_{ref}} = k_{pv}(\dot{V}_{cd_{ref}} - \dot{V}_{cd}) + k_{iv}(V_{cd_{ref}} - V_{cd}) \tag{3.49b}$$

$$\dot{V}_q = k_{pi}(\dot{I}_{iq_{ref}} - \dot{I}_{iq}) + k_{ii}(I_{iq_{ref}} - I_{iq}) \tag{3.49c}$$

$$\dot{I}_{iq_{ref}} = k_{pv}(0 - \dot{V}_{cq}) + k_{iv}(V_{cq_{ref}} - V_{cq}) \tag{3.49d}$$

Notably, the q axis voltage reference $V_{cq_{ref}}$ is 0. Combine (3.49) and VSI's power stage equations shown in (3.1), the closed loop equations of VSI with PI control are obtained as

$$\begin{cases} \dot{x}^{cl}_{vsi} = A^{cl}_{vsi}x^{cl}_{vsi} + G^{cl}_{vsi}r_{vsi} \\ y_{vsi} = C^{cl}_{vsi}x^{cl}_{vsi} \end{cases} \tag{3.50}$$

where

$$x^{cl}_{vsi} = \begin{bmatrix} v_{cd} & v_{cq} & i_{id} & i_{iq} & V_d & I_{id_{ref}} & V_q & I_{iq_{ref}} \end{bmatrix}^T \tag{3.51}$$

$$A_{vsi}^{cl} = \begin{bmatrix} 0 & \omega & \frac{1}{C} & 0 & 0 & 0 & 0 & 0 \\ -\omega & 0 & 0 & \frac{1}{C} & 0 & 0 & 0 & 0 \\ -\frac{1}{L} & 0 & -\frac{R}{L} & \omega & \frac{1}{L} & 0 & 0 & 0 \\ 0 & -\frac{1}{L} & -\omega & -\frac{R}{L} & 0 & 0 & \frac{1}{L} & 0 \\ \sigma_2 & -k_{pi}k_{pv}\omega & \sigma_1 & -k_{pi}\omega & -\frac{k_{pi}}{L} & k_{ii} & 0 & 0 \\ -k_{iv} & -k_{pv}\omega & -\frac{k_{pv}}{C} & 0 & 0 & 0 & 0 & 0 \\ k_{pi}k_{pv}\omega & \sigma_2 & k_{pi}\omega & \sigma_1 & 0 & 0 & -\frac{k_{pi}}{L} & k_{ii} \\ k_{pv}\omega & -k_{iv} & 0 & -\frac{k_{pv}}{C} & 0 & 0 & 0 & 0 \end{bmatrix} \tag{3.52}$$

$$\sigma_1 = -k_{ii} - k_{pi}\left(\frac{k_{pv}}{C} - \frac{R}{L}\right) \tag{3.53}$$

$$\sigma_2 = -k_{pi}\left(k_{iv} - \frac{1}{L}\right) \tag{3.54}$$

$$G_{vsi}^{cl} = \begin{bmatrix} -\frac{1}{C} & 0 \\ 0 & -\frac{1}{C} \\ 0 & 0 \\ 0 & 0 \\ \frac{k_{pi}k_{pv}}{C} & 0 \\ \frac{k_{pv}}{C} & 0 \\ 0 & \frac{k_{pi}k_{pv}}{C} \\ 0 & \frac{k_{pv}}{C} \end{bmatrix} \tag{3.55}$$

$$C_{vsi}^{cl} = \begin{bmatrix} 1 & 0 & 0 & 0 & 0 & 0 & 0 & 0 \\ 0 & 1 & 0 & 0 & 0 & 0 & 0 & 0 \end{bmatrix} \tag{3.56}$$

The input of closed loop model (3.50) is $r_{vsi} = \begin{bmatrix} i_{ad} & i_{aq} \end{bmatrix}^T$ and output is $y_{vsi} = \begin{bmatrix} v_{cd} & v_{cq} \end{bmatrix}^T$. Therefore the transfer function from the input to output is the impedance model (3.57). Pay attention to that the positive direction of current $\begin{bmatrix} i_{ad} & i_{aq} \end{bmatrix}^T$ is defined as flowing out of VSI. Therefore there is a minus sign in (3.57) right after the equal sign.

$$Z_{vsi} = -C_{vsi}^{cl}(sI - A_{vsi}^{cl})^{-1}G_{vsi}^{cl} \tag{3.57}$$

A typical bode diagram of a VSI' impedance is shown in Fig.3.10. The parameters used to plot the bode diagram are shown in Table.4.1 and (4.56). Due to symmetry between d axis and q axis in both control link and power stage, the d-d axis impedance is same with q-q axis impedance shown here.
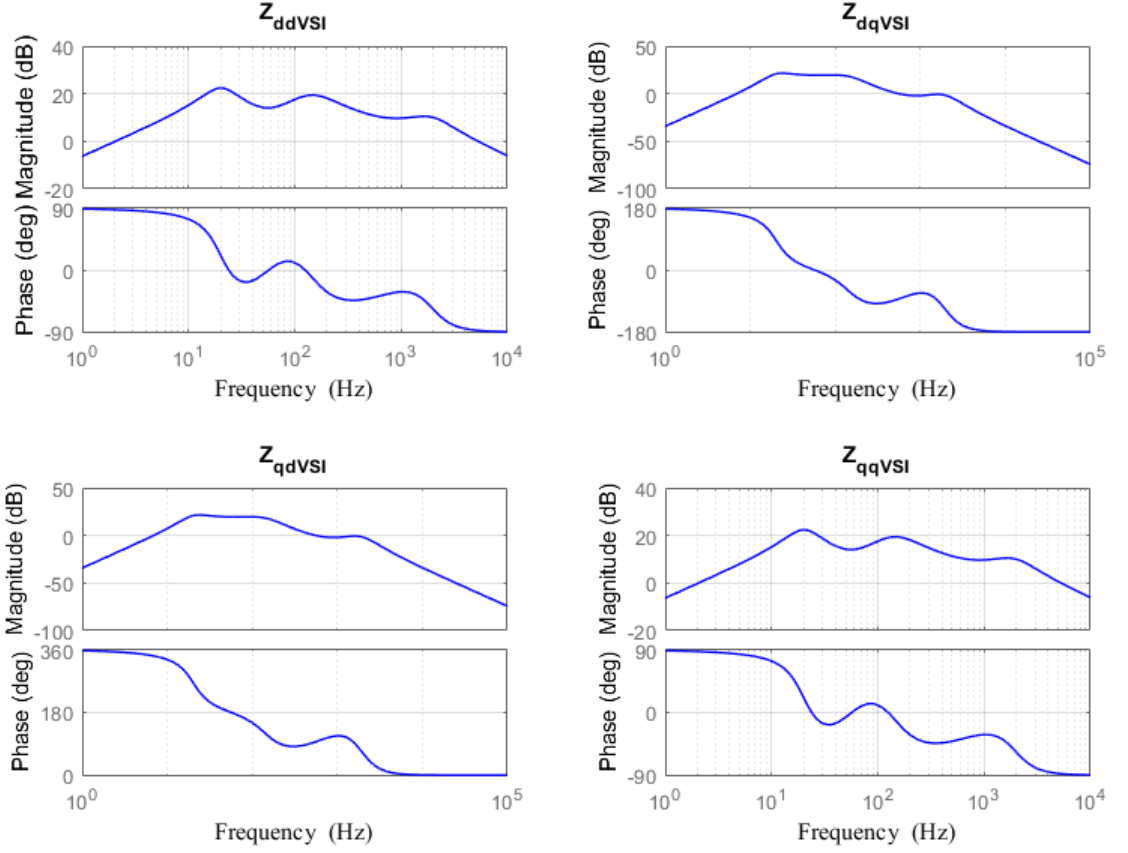
Figure 3.10: Bode diagram of impedance of VSI

3.3.3 Analytical impedance model of PI AFE

Notably, analytical models of AFE derived in this section are viewed in the VSI-dq frame, rather than in the PLL-dq frame which is generated by the PLL's estimated angle θ_p. Therefore, in addition to the equations of AFE (3.23) which are viewed in PLL-dq frame, the PLL equations are also engaged in the derivation of AFE impedance model here. It is also worth to point out that the choice of reference frame does not impact the judgement of system stability, as long as impedance models of the two inter-connected subsystems are examined in a same reference frame. As the VSI's impedance models are previously derived in the VSI-dq frame, the impedance of AFE is chosen to be derived in the VSI-dq frame as well.

According to the cascade PI control loop of AFE shown in Fig.3.11, control link equations of AFE can be formulated as

$$\dot{I}_{ad_{ref}} = k_{pv}(\dot{V}_{dca_{ref}} - \dot{V}_{dca}) + k_{iv}(V_{dca_{ref}} - V_{dca}) \tag{3.58a}$$

$$\dot{U}_d = k_{pi}(\dot{I}_{ad_{ref}} - \dot{I}_{ad}^p) + k_{ii}(I_{ad_{ref}} - I_{ad}^p) \tag{3.58b}$$
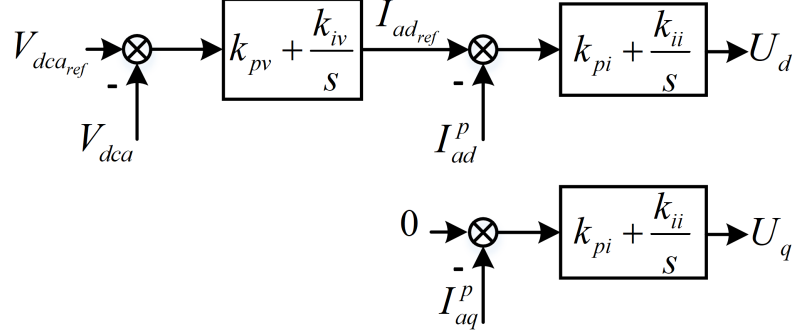
Figure 3.11: PI AFE control loop

$$\dot{U}_q = k_{pi}(\dot{I}_{aq_{ref}} - \dot{I}^p_{aq}) + k_{ii}(I_{aq_{ref}} - I^p_{aq}) \tag{3.58c}$$

$$p_d = \frac{2U_d}{V_{dca}} \tag{3.59}$$

$$p_q = \frac{2U_q}{V_{dca}} \tag{3.60}$$

where voltage command generated by the PI control link are denoted as U_d and U_q. Combine these equations with power stage equations (3.23) and reference frame transformation equations relating to PLL (3.11)(3.13)(3.14), and linearise the equations in the VSI-dq frame, the impedance model of AFE can be obtained as

$$\begin{cases} \dot{x}^{cl}_{afe} = A^{cl}_{afe}x^{cl}_{afe} + G^{cl}_{afe}r_{afe} \\ y_{afe} = C^{cl}_{afe}x^{cl}_{afe} \end{cases} \tag{3.61}$$

$$x^{cl}_{afe} = \begin{bmatrix} i_{ad} & i_{aq} & v_{dca} & I_{ad_{ref}} & U_d & U_q & \tilde{\theta}_e & \omega_i \end{bmatrix} \tag{3.62}$$

$$r_{afe} = \begin{bmatrix} v_{cd} & v_{cq} \end{bmatrix}^T \tag{3.63}$$

$$y_{afe} = \begin{bmatrix} i_{ad} & i_{aq} \end{bmatrix}^T \tag{3.64}$$

The content of those matrices including A^{cl}_{afe}, G^{cl}_{afe}, and C^{cl}_{afe} can be found in (B.2). Then the admittance of AFE with a PI controller can be formulated as the transfer function from interference $r_{afe} = \begin{bmatrix} v_{cd} & v_{cq} \end{bmatrix}^T$ to output $y_{afe} = \begin{bmatrix} i_{ad} & i_{aq} \end{bmatrix}^T$,

$$Y_{afe} = C^{cl}_{afe}(sI - A^{cl}_{afe})^{-1}G^{cl}_{afe} \tag{3.65}$$

3.3.4   Analytical impedance model of AFE with state feedback control

Assume K_{afe} is a general state feedback controller for AFE. Therefore, the output of AFE's controller is

$$u_{afe} = K_{afe}x_{afe} \tag{3.66}$$

Substitute it into (3.24), and the closed loop model of AFE is

$$\begin{cases} \dot{x}_{afe} = (A_{afe} + B_{afe}K_{afe})x_{afe} + G_{afe}r_{afe} \\ y_{afe} = C_{afe}x_{afe} \end{cases} \tag{3.67}$$

Impedance model obtained on the basis of this closed loop model is viewed in PLL-dq frame. In this case, bode diagrams of AFE's d-d axis impedance z_{dd} and q-q axis impedance z_{qq} in a typical design are shown in Fig.3.12.
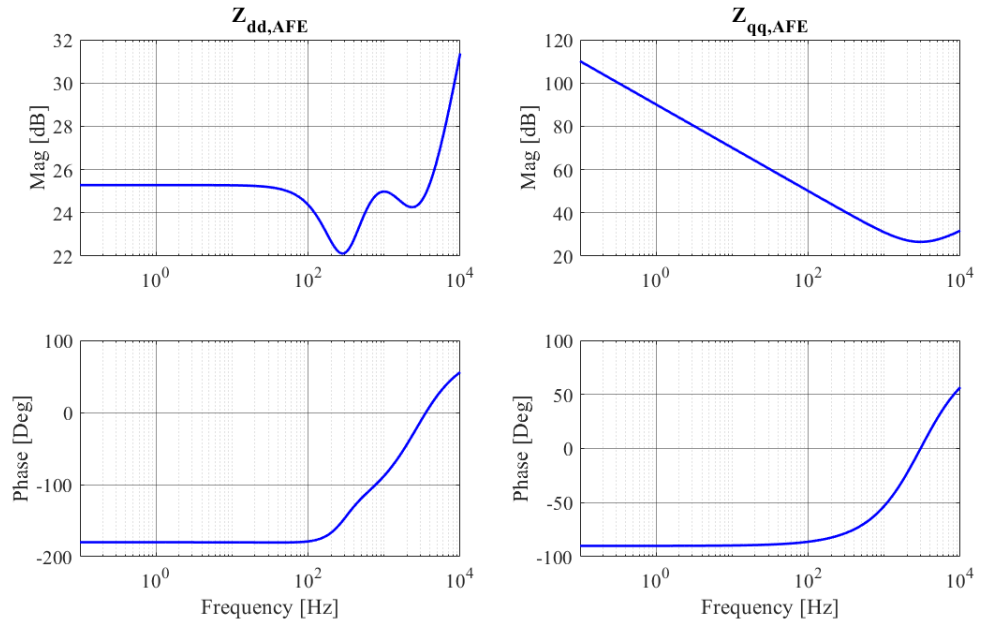
Figure 3.12: A typical bode diagram of the d-d and q-q axis impedance of AFE when it uses a state feedback controller without considering PLL

As can be seen from the figure, the phase of z_{dd} is $-180°$ in low frequencies. It means a negative resistance behavior in AFE's power deliver channel, namely d-d axis as a result of regulating output voltage. The negative resistance feature will create a $180°$ traverse in the phase plot and therefore an instability concern when the AFE interacts with a VSI. The Fig.3.12 is provided here as a

reference for analysis in later chapters when plotting and inspecting the bode plot of impedance ratio from VSI to AFE.

For the ease of formatting equations, define $a = A_{afe} + B_{afe}K_{afe}$. Apparently, a is the closed loop state matrix of AFE and a 5 by 5 matrix. Denote its element on ith row and jth column as a_{ij}. In this equation, all the variables are in the PLL-dq frame, therefore it needs to be transformed into the VSI-dq frame.

Expand (3.67),

$$\dot{I}_{ad}^p = a_{11}I_{ad}^p + a_{12}I_{aq}^p + a_{13}V_{dca} + a_{14}W_{i_{aq}} + a_{15}W_{v_{dca}} + \frac{1}{L_a}V_{cd}^p \tag{3.68a}$$

$$\dot{I}_{aq}^p = a_{21}I_{ad}^p + a_{22}I_{aq}^p + a_{23}V_{dca} + a_{24}W_{i_{aq}} + a_{25}W_{v_{dca}} + \frac{1}{L_a}V_{cq}^p \tag{3.68b}$$

$$\dot{V}_{dca} = a_{31}I_{ad}^p + a_{32}I_{aq}^p + a_{33}V_{dca} + a_{34}W_{i_{aq}} + a_{35}W_{v_{dca}} \tag{3.68c}$$

$$\dot{W}_{i_{aq}} = a_{41}I_{ad}^p + a_{42}I_{aq}^p + a_{43}V_{dca} + a_{44}W_{i_{aq}} + a_{45}W_{v_{dca}} \tag{3.68d}$$

$$\dot{W}_{v_{dca}} = a_{51}I_{ad}^p + a_{52}I_{aq}^p + a_{53}V_{dca} + a_{54}W_{i_{aq}} + a_{55}W_{v_{dca}} \tag{3.68e}$$

Substitute (3.12) into the equations above,

$$\dot{I}_{ad}^p = \dot{I}_{ad} = a_{11}I_{ad} + a_{12}(-\tilde{\theta}_e I_{ad}^* + I_{aq}) + a_{13}V_{dca} + a_{14}W_{i_{aq}} + a_{15}W_{v_{dca}} + \frac{1}{L_a}V_{cd} \tag{3.69a}$$

$\Rightarrow$

$$\dot{I}_{ad} = a_{11}I_{ad} + a_{12}I_{aq} + a_{13}V_{dca} + a_{14}W_{i_{aq}} + a_{15}W_{v_{dca}} - a_{12}I_{ad}^*\tilde{\theta}_e + \frac{1}{L_a}V_{cd} \tag{3.69b}$$

$$\dot{I}_{aq}^p = -I_{ad}^*\dot{\tilde{\theta}}_e + \dot{I}_{aq} = a_{21}I_{ad} + a_{22}(-\tilde{\theta}_e I_{ad}^* + I_{aq}) + a_{23}V_{dca} + a_{24}W_{i_{aq}} + a_{25}W_{v_{dca}} + \frac{1}{L_a}(-\tilde{\theta}_e V_{cd}^* + V_{cq}) \tag{3.70a}$$

$\Rightarrow$

$$\dot{I}_{aq} = a_{21}I_{ad} + a_{22}(-\tilde{\theta}_e I_{ad}^* + I_{aq}) + a_{23}V_{dca} + a_{24}W_{i_{aq}} + a_{25}W_{v_{dca}} - \frac{1}{L_a}V_{cd}^*\tilde{\theta}_e + \frac{1}{L_a}V_{cq} + I_{ad}^*\dot{\tilde{\theta}}_e \tag{3.70b}$$

According to (3.13),

$$\dot{\theta}_e = k_p^p(-V_{cd}^*\tilde{\theta}_e + V_{cq}) + \omega_i \tag{3.71}$$

Substitute it into (3.70b),

$$\dot{I}_{aq} = a_{21}I_{ad} + a_{22}(-\tilde{\theta}_e I_{ad}^* + I_{aq}) + a_{23}V_{dca} + a_{24}W_{i_{aq}} + a_{25}W_{v_{dca}}$$
$$- \frac{1}{L_a}V_{cd}^*\tilde{\theta}_e + \frac{1}{L_a}V_{cq} + I_{ad}^*(k_p^p(-V_{cd}^*\tilde{\theta}_e + V_{cq}) + \omega_i) \tag{3.72a}$$

$\Rightarrow$

$$
\begin{aligned}
\dot{I}_{aq} =&\, a_{21}I_{ad} + a_{22}I_{aq} + a_{23}V_{dca} + a_{24}W_{i_{aq}} + a_{25}W_{v_{dca}} \\
&+ (k_p^p I_{ad}^* + \frac{1}{L_a})V_{cq} - (a_{22}I_{ad}^* + \frac{1}{L_a}V_{cd}^* + k_p^p I_{ad}^* V_{cd}^*)\tilde{\theta}_e + I_{ad}^*\omega_i
\end{aligned}
\tag{3.72b}
$$

$$
\dot{V}_{dca} = a_{31}I_{ad} + a_{32}(-\tilde{\theta}_e I_{ad}^* + I_{aq}) + a_{33}V_{dca} + a_{34}W_{i_{aq}} + a_{35}W_{v_{dca}}
\tag{3.73}
$$

$$
\dot{W}_{i_{aq}} = a_{41}I_{ad} + a_{42}(-\tilde{\theta}_e I_{ad}^* + I_{aq}) + a_{43}V_{dca} + a_{44}W_{i_{aq}} + a_{45}W_{v_{dca}}
\tag{3.74}
$$

$$
\dot{W}_{v_{dca}} = a_{51}I_{ad} + a_{52}(-\tilde{\theta}_e I_{ad}^* + I_{aq}) + a_{53}v_{dca} + a_{54}W_{i_{aq}} + a_{55}W_{v_{dca}}
\tag{3.75}
$$

Combine (3.69b)(3.72b)(3.73)(3.74)(3.75) together, full closed-loop model of the AFE including PLL in VSI-dq frame can be obtained as

$$
\begin{bmatrix}
\dot{i}_{ad} \\
\dot{i}_{aq} \\
\dot{v}_{dca} \\
\dot{w}_{i_{aq}} \\
\dot{w}_{v_{dca}} \\
\dot{\theta}_e \\
\dot{\omega}_i
\end{bmatrix}
=
\begin{bmatrix}
a_{11} & a_{12} & a_{13} & a_{14} & a_{15} & -a_{12}I_{ad}^* & 0 \\
a_{21} & a_{22} & a_{23} & a_{24} & a_{25} & -(\frac{1}{L_a}V_{cd}^* + a_{22}I_{ad}^* + k_p^p I_{ad}^* V_{cd}^*) & I_{ad}^* \\
a_{31} & a_{32} & a_{33} & a_{34} & a_{35} & -a_{32}I_{ad}^* & 0 \\
a_{41} & a_{42} & a_{43} & a_{44} & a_{45} & -a_{42}I_{ad}^* & 0 \\
a_{51} & a_{52} & a_{53} & a_{54} & a_{55} & -a_{52}I_{ad}^* & 0 \\
0 & 0 & 0 & 0 & 0 & -k_p^p V_{cd}^* & 1 \\
0 & 0 & 0 & 0 & 0 & -k_i^p V_{cd}^* & 0
\end{bmatrix}
\begin{bmatrix}
i_{ad} \\
i_{aq} \\
v_{dca} \\
w_{i_{aq}} \\
w_{v_{dca}} \\
\tilde{\theta}_e \\
\omega_i
\end{bmatrix}
$$

$$
+
\begin{bmatrix}
\frac{1}{L_a} & 0 \\
0 & k_p^p I_{ad}^* + \frac{1}{L_a} \\
0 & 0 \\
0 & 0 \\
0 & 0 \\
0 & k_p^p \\
0 & k_i^p
\end{bmatrix}
\begin{bmatrix}
v_{cd} \\
v_{cq}
\end{bmatrix}
\tag{3.76}
$$

If denote it in a compressed form,

$$
\begin{cases}
\dot{x}_{afe}' = A_{afe}' x_{afe}' + G_{afe}' r_{afe}' \\
y_{afe}' = C_{afe}' x_{afe}'
\end{cases}
\tag{3.77}
$$

where

$$
\dot{x}_{afe}' = \begin{bmatrix} i_{ad} & i_{aq} & v_{dca} & w_{i_{aq}} & w_{v_{dca}} & \tilde{\theta}_e & \omega_i \end{bmatrix}^T
\tag{3.78}
$$

$$
r_{afe}' = \begin{bmatrix} v_{cd} & v_{cq} \end{bmatrix}^T
\tag{3.79}
$$

$$y'_{afe} = \begin{bmatrix} i_{ad} & i_{aq} \end{bmatrix}^T \tag{3.80}$$

$$C'_{afe} = \begin{bmatrix} 1 & 0 & 0 & 0 & 0 & 0 & 0 \\ 0 & 1 & 0 & 0 & 0 & 0 & 0 \end{bmatrix} \tag{3.81}$$

then the admittance of AFE with a state feedback controller in VSI-dq frame is

$$Y_{afe} = C'_{afe}(sI - A'_{afe})^{-1}G'_{afe} \tag{3.82}$$

3.3.5 PLL's impact on admittance of AFE

In the equations above, the admittance of AFE is calculated with consideration of PLL. It is well known that regarding to grid-connected voltage source inverters, the presence of PLL makes the inverters feature negative resistance behavior in its q-q axis and introduces a significant concern of instability [13, 127]. The bandwidth of PLL determines the frequency range of negative resistance behavior. As for a load-interfaced converter, due to its feature of regulating output voltage, it also shows negative resistance behavior in its power deliver channel, namely d-d axis, which can be seen in the Fig.3.12. In this part, the impact of PLL on AFE's admittance and further system stability is assessed in detail.

At first, a schematic figure showing different definitions of AFE's admittance relating to PLL is presented in Fig.3.13.
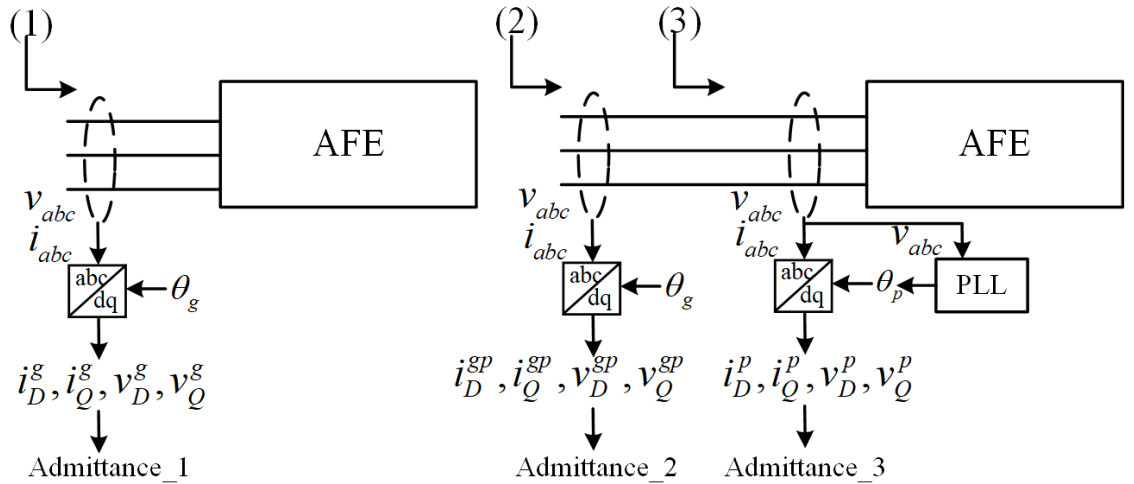
Figure 3.13: PLL and definitions of AFE's admittance

In the Fig.3.13, i_D^g, i_Q^g, v_D^g, v_Q^g denote the instant value of AC bus currents and voltages in the grid-dq frame when the AFE does not include a PLL. i_D^{gp}, i_Q^{gp}, v_D^{gp}, v_Q^{gp} denote the instant value of

currents and voltages in grid-dq frame when the AFE includes a PLL. i_D^p, i_Q^p, v_D^p, v_Q^p denote the instant value of currents and voltages in PLL-dq frame when the AFE includes a PLL.

The instant values can be expressed as sum of a dc value (i.e. the equilibrium value of corresponding variable) and a tiny variation. Take the voltages in PLL-dq frame as an example,

$$\begin{bmatrix} v_D^p \\ v_Q^p \end{bmatrix} = \begin{bmatrix} V_D + v_d^p \\ V_Q + v_q^p \end{bmatrix} \tag{3.83}$$

The terms denoted with capital letters are dc values of the corresponding quantities. Apparently, V_D equals the d-axis voltage equilibrium value V_{cd}^* and V_Q equals the q-axis voltage equilibrium value 0. The terms with lower-case letter subscripts are tiny variations.

Depending on the different positions where we look into AFE, marked as (1), (2) and (3) in the Fig.3.13, the admittance of AFE has 3 different forms. The currents and voltages obtained at (3) are in the PLL-dq frame, which is transformed by rotating the grid-dq reference frame with $\tilde{\theta}_e$, as shown in the Fig.3.5.

$$\begin{bmatrix} v_D^p \\ v_Q^p \end{bmatrix} = T(\tilde{\theta}_e) \begin{bmatrix} v_D^g \\ v_D^g \end{bmatrix}, \begin{bmatrix} i_D^p \\ i_Q^p \end{bmatrix} = T(\tilde{\theta}_e) \begin{bmatrix} i_D^g \\ i_D^g \end{bmatrix}, \tag{3.84}$$

Both the voltage axis and current axis are rotated by the same degree $\tilde{\theta}_e$. Therefore their ratio, i.e. the admittance obtained at position (3) is same with the one obtained at position (1). Namely, in the Fig.3.13, *admittance_1* is equal to *admittance_3*, as shown in (3.85)(3.86).

$$y_{dd\_afe} = \frac{i_d^g}{v_d^g} = \frac{i_d^p}{v_d^p}, y_{dq\_afe} = \frac{i_d^g}{v_q^g} = \frac{i_d^p}{v_q^p} \tag{3.85}$$

$$y_{qd\_afe} = \frac{i_q^g}{v_d^g} = \frac{i_q^p}{v_d^p}, y_{qq\_afe} = \frac{i_q^g}{v_q^g} = \frac{i_q^p}{v_q^p} \tag{3.86}$$

In a conclusion, when the AFE includes a PLL, the AFE's admittance obtained in the AFE's own dq frame is equal to the admittance seen from the grid when the AFE does not includes a PLL.

And the impact of PLL on the admittance of AFE will be manifested by the *admittance_2*, which is obtained at (2) in the Fig.3.13. It is the admittance seen from grid side when the AFE includes a PLL. Current and voltage quantities obtained here are marked with superscripts 'gp'. It is obvious that

$$\begin{bmatrix} v_D^p \\ v_Q^p \end{bmatrix} = \begin{bmatrix} V_D + v_d^p \\ V_Q + v_q^p \end{bmatrix} = \begin{bmatrix} cos\tilde{\theta}_e & sin\tilde{\theta}_e \\ -sin\tilde{\theta}_e & cos\tilde{\theta}_e \end{bmatrix} \begin{bmatrix} v_D^{gp} \\ v_Q^{gp} \end{bmatrix} = \begin{bmatrix} cos\tilde{\theta}_e & sin\tilde{\theta}_e \\ -sin\tilde{\theta}_e & cos\tilde{\theta}_e \end{bmatrix} \begin{bmatrix} V_D + v_d^{gp} \\ V_Q + v_q^{gp} \end{bmatrix} \tag{3.87}$$

$$\begin{bmatrix} V_D + v_d^p \\ V_Q + v_q^p \end{bmatrix} \approx \begin{bmatrix} 1 & \tilde{\theta}_e \\ -\tilde{\theta}_e & 1 \end{bmatrix} \begin{bmatrix} V_D + v_d^{gp} \\ V_Q + v_q^{gp} \end{bmatrix} \tag{3.88}$$

Neglect the second order infinitesimals (i.e. $\tilde{\theta}_e v_q^{gp}$ and $\tilde{\theta}_e v_d^{gp}$),

$$\begin{bmatrix} v_d^p \\ v_q^p \end{bmatrix} \approx \begin{bmatrix} v_d^{gp} \\ -V_D \tilde{\theta}_e + v_q^{gp} \end{bmatrix} \tag{3.89}$$

Hence the d-axis voltage small variations in the two reference frames i.e. v_d^p and v_d^{gp} are equal. Similarly, i_d^p and i_d^{gp} are equal as well, as shown in the (3.90).

$$\begin{bmatrix} i_d^p \\ i_q^p \end{bmatrix} \approx \begin{bmatrix} i_d^{gp} \\ -I_D \tilde{\theta}_e + i_q^{gp} \end{bmatrix} \tag{3.90}$$

Therefore, their ratio, namely d-d axis admittance are the same as well. In other words, PLL has no impact on d-d axis admittance of AFE.

$$y_{dd\_afe}^{gp} = \frac{i_d^{gp}}{v_d^{gp}} = \frac{i_d^p}{v_d^p} = y_{dd\_afe} \tag{3.91}$$

Next, the situation of q-q axis is analysed. According to Fig.3.4, the open loop transfer function of PLL PI is

$$G^p = (k_p^p + k_i^p \frac{1}{s}) \tag{3.92}$$

Therefore the identified phase angle by PLL can be expressed as

$$\tilde{\theta}_e = G^{op} v_q^p \tag{3.93}$$

where

$$G^{op} = G^p \frac{1}{s} \tag{3.94}$$

Therefore,

$$s\tilde{\theta}_e = G^p(-V_D \tilde{\theta}_e + v_q^{gp}) \tag{3.95}$$

Simplify above equation

$$\tilde{\theta}_e = \frac{G^p}{s + V_D G^p} v_q^{gp} \tag{3.96}$$

Therefore the output of PLL $\tilde{\theta}_e$ is not related to the d-axis voltage variations v_d^{gp}. In other words, the PLL will not affect the admittances associated with d-axis perturbations, namely y_{dd_afe} and y_{qd_afe}.

$$y_{dd\_afe}^{gp} = y_{dd\_afe} \tag{3.97}$$

$$y_{qd\_afe}^{gp} = y_{qd\_afe} \tag{3.98}$$

As to the q-axis perturbations v_q^{gp}, it will be filtered by the PLL's internal PI in the high frequency range, hence it will not affect PLL's output as well. So in the high frequency range,

$$y_{dq\_afe}^{gp} = y_{dq\_afe} \tag{3.99}$$

$$y_{qq\_afe}^{gp} = y_{qq\_afe} \tag{3.100}$$
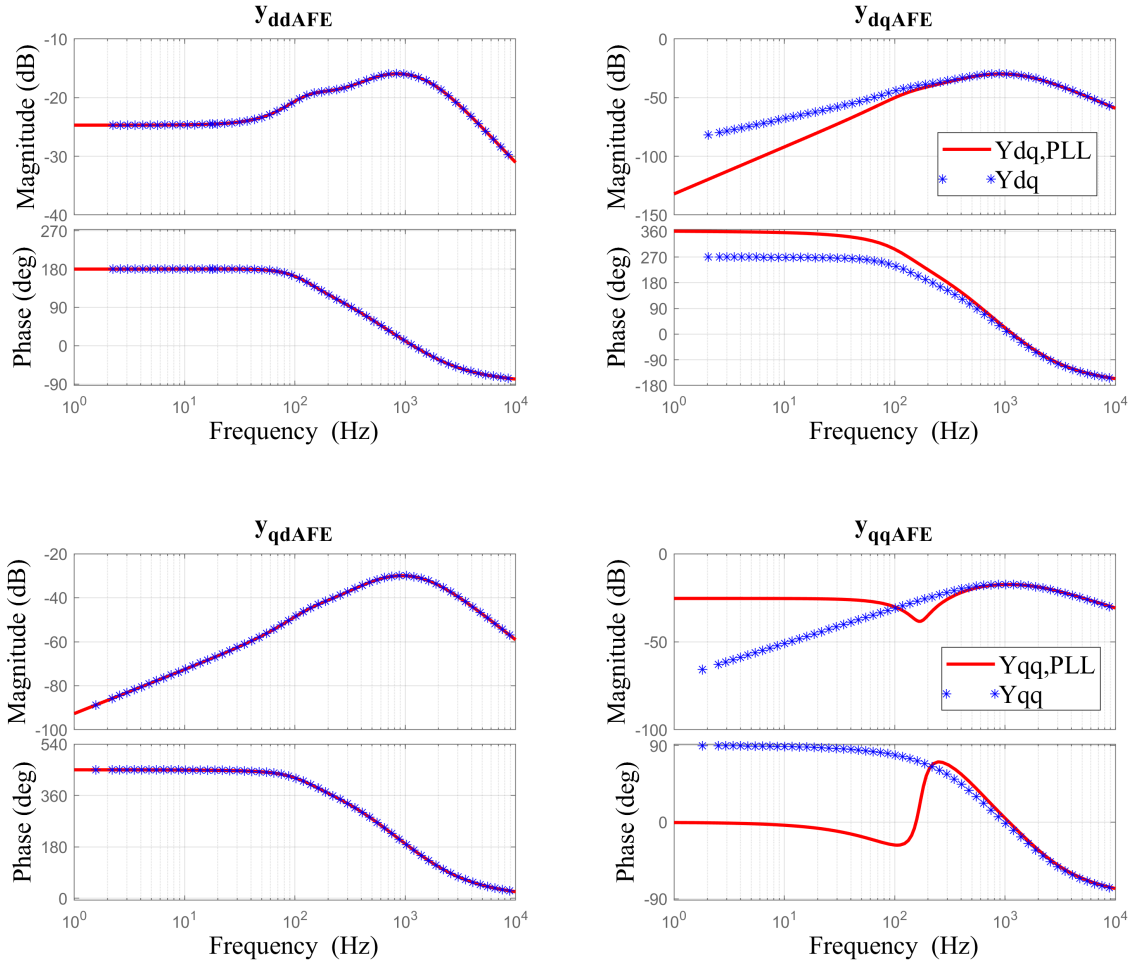
Figure 3.14: PLL's impact on the shape of AFE's admittance

It is confirmed by Fig.3.14. In the Fig.3.14, AFE's admittance with and without PLL are plotted together. Red curves show the bode diagrams of AFE's admittance including a PLL while the blue curves show results when AFE does not have a PLL. Therefore only the situation of y_{dq_afe} and y_{qq_afe} in low frequency range remains to be investigated. According to (3.89)(3.90)(3.93),

$$y_{dq\_afe}^{gp} = \frac{i_d^{gp}}{v_q^{gp}} \approx \frac{i_d^p}{V_D \tilde{\theta}_e + v_q^p} = \frac{i_d^p}{V_D G^{op} v_q^p + v_q^p} = \frac{1}{V_D G^{op} + 1} y_{dq\_afe} \tag{3.101}$$

$$y_{qq\_afe}^{gp} = \frac{i_q^{gp}}{v_q^{gp}} \approx \frac{I_D \tilde{\theta}_e + i_q^p}{V_D \tilde{\theta}_e + v_q^p} = \frac{I_D G^{op} v_q^p + i_q^p}{V_D G^{op} v_q^p + v_q^p} = \frac{I_D G^{op} + y_{qq\_afe}}{V_D G^{op} + 1} \tag{3.102}$$

As can be seen in Fig.3.15, in the low frequency range,

$$\|I_D G^{op}\| >> \|y_{qq\_afe}\| \tag{3.103}$$

$$\|V_D G^{op}\| >> 1 \tag{3.104}$$
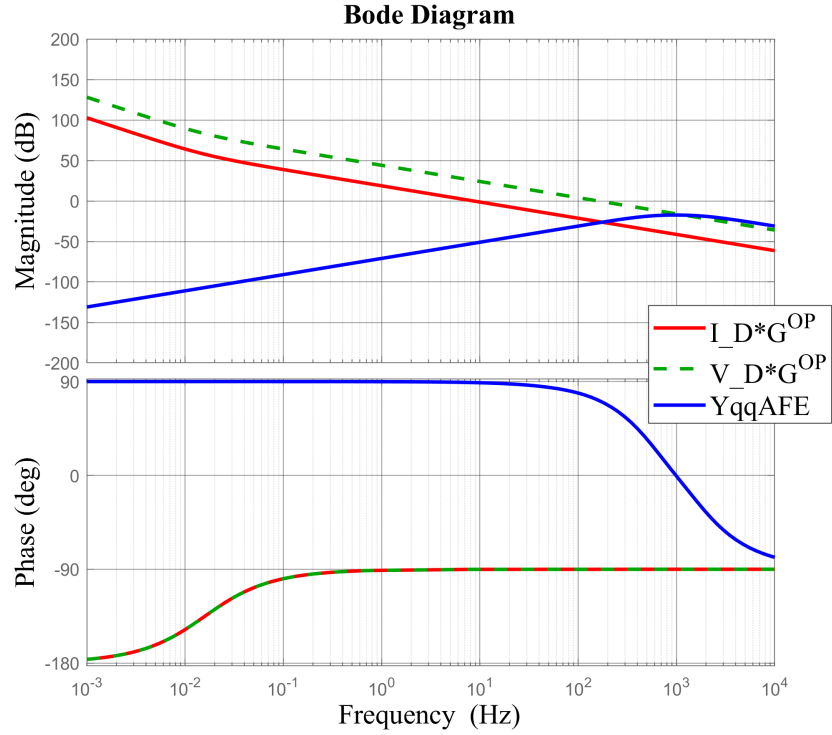
Figure 3.15: Bode diagrams of $I_D G^{op}$, $V_D G^{op}$ and y_{qq_afe}

Therefore, (3.102) is degraded to

$$y_{qq\_afe}^{gp} \approx \frac{I_D G^{op}}{V_D G^{op}} = \frac{I_D}{V_D} = 20 \cdot log_{10}(I_{ad}^*/V_{cd}^*)[dB] \tag{3.105}$$

It means the q-q axis admittance $y_{qq\_afe}^{gp}$ is pure resistive in the low frequency range, as shown in the Fig.3.14. The resistance value is determined by the ratings of AFE, as shown in (3.105). As for the d-q axis admittance $y_{dq\_afe}^{gp}$, the magnitude is attenuated by the term $V_D G^{op} + 1$ furthermore.

As the frequency increases, the magnitude of y_{qq_afe} increases and $I_D G^{op}$ decrease. In the middle frequency range, there exists one frequency (here around 180Hz as shown in the Fig.3.14)

at which $I_D G^{op}$ and y_{qq_afe} are cancelled so it appears a valley in the shape of $y_{qq\_afe}^{gp}$. The cancellation is due to comparable magnitude and inverted phase of y_{qq_afe} and $I_D G^{op}$, as shown in the Fig.3.15.

By the use of impedance model of VSI, of which the bode diagram in a typical design is shown in Fig.3.10, impedance ratio for the VSI-AFE+PLL system can be obtained and its bode diagram is shown in the Fig.3.16. The analytical expression of impedance ratio is provided by (3.114).
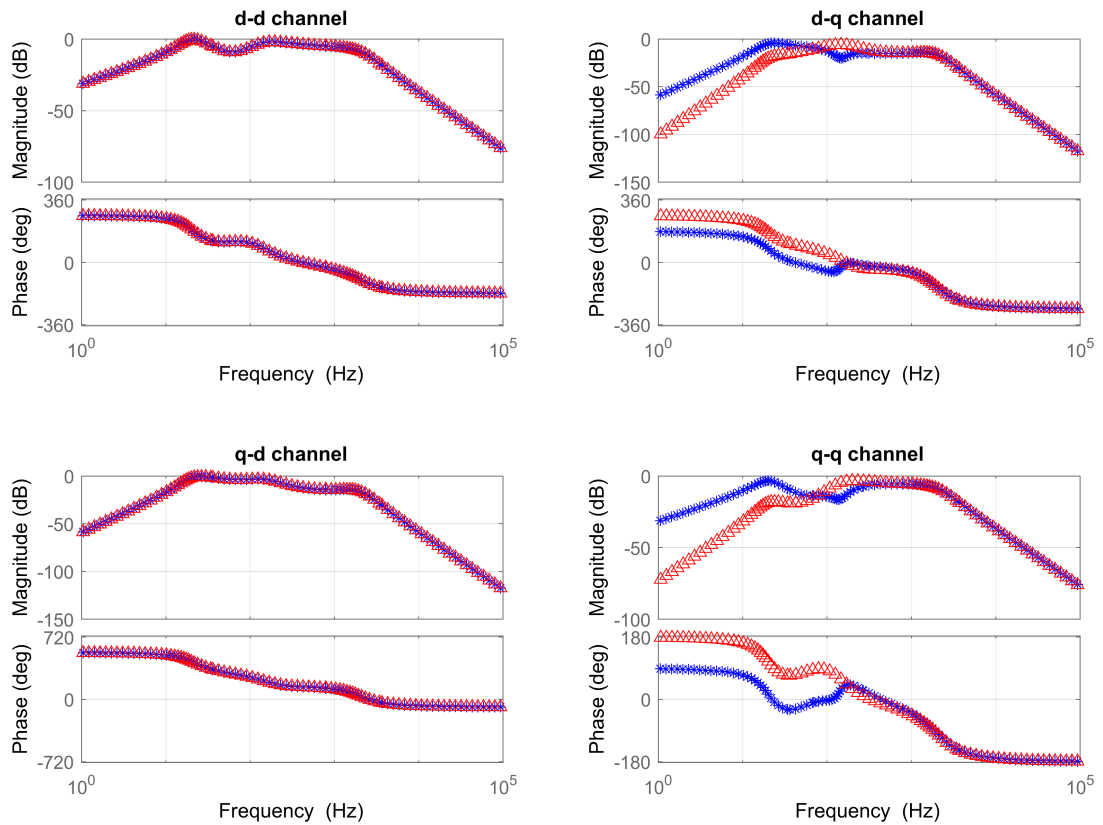
Figure 3.16: Bode diagram of impedance ratio between VSI and AFE when AFE does not include a PLL (shown by red curves) and does include a PLL (shown by blue curves)

The impedance ratio when AFE does not include a PLL is shown with red curves. The case when AFE has a PLL is shown with blue curves. As can be seen, the addition of PLL does not create new $-180°$ traverses on the basis of red curves. In conclusion, the presence of PLL will not introduce additional concerns with system instability.

3.4 Characteristic loci of VSI-AFE system

In this research, both the source converter (VSI) and load converter (AFE) are modelled in the dq reference frame and can be characterized by 2 by 2 impedance matrices. Denote VSI's impedance and AFE's admittance matrices as $Z_s(s)$ and $Y_l(s)$ respectively.

$$Z_s(s) = \begin{bmatrix} Z_{dd}(s) & Z_{dq}(s) \\ Z_{qd}(s) & Z_{qq}(s) \end{bmatrix} \tag{3.106}$$

$$Y_l(s) = \begin{bmatrix} Y_{dd}(s) & Y_{dq}(s) \\ Y_{qd}(s) & Y_{qq}(s) \end{bmatrix} \tag{3.107}$$

Therefore the transfer function defined in (2.15) becomes

$$
\begin{aligned}
H(s) &= \frac{I}{I + Z_s(s)Y_l(s)} \\
&= \frac{I}{\begin{bmatrix} 1 & 0 \\ 0 & 1 \end{bmatrix} + \begin{bmatrix} Z_{dd}(s) & Z_{dq}(s) \\ Z_{qd}(s) & Z_{qq}(s) \end{bmatrix} \begin{bmatrix} Y_{dd}(s) & Y_{dq}(s) \\ Y_{qd}(s) & Y_{qq}(s) \end{bmatrix}} \\
&= \frac{I}{\begin{bmatrix} 1 & 0 \\ 0 & 1 \end{bmatrix} + \begin{bmatrix} Z_{dd}(s)Y_{dd}(s) + Z_{dq}(s)Y_{qd}(s) & Z_{dd}(s)Y_{dq}(s) + Z_{dq}(s)Y_{qq}(s) \\ Z_{qd}(s)Y_{dd}(s) + Z_{qq}(s)Y_{qd}(s) & Z_{qd}(s)Y_{dq}(s) + Z_{qq}(s)Y_{qq}(s) \end{bmatrix}}
\end{aligned}
\tag{3.108}
$$

If the d-axis and q-axis are decoupled well through the proper control design, the $Z_{dq}(s)$ and $Z_{qd}(s)$ would be much less than $Z_{dd}(s)$ and $Z_{qq}(s)$, and $Y_{dq}(s)$ and $Y_{qd}(s)$ would be much less than $Y_{dd}(s)$ and $Y_{qq}(s)$. Then (3.108) will degrade to be

$$
\begin{aligned}
H(s) &= \frac{I}{I + Z_s(s)Y_l(s)} = \frac{I}{\begin{bmatrix} 1 & 0 \\ 0 & 1 \end{bmatrix} + \begin{bmatrix} Z_{dd}(s)Y_{dd}(s) & 0 \\ 0 & Z_{qq}(s)Y_{qq}(s) \end{bmatrix}} \\
&= \begin{bmatrix} \frac{1}{1+Z_{dd}(s)Y_{dd}(s)} & 0 \\ 0 & \frac{1}{1+Z_{qq}(s)Y_{qq}(s)} \end{bmatrix}
\end{aligned}
\tag{3.109}
$$

Therefore, the system stability is equivalent to that of two terms, i.e.

$$\frac{1}{1 + Z_{dd}(s)Y_{dd}(s)}, \frac{1}{1 + Z_{qq}(s)Y_{qq}(s)} \tag{3.110}$$

Hence the system stability can be assessed in two separate channels (d-d axis and q-q axis) sequentially. The system is deemed as stable if both the two channels satisfy the stability criterion. It is convenient to implement the system stability analysis by plotting the Nyquist curves of the two impedance ratios (i.e. $Z_{dd}(s)Y_{dd}(s)$ and $Z_{qq}(s)Y_{qq}(s)$). It is worth noting that this is an accurate way only if the coupling impedances $Z_{dq}(s)$, $Z_{qd}(s)$, $Y_{dq}(s)$ and $Y_{qd}(s)$ are negligible.

In the following, the rigorous approach without neglecting the coupling impedances will be detailed.

Consider a SISO system with negative unity feedback control and $L(s)$ as the loop transfer function matrix shown in Fig.3.17. The system stability is determined by the characteristic polynomial $1 + L(s)$. As noted the stability of a linear system is equivalent to the system having no poles in the closed right half plane. Namely, there are no solutions of $1 + L(s) = 0$ locating in right half plane. Otherwise, the system is unstable.
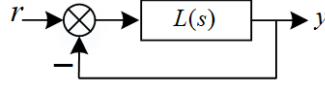
Figure 3.17: A SISO system with negative unity feedback

However, for a MIMO system, the $I + L(s)$ is a matrix instead of a scalar. According to derivations in Appendix (B.1) [128],

$$det(I + L(s)) = \frac{\phi_{cl}(s)}{\phi_{ol}(s)}c \tag{3.111}$$

$\phi_{cl}(s)$ and $\phi_{ol}(s)$ are the closed loop and open loop characteristic polynomials of the system. c is a constant which is of no significance when evaluating the poles. Therefore, we have that the closed-loop poles are solutions to

$$det(I + L(s)) = 0 \tag{3.112}$$

According to the knowledge of eigen value properties, the solutions of $det(I + L(s)) = 0$ are equivalent to roots of

$$\prod_{i=1}^{m}(1 + \lambda_i(s)) = 0 \tag{3.113}$$

$\lambda_i(s)$ denotes the eigenvalues of $L(s)$ and m denotes the dimension of $L(s)$. In all, the MIMO system closed loop stability could be determined by checking whether $1 + \lambda_i(s) = 0$ has right half plane solutions. This is identical to checking the Nyquist contours of $\lambda_i(s)$. If the contours encircle $(-1, j0)$, the system is unstable. These Nyquist contours are called as characteristic loci.

In this research, the impedance of VSI (3.106) and admittance of AFE (3.107) are calculated by the method stated in Sec.3.3. Then $L(s)$ could be built upon such impedance/admittance models.

$$L(s) = \begin{bmatrix} Z_{dd}(s)Y_{dd}(s) + Z_{dq}(s)Y_{qd}(s) & Z_{dd}(s)Y_{dq}(s) + Z_{dq}(s)Y_{qq}(s) \\ Z_{qd}(s)Y_{dd}(s) + Z_{qq}(s)Y_{qd}(s) & Z_{qd}(s)Y_{dq}(s) + Z_{qq}(s)Y_{qq}(s) \end{bmatrix} \tag{3.114}$$

Then the 2 eigenvalues of this matrix, λ_1 and λ_2, could be calculated at each specific frequency. Sweep the frequency range and calculate the eigenvalues for every frequency, and the 2 characteristic loci could be plotted by concatenating the λ_1 and λ_2 respectively in the complex plane. A Matlab script used in this research to implement this procedure is included in Appendix C.2.

In an exemplary figure of characteristic loci shown in Fig.3.18, the two contours do not encircle the critical point $(-1, 0i)$ and therefore the system that it is representing is predicted to be stable. Notably, the impedance-based stability criterion has 2 preconditions, i.e. the subsystems should be stable in standalone conditions.
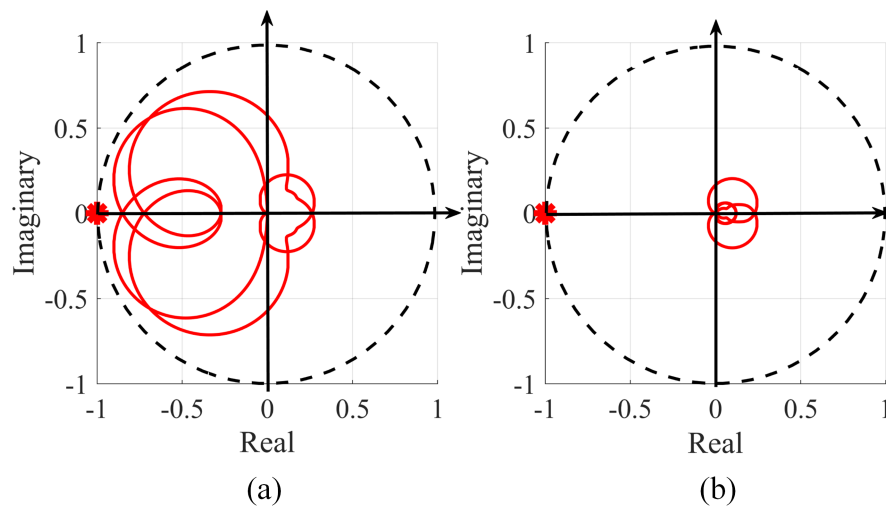
Figure 3.18: Characteristic loci of an exemplary stable system

A conservative stability criterion is that the source impedance should be smaller than the load impedance, i.e. $\|Z_{source}\| < \|Z_{load}\|$ at all frequencies, which means the contours should locate inside the unity circle. However, the system shown in Fig.3.18 is stable while its characteristic loci do not meet this condition. Actually, a more general criterion is the curve never traverse the negative real axis on the left of $(-1, j0)$. If so, the system is stable. Interpreting it into scenario of impedance specification, it means in the frequency range where the source impedance magnitude is bigger than that of the load impedance, the phase difference never exceeds $180°$.

3.5 Poles of the VSI-AFE system model

System stability could also be judged by poles of system model. If all the poles have negative real part, the system is stable. In this research, calculation of the system poles serves as an ancillary method to assess system stability. In this section, analytical system models for poles calculation

are built when VSI and AFE adopting different control schemes. Once the system closed loop model is available, the poles can be worked out by calculating eigenvalues of the state matrices.

3.5.1   Poles of the PI VSI - PI AFE system

The closed loop model of VSI with a PI controller is shown in (3.50) and copied to here as

$$\begin{cases} \dot{x}_{vsi}^{cl} = A_{vsi}^{cl} x_{vsi}^{cl} + G_{vsi}^{cl} r_{vsi} \\ y_{vsi} = C_{vsi}^{cl} x_{vsi}^{cl} \end{cases} \tag{3.115}$$

Input and output of the model are $r_{vsi} = \begin{bmatrix} i_{ad} & i_{aq} \end{bmatrix}^T$ and $y_{vsi} = \begin{bmatrix} v_{cd} & v_{cq} \end{bmatrix}^T$ respectively. The closed loop model of AFE with a PI controller is shown in (3.61) and copied to here as

$$\begin{cases} \dot{x}_{afe}^{cl} = A_{afe}^{cl} x_{afe}^{cl} + G_{afe}^{cl} r_{afe} \\ y_{afe} = C_{afe}^{cl} x_{afe}^{cl} \end{cases} \tag{3.116}$$

Input and output of the model are $r_{afe} = \begin{bmatrix} v_{cd} & v_{cq} \end{bmatrix}^T$ and $y_{afe} = \begin{bmatrix} i_{ad} & i_{aq} \end{bmatrix}^T$ respectively. Obviously,

$$r_{vsi} = \begin{bmatrix} i_{ad} \\ i_{aq} \end{bmatrix} = y_{afe} = C_{afe}^{cl} x_{afe}^{cl} \tag{3.117}$$

Substitute it into (3.115),

$$\dot{x}_{vsi}^{cl} = A_{vsi}^{cl} x_{vsi}^{cl} + G_{vsi}^{cl} C_{afe}^{cl} x_{afe}^{cl} \tag{3.118}$$

Likewise notice that

$$r_{afe} = \begin{bmatrix} v_{cd} \\ v_{cq} \end{bmatrix} = y_{vsi} = C_{vsi}^{cl} x_{vsi}^{cl} \tag{3.119}$$

Substitute it into (3.116),

$$\dot{x}_{afe}^{cl} = A_{afe}^{cl} x_{afe}^{cl} + G_{afe}^{cl} C_{vsi}^{cl} x_{vsi}^{cl} \tag{3.120}$$

Merge (3.118)(3.120) and the global closed loop model in this case is obtained as

$$\begin{bmatrix} \dot{x}_{vsi}^{cl} \\ \dot{x}_{afe}^{cl} \end{bmatrix} = \begin{bmatrix} A_{vsi}^{cl} & G_{vsi}^{cl} C_{afe}^{cl} \\ G_{afe}^{cl} C_{vsi}^{cl} & A_{afe}^{cl} \end{bmatrix} \begin{bmatrix} x_{vsi}^{cl} \\ x_{afe}^{cl} \end{bmatrix} \tag{3.121}$$

3.5.2 Poles of the PI VSI - state feedback control AFE system

Depending on the reference frames (VSI-dq frame or PLL-dq frame) where the current and voltage interactions on the AC bus is expressed, there are two different methods to build the system model.

Method A: Interactive voltages and currents are viewed in the VSI-dq frame

It is obvious that such a system could be built by merging the closed model of VSI (3.50) and that of AFE (3.77).

$$
\begin{bmatrix} \dot{x}_{vsi} \\ \dot{x}'_{afe} \end{bmatrix} = \begin{bmatrix} A^{cl}_{vsi} & G^{cl}_{vsi}C'_{afe} \\ G'_{afe}C^{cl}_{vsi} & A'_{afe} \end{bmatrix} \begin{bmatrix} x_{vsi} \\ x'_{afe} \end{bmatrix}
\tag{3.122}
$$

Method B: Interactive voltages are viewed in the VSI-dq frame while currents in the PLL-dq frame

In this situation, when the closed loop equations of VSI (3.50) is combined with AFE, its current interference r_{vsi} should be transformed into the PLL-dq frame. According to (3.12b), the term $G^{cl}_{vsi}r_{vsi}$ in (3.50) turns to be

$$
\begin{bmatrix} -\frac{1}{C} & 0 \\ 0 & -\frac{1}{C} \\ 0 & 0 \\ 0 & 0 \\ \frac{k_{pi}k_{pv}}{C} & 0 \\ \frac{k_{pv}}{C} & 0 \\ 0 & \frac{k_{pi}k_{pv}}{C} \\ 0 & \frac{k_{pv}}{C} \end{bmatrix} \begin{bmatrix} i_{ad} \\ i_{aq} \end{bmatrix} = \begin{bmatrix} -\frac{1}{C} & 0 \\ 0 & -\frac{1}{C} \\ 0 & 0 \\ 0 & 0 \\ \frac{k_{pi}k_{pv}}{C} & 0 \\ \frac{k_{pv}}{C} & 0 \\ 0 & \frac{k_{pi}k_{pv}}{C} \\ 0 & \frac{k_{pv}}{C} \end{bmatrix} \begin{bmatrix} i^p_{ad} \\ i^p_{aq} + \tilde{\theta}_e I^*_{ad} \end{bmatrix}
$$

$$
= \begin{bmatrix} -\frac{1}{C} & 0 \\ 0 & -\frac{1}{C} \\ 0 & 0 \\ 0 & 0 \\ \frac{k_{pi}k_{pv}}{C} & 0 \\ \frac{k_{pv}}{C} & 0 \\ 0 & \frac{k_{pi}k_{pv}}{C} \\ 0 & \frac{k_{pv}}{C} \end{bmatrix} \begin{bmatrix} i^p_{ad} \\ i^p_{aq} \end{bmatrix} + \begin{bmatrix} 0 \\ -\frac{1}{C} \\ 0 \\ 0 \\ 0 \\ 0 \\ \frac{k_{pi}k_{pv}}{C} \\ \frac{k_{pv}}{C} \end{bmatrix} I^*_{ad}\tilde{\theta}_e
\tag{3.123}
$$

According to (3.12d),

$$
\tilde{\theta}_e = \frac{v_{cq} - v^p_{cq}}{V^*_{cd}}
\tag{3.124}
$$

Substitute it into (3.123)

$$
G_{vsi}^{cl} r_{vsi} =
\begin{bmatrix}
-\frac{1}{C} & 0 \\
0 & -\frac{1}{C} \\
0 & 0 \\
0 & 0 \\
\frac{k_{pi}k_{pv}}{C} & 0 \\
\frac{k_{pv}}{C} & 0 \\
0 & \frac{k_{pi}k_{pv}}{C} \\
0 & \frac{k_{pv}}{C}
\end{bmatrix}
\begin{bmatrix}
i_{ad} \\
i_{aq}
\end{bmatrix}
=
\begin{bmatrix}
-\frac{1}{C} & 0 \\
0 & -\frac{1}{C} \\
0 & 0 \\
0 & 0 \\
\frac{k_{pi}k_{pv}}{C} & 0 \\
\frac{k_{pv}}{C} & 0 \\
0 & \frac{k_{pi}k_{pv}}{C} \\
0 & \frac{k_{pv}}{C}
\end{bmatrix}
\begin{bmatrix}
i_{ad}^p \\
i_{aq}^p
\end{bmatrix}
+
\begin{bmatrix}
0 \\
-\frac{I_{ad}^*}{CV_{cd}^*} \\
0 \\
0 \\
0 \\
0 \\
\frac{k_{pi}k_{pv}I_{ad}^*}{CV_{cd}^*} \\
\frac{k_{pv}I_{ad}^*}{CV_{cd}^*}
\end{bmatrix}
(v_{cq} - v_{cq}^p) \quad (3.125)
$$

The closed loop model of AFE with a state feedback controller when its state variables are represented in PLL-dq frame is shown in (3.67). Transform its voltage interference $\begin{bmatrix} v_{cd}^p & v_{cq}^p \end{bmatrix}^T$ into VSI-dq frame,

$$
\begin{aligned}
\dot{x}_{afe} &= (A_{afe} + B_{afe}K_{afe})x_{afe} +
\begin{bmatrix}
\frac{1}{L_a} & 0 \\
0 & \frac{1}{L_a} \\
0 & 0 \\
0 & 0 \\
0 & 0
\end{bmatrix}
\begin{bmatrix}
v_{cd}^p \\
v_{cq}^p
\end{bmatrix} \\
&= (A_{afe} + B_{afe}K_{afe})x_{afe} +
\begin{bmatrix}
\frac{1}{L_a} & 0 \\
0 & 0 \\
0 & 0 \\
0 & 0 \\
0 & 0
\end{bmatrix}
\begin{bmatrix}
v_{cd} \\
v_{cq}
\end{bmatrix}
+
\begin{bmatrix}
0 & 0 \\
\frac{1}{L_a} & 0 \\
0 & 0 \\
0 & 0 \\
0 & 0
\end{bmatrix}
\begin{bmatrix}
v_{cq}^p \\
\omega_i
\end{bmatrix}
\end{aligned}
\quad (3.126)
$$

Merge VSI's model (3.125), AFE's model (3.126) and PLL's model (3.22), then the whole closed loop model of VSI-AFE-PLL system is

$$
\dot{x} = Ax \quad (3.127)
$$

where

$$
\begin{aligned}
x = [&v_{cd} \quad v_{cq} \quad i_{id} \quad i_{iq} \quad V_d \quad I_{id_{ref}} \quad V_q \quad I_{iq_{ref}} \\
&i_{ad}^p \quad i_{aq}^p \quad v_{dca} \quad w_{i_{aq}} \quad w_{v_{dca}} \quad v_{cq}^p \quad \omega_i]
\end{aligned}
\quad (3.128)
$$

$$
A =
\begin{bmatrix}
A_{11} & A_{12} & A_{13} \\
A_{21} & A_{22} & A_{23} \\
A_{31} & A_{32} & A_{33}
\end{bmatrix}
\quad (3.129)
$$

$$A_{11} = \begin{bmatrix} 0 & \omega & \frac{1}{C} & 0 & 0 & 0 & 0 & 0 \\ -\omega & -\frac{I_{ad}^*}{CV_{cd}^*} & 0 & \frac{1}{C} & 0 & 0 & 0 & 0 \\ -\frac{1}{L} & 0 & -\frac{R}{L} & \omega & \frac{1}{L} & 0 & 0 & 0 \\ 0 & -\frac{1}{L} & -\omega & -\frac{R}{L} & 0 & 0 & \frac{1}{L} & 0 \\ \sigma_2 & -k_{pi}k_{pv}\omega & \sigma_1 & -k_{pi}\omega & -\frac{k_{pi}}{L} & k_{ii} & 0 & 0 \\ -k_{iv} & -k_{pv}\omega & -\frac{k_{pv}}{C} & 0 & 0 & 0 & 0 & 0 \\ k_{pi}k_{pv}\omega & \sigma_2 + \frac{k_{pi}k_{pv}I_{ad}^*}{CV_{cd}^*} & k_{pi}\omega & \sigma_1 & 0 & 0 & -\frac{k_{pi}}{L} & k_{ii} \\ k_{pv}\omega & -k_{iv} + \frac{k_{pv}I_{ad}^*}{CV_{cd}^*} & 0 & -\frac{k_{pv}}{C} & 0 & 0 & 0 & 0 \end{bmatrix} \tag{3.130}$$

$$A_{12} = \begin{bmatrix} -\frac{1}{C} & 0 & 0 & 0 & 0 \\ 0 & -\frac{1}{C} & 0 & 0 & 0 \\ 0 & 0 & 0 & 0 & 0 \\ 0 & 0 & 0 & 0 & 0 \\ \frac{k_{pi}k_{pv}}{C} & 0 & 0 & 0 & 0 \\ \frac{k_{pv}}{C} & 0 & 0 & 0 & 0 \\ 0 & \frac{k_{pi}k_{pv}}{C} & 0 & 0 & 0 \\ 0 & \frac{k_{pv}}{C} & 0 & 0 & 0 \end{bmatrix}, A_{13} = \begin{bmatrix} 0 & 0 \\ \frac{I_{ad}^*}{CV_{cd}^*} & 0 \\ 0 & 0 \\ 0 & 0 \\ 0 & 0 \\ 0 & 0 \\ -\frac{k_{pi}k_{pv}I_{ad}^*}{CV_{cd}^*} & 0 \\ -\frac{k_{pv}I_{ad}^*}{CV_{cd}^*} & 0 \end{bmatrix} \tag{3.131}$$

$$A_{21} = \begin{bmatrix} \frac{1}{L_a} & 0 & 0 & 0 & 0 & 0 & 0 & 0 \\ 0 & 0 & 0 & 0 & 0 & 0 & 0 & 0 \\ 0 & 0 & 0 & 0 & 0 & 0 & 0 & 0 \\ 0 & 0 & 0 & 0 & 0 & 0 & 0 & 0 \\ 0 & 0 & 0 & 0 & 0 & 0 & 0 & 0 \end{bmatrix}, A_{22} = A_{afe} + B_{afe}K_{afe}, A_{23} = \begin{bmatrix} 0 & 0 \\ \frac{1}{L_a} & 0 \\ 0 & 0 \\ 0 & 0 \\ 0 & 0 \end{bmatrix} \tag{3.132}$$

$$A_{31} = \begin{bmatrix} -\omega & -\frac{I_{ad}^*}{CV_{cd}^*} & 0 & \frac{1}{C} & 0 & 0 & 0 & 0 \\ 0 & 0 & 0 & 0 & 0 & 0 & 0 & 0 \end{bmatrix} \tag{3.133}$$

$$A_{32} = \begin{bmatrix} 0 & -\frac{1}{C} & 0 & 0 & 0 \\ 0 & 0 & 0 & 0 & 0 \end{bmatrix} \tag{3.134}$$

$$A_{33} = \begin{bmatrix} -k_p^p V_{cd}^* + \frac{I_{ad}^*}{CV_{cd}^*} & -V_{cd}^* \\ k_i^p & 0 \end{bmatrix} \tag{3.135}$$

The entries marked in red are used to replicate the $\dot{v}_{cq}$ in (3.22), which is exactly the second row of A_{11}. The poles of the VSI-AFE-PLL system are the eigenvalues of (3.129).

It is worth to point out that the above two methods work out same poles. Although the first method is more clear and straightforward, it is still necessary to present the second method here. As will be shown in the next chapter, when implement the optimal control design for AFE, it is

required to build a global model of the VSI-AFE system based on the closed loop model of VSI and the open loop model of AFE, the techniques to develop equations there is very similar to the second method of formulating system global model here.

3.6   Conclusion

In the chapter 3, the system being discussed in this research was detailed described. The state space modelling of its three subsystems including VSI, AFE and PLL was presented. It laid the foundation for analysis in later chapters. The PI control design of VSI and AFE was also discussed. The PI control of AFE will be compared with the optimal H_2 control design that will be proposed in later chapters. Moreover, a critical conception of MIMO system namely the impedance of power converters was introduced. The impedance model of those converter of different topologies were derived. The system global closed loop models were established to calculate the system poles and analyse the stability condition. Another tool of system stability judgement namely the characteristic loci based on impedances at the PCC was also included.

Chapter 4

Optimal H_2 control design for AFE

Prior to this research, control design of grid-connected power converters aiming to achieve a good dynamic performance and reliable system stability is mainly delivered by elaborate local design, without considering specific dynamic characteristic of the grid, or considering a nonparametric approximation of the grid at most. It usually works out a suboptimal solution, either an overly conservative control design or even a failure in challenging grid conditions.

Hence in this research, an optimal control design method is proposed, in which a parametric model of the grid is integrated into the control design of a local converter. The method has a great capacity in mitigating grid interactions and ensuring system stability.

In this chapter, details about the optimal control design method is presented. It is based on a mathematical technique to build a global model by merging a parametric model of the grid and a open loop model of the to be designed converter in question in a coordinated way. In this chapter, the procedure to build such a global model is detailed.

As the optimal controller is synthesized by the structured H_2 algorithm based on the global system model, knowledge about the H_2 control algorithm will be introduced at first.

The effectiveness and advantages of the proposed method is proved by time-domain simulations, in which the proposed optimal control design method is applied to the design of an AFE. And dynamic performance of the VSI-AFE system when the AFE uses the proposed method and the traditional PI method is compared.

4.1   Introduction of H_2 control

The two most frequently used techniques of optimization-based feedback design are H_2 and H_∞ optimization. Both are normally applied to what can be referred to as the standard LTI (Linear

Time-invariant) feedback optimization setup.

In order to define a standard LTI feedback optimization problem, sketched on Fig.4.1, one has to specify the plant P, and a performance measure.
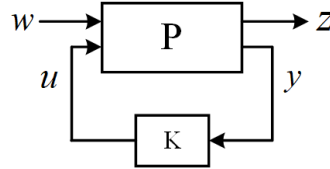
Figure 4.1: Standard LTI feedback optimization setup

The plant is a finite order linear time-invariant system with two inputs, w and u, and two outputs, z and y. Inputs and outputs can be multi-variable. The first input w is called disturbance, and is typically used to describe external noises and internal perturbations caused by nonlinearity and uncertainty. The second input u is called actuator, and describes the output of the feedback controller K (to be designed via optimization). The first output z is called cost, and represents signals which the designer wants to be small. Finally, the second output y, usually referred to as sensor, or measurement, represents input of the controller K (to be designed).

The performance measure specifies a particular quantitative measure of 'smallness' for the cost output z. The optimization process will aim at finding a LTI feedback system K which makes the feedback system in Fig.4.1 stable, and 'minimizes' the closed loop system from w to z. Two measures (also called norms) of how 'large' a stable LTI system is are most popular in feedback optimization: H_2 norm and H_∞ norm. The H_2 norm measures the size of a LTI system as an integral of square of amplitude of its frequency response, while the H_∞ norm uses the maximal (over all frequencies) amplitude [129].

The system shown in Fig.4.1 can be modelled as

$$
\begin{bmatrix} \dot{x} \\ z \\ y \end{bmatrix} = \begin{bmatrix} A & B_1 & B_2 \\ C_1 & D_{11} & D_{12} \\ C_2 & D_{21} & D_{22} \end{bmatrix} \begin{bmatrix} x \\ w \\ u \end{bmatrix}
\tag{4.1}
$$

x represent the system states. A is the state matrix, B_1 is the disturbance input matrix, and B_2 is the control input matrix. Assume number of states is n and number of inputs is m. Usually, $D_{11} = D_{21} = D_{22} = 0$. If all states are accessible and measurable, C_2 is an identity matrix.

H_2 optimization is a process to minimize h_2 norm of the transfer function from interference w to output z.

4.1.1 Definition of h_2 norm

H_2 norm can be seen as the energy of output z for the system shown in (4.1) obtained in response to a m dimension vector impulse function w.

$$\dot{x} = A_c x + B_1 w \tag{4.2}$$

$$A_c = A + B_2 K \tag{4.3}$$

$$z = Cx \tag{4.4}$$

$$w = \begin{bmatrix} \delta_1 & \ldots & \delta_m \end{bmatrix}^T \tag{4.5}$$

where z is a p dimension vector

$$z = \begin{bmatrix} z_1 & \ldots & z_p \end{bmatrix}^T \tag{4.6}$$

C is a p dimension vector

$$C = \begin{bmatrix} c_1 & \ldots & c_p \end{bmatrix}^T \tag{4.7}$$

B_1 is a m dimension vector

$$B_1 = \begin{bmatrix} b_1 & \ldots & b_m \end{bmatrix} \tag{4.8}$$

Assume the $p \times m$ transfer function matrix from w to z is $G(s)$

$$G(s) = \begin{bmatrix} c_1 & \ldots & c_p \end{bmatrix}^T (sI - A_c)^{-1} \begin{bmatrix} b_1 & \ldots & b_m \end{bmatrix} \tag{4.9}$$

Then the $z_i(t)$ component to the impulse $\delta_j(t)$ is

$$z_{ij}(t) = \begin{cases} c_i e^{A_c t} b_j, & t > 0 \\ 0, & t \leq 0 \end{cases} \tag{4.10}$$

Define $g(t)$ as

$$g(t) = \begin{bmatrix} z_{11}(t) & \ldots & z_{1m}(t) \\ \ldots & & \ldots \\ z_{p1}(t) & \ldots & z_{pm}(t) \end{bmatrix} \tag{4.11}$$

The H_2 norm of the system is the sum of the energies of $z_{ij}(t)$ [130]

$$\|G\|_2 = \sqrt{\int_0^{+\infty} \sum_{i=1}^{p} \sum_{j=1}^{m} z_{ij}^2(t) dt} = \sqrt{\int_0^{+\infty} trace[g^T(t)g(t)] dt} \tag{4.12}$$

$$\|G\|_2 = \sqrt{\int_0^{+\infty} trace\big[(Ce^{A_c t}B_1)^T Ce^{A_c t}B_1\big]dt}$$

$$= \sqrt{\int_0^{+\infty} trace\big[B_1^T e^{A_c^T t}C^T Ce^{A_c t}B_1\big]dt}$$

$$= \sqrt{trace\Big[B_1^T \int_0^{+\infty} e^{A_c^T t}C^T Ce^{A_c t}dt B_1\Big]}$$ (4.13)

$$= \sqrt{trace\big[B_1^T Q B_1\big]}$$

$$Q = \int_0^{+\infty} e^{A_c^T t}C^T Ce^{A_c t}dt$$ (4.14)

The observability Grammian Q can be computed without integration as a solution of the Lyapunov equation

$$QA_c + A_c^T Q + C^T C = 0$$ (4.15)

If $G(s)$ is the Laplace transform of $g(t)$

$$\mathcal{L}_{g(t)}(s) = \int_0^{+\infty} g(t)e^{-st}dt = G(s)$$ (4.16)

Then according to the Parceval theorem,

$$\|G\|_2 = \sqrt{\int_0^{+\infty} trace[g^T(t)g(t)]dt}$$

$$= \sqrt{\frac{1}{2\pi}\int_0^{+\infty} trace\big[G^*(j\omega)G(j\omega)\big]d\omega}$$ (4.17)

It means the H_2 norm measures the size of a LTI system as an integral of square of amplitude of its frequency response.

Similar to LQR (Linear Quadratic Regulator) optimization [131] of which the cost function is defined as (4.18),

$$J_{LQR} = \int_0^{\infty} (x^T Qx + u^T Ru)dt$$ (4.18)

two weighting matrices Q and R are defined to adjust how much each variable contributes to the value of H_2 norm in (4.13). Q puts a penalty on deviations of the state variables from their reference values. R puts a penalty on the energy consumed in the control.

$$Q = \begin{bmatrix} q_1 & 0 & 0 & ... \\ 0 & q_2 & 0 & ... \\ 0 & 0 & ... & 0 \\ 0 & 0 & ... & q_n \end{bmatrix}, R = \begin{bmatrix} r_1 & 0 & ... & 0 \\ 0 & r_2 & ... & 0 \\ 0 & 0 & ... & 0 \\ 0 & 0 & 0 & r_m \end{bmatrix}$$ (4.19)

Then the output z could be formulated as

$$z = C_1 x + D_{12} u = \begin{bmatrix} \sqrt{Q} \\ 0 \end{bmatrix} x + \begin{bmatrix} 0 \\ \sqrt{R} \end{bmatrix} u = (\begin{bmatrix} \sqrt{Q} \\ 0 \end{bmatrix} + \begin{bmatrix} 0 \\ \sqrt{R} \end{bmatrix} K) x \tag{4.20}$$

$$C_1 = \begin{bmatrix} \sqrt{q_1} & 0 & 0 & \dots \\ 0 & \sqrt{q_2} & 0 & \dots \\ 0 & 0 & \dots & 0 \\ 0 & 0 & \dots & \sqrt{q_n} \\ 0 & 0 & 0 & 0 \\ \vdots & \vdots & \vdots & \vdots \end{bmatrix}, D_{12} = \begin{bmatrix} 0 & 0 & 0 & 0 \\ \vdots & \vdots & \vdots & \vdots \\ \sqrt{r_1} & 0 & \dots & 0 \\ 0 & \sqrt{r_2} & \dots & 0 \\ 0 & 0 & \dots & 0 \\ 0 & 0 & 0 & \sqrt{r_m} \end{bmatrix} \tag{4.21}$$

Therefore the C in (4.4) becomes

$$C = \begin{bmatrix} \sqrt{Q} \\ 0 \end{bmatrix} + \begin{bmatrix} 0 \\ \sqrt{R} \end{bmatrix} K \tag{4.22}$$

$$C^T C = K^T R K + Q \tag{4.23}$$

Substitute (4.23) into (4.13)

$$J_{H_2} = \|G\|_2 = \sqrt{tr\left(B_1^T \int_0^\infty e^{(A+B_2 K)^T t}(Q + K^T R K)e^{(A+B_2 K)t} dt B_1 \right)} \tag{4.24}$$

The H_2 optimization aims to find a K minimize J_{H_2}

$$K = \min_K J_{H_2} \tag{4.25}$$

Define $S = \int_0^\infty e^{(A+B_2 K)^T t}(Q + K^T R K)e^{(A+B_2 K)t} dt$. The S can be computed without integration as a solution of the Lyapunov equation.

$$A_c^T S + S A_c + Q + K^T R K = 0 \tag{4.26}$$

4.1.2 H_2 optimization and tuning of the H_2 optimal controller

Essentially, the tuning of H_2 controller, is mainly about finding a good choice of Q and R matrices. Once the Q and R are determined, the shape of the H_2 norm relating to K is determined. For the ease of explaining, assume the argument of H_2 norm, namely the state feedback controller gain matrix K is of one dimension. Hence the H_2 norm can be illustrated as a curve in a 2 dimension plane, as shown in Fig.4.2, where the horizontal axis is K and the vertical axis is J_{H_2}. The H_2 optimization is a process of iteratively and numerically searching the minimum along with the curve corresponding to the chosen Q and R. The K where the curve reaches the global minimum

is the optimal solution. In the Fig.4.2, depending on the different choices of Q and R, three curves in different shapes of H_2 norms are depicted. If Q_2 and R_2 are chosen as the tuning parameters, searching of the optimal solution will proceed along with the curve $J_2(Q_2, R_2)$.
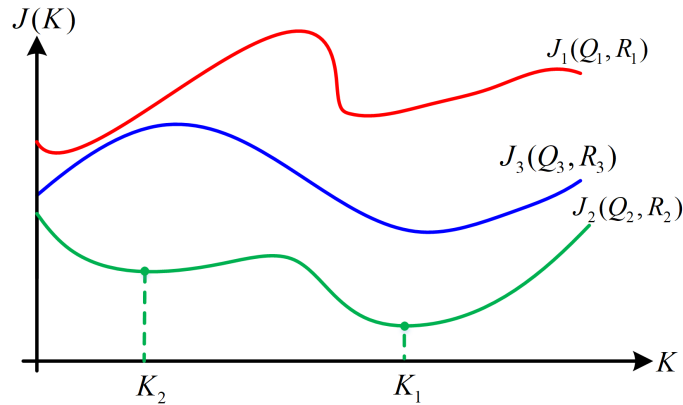
Figure 4.2: A fictitious diagram of the H_2 norm curves

In this research, a toolbox 'hifoo' [132–134] in Matlab is used to deliver this task. In case of trapped in a local minimum in the searching process, for example K_2 in the Fig.4.2, several starting points on the curve will randomly be selected. The searching will start from these points and end when searching in these different search paths all converged to a minimum respectively.

Specifically, numbers of different guesses of K are firstly initialized, and (4.26) is solved. Based on the obtained solution S, the h_2 norm is calculated by (4.24). According to newton-gauss method, the estimated point on the searching path in the next step would be

$$k(n+1) = k(n) - \frac{J(k(n))}{J'(k(n))} \tag{4.27}$$

The $J'(k(n))$ is the gradient of H_2 norms at the current point. When the decrement of J_{H_2} in one step is smaller than a pre-defined threshold, the searching is stopped. And the minimum of these J_{H_2}s is picked out and the corresponding K is deemed as the global solution of h_2 optimization.

As the cost function in H_2 optimization (4.24) is defined similarly to the cost function of LQR algorithm (4.18), the tuning procedure will be explained referring to the LQR problem. No precise mathematical relationship between the weight matrices Q and R and time or frequency domain performance indexes exists and often a trial and error approach is used. Actually according to the experience of practising, the H_2 optimization could result in a satisfactory solution for most reasonable choices of Q and R. Therefore, general empirical advise for tuning Q and R is enough.

First of all, both the Q and R are usually set to be diagonal in order to have only quadratic terms in H_2 norm. When the system is extended with integral states, it is convenient to weight

only these states in the H_2 norm in order to ensure both good reference tracking and disturbance rejection. Finally, there is no need to have different bandwidths for d- and q- axes. Therefore the modulation indexes (p_d and p_q for AFE and u_p for PLL) have been assigned with the same weights in the d- and q-frame. Increasing the weights in R matrix reduces the control effort realized by the inputs during transients and therefore decreases the system response speed. On the other hand, increasing the weights in Q on states means a bigger penalty on corresponding states in transients and force them to respond faster, in order to reduce their share in the H_2 norm value. Specifically for the AFE tuning, if $w_{v_{dca}}$ (integral error of V_{dca}) weight in Q is increased, a faster dynamic response of V_{dca} is obtained and thus a bigger voltage bandwidth of AFE. If $w_{i_{aq}}$ (integral error of I_{aq}) weight in Q is increased a faster dynamic response of I_{aq} is obtained and thus a bigger current bandwidth of AFE.
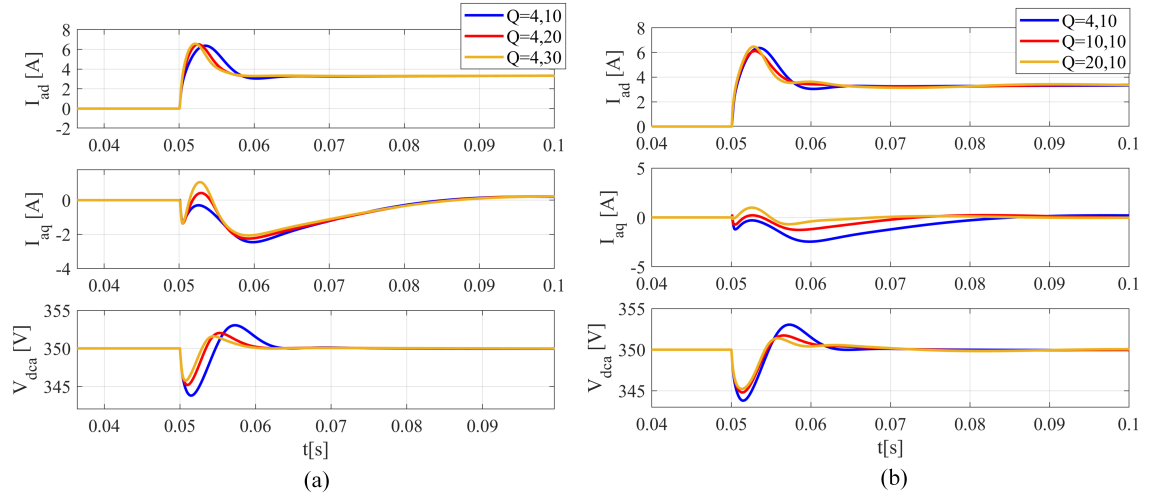
Figure 4.3: Time-domain response of I_{ad}, I_{aq} and V_{dca} with respect to different Q values

The Fig.4.3 shows time-domain response waveforms of I_{ad}, I_{aq} and V_{dca} obtained a simulation where a step load of 500W is attached on at t=0.05s when Q is tuned with different values. In the simulation linked with Fig.4.3(a), the weighting of $w_{i_{aq}}$ in Q is fixed as 4 and the weighting of $w_{v_{dca}}$ is tuned as 10, 20, and 30 respectively. As can be seen, as the weightings of $w_{v_{dca}}$ increases, the speed of V_{dca} increases. In the simulation linked with Fig.4.3(b), the weighting of $w_{i_{aq}}$ in Q is tuned as 4, 10 and 20 respectively and the weighting of $w_{v_{dca}}$ is fixed as 10. As can be seen, as the weightings of $w_{i_{aq}}$ increases, the speed of I_{aq} increases.

A typical choice of Q and R used in this research is,

$$Q = diag(0, 0, 0, 4, 40, 0, 1)$$
$$R = diag(1, 1, 1, 1)$$

(4.28)

In the (4.28), the first 3 zeros of Q matrix are related to the states I_{ad}^p, I_{aq}^p, and V_{dca} respectively. The 4 and 40 are related to the integral states $w_{i_{aq}}$ and $w_{v_{dca}}$ respectively. The next 0 and 1 are related to the PLL states V_{cq}^p and w_i respectively. As the ratio between Q and R does not take effect when the optimization tries to minimize the H_2 norm, it is convenient to set weights in R as all ones and only focus on the tuning of Q matrix.

It is worth to note that the goal of H_2 optimization is to find a K that minimizes H_2 norms defined by (4.24) for a given set of Q and R. The resultant value of H_2 norm is not necessarily the global minimum. The H_2 optimization tuning does not need to find the Q and R which work out minimum value of the H_2 norm.

An overview of recommendations to tune the Q and R:

1, Set the Q and R as diagonal matrices in order to have only quadratic terms in H_2 norm.

2, When the system is extended with integral states, it is convenient to weight only these states in the H_2 norm in order to ensure both good reference tracking and disturbance rejection.

3, Assign same weights for the d- and q-axis in the Q and R.

4, Fix the weights for input, namely the R with all ones, and focus on the tuning of Q matrix.

5, Increasing weights in Q in the simulation, until the speed of corresponding state variable is satisfactory.

6, Evaluate the choice of Q and R in the experiment. And iterate the 5th step if the system dynamic performance is not satisfactory.

4.2 Optimal global controller for the VSI-AFE system

Ideally, if the system being investigated is entirely open to the designer, great performance can be expected through integrally modelling and fully control. In the context of this research, it means all the state variables of the VSI-AFE system shown in the Fig.3.1 are measurable and available for control design. Although it is usually not the common case in practice for the system assemblers, it is still worth to investigate the modelling and control design in this situation. In this section, some conceptions used in the chapters to follow will be introduced and lay the groundwork for discussions of more complex situations.

4.2.1 Global open loop model for the VSI-AFE system

In this case, all the state variables are measurable and available for control design. Therefore, a global model based on the open loop models of the VSI and AFE including PLL can be built. The following context will discuss the details about how it could be built by the individual models of VSI, AFE and PLL obtained in the Chapter 3.

In the Chapter 3, the open loop model of VSI (3.2) is developed in VSI-dq frame while that of AFE (3.24) is developed in AFE's PLL-dq frame. When merging VSI's and AFE's models together and building a model characterizing the whole system, some transformations are needed in order to deal with them in a same reference frame.

For VSI, the current interferences I_{ad} and I_{aq} (3.5) needs to be transformed into the AFE's PLL-dq frame and represented by I_{ad}^p and I_{aq}^p.

$$\begin{bmatrix} I_{ad} \\ I_{aq} \end{bmatrix} = \begin{bmatrix} cos(\theta_e) & -sin(\theta_e) \\ sin(\theta_e) & cos(\theta_e) \end{bmatrix} \begin{bmatrix} I_{ad}^p \\ I_{aq}^p \end{bmatrix} = \begin{bmatrix} cos(\theta_e)I_{ad}^p - sin(\theta_e)I_{aq}^p \\ sin(\theta_e)I_{ad}^p + cos(\theta_e)I_{aq}^p \end{bmatrix} \tag{4.29}$$

For AFE, the voltage input V_{cd}^p and V_{cq}^p (3.27) needs to be transformed into the VSI-dq frame and represented by V_{cd} and V_{cq}.

$$\begin{bmatrix} V_{cd}^p \\ V_{cq}^p \end{bmatrix} = \begin{bmatrix} cos(\theta_e) & sin(\theta_e) \\ -sin(\theta_e) & cos(\theta_e) \end{bmatrix} \begin{bmatrix} V_{cd} \\ V_{cq} \end{bmatrix} = \begin{bmatrix} cos(\theta_e)V_{cd} + sin(\theta_e)V_{cq} \\ -sin(\theta_e)V_{cd} + cos(\theta_e)V_{cq} \end{bmatrix} \tag{4.30}$$

Substitute (4.29) into (3.1), and the state space equations of V_{cd} and V_{cq} in the VSI's model become

$$\dot{V}_{cd} = \omega V_{cq} + \frac{1}{C}I_{id} - \frac{1}{C}(cos(\theta_e)I_{ad}^p - sin(\theta_e)I_{aq}^p) \tag{4.31}$$

$$\dot{V}_{cq} = -\omega V_{cd} + \frac{1}{C}I_{iq} - \frac{1}{C}(sin(\theta_e)I_{ad}^p + cos(\theta_e)I_{aq}^p) \tag{4.32}$$

Substitute (4.30) into (3.23), and the state space equations of I_{ad}^p and I_{aq}^p in the AFE's model become

$$\dot{I}_{ad}^p = -\frac{R_a}{L_a}I_{ad}^p + \omega I_{aq}^p - \frac{V_{dca}p_d}{2L_a} + \frac{cos(\theta_e)V_{cd} + sin(\theta_e)V_{cq}}{L_a} \tag{4.33}$$

$$\dot{I}_{aq}^p = -\omega I_{ad}^p - \frac{R_a}{L_a}I_{aq}^p - \frac{V_{dca}p_q}{2L_a} + \frac{-sin(\theta_e)V_{cd} + cos(\theta_e)V_{cq}}{L_a} \tag{4.34}$$

According to (3.12d),

$$\theta_e = \frac{V_{cq} - V_{cq}^p}{V_{cd}^*} \tag{4.35}$$

Substitute it into (4.31)-(4.34) and linearise the equations around the equilibrium point $V_{cq}^* = 0$, $V_{cq}^{p*} = 0$, and $I_{aq}^* = 0$.

$$\dot{V}_{cd} = \omega V_{cq} + \frac{1}{C}I_{id} - \frac{1}{C}I_{ad}^p \tag{4.36}$$

$$\begin{aligned} \dot{V}_{cq} &= -\omega V_{cd} + \frac{1}{C}I_{iq} - \frac{1}{C}(\frac{V_{cq} - V_{cq}^p}{V_{cd}^*}I_{ad}^p + I_{aq}^p) \\ &= -\omega V_{cd} - \frac{1}{C}\frac{I_{ad}^*}{V_{cd}^*}V_{cq} + \frac{1}{C}I_{iq} - \frac{1}{C}I_{aq}^p + \frac{1}{C}\frac{I_{ad}^*}{V_{cd}^*}V_{cq}^p \end{aligned} \tag{4.37}$$

$$\dot{I}_{ad}^p = -\frac{R_a}{L_a}I_{ad}^p + \omega I_{aq}^p - \frac{V_{dca}p_d}{2L_a} + \frac{V_{cd}}{L_a} \tag{4.38}$$

$$\dot{I}_{aq}^p = -\omega I_{ad}^p - \frac{R_a}{L_a}I_{aq}^p - \frac{V_{dca}p_q}{2L_a} + \frac{V_{cq}^p}{L_a} \tag{4.39}$$

Combine open loop equations of VSI (4.36)(4.37)(3.1c)(3.1d), open loop equations of AFE (4.38)(4.39)(3.23c)(3.31)(3.32) and open loop equations of PLL (3.17) together, a global open loop model is built for the whole system, which can be used to synthesize a global controller for both the VSI, AFE and PLL. In this way, each part can be synthesized considering the dynamic characteristics of other parts in the system and interactions between them.

State space representation of the obtained global open loop model is

$$\begin{cases} \dot{x} = Ax + Bu \\ y = Cx \end{cases} \tag{4.40}$$

$$\begin{cases} x = \begin{bmatrix} x_{vsi} & x_{afe} & x_p \end{bmatrix}^T \\ u = \begin{bmatrix} u_{vsi} & u_{afe} & u_p \end{bmatrix}^T \\ y = \begin{bmatrix} y_{vsi} & y_{afe} \end{bmatrix}^T \end{cases} \tag{4.41}$$

$A =$

$$\left[\begin{array}{cccccc|ccccc|cc} 0 & \omega & \frac{1}{C} & 0 & 0 & 0 & -\frac{1}{C} & 0 & 0 & 0 & 0 & 0 & 0 \\ -\omega & -\frac{I_{ad}^*}{CV_{cd}^*} & 0 & \frac{1}{C} & 0 & 0 & 0 & -\frac{1}{C} & 0 & 0 & 0 & \frac{I_{ad}^*}{CV_{cd}^*} & 0 \\ -\frac{1}{L} & 0 & -\frac{R}{L} & \omega & 0 & 0 & 0 & 0 & 0 & 0 & 0 & 0 & 0 \\ 0 & -\frac{1}{L} & -\omega & -\frac{R}{L} & 0 & 0 & 0 & 0 & 0 & 0 & 0 & 0 & 0 \\ -1 & 0 & 0 & 0 & 0 & 0 & 0 & 0 & 0 & 0 & 0 & 0 & 0 \\ 0 & -1 & 0 & 0 & 0 & 0 & 0 & 0 & 0 & 0 & 0 & 0 & 0 \\ \hline \frac{1}{L_a} & 0 & 0 & 0 & 0 & 0 & -\frac{R_a}{L_a} & \omega & -\frac{p_d^*}{2L_a} & 0 & 0 & 0 & 0 \\ 0 & 0 & 0 & 0 & 0 & 0 & -\omega & -\frac{R_a}{L_a} & -\frac{p_q^*}{2L_a} & 0 & 0 & \frac{1}{L_a} & 0 \\ 0 & 0 & 0 & 0 & 0 & 0 & \frac{3p_d^*}{4C_a} & \frac{3p_q^*}{4C_a} & \frac{P}{C_aV_{dca}^2} & 0 & 0 & 0 & 0 \\ 0 & 0 & 0 & 0 & 0 & 0 & 0 & -1 & 0 & 0 & 0 & 0 & 0 \\ 0 & 0 & 0 & 0 & 0 & 0 & 0 & 0 & -1 & 0 & 0 & 0 & 0 \\ \hline -\omega & -\frac{I_{ad}^*}{CV_{cd}^*} & 0 & \frac{1}{C} & 0 & 0 & 0 & \frac{-1}{C} & 0 & 0 & 0 & \frac{I_{ad}^*}{CV_{cd}^*} & -V_{cd}^* \\ 0 & 0 & 0 & 0 & 0 & 0 & 0 & 0 & 0 & 0 & 0 & 0 & 0 \end{array}\right] \tag{4.42}$$

$$B = \begin{bmatrix} B_{vsi} & 0 & 0 \\ 0 & B_{afe} & 0 \\ 0 & 0 & B_p \end{bmatrix} \tag{4.43}$$

$$C = \begin{bmatrix} C_{vsi} & 0 & 0 \\ 0 & C_{afe} & 0 \end{bmatrix} \tag{4.44}$$

Specific definitions of those notation entries in the equations (4.41)(4.43)(4.44) can be found in Chapter 3. In the diagonal positions of A matrix, there are state matrices of VSI, AFE and PLL respectively. And the off-the-diagonal entries represent the interactions between them.

Notably, in the (4.42), the VSI equations are extended with 2 integral states $w_{v_{cd}}, w_{v_{cq}}$.

$$x_{vsi} = \begin{bmatrix} V_{cd} & V_{cq} & I_{id} & I_{iq} & w_{v_{cd}} & w_{v_{cq}} \end{bmatrix}^T \tag{4.45}$$

Here, integral states $w_{v_{cd}}$ and $w_{v_{cq}}$ are introduced to eliminate steady state error of V_{cd} and V_{cq} as the control of VSI is voltage-oriented. The reference value of V_{cd} is denoted as $V_{cd,ref}$. V_{cq} should be regulated to $V_{cq,ref} = 0V$.

$$w_{v_{cd}} = \int_0^{+\infty} (V_{cd,ref} - V_{cd}) dt \tag{4.46}$$

$$w_{v_{cq}} = \int_0^{+\infty} (V_{cq,ref} - V_{cq}) dt \tag{4.47}$$

4.2.2 Global centralized controller

Based on the global open loop model of the VSI-AFE system, a centralized controller can be synthesized by the H_2 algorithm. The term 'centralized' means control of the two converters is realized by one single controller. It collects all the sensors' signals and computes the duty cycle for both the two converters' switching device.

To prove capability of the centralized controller, it is applied to the VSI-AFE system and time domain waveforms obtained in Matlab Simulink simulation are shown in Fig.4.4. A transient is created by a CPL with its power step up from $750W$ to $800W$ at $t = 1s$. Main variables including V_{cd}, V_{cq}, I_{id}, I_{iq} of the VSI, I_{ad}, I_{aq}, V_{dca} of the AFE, power of the CPL, and error of the PLL θ_e are shown in the figure. As can be seen, the system reached steady state with a short transient and a small undershoot on V_{dca}.

The Q and R matrices used for the optimal H_2 controller tuning are

$$Q = diag(0, 0, 0, 0, 3, 3, 0, 0, 0, 3, 10, 0, 10)$$
$$R = diag(1, 1, 1, 1, 1, 1) \tag{4.48}$$

The resulting state feedback control gains matrix for AFE is

$$K = \begin{bmatrix} -0.0004 & 0.0005 & -0.0057 & -0.0006 & 8.0911 & -1.1495 & -0.0005 & -0.0017 & -0.0037 & -3.4284 & 4.9120 & 0 & 0 \\ -0.0006 & -0.0004 & -0.0005 & -0.0058 & 1.3095 & 9.6425 & -0.0005 & 0.0031 & -0.0020 & 1.5549 & 2.0076 & 0 & 0 \\ 0.0001 & -0.0000 & 0.0005 & 0.0005 & 5.9825 & -0.4704 & 0.0061 & 0.0016 & 0.0036 & 5.0209 & -6.2961 & 0 & 0 \\ -0.0002 & -0.0007 & 0.0014 & -0.0017 & 0.9249 & 2.6151 & 0.0019 & 0.0113 & 0.0056 & -8.0652 & -5.4376 & 0 & 0 \\ 0 & 0 & 0 & 0 & 0 & 0 & 0 & 0 & 0 & 0 & 0 & 553.9003 & 0 \\ 0 & 0 & 0 & 0 & 0 & 0 & 0 & 0 & 0 & 0 & 0 & 3.7984 & 0 \end{bmatrix} \quad (4.49)$$

$$k_p^p = 553.9003; k_i^p = 3.7984; \quad (4.50)$$
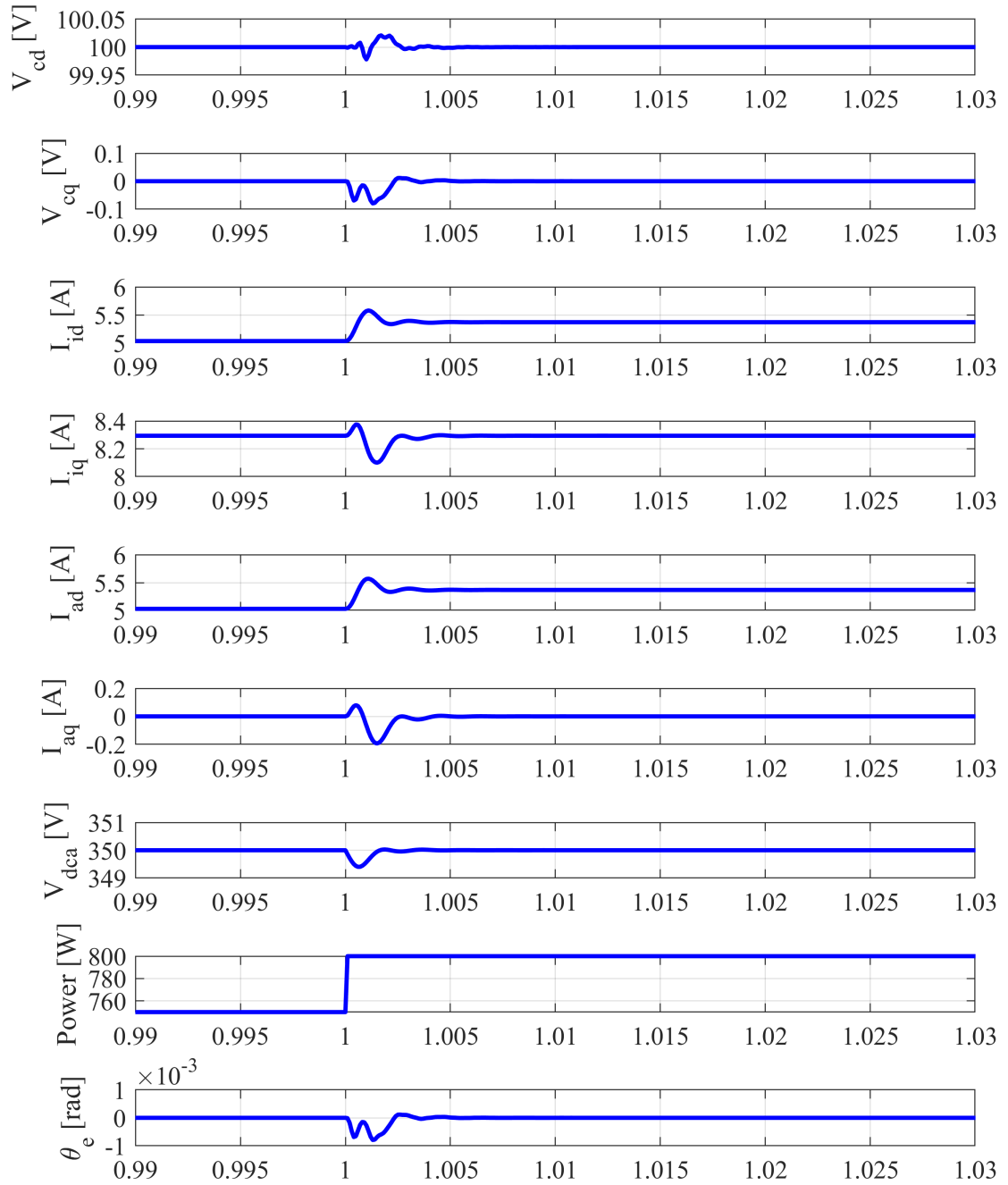
Figure 4.4: Simulation results of a centralized controller based on the global system model

Component values and some parameters used in the simulation are presented in Table.4.1.

Table 4.1: Parameters used in the simulation

VSI			
R	$900m\Omega$	V_{dc}	$320V$
L	460μH	V_{cdref}	$100V$
C	33μF	V_{cqref}	$0V$
AFE			
R_a	$200m\Omega$	P	0.8kW
L_a	585μH	$V_{dca_{ref}}$	$350V$
C_a	100μF	$I_{aq_{ref}}$	$0A$

In this case, the VSI and AFE are controlled by one controller utilizing all the 11 states of VSI and AFE. However this centralized controller demands long distance communication between converters and the central controller, if the converters are deployed far from each other. The failure of one converter's operation will directly and severely affect the operation of the other converter, and therefore centralized controllers are very limited in practise.

4.2.3 Global decentralized controller

In engineering practise, different sources and loads in a power grid often come from different manufacturers. Engineers deal with tasks to design their converters and attach them with such existing power grids, of which inner parameters are not accessible and measurable. Therefore, in most cases, the to be designed power converters are intended to work only on local states.

Hence the notion of decentralized controller is proposed. The decentralized controllers are installed for every single converter and operate locally based on the states of their own converters. Meanwhile, it could avoid defects of centralized controllers i.e. requiring communication between subsystems.

For the best system performance, the dynamic feature of the peripheral network is still intended to be accounted for when designing local converters. Namely, it is aimed to synthesize controllers based on a global model characterizing all states of the whole system while the implementation does not depend on part of the states. It means a structural constraint should be imposed on the control gains matrix K. That is why the H_2 structural optimization algorithm is here adopted. By the use of structured H_2-optimization algorithm, before a controller K is synthesized, the control system designer could specify a structure for the K [135]. In this case, as the VSI's and AFE's controllers could not access to state variables of the other converter, the form of K's structure should be specified as

$$S = \begin{bmatrix} 1 & 1 & 1 & 1 & 1 & 1 & 0 & 0 & 0 & 0 & 0 & 0 & 0 \\ 1 & 1 & 1 & 1 & 1 & 1 & 0 & 0 & 0 & 0 & 0 & 0 & 0 \\ 0 & 0 & 0 & 0 & 0 & 0 & 1 & 1 & 1 & 1 & 1 & 0 & 0 \\ 0 & 0 & 0 & 0 & 0 & 0 & 1 & 1 & 1 & 1 & 1 & 0 & 0 \\ 0 & 0 & 0 & 0 & 0 & 0 & 0 & 0 & 0 & 0 & 0 & 1 & 0 \\ 0 & 0 & 0 & 0 & 0 & 0 & 0 & 0 & 0 & 0 & 0 & 1 & 0 \end{bmatrix} \tag{4.51}$$

In the specified structure S, the first six columns correspond to the six state variables of VSI, the next five columns to the five state variables of AFE, and the last two columns to the two state variables of PLL. The first two rows correspond to the control input of VSI m_d, m_q, next two rows to the control input of AFE p_d, p_q, and last two rows to the control input of PLL u_p.

Zeros in the S indicate that corresponding entries in the synthesized K (i.e. controller gains) will be zeros. It means that the control will not need to measure the state variables because their product (i.e. $u = Kx$) will anyway be zero when computing the modulation indexes.

Then the resultant K could be partitioned into three matrices as decentralized controllers for the VSI, AFE and PLL respectively, as shown in (4.52). The zero matrices are of proper dimensions. Consequently, the modulation index calculation of one controller does not depend on state variables of the other converter, and the controllers of VSI, AFE and PLL could work individually. Meanwhile, long distance communication is avoided and system reliability is further guaranteed.

$$\begin{bmatrix} K_{vsi} & \mathbf{0} & \mathbf{0} \\ \mathbf{0} & K_{afe} & \mathbf{0} \\ \mathbf{0} & \mathbf{0} & K_{PLL} \end{bmatrix} \tag{4.52}$$

The performance of decentralized controllers in time domain simulation is shown in Fig.4.5. As can be seen, the performance is very similar to that of a centralized controller. Notably, these two different controllers are tuned with the same global open loop model shown in (4.40).

The Q and R matrices used for the optimal H_2 controller tuning are

$$Q = diag(0, 0, 0, 0, 3, 3, 0, 0, 0, 3, 10, 0, 10)$$
$$R = diag(1, 1, 1, 1, 1, 1) \tag{4.53}$$

The resulting state feedback control gains matrix for AFE is

$$K = \begin{bmatrix} -0.0049 & -0.0005 & -0.0023 & -0.0054 & 3.5273 & -0.0714 & 0 & 0 & 0 & 0 & 0 \\ -0.0013 & -0.0021 & 0.0013 & -0.0006 & 0.3414 & 2.6757 & 0 & 0 & 0 & 0 & 0 \\ 0 & 0 & 0 & 0 & 0 & 0 & 0.0119 & 0.0021 & 0.0065 & 1.7676 & -10.2377 \\ 0 & 0 & 0 & 0 & 0 & 0 & 0.0068 & 0.0163 & 0.0085 & -4.3498 & -6.1603 \end{bmatrix} \quad (4.54)$$

$$k_p^p = 0.6055; k_i^p = 3.510; \quad (4.55)$$
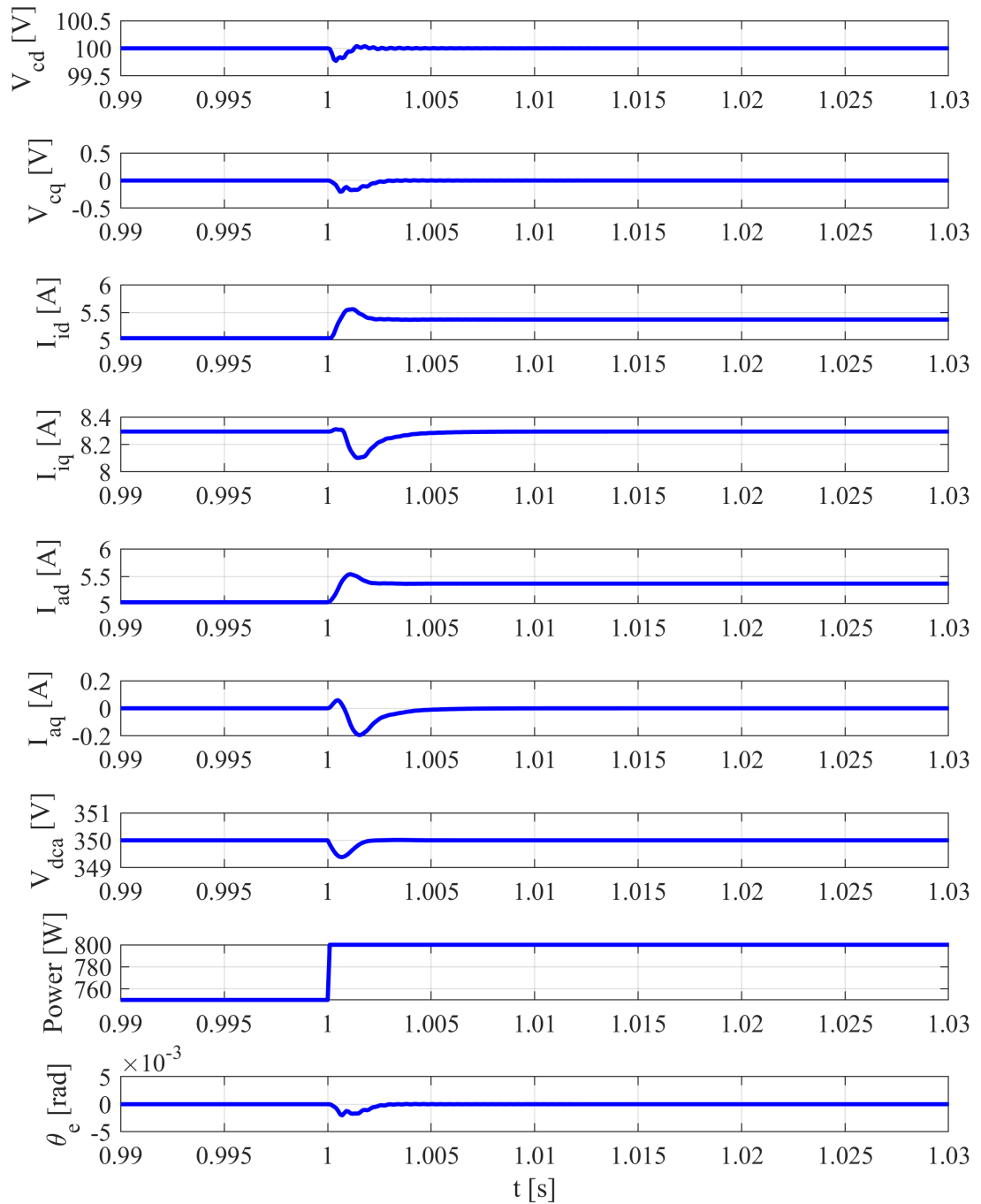
Figure 4.5: Simulation results of decentralized controllers based on the global system model

4.3   Optimal control design of AFE

In this research, a VSI based on PI control is installed to emulate a power grid, and it supplies power to the to be designed AFE. In the design of decentralized controllers discussed in last section, the VSI or grid is represented by its open loop model. All the subsystems (i.e. the VSI and AFE) are open for control design. However, it is not consistent with common practise. For the system assemblers designing commercial power converters, the grids that their product will attach onto already have their control loop closed. They do not need to concern with the design of power grid.

Therefore in this situation, it is natural to design the controllers without considering the dynamic feature of the existing power grid. The converters synthesized in this way are denoted as 'standalone controllers' in this thesis.

An optional way is to replace the open loop model of grid (represented by the VSI in last section) with its nominal closed loop model. Then the grid dynamic feature could still be considered in the control design. Controllers designed in this way and synthesized by the H_2 algorithm are denoted as 'optimal H_2 controllers tuned with nominal models' hereafter. In the Sec.4.3.2, mathematical approach to combine nominal closed loop model of the grid and open loop model of the local converter is presented.

As shown in the Fig.4.6, three kinds of controllers including the standalone PI controller, standalone controller based on H_2 algorithm and the proposed optimal H_2 controller are synthesized for the AFE.

Dynamic performance of the VSI-AFE system are compared when the AFE adopts these 3 different types of controllers respectively and powered by a same VSI. The VSI uses a standalone PI controller and is set to emulate an existing power grid. Its control parameters are shown in (4.56). The tuning methods of PI parameters in such applications are well documented in [126] [144]. The f_i and f_v are the desired current and voltage bandwidths of the PI controllers respectively. Their definitions is presented in (3.41).
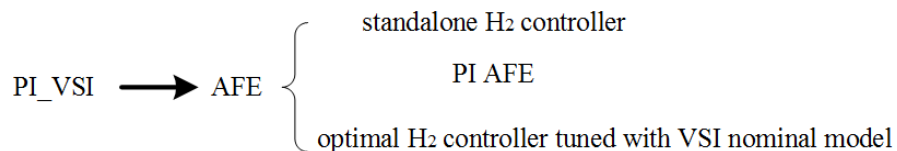
Figure 4.6: Different AFE controllers in the comparison test

$$\begin{cases} f_i = 800 \qquad f_v = 80 \\ k_{pv,vsi} = 0.033 \qquad k_{iv,vsi} = 8.337 \\ k_{pi,vsi} = 3.554 \qquad k_{ii,vsi} = 9095.827 \end{cases} \tag{4.56}$$

4.3.1 Standalone PI control design for AFE

In the second case, a standalone PI controller based on open loop model of the AFE is synthesized. It is a trade-off between fast response and keeping low oscillations in steady state. The AFE's PI controller used in the simulation was tuned elaborately to achieve its fastest speed by increasing the f_i and f_v in (3.41) gradually by a fixed ratio before introducing much oscillations in steady state. The control parameters are shown in (4.57). The average model simulation result is shown in Fig.4.7. As can be seen, the system exhibits strong oscillations when CPL increases. And the transient time is extremely long.

$$\begin{cases} f_i = 1000 \qquad f_v = 150 \\ k_{pv,afe} = 0.025 \qquad k_{iv,afe} = 1.579 \\ k_{pi,afe} = -4.134 \qquad k_{ii,afe} = -8029.910 \end{cases} \tag{4.57}$$
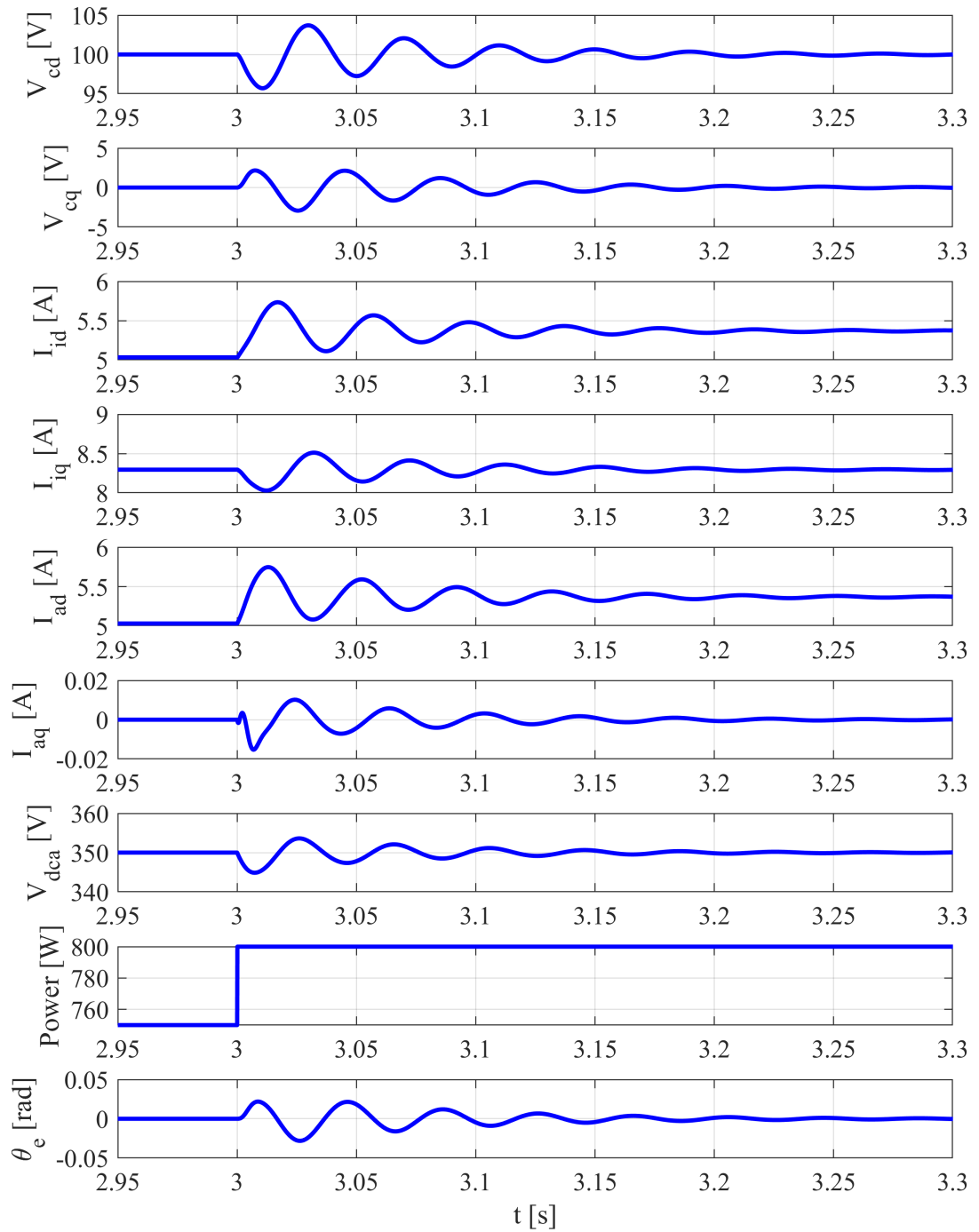
Figure 4.7: Simulation results of the VSI-AFE system when the AFE adopts a best tuned PI controller

4.3.2 Optimal H_2 controller for AFE based on nominal model of VSI

In the third case, an optimal H_2 controller based on nominal closed loop model of VSI is synthesized for AFE. Firstly, a global model is built by combining nominal closed loop model of the VSI and open loop model of the AFE. The technique used is very similar to that shown in the section 3.5.2, where closed loop model of VSI with a PI controller is combined with closed loop model of AFE with a state feedback controller for the purpose of system stability analysis. Apparently, the only difference is the A_{22} and A_{33} in (3.132) and (3.135) are open loop state matrices in this case. Namely, the A_{22} and A_{33} in (3.132) and (3.135) are replaced by (3.28) and (3.20) respectively, as shown in (4.58).

$$
A = \begin{bmatrix} A_{11} & A_{12} & A_{13} \\ A_{21} & A_{afe} & A_{23} \\ A_{31} & A_{32} & A_p \end{bmatrix}
\tag{4.58}
$$

Meanwhile, the new control input matrix is defined as (4.59).

$$
B = \begin{bmatrix} 0 & 0 \\ B_{afe} & 0 \\ 0 & B_p \end{bmatrix}
\tag{4.59}
$$

Then the structure of control gains matrix S is specified as (4.60) and the structured H_2 algorithm is applied to synthesize a controller for AFE. In this way, the control of AFE does not depend on state variables of VSI, while considering its dynamic feature inherently.

$$
S = \left[\begin{array}{cccccc|ccccc|cc} 0 & 0 & 0 & 0 & 0 & 0 & 0 & 0 & 0 & 0 & 0 & 0 & 0 \\ 0 & 0 & 0 & 0 & 0 & 0 & 0 & 0 & 0 & 0 & 0 & 0 & 0 \\ \hline 0 & 0 & 0 & 0 & 0 & 0 & 1 & 1 & 1 & 1 & 1 & 0 & 0 \\ 0 & 0 & 0 & 0 & 0 & 0 & 1 & 1 & 1 & 1 & 1 & 0 & 0 \\ \hline 0 & 0 & 0 & 0 & 0 & 0 & 0 & 0 & 0 & 0 & 0 & 1 & 0 \\ 0 & 0 & 0 & 0 & 0 & 0 & 0 & 0 & 0 & 0 & 0 & 1 & 0 \end{array} \right]
\tag{4.60}
$$

Average model simulation results when AFE adopts the synthesized optimal H_2 controller are shown in Fig.4.8. As can be seen, the dynamic performance of all variables is much better than that of the PI case.
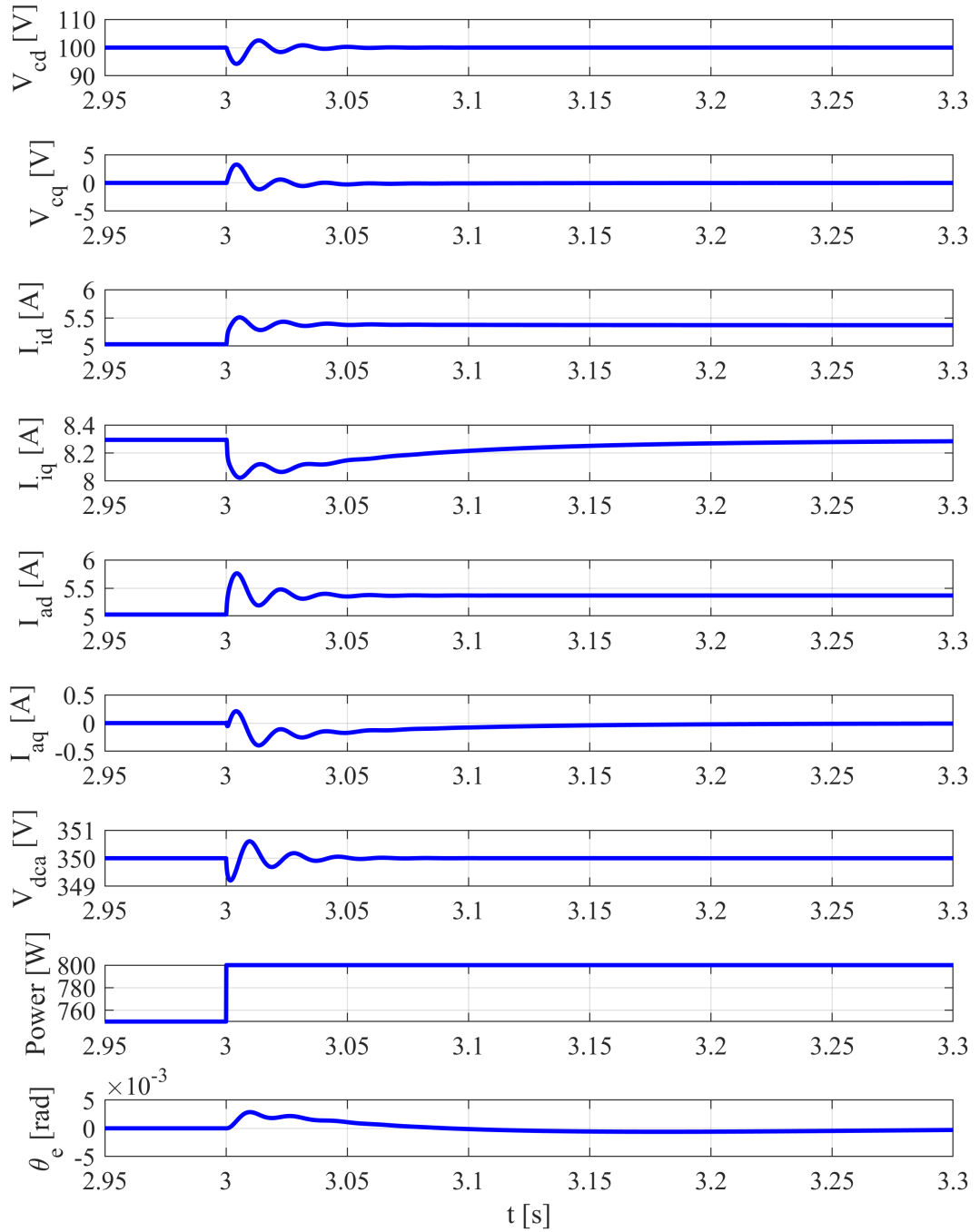
Figure 4.8: Simulation results of the VSI-AFE system when the AFE adopts an optimal H_2 controller based on the nominal model of VSI

The Q and R matrices used for the optimal H_2 controller tuning are

$$Q = diag(0, ..., 0, 0, 0, 1, 10, 0, 10)$$
$$R = diag(1, 1, 1, 1)$$

(4.61)

The resulting state feedback control gains matrix for AFE is

$$K = \begin{bmatrix} -0.0053 & -0.0176 & 0.0097 & 0.2635 & -7.2877 \\ 0.0303 & 0.0433 & 0.0079 & -0.4842 & -6.1075 \end{bmatrix}$$

(4.62)

$$k_p^p = 0.1483; k_i^p = 1.2246;$$

(4.63)

In the steady state, the equilibrium values of I_{id}, I_{iq}, m_d, m_q, I_{ad}, I_{aq}, p_d and p_q can be extracted from the waveforms and the values are 5.37A, 8.30A, 0.626, 0.047, 5.37A, 0A, 0.5676 and -0.045. Notably, the power-variant Clark transformation (namely the peak conventions described in A.1) is used in this research. From a view of power balance, according to the Fig.3.2, the power on the DC-link of AFE is

$$\frac{3V_{dca}}{4} p_d I_{ad} = 350 * 3/4 * 0.5676 * 5.37A = 800.1W$$

(4.64)

The active power supplied by the VSI is

$$V_{cd} * I_{ad} * 3/2 = 805.5W$$

(4.65)

Their difference comes from the dissipation on the power transmission line.

$$R_a * I_{ad}^2 * 3/2 = 5.45W$$

(4.66)

4.3.3 Standalone H_2 control design for AFE

In this case, a standalone H_2 controller based open loop model of the AFE shown in (3.24) is synthesized for AFE. Of course such a controller of AFE is tuned without considering dynamic feature of the VSI. Actually, it is difficult to find a standalone H_2 controller that could stabilize the VSI-AFE system when the AFE has a load bigger than 200W, even if different weights on Q and R are tried in tuning process. Average model simulation result of the VSI-AFE system when AFE adopts such a standalone H_2 controller is shown in Fig.4.9.

The Q and R matrices used for the optimal H_2 controller tuning are

$$Q = diag(0, ..., 0, 0, 0, 1, 10, 0, 10)$$
$$R = diag(1, 1, 1, 1)$$

(4.67)

The resulting state feedback control gains matrix for AFE is

$$K = \begin{bmatrix} 0.0156 & 0.0051 & 0.0135 & 3.3042 & -28.3505 \\ 0.0051 & 0.0101 & 0.0076 & -9.4350 & -9.7654 \end{bmatrix} \tag{4.68}$$

$$k_p^p = 1.0875; k_i^p = 9.9410; \tag{4.69}$$

As can bee in the figure, the controller works stably before t=2s when the CPL load on AFE is 200W. However when the load increased to 300W at t=2s, the system is unstable.
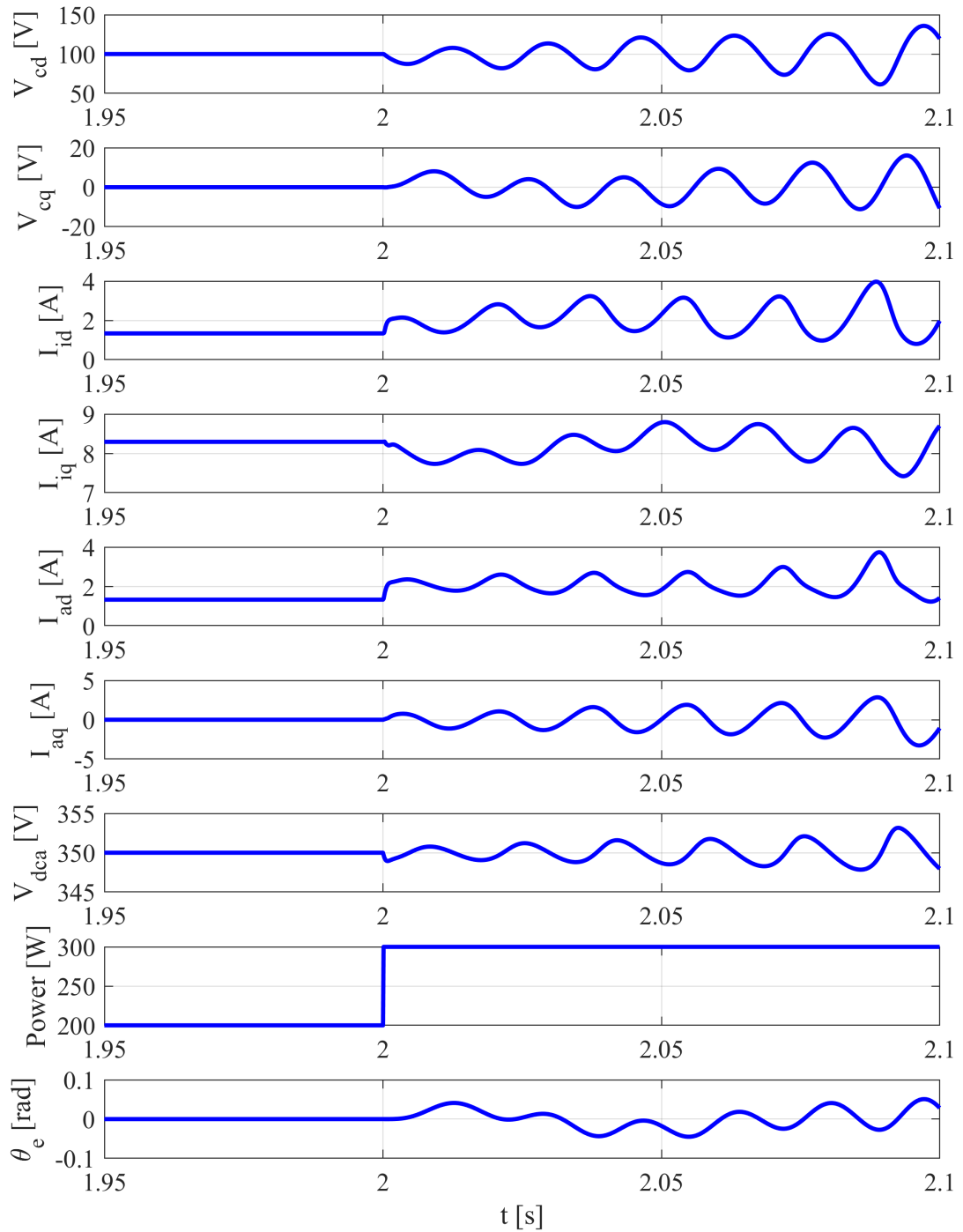
Figure 4.9: Simulation results of the VSI-AFE system when the AFE adopts a standalone H_2 controller

It is difficult to tune a standalone H_2 controller for AFE that could stabilize the VSI-AFE

system when AFE has a load of 800W. In the Fig.4.10, the top subdiagram shows the comparison of d-d axis impedance magnitude between VSI and AFE when AFE uses an optimal H_2 controller tuned by a nominal model of VSI, a PI controller, and a standalone H_2 controller respectively. The two diagrams below shows the d-d axis phase difference of VSI and AFE impedance. The bottom one is detailed drawing of the middle figure and indicates the 180° crossover frequencies. The figure helps to illustrate how instability occurs when a standalone H_2 controller is adopted. The standalone H_2 controller could not damping the d-d axis impedance of AFE sufficiently. As a result, the d-d axis impedance of AFE decreases to be smaller than that of VSI at the crossover frequency, which is around 100Hz here.
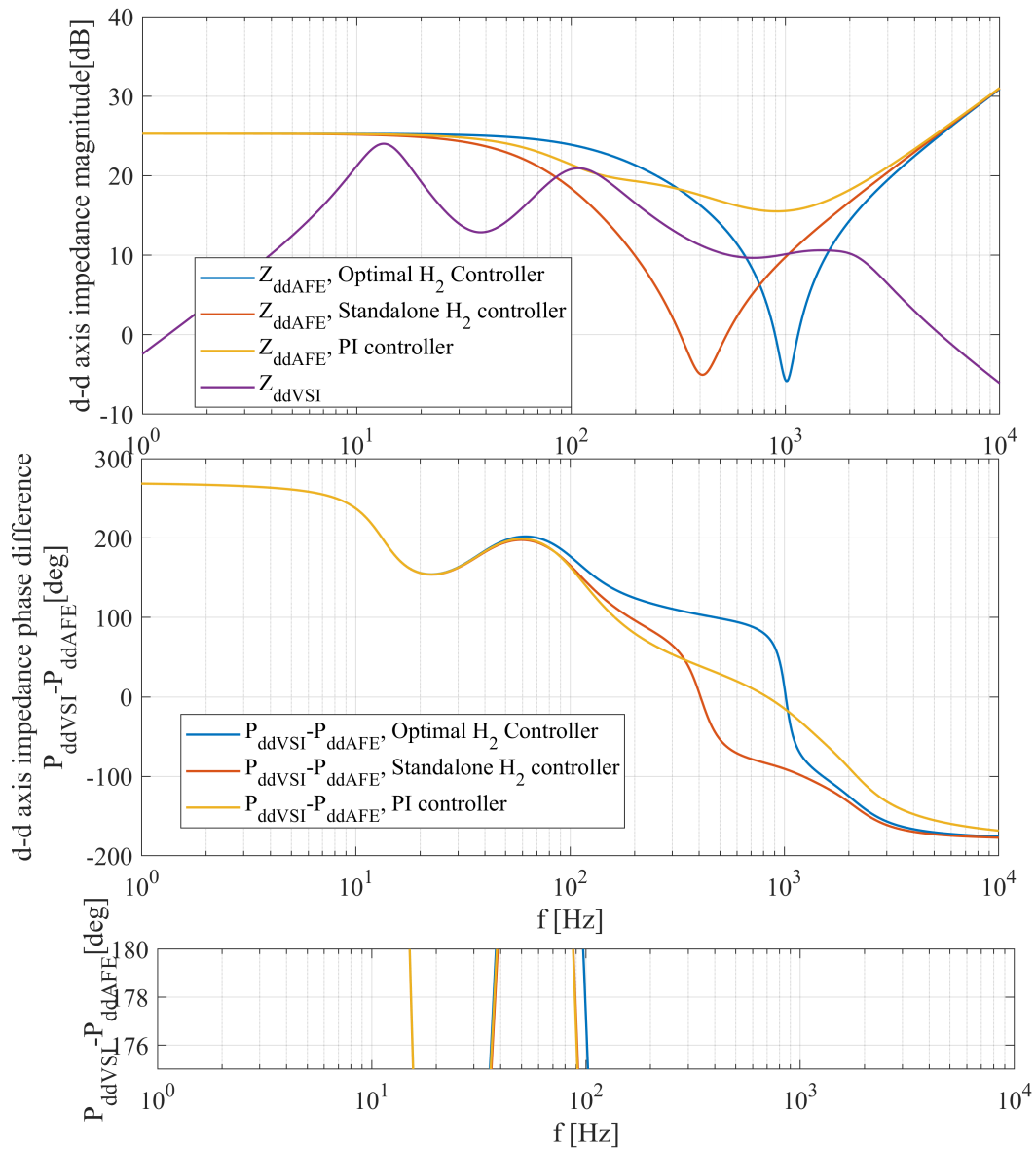
Figure 4.10: d-d axis impedance comparison between VSI and AFE when AFE uses an optimal H_2 controller tuned by a nominal model of VSI, a standalone H_2 controller, and a PI controller respectively

4.4   Conclusion

At the beginning of this chapter, knowledge about H_2 control algorithm was provided. After having a system global model, optimal H_2 controllers would be synthesized by the H_2 control algorithm. Some recommendations for H_2 controllers tuning were presented. In the next, as the core of this

research, derivation process of the optimal H_2 control design was provided. The details about how to build a system global model by merging grid model and model of the to be designed converter in the presence of PLL was given. Notably here the grid model was its nominal model, which is not available in normal practice. Adaptation of the method for the case when the grid feature needs to be identified will be provided in chapter 6. Based on the global model, two kinds of global controllers were synthesized, of which the performance in simulation were shown. More important, the time domain comparisons in simulation between PI control of AFE and optimal H_2 control of AFE were provided and the superiority of the latter was demonstrated.

Chapter 5

Robustness analysis with different system configurations

Passive components of converters especially those are parts of LC filters, play significant roles in characterizing impedance and dynamic behaviour of the converter. In industrial practice, it is common to employ bulky passive filters to mitigate the interactions between subsystems and guarantee the system stability. Therefore, it will be beneficial if the control design method that the converters are built upon has a great ability in mitigating the interactions and allows smaller filters. In this chapter, the impact of some main passive components of the VSI-AFE system on the converter impedance and further system stability is assessed. And more important, performance of the PI controllers and optimal H_2 controllers is investigated when these components deviate from their nominal values. The components are the VSI LC filter capacitor C and AFE DC-link capacitor C_a. The VSI LC filter inductor L and AFE inductor L_a have almost no impact on the converter impedance according to simultions. Therefore, they were not discussed in this chapter. The PI controllers involved are tuned locally with nominal values of the passive components. It is worth to note that, in order to make the comparisons in this chapter be fair, the PI controllers were elaborately tuned to their best performance. The comparisons are implemented by applying the two different control design methods, i.e. the PI control and optimal H_2 control, on the AFE sequentially. In addition to the passive components, impact of the converter control loop bandwidth on the converter impedance and system stability is also assessed.

5.1 VSI LC filter capacitance and system stability

The discussion starts with investigating how the capacitor value of the VSI's output LC filter (i.e. the 'C' in the Fig.3.1) affects the output impedance of VSI. It would help us to understand how to create a challenge for the control design of AFE by shaping the output impedance of VSI through C.

In Fig.5.1, the capacitance of C is set to different values while PI control parameters of the VSI are kept constant, and bode diagrams of the resulting d-d axis impedance of the VSI are plotted. It is envisioned that the d-d axis impedance magnitude decreases with the increment of C. According to the analysis in previous chapters, a voltage source should have a low impedance. Therefore, a bigger C means a better system stability condition of the VSI-AFE system. The AFE's d-d axis input impedance is plotted here as well to be compared with impedance of VSI and illustrate how instability could occur due to the decrease of C. The AFE employs a PI controller when plotting this figure. As can be seen in the Fig.5.1, when the C is decreased to $10\mu F$, the d-d axis impedance magnitude of AFE is smaller than that of VSI at the 180° crossover frequency and indicates an instability.
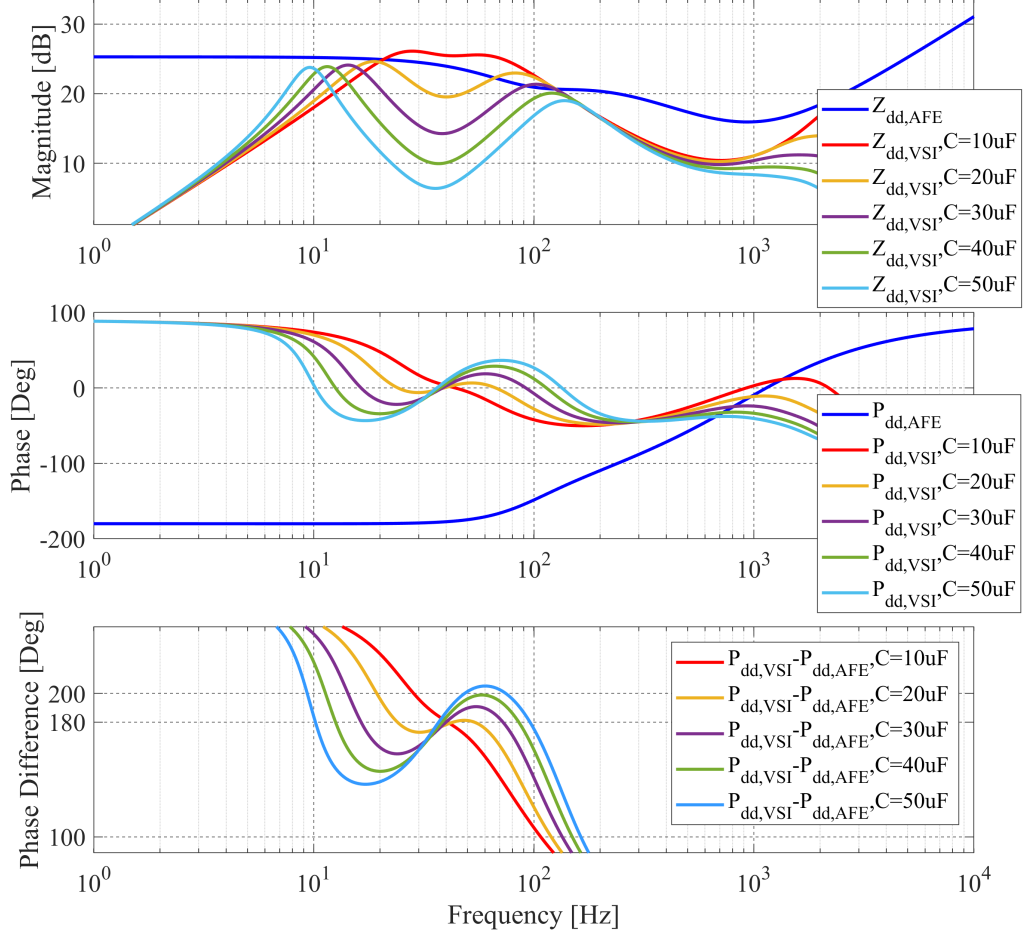
Figure 5.1: D-d axis impedance of AFE and VSI with different C

In the next, a simulation is implemented to compare the PI control and optimal H_2 control in presence of different C. Capacitance of the C is set as different values in the proximity of its nominal value $C = 33\mu F$. The simulation tries to replicate a situation where the AFE is working with a varying grid. The PI controller of VSI does not change as the variation of C in the simulation.

In the simulation, both the PI controller and optimal H_2 controller are tuned to their best performance considering the C is equal to its nominal value, i.e. $33\mu F$. The parameters tuned for the PI controller are $f_i = 1000$ and $f_v = 150$. And both the PI controller and H_2 controller keep constant in the simulation when the C changes. This case is designed to evaluate the robustness of these two control design methods against parameter drifting, here the capacitance of the VSI LC filter or grid impedance variation.

Figure 5.2: Locations of system dominant poles when the AFE uses a PI controller or an optimal H_2 controller under different VSI LC filter capacitance. Circles are PI poles and triangles are H_2 poles

In Fig.5.2, locations of the system closed loop model dominant poles are shown, when the AFE uses the invariant PI controller and optimal H_2 controller. The circles indicate the positions of PI poles while triangles indicate those of H_2 poles. As can be seen, the VSI-AFE system is unstable for the PI controller when the C is smaller than $21\mu F$. As can been clearly seen, if the H_2 controller is adopted, the dominant poles are generally with faster speed and more damping than those of the PI controller. It means under these capacitances, VSI-AFE system with AFE adopting an optimal H_2 controller has a much better performance than adopting a PI controller.

5.2   AFE DC-link capacitance and system stability

In this section, it is assumed that the capacitance value of the AFE dc-link capacitor (the C_a in the Fig.3.1) is not consistent with its nominal value $100\mu F$. It means the control design of AFE is

implemented based on an inaccurate open loop model. And this section will discuss how it impacts the system performance when the AFE control loop is closed. 7 sets of capacitance are chosen to test whether the system could perform well under these different dc-link filter capacitance. The AFE's model for time-domain simulation and poles location drawing are updated along with C_a, while both the PI and optimal H_2 controller remain unchanged throughout the comparison simulations. They are both designed with C_a of its nominal value. The dominant poles of the VSI-AFE system when AFE uses the PI controller and optimal H_2 controller are plotted in Fig.5.3.
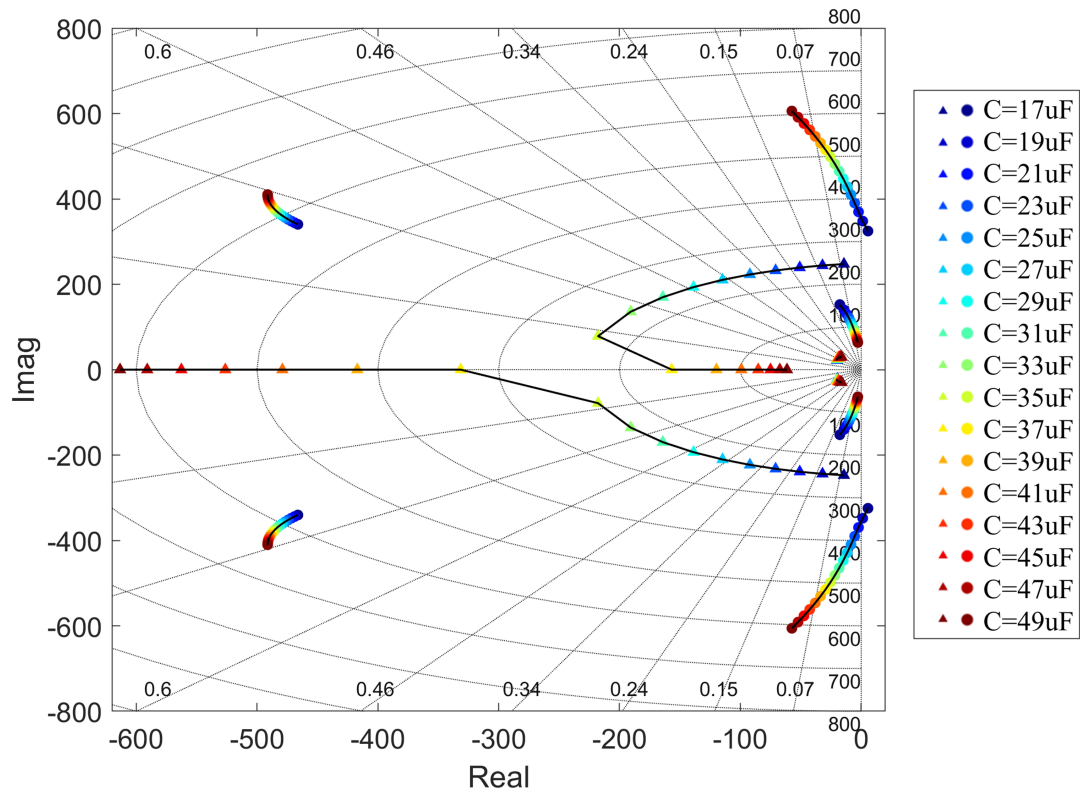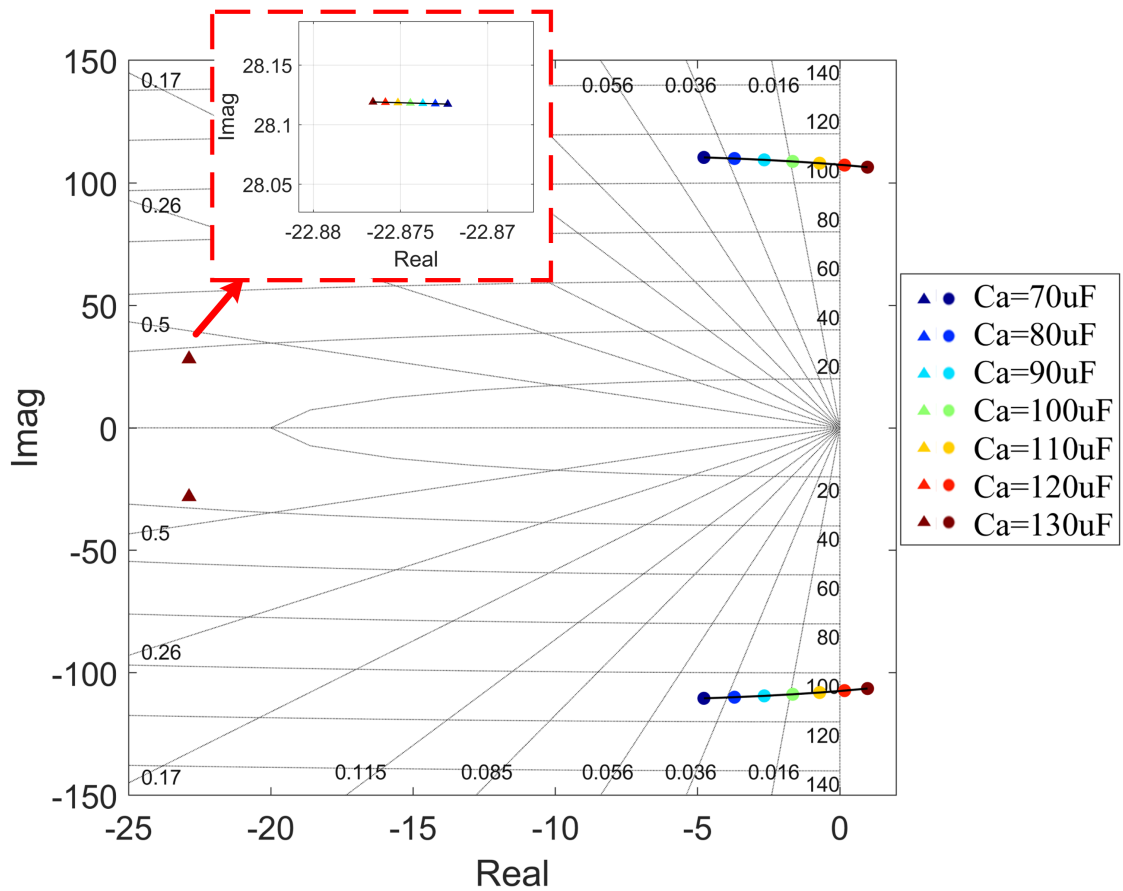

Figure 5.3: Locations of system dominant poles when the AFE uses a PI controller or an optimal H_2 controller under different dc-link capacitance. Circles are PI poles and triangles are H_2 poles.

As can be seen in the zoomed sub-figure in the Fig.5.3, the system model dominant poles with the H_2 controller under different capacitance of C_a all gather together and indicate that system is barely affected by C_a when AFE adopts the H_2 controller. And under all the different value of C_a, the optimal H2 controller can always stabilize the system. However for the PI controller, the poles move to the right half plane as the C_a increases. If the C_a deviates 20% and is bigger than

$120\mu F$, the system is unstable.
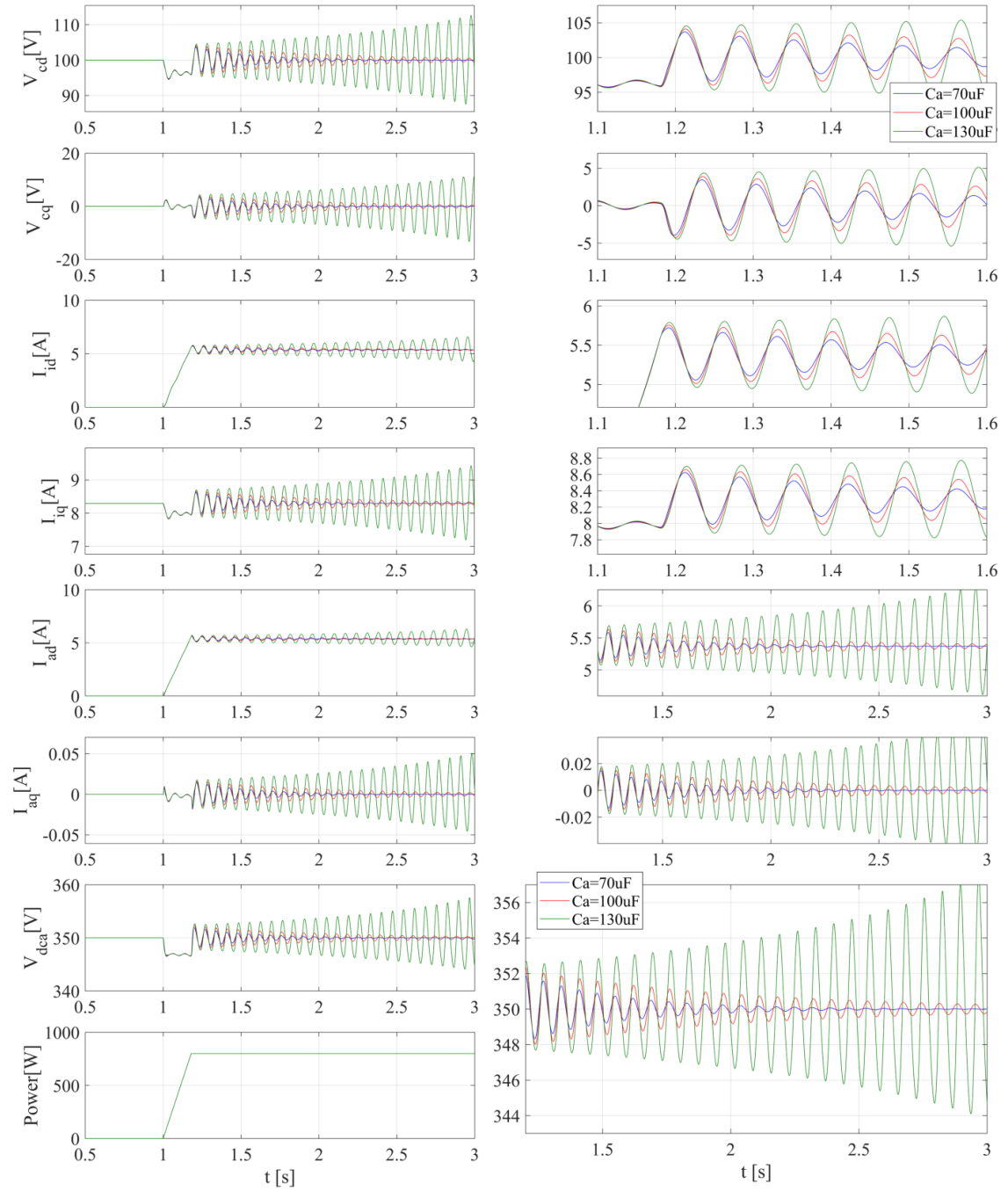
Figure 5.4: Time domain performance of main variables when the AFE uses the PI controller in presence of three sets of AFE dc-link capacitance
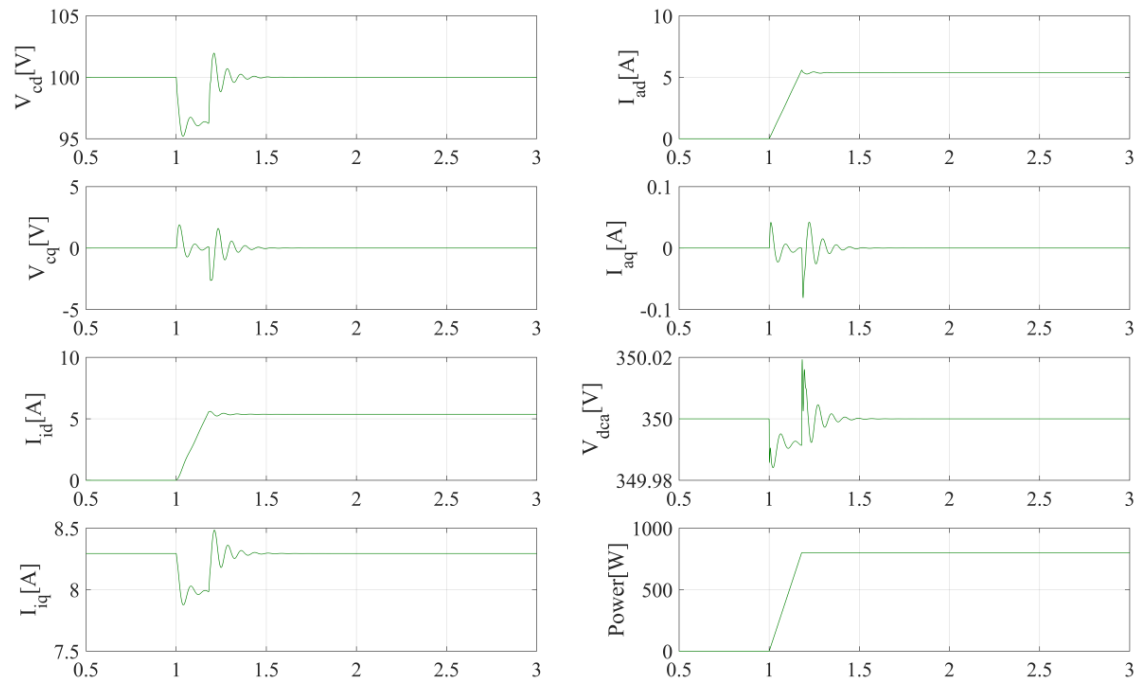
Figure 5.5: Time domain performance of main variables when the AFE uses the optimal H_2 controller in presence of three sets of AFE dc-link capacitance. Three experiments ($C_a = 70\mu F, 100\mu F, 130\mu F$) yield overlapped waveforms.

In the Fig.5.4 and Fig.5.5, system performance in time domain simulation when AFE adopts the PI controller and the optimal H_2 controller is shown when the C_a is $70\mu F$, $100\mu F$, and $130\mu F$ respectively. In the Fig.5.4, the system dynamic performance deteriorates as the C_a increases. The details in the transients are obtained by zooming in the waveforms and shown on the right column. While in the Fig.5.5, the VSI-AFE system with the three different AFE DC-link capacitance exhibits almost same performance and the waveforms are overlapped with each other. Obviously, the system performance comparison in the time domain coincides with the pole map shown in the Fig.5.3.

In all, the system dominant poles and dynamic response demonstrate that the H_2 controller has a greater robustness against the deviation of C_a. While for the PI controller, a 20% deviation of C_a could cause instability.

5.3 AFE CPL power and system stability

On the output of AFE, a CPL is attached as load and creates a more challenging situation for the control design of AFE, comparing to powering a resistive load. In this section, how the power of

the CPL affects the AFE impedance and further system stability is investigated.
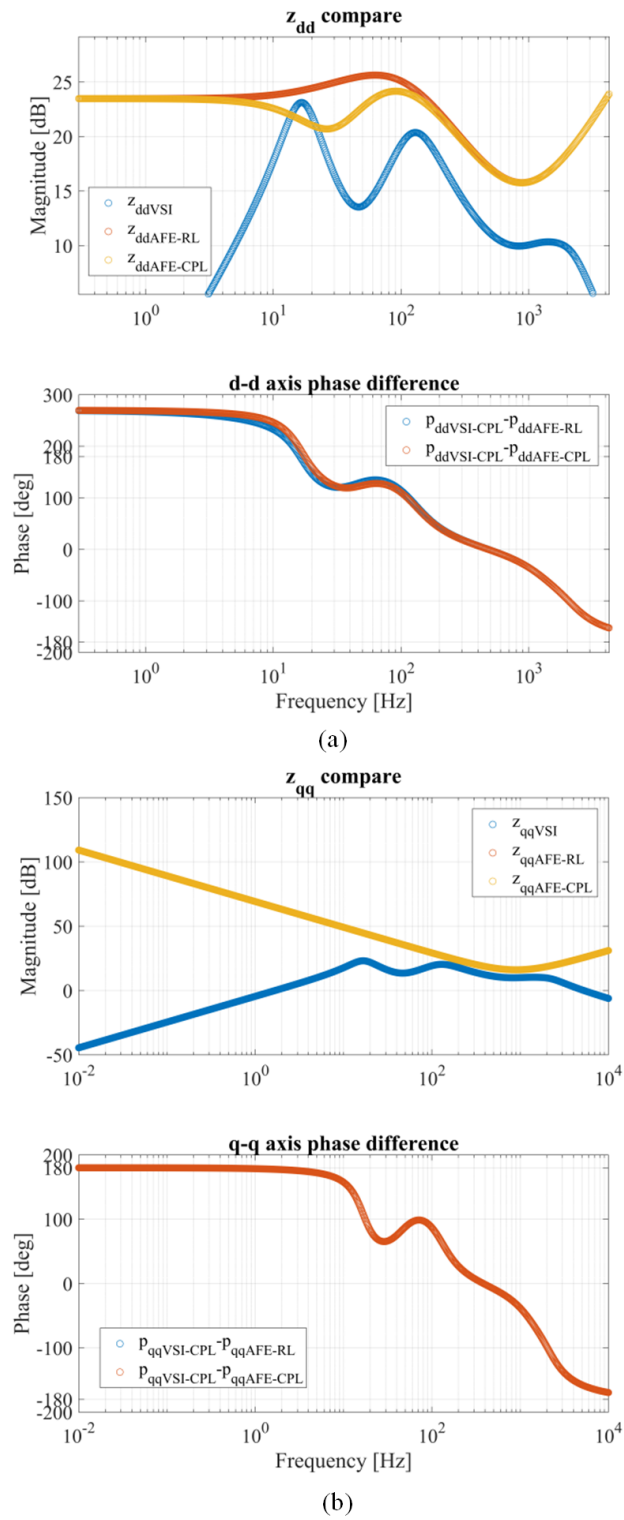
Figure 5.6: (a) d-d axis impedance of VSI z_{dd_vsi} and d-d axis impedance of AFE z_{dd_afe} when AFE feeds a RL (resistive load) or a CPL (b) q-q axis impedance of VSI z_{qq_vsi} and q-q axis impedance of AFE z_{qq_afe} when AFE feeds a RL or a CPL

In the Fig.5.6, the d-d and q-q axis impedance of AFE when it feeds a resistive load, or a CPL is plotted together with the impedance of VSI. Both the resistive load and CPL have a power rating of $1kW$. The AFE here uses a same PI controller for the resistive load and CPL. The d-d axis and q-q axis impedance magnitude and phase difference between VSI and AFE are plotted. As can be seen, the q-q axis impedance of AFE has no difference between a RL and CPL (the curves of these two cases are overlapped). It is shown in the Fig.5.6(a) that the d-d axis impedance of AFE with a CPL exhibits lower magnitude than the resistive load case in the frequency range from 10Hz to 100Hz, which may cause instability. It actually happened because at the $180°$ crossover frequency of phase difference, about 16Hz here, the reduced d-d axis impedance magnitude of AFE becomes smaller than that of VSI. It proves that a CPL causes more difficulty for the control design of AFE. Meanwhile, the Fig.5.6(b) shows that the phase difference curve in q-q axis never cross $180°$, which means q-q axis impedance is not a concern when analysing system stability.
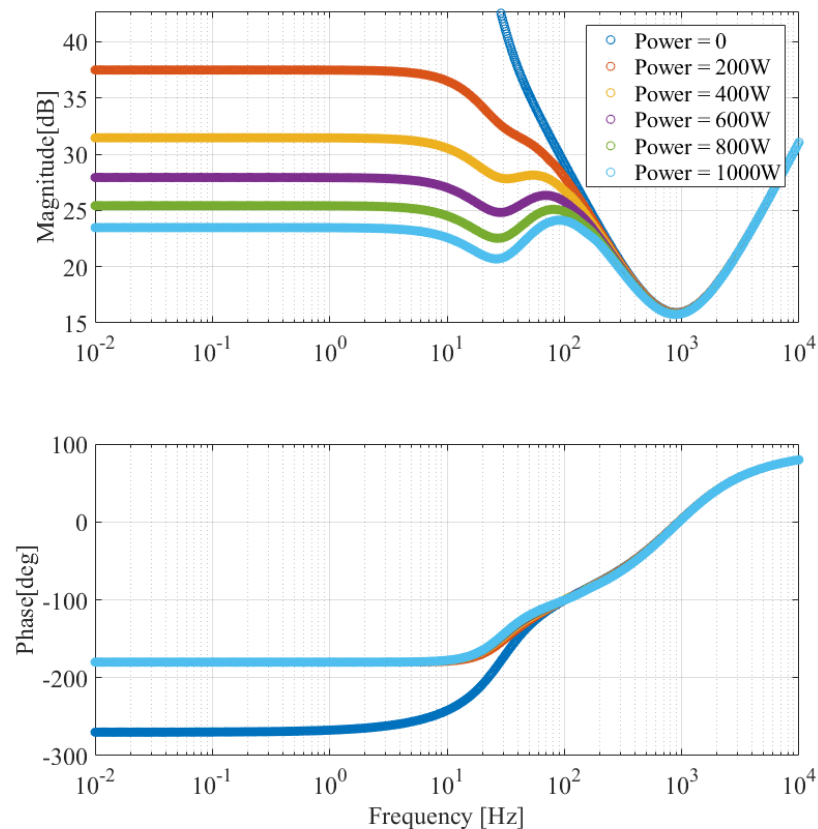
Figure 5.7: z_{dd_afe}'s variation due to the power change of CPL when AFE adopts a PI controller
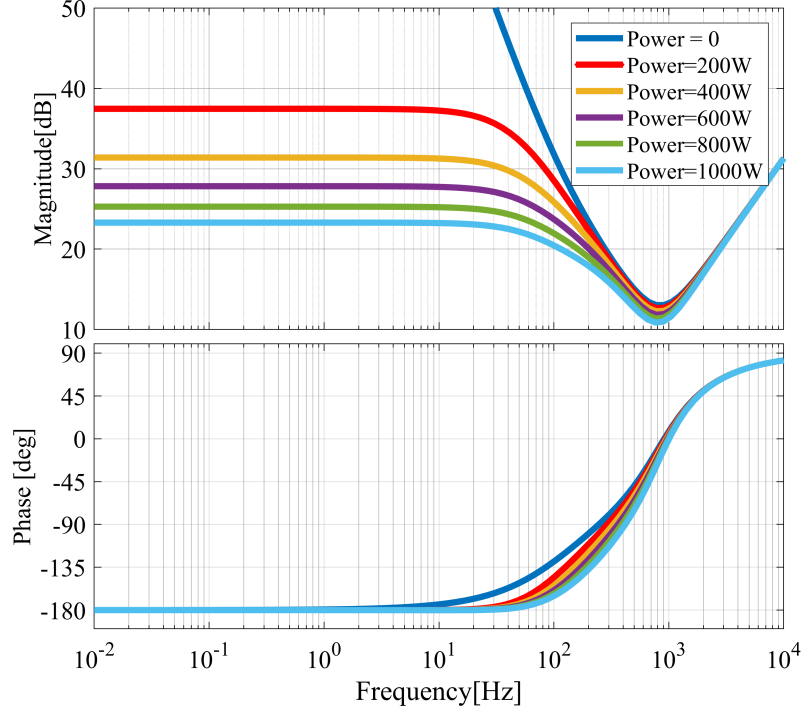
Figure 5.8: z_{dd_afe}'s variation due to the power change of CPL when AFE adopts an optimal H_2 controller

In last paragraph, the different impact of a resistive load and a CPL on AFE's impedance is presented. In the next, impact of the power of CPL on the AFE's impedance is analysed. As the q-q axis impedance is not a concern for stability analysis, only the d-d axis impedance is analysed here. In the Fig.5.7, d-d axis impedance of AFE adopting a PI controller when it feeds CPL of different power rating is shown. The case when the AFE adopts an optimal H_2 controller is shown in Fig.5.8. As can be seen, the tendency of impedance variation due to the power variation is same with the case of PI.

As the output voltage of AFE V_{dca} is regulated by d-axis, the d-d axis impedance of AFE features a negative resistance behaviour in the low frequency range [14]. Meanwhile, as current on the q-axis I_{aq} is regulated to 0 to maintain a unity power factor, the d-d axis is the path to deliver power. Therefore, the d-d axis impedance of AFE in the low frequency range is

$$z_{dd\_afe} = -20 \cdot log_{10} \frac{V_{cd}^*}{I_{ad}^*} \tag{5.1}$$

A bigger power rating the CPL has, a smaller z_{dd_afe} is, and further more risk of system insta-

bility. In the Fig.5.7 and Fig.5.8, as the power of CPL increases from 0 to 1000W, the d-d axis impedance magnitude of AFE decreases drastically.
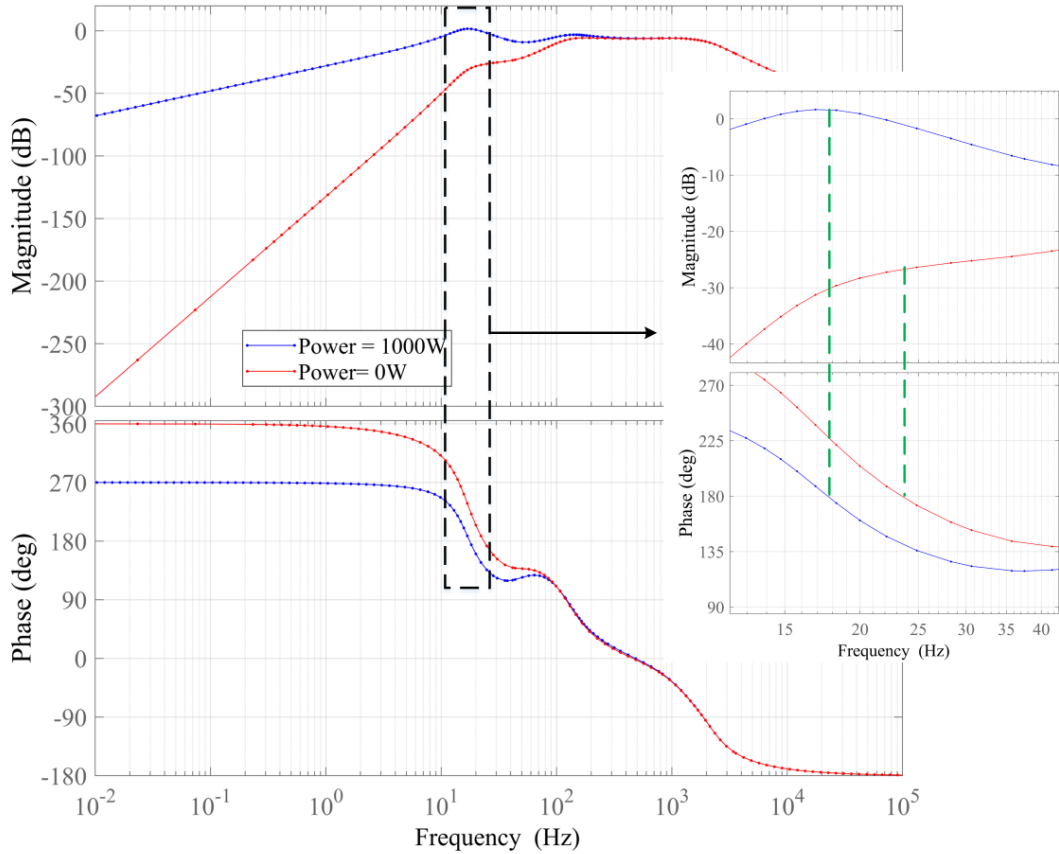
Figure 5.9: z_{dd_vsi}/z_{dd_afe} when $Power = 0W$ and $Power = 1000W$

In Fig.5.9, the d-d axis impedance ratio from the VSI to AFE in bode diagram is shown. As can be seen, when the power of CPL is increased to 1000w, the AFE d-d axis impedance magnitude is smaller than VSI (i.e. the VSI-AFE impedance ratio is bigger than 0 dB) at the $180°$ crossover frequency (around 16Hz here) which indicates instability.

5.4   Impedance of a multi-converter network

When installing a new AFE into an existing power grid comprised of multi-converters, it is natural to design it under the most harsh grid conditions. Namely, it should be able to work when the multi-converter grid shows its greatest impedance. Therefore, it is worth to investigate how the overall

impedance of an exemplary multi-converter network (shown in peach block in Fig.5.10) which is comprised of a load converter (i.e. the AFE1) and a source converter (i.e. the VSI) changes due to power change of the load (i.e. the 'Load1' in the Fig.5.10). It would be beneficial to the control design for the new AFE (i.e. the AFE2) which will be installed into the multi-converter grid.
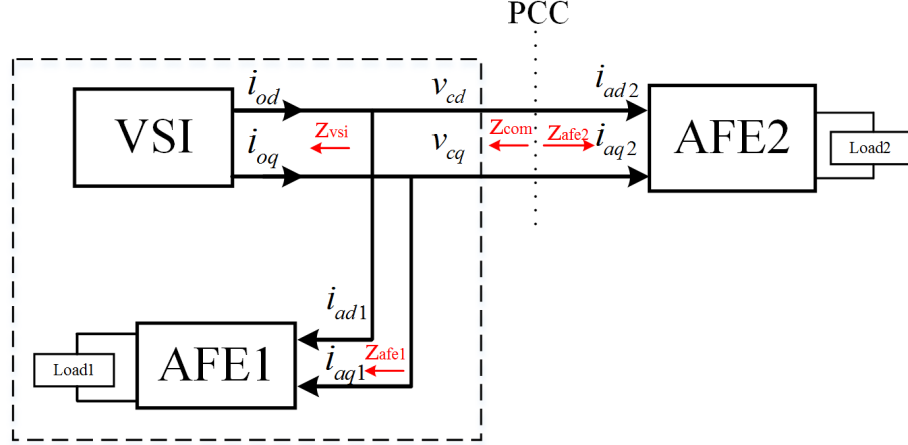
Figure 5.10: Multi-converter system in discussion

In the Fig.5.10, the input current of AFE1 in d-axis and q-axis are denoted as i_{ad1} and i_{aq1} respectively. The input current of AFE2 are denoted as i_{ad2} and i_{aq2}. i_{od} and i_{oq} are the VSI's output current. z_{com} is equivalent impedance of the VSI-AFE1 network. z_{afe1} and z_{afe2} are input impedance of the AFE1 and AFE2 respectively. z_{vsi} is output impedance of the VSI. The positive directions of those currents and impedances are signified by the arrows in the Fig.5.10.

It is clear that

$$i_{od} = i_{ad1} + i_{ad2} \tag{5.2}$$

$$i_{oq} = i_{aq1} + i_{aq2} \tag{5.3}$$

The AC bus voltage can be expressed as product of the impedance and input current,

$$\begin{bmatrix} v_{cd} \\ v_{cq} \end{bmatrix} = -z_{vsi} \begin{bmatrix} i_{od} \\ i_{oq} \end{bmatrix} = z_{afe1} \begin{bmatrix} i_{ad1} \\ i_{aq1} \end{bmatrix} = z_{com} \begin{bmatrix} -i_{ad2} \\ -i_{aq2} \end{bmatrix} \tag{5.4}$$

$$\begin{bmatrix} v_{cd} \\ v_{cq} \end{bmatrix} = z_{com} \begin{bmatrix} i_{ad1} - i_{od} \\ i_{aq1} - i_{oq} \end{bmatrix} = z_{com} \begin{bmatrix} i_{ad1} \\ i_{aq1} \end{bmatrix} - z_{com} \begin{bmatrix} i_{od} \\ i_{oq} \end{bmatrix} \tag{5.5}$$

$$\begin{bmatrix} v_{cd} \\ v_{cq} \end{bmatrix} = z_{com} z_{afe1}^{-1} \begin{bmatrix} v_{cd} \\ v_{cq} \end{bmatrix} + z_{com} z_{vsi}^{-1} \begin{bmatrix} v_{cd} \\ v_{cq} \end{bmatrix} \tag{5.6}$$

Therefore, the equivalent impedance of the VSI-AFE1 network is

$$z_{com} = (z_{afe1}^{-1} + z_{vsi}^{-1})^{-1} \tag{5.7}$$

Eq.(5.7) gives out the way of calculating impedance of the VSI-AFE1 network by individual impedance of the two converters. Based this equation, the relationship between power of AFE1's CPL and d-d axis impedance of the VSI-AFE1 network is shown in Fig.5.11. In the following multi-converter simulations, the AFE1 adopts a PI controller.
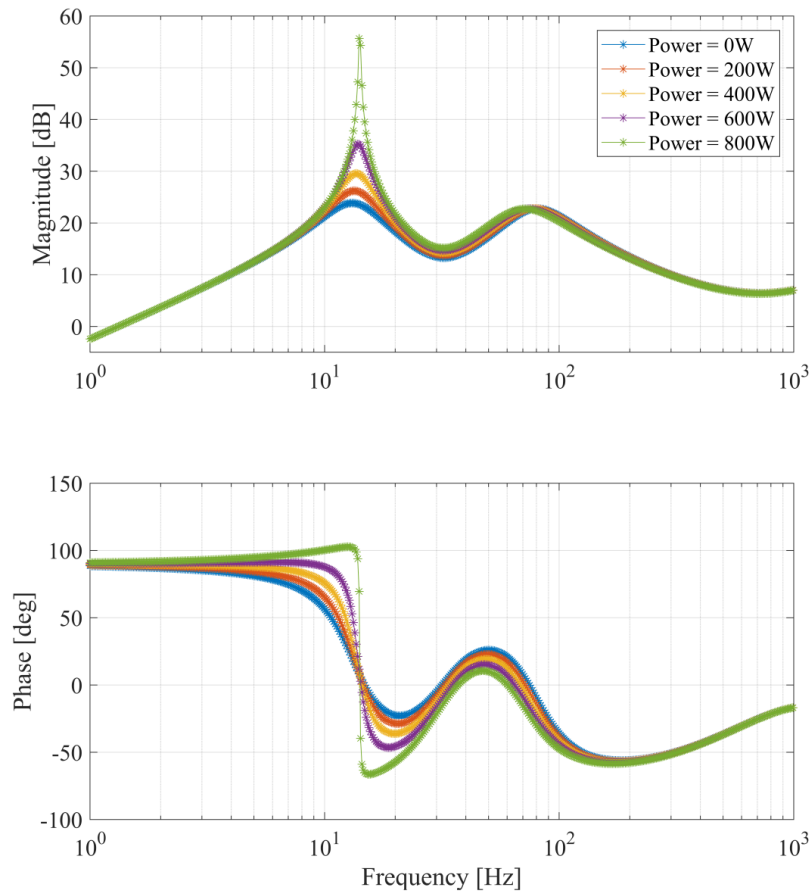
Figure 5.11: $z_{dd,com}$, d-d axis impedance of the VSI-AFE1 network

As can be seen in the Fig.5.11, d-d axis impedance magnitude of VSI-AFE1 network increases when the power of AFE1's load increases and causes more risk of instability. Therefore, the design of AFE2 should be implemented under the condition that AFE1 is working with its maximum load. This conclusion is also verified by simulations below.

In the first simulation, a controller is synthesized by the proposed optimal H_2 control design method for the AFE2, with the nominal model of VSI-AFE1 network when the AFE1 feeds its full load P_1 =800W. In the time domain simulation, the AFE1 starts with no load and the load of AFE2 is increased from 0 to 700W at from t=1s to t=1.18s. After the system is in steady state, the load of AFE1 then gradually increases from 0 to 800W. The load of AFE1 steps up 100W every 0.5s from t=3s to t=7s. Time-domain waveforms obtained in the simulation are shown in Fig.5.12. As can be seen, this process goes steadily. The first top 4 waveforms are of VSI's variables, next 3 are of AFE1's variables, and last 3 are of AFE2's variables.
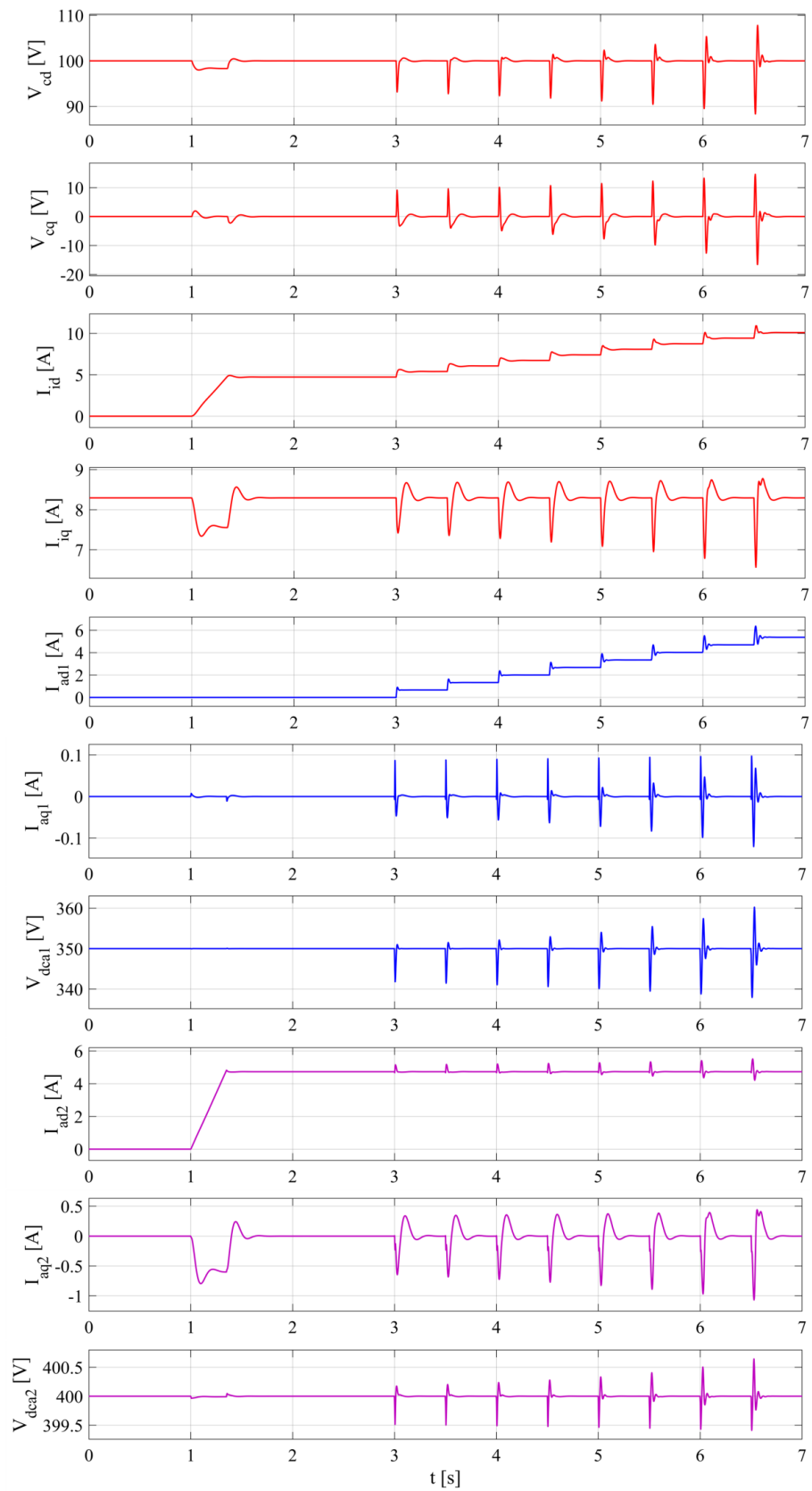
Figure 5.12: Waveforms of system response when AFE2 is designed considering AFE1 feeds a full load

Whereas in the second simulation, the AFE2's optimal H_2 controller is tuned with nominal model of the VSI-AFE1 network when AFE1 has no load. It means the AFE2's controller is designed in a relatively permissive grid condition. The simulation results in this case are shown in Fig.5.13. As can be seen, when the load of AFE1 reaches $P_1 = 700W$ at t=6s, instability is yielded.

In conclusion, when the proposed control design method is applied to the control design of a local converter, model identification of the unknown multi-converter grid should be implemented when the converters in the grid are working with their heaviest load.
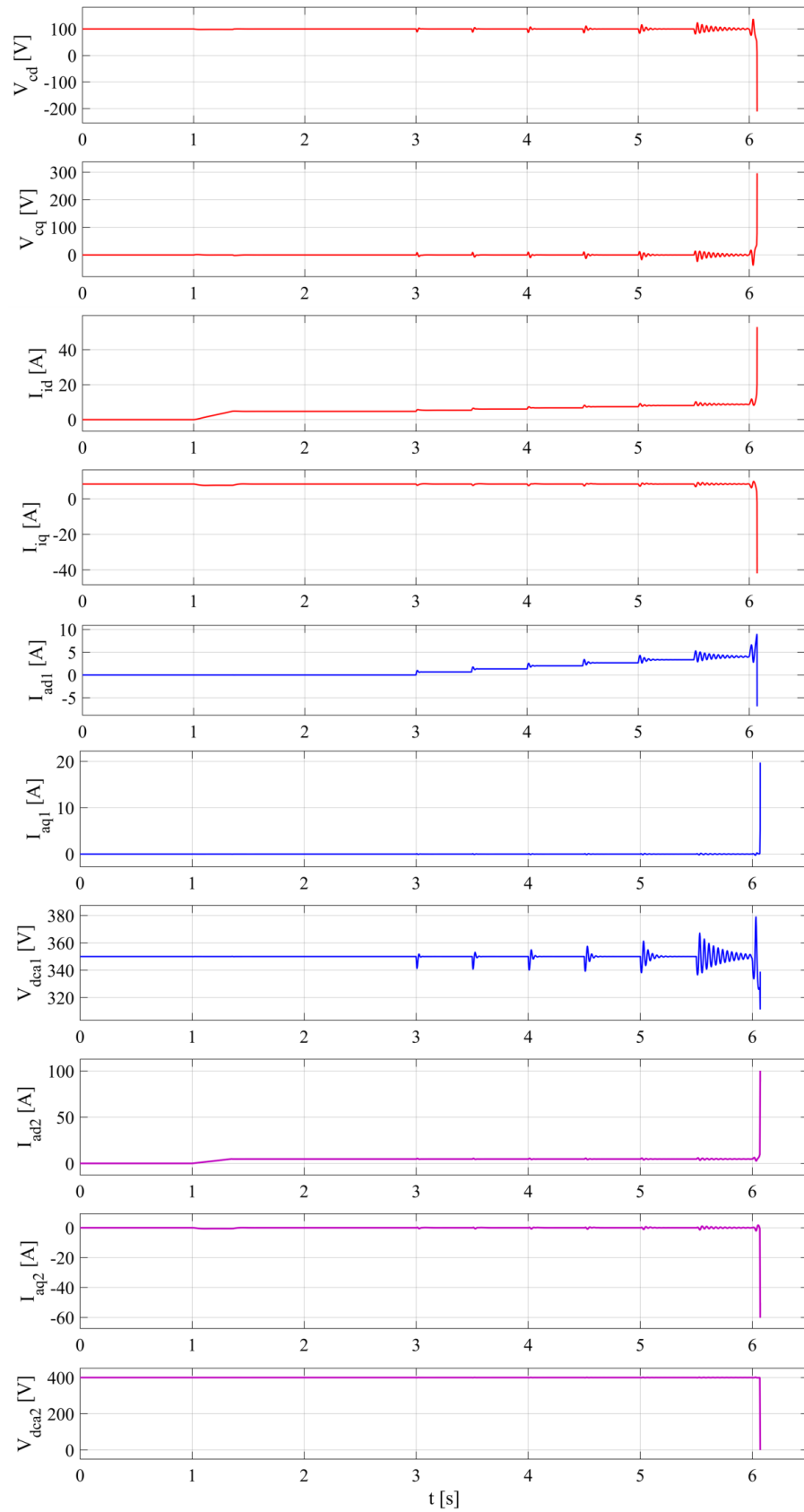
Figure 5.13: Waveforms of system response when the AFE2 is designed considering AFE1 has no load

5.5 Optimal H_2 control design in multi-converter network

In this part, effectiveness of the proposed optimal H_2 control design method in multi-converter application is investigated. Structure of the multi-converter network in question is same with the network shown in Fig.5.10. Dynamic performance of the VSI-AFE1-AFE2 system in transients when the AFE2 is designed based on the standalone PI control and the proposed optimal H_2 control design method will be compared by time-domain simulations.

In the simulations, a VSI supplies power for 2 AFEs as shown in Fig.5.10. Both the VSI and AFE1 employ the PI control scheme. Table 5.1 shows parameters of the 3 converters used in the simulations. The parameters of VSI and AFE1 are consistent with their values of components used in the experimental rig. The AFE2 parameters are assumed by the authors. According to simulation results, different selections of the parameters' values do not affect the basic conclusions drawn by the following simulations.

Table 5.1: Parameters in the multi-converter simulation

VSI				AFE1				AFE2			
R	$65m\Omega$	V_{dc}	320V	R_a	$126m\Omega$	P	0.8kW	R_a	$300m\Omega$	P	0.1kW
L	$360\mu H$	V_{cdref}	100V	L_a	$565\mu H$	$V_{dca_{ref}}$	350V	L_a	$400\mu H$	$V_{dca_{ref}}$	400V
C	$33\mu F$	V_{cqref}	0V	C_a	$100\mu F$	$I_{aq_{ref}}$	0A	C_a	$200\mu F$	$I_{aq_{ref}}$	0
f_v	80	f_i	800	f_v	45	f_i	900	f_v	60	f_i	600

In the first simulation, the AFE2 adopts a best tuned PI controller. And the heaviest load it could handle is only 100W. A load with power $P_2 > 100W$ will cause instability of the whole system. The waveforms obtained in the simulation are shown in Fig.5.14. The simulation starts with no load for AFE1 and AFE2. At t=1s, the CPL of AFE1 P_1=0.8kW is attached on AFE1. At t=3s, the CPL of AFE2 P_2=0.1kW is attached on AFE2. Characteristic loci of the impedance ratio from z_{com} to z_{afe2} are plotted in Fig.5.15. The loci are very close to encircling the critical point $(-1, 0i)$.

Figure 5.14: Time domain simulation waveforms when AFE2 uses a PI controller and has a load of 100W
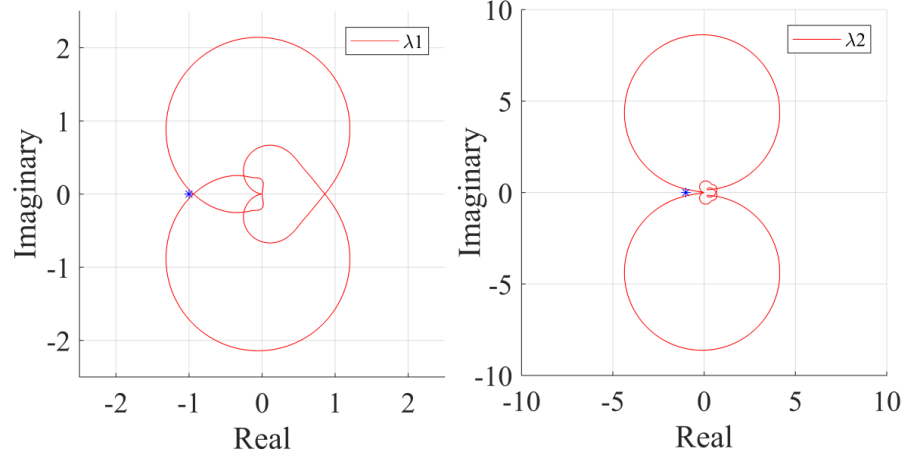
Figure 5.15: Characteristic loci from z_{com} to z_{afe2} when AFE2 adopts a PI controller. The CPL load on the AFE1 is 800W. The CPL load on the AFE2 is 100W.

In the second simulation, the AFE2 adopts an optimal H_2 controller tuned with the nominal model of VSI-AFE1 network. The load power that AFE2 handles is 700W. Time domain waveforms obtained in the simulation are shown in Fig.5.16. Characteristic loci in this case are shown in Fig.5.17. As can be seen, the VSI-AFE1-AFE2 system works smoothly in presence of the load change.

The Q and R matrices used for the optimal H_2 controller tuning are

$$Q = diag(0, ..., 0, 0, 0, 0, 1, 10)$$
$$R = diag(1, 1)$$

(5.8)

The resulting state feedback control gains matrix for AFE2 is

$$K = \begin{bmatrix} 0.0032 & -0.0027 & 0.0195 & 0.0622 & -11.8318 \\ 0.0104 & 0.0327 & -0.0267 & -0.4507 & 13.4201 \end{bmatrix}$$

(5.9)

In can be concluded that in multi-converter applications, the proposed optimal H_2 control design method outperforms standalone PI control method with faster dynamic and bigger loading capacity. According the average model simulations not included here, the upper limit of constant power ramp load that AFE2 can handle when it adopts an optimal H_2 controller is about 1300W. The ramp up speed is 2000W/s. The nominal model of VSI-AFE1 network z_{com} used for optimal H_2 controller tuning has a order of 14, and the order of AFE2 model is 5. Therefore, the system global model used for H_2 optimization is 19. And the structured H_2 algorithm could work well with such a high order model.
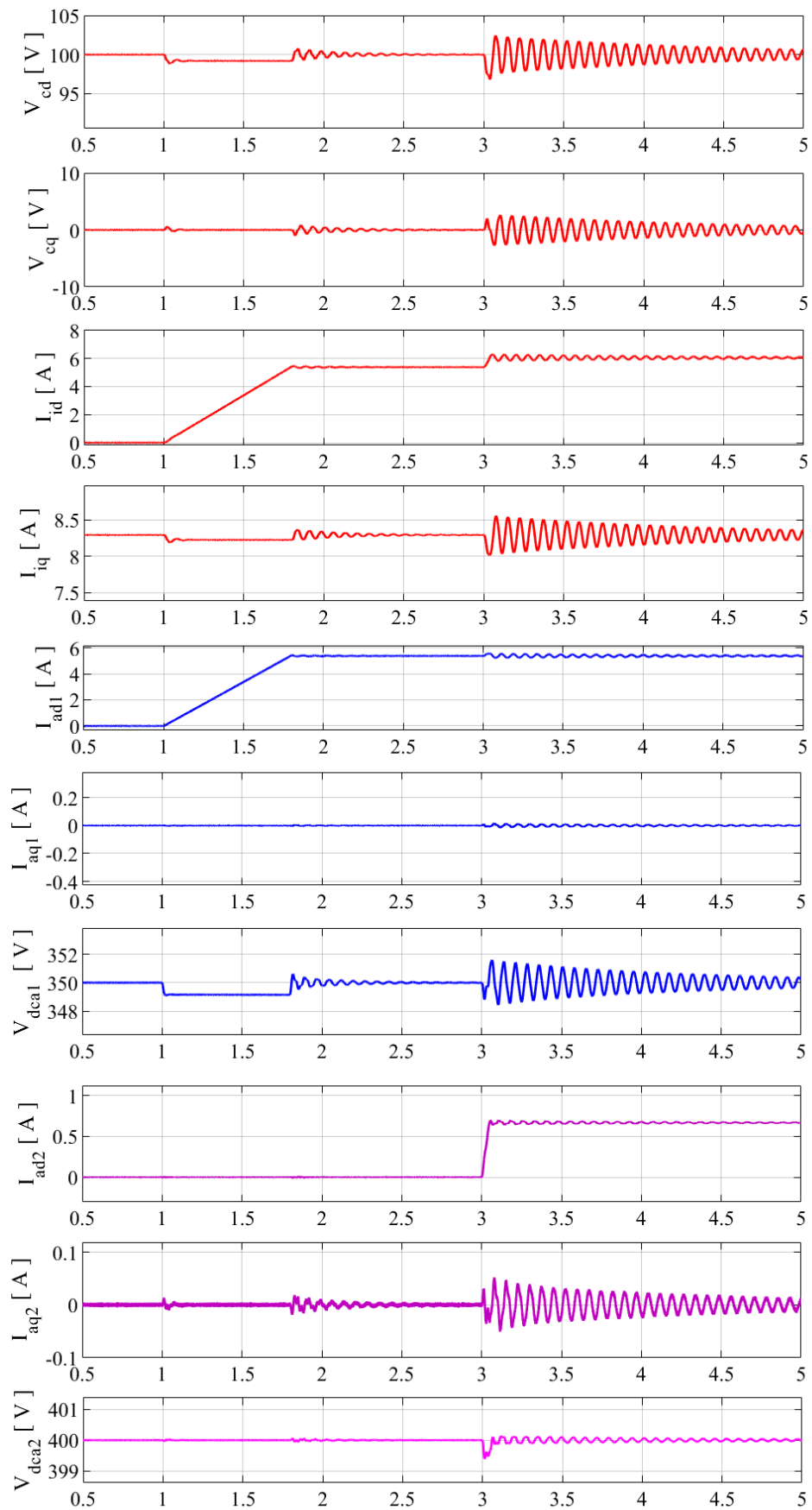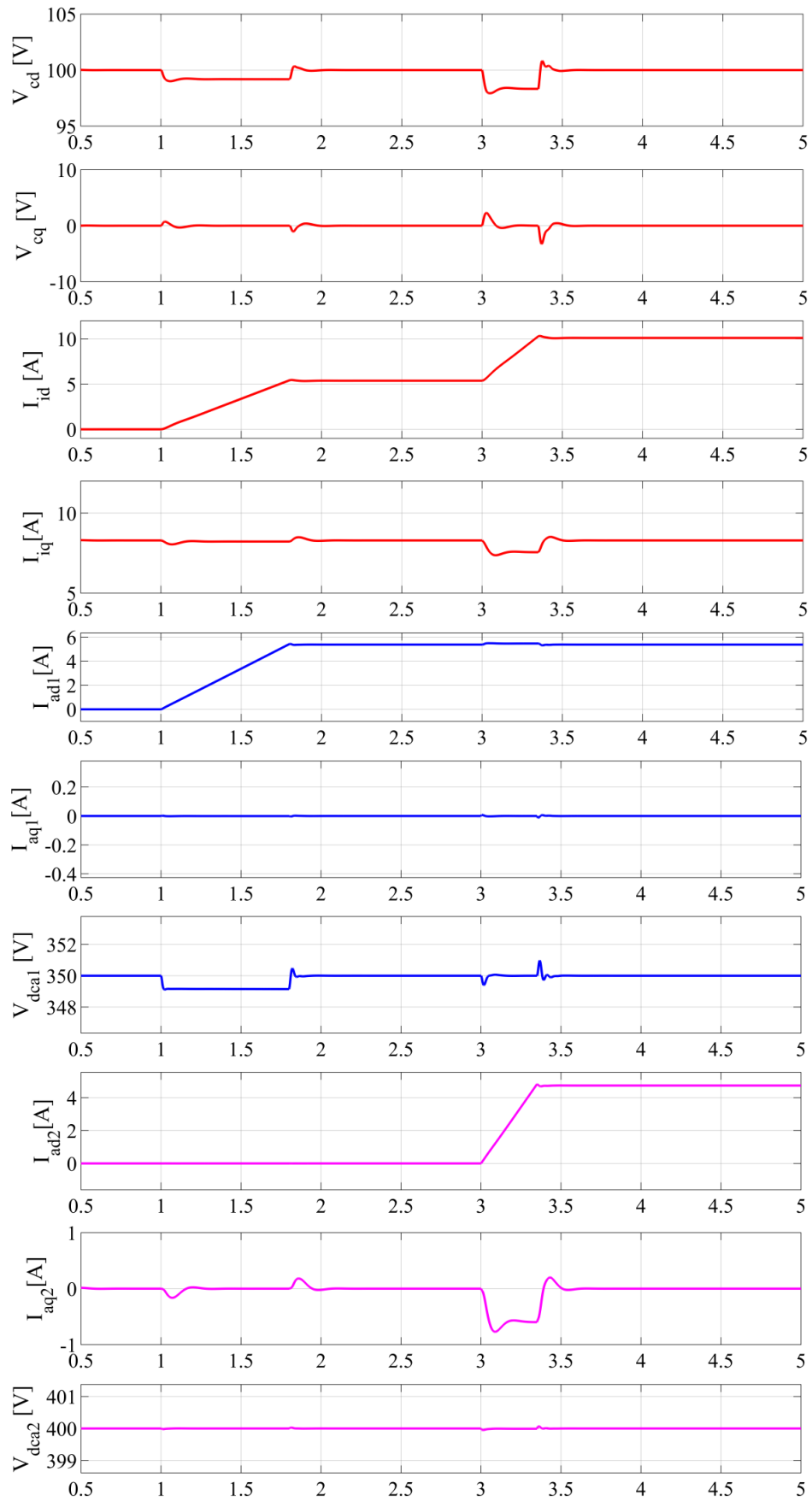
Figure 5.16: Time domain simulation waveforms when AFE2 uses an optimal H_2 controller and has a load of 700W
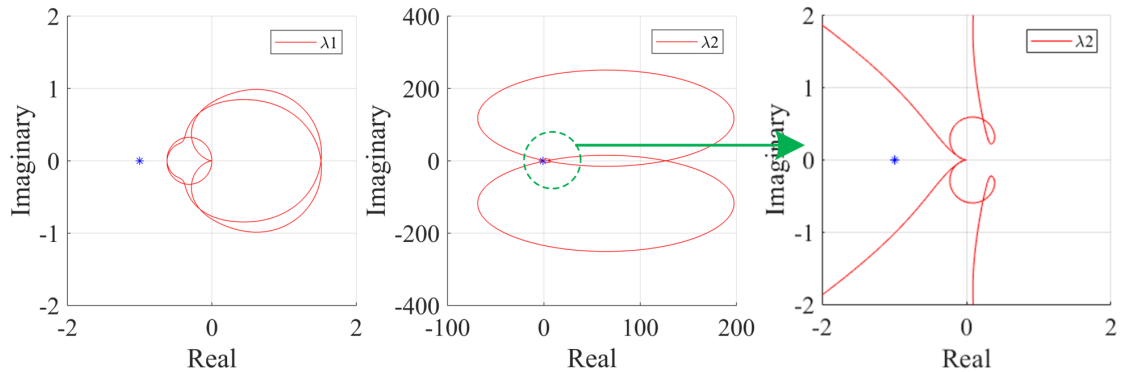
Figure 5.17: Characteristic loci from z_{com} to z_{afe2} when the AFE2 adopts an optimal H_2 controller. The second characteristic locus for λ_2 is zoomed in on the right for clarity.

5.6 Voltage bandwidth of PI VSI and system stability

The VSI in this research employs a PI control scheme. In this section, the impact of its voltage bandwidth on its output impedance and stability of the VSI-AFE system will be assessed. In the Sec.4.3, performance of the VSI-AFE system when the AFE is designed by PI control and optimal H_2 control are compared. The AFEs are powered by a same VSI which is introduced to emulate the grid. To highlight the advantages of optimal H_2 control design method, it is desirable to create a weak grid for the AFE. Therefore, it is worth to investigate how to create a weak grid i.e. a more challenging condition for the control design of AFE by changing the bandwidth of VSI.

According to (3.41), the bandwidth of a VSI based on PI control scheme can be adjusted by setting different values for f_i and f_v. In the Fig.5.18, bode diagrams of the VSI's d-d axis impedance are plotted when the VSI is tuned with different f_i and f_v.

In the Fig.5.18, the voltage bandwidth of VSI varies from 8Hz to 24Hz. For the ease of judging the VSI-AFE system stability in these difference cases, the d-d axis impedance of AFE and phase difference between the VSI and AFE are also plotted. According to the zoomed-in figure, magnitude of VSI's d-d axis impedance at 180° crossover frequency decreases with the increment of VSI's voltage bandwidth. As discussed before, it means a better stability condition. Hence, decrease of VSI's voltage bandwidth will be bad for the system stability. Specifically in the case shown in Fig.5.18, when the VSI's voltage bandwidth is less than 15Hz, the VSI-AFE system will be unstable.
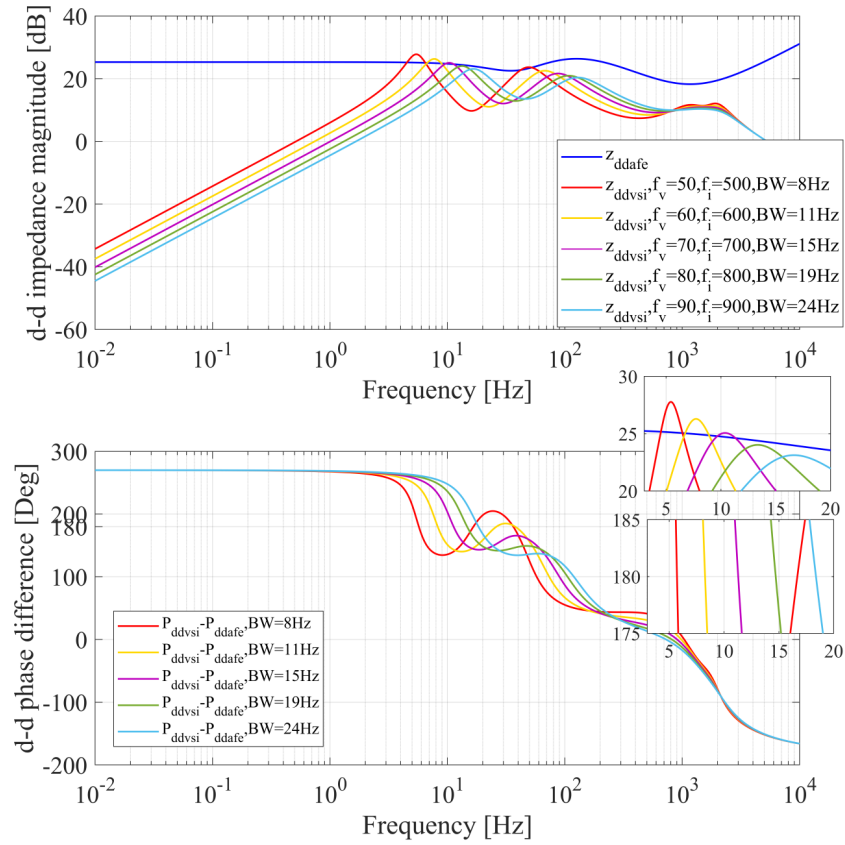
Figure 5.18: D-d axis impedance comparison when the VSI has different voltage bandwidths

It is also verified by time domain simulations. In the simulations, the VSI is equipped with PI controllers of different voltage bandwidths. The response of VSI-AFE system to a CPL ramping up to 800W is plotted in Fig.5.19. As can be seen, the time domain simulation results coincide with the bode diagram shown in the Fig.5.18.
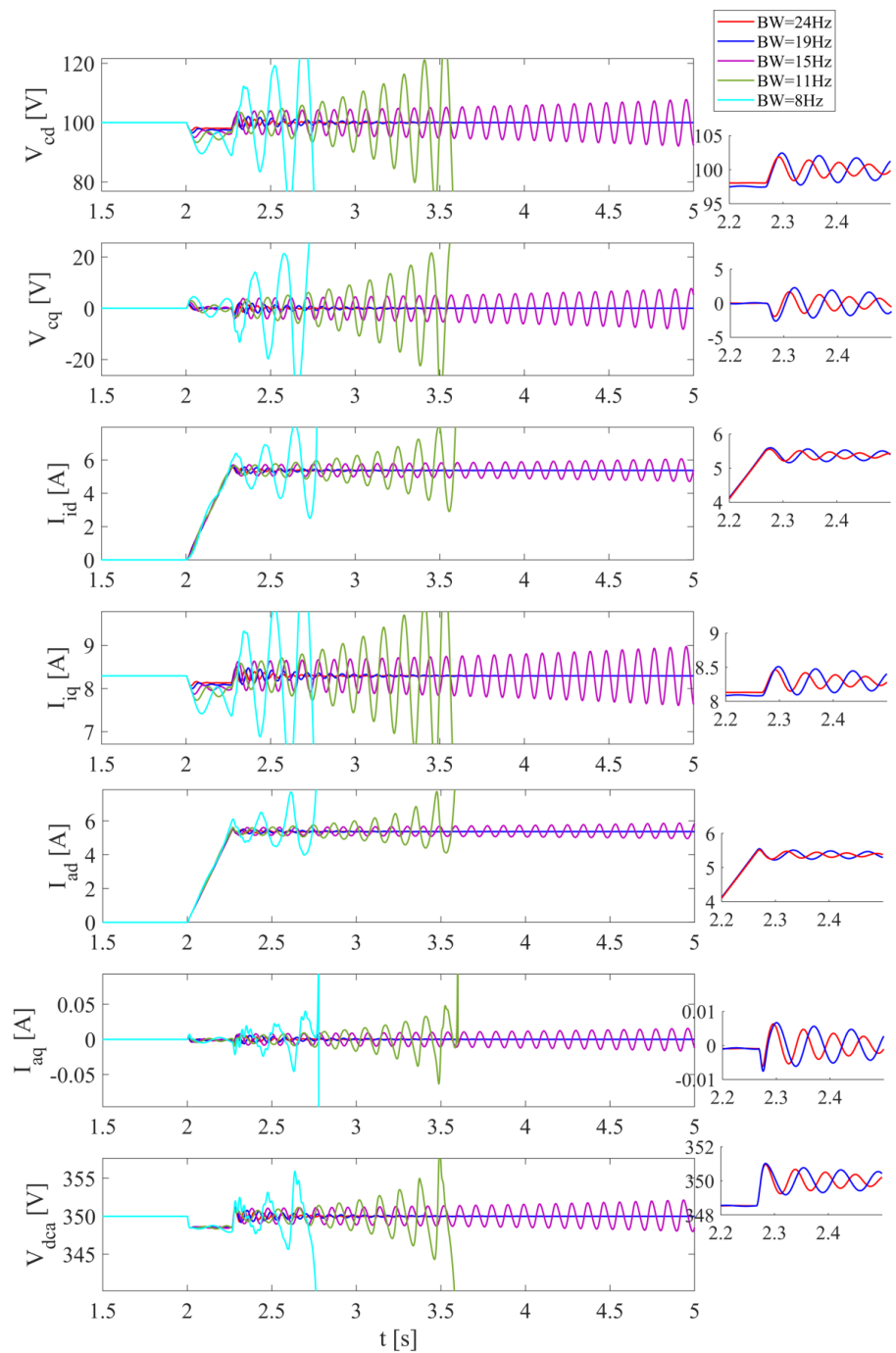
Figure 5.19: Waveforms of system response when the VSI adopts PI controllers of different voltage bandwidths

5.7 AFE dynamic performance and stability

5.7.1 Bandwidth calculation of AFE

In the PI control of VSI and AFE, the coupling effect between d- and q-axis for example $\omega L I_{iq}$, $\omega L I_{id}$, $\omega L_a I_{aq}^p$, and $\omega L_a I_{ad}^p$, which were shown in the Fig.3.2, could be compensated by control design. However, those cross-links are usually not perfectly decoupled due to control delay and sampling errors. In addition, the coupling introduced by capacitors, i.e. $\omega C V_{cd}$ and $\omega C V_{cq}$ shown in Fig.3.2 could not compensated by adding an extra quantity in PI control. As a result, the f_i and f_v which is based on the perfect decoupling could be different from the actual current and voltage bandwidth. Therefore, in the following, the way to calculate actual bandwidth of AFE will be presented when it adopts a PI controller.

Generally, the current and voltage bandwidth could be determined by the transfer function from their references to the output. They are the frequencies where the magnitude attenuated by 3dB. Therefore, it is key to establish transfer functions of the current and voltage loop from reference to output.

The state space model representation of AFE (3.61) adopting a PI controller is copied to here.

$$\begin{cases} \dot{x}_{afe}^{cl} = A_{afe}^{cl} x_{afe}^{cl} + G_{afe}^{cl} r_{afe} \\ y_{afe} = C_{afe}^{cl} x_{afe}^{cl} \end{cases} \tag{5.10}$$

This model is derived by applying the Jacobian Linearisation method [118, 121] on the closed loop differential equations of AFE f .

$$A_{afe}^{cl} = J_x(f) = \begin{bmatrix} \frac{\partial f}{\partial x_1} & \dots & \frac{\partial f}{\partial x_n} \end{bmatrix} = \begin{bmatrix} \frac{\partial f_1}{\partial x_1} & \dots & \frac{\partial f_1}{\partial x_n} \\ \dots & \dots & \dots \\ \frac{\partial f_m}{\partial x_1} & \dots & \frac{\partial f_m}{\partial x_n} \end{bmatrix} \tag{5.11}$$

$$G_{afe}^{cl} = J_r(f) = \begin{bmatrix} \frac{\partial f}{\partial r_1} & \dots & \frac{\partial f}{\partial r_n} \end{bmatrix} = \begin{bmatrix} \frac{\partial f_1}{\partial r_1} & \dots & \frac{\partial f_1}{\partial r_n} \\ \dots & \dots & \dots \\ \frac{\partial f_m}{\partial r_1} & \dots & \frac{\partial f_m}{\partial r_n} \end{bmatrix} \tag{5.12}$$

Eq.(5.11) models all the dynamics of the closed loop AFE. It is developed for the impedance calculation of AFE. Therefore the input of the impedance model r_{afe} is the AC bus voltage $\begin{bmatrix} V_{cd} & V_{cq} \end{bmatrix}^T$ and the output y_{afe} is its input current $\begin{bmatrix} I_{ad} & I_{aq} \end{bmatrix}^T$. And the admittance of AFE is defined as the transfer function from r_{afe} to output y_{afe}. Just as shown in the (3.65),

$$Y = C_{afe}^{cl}(sI - A_{afe}^{cl})^{-1} G_{afe}^{cl} \tag{5.13}$$

However when calculating the bandwidth of AFE, the transfer function is from

$$r = \begin{bmatrix} I_{aq,ref} & V_{dca,ref} \end{bmatrix}^T \tag{5.14}$$

to output $y = \begin{bmatrix} I_{aq} & V_{dca} \end{bmatrix}^T$. Therefore, when calculating the input matrix G_{afe} by (5.12), the r should be $r = \begin{bmatrix} I_{aq,ref} & V_{dca,ref} \end{bmatrix}^T$. The new G_{afe} could be easily obtained as

$$
G_{afe} = \begin{bmatrix} 0 & 0 \\ 0 & 0 \\ 0 & 0 \\ k_{iv} & 0 \\ k_{pi}k_{iv} & 0 \\ 0 & k_{ii} \\ 0 & 0 \\ 0 & 0 \end{bmatrix}
\tag{5.15}
$$

And the output matrix is defined as

$$
C_{afe} = \begin{bmatrix} 0 & 1 & 0 & 0 & 0 & 0 & 0 & 0 \\ 0 & 0 & 1 & 0 & 0 & 0 & 0 & 0 \end{bmatrix}
\tag{5.16}
$$

In this way, the output of the model becomes

$$
y = C_{afe}x_{afe} = \begin{bmatrix} 0 & 1 & 0 & 0 & 0 & 0 & 0 & 0 \\ 0 & 0 & 1 & 0 & 0 & 0 & 0 & 0 \end{bmatrix} \begin{bmatrix} I_{ad} \\ I_{aq} \\ V_{dca} \\ I_{ad_{ref}} \\ U_d \\ U_q \\ \theta_e \\ \omega_i \end{bmatrix} = \begin{bmatrix} I_{aq} \\ V_{dca} \end{bmatrix}
\tag{5.17}
$$

as expected.

Hence the transfer function for bandwidth calculation of AFE is

$$
T_{bw} = C_{afe}(sI - A_{afe}^{cl})^{-1}G_{afe}
\tag{5.18}
$$

The T_{bw} obtained is a 2 by 2 transfer function matrix, of which the top left term describes the current loop and right bottom one describes the voltage loop. The bandwidths of these two transfer functions are the current bandwidth and voltage bandwidth respectively. Fig.5.20 shows an example of the bode diagrams of the two transfer functions when $f_i = 800$ and $f_v = 40$.
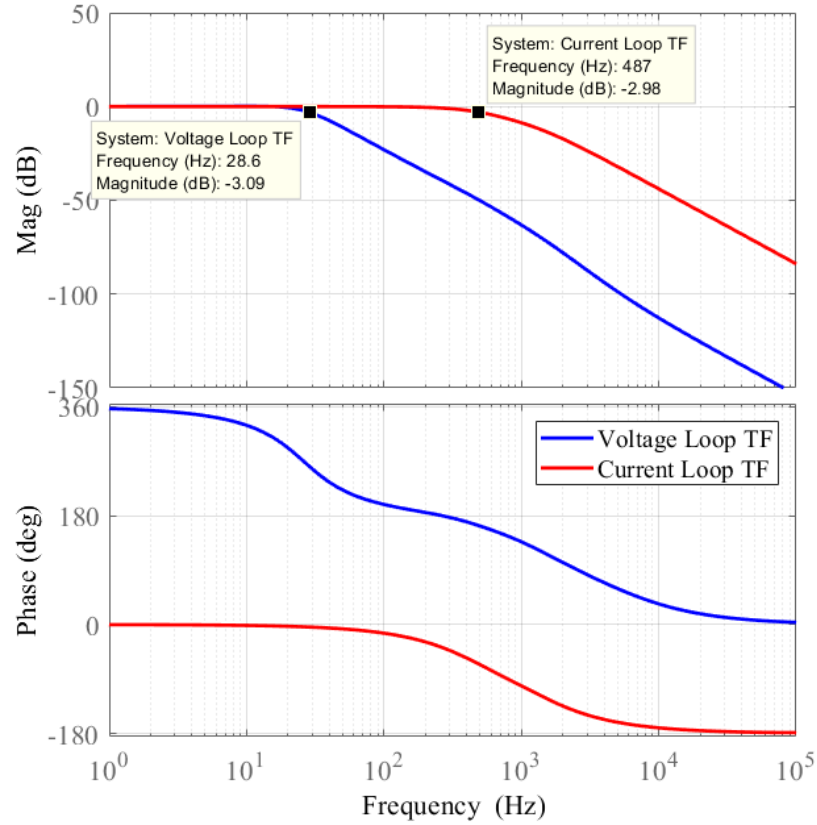
Figure 5.20: Bode diagrams of voltage and current loop transfer functions of AFE when AFE uses a PI controller

Regarding to the AFE using a H_2 controller, the calculation follows in the same way, except that the closed loop differential equations are different. The closed loop differential equations of AFE with a H_2 controller are shown as (3.69b)(3.72b)(3.73)(3.74)(3.75).

5.7.2 Bandwidth of PI AFE, impedance and system stability

For the control design of AFE, it is desirable to synthesize an as fast as possible controller. When the grid, or the VSI in this research, is stiff enough, it is true that the system response will be faster if the AFE has a bigger bandwidth. However, it will be demonstrated in this section that the benefit of increasing bandwidth of AFE's PI controller is limiting. When the AFE's bandwidth is higher than a certain value (about 600Hz for the current loop and 100Hz for the voltage loop in this research), the system response speed will not increase any more. However for the AFE adopting an optimal H_2 controller, it is easy to achieve a much faster speed.

In the Fig.5.21, the AFE uses PI controllers of different bandwidths. And time domain response of the VSI-AFE system in simulation in presence of a load ramp is shown. The f_i and f_v used for PI controllers tuning are set as different values to synthesize controllers of different bandwidths. The bandwidths resulted from those values are shown in Table.5.2. As can be seen in the Fig.5.21, the system is stable when $f_i = 400$ and $f_v = 10$. However, due to relatively low voltage bandwidth, there is a drastic drop in DC-link voltage V_{dca} during the transient. When the f_i and f_v are increased further to $f_i = 600$ and $f_v = 20$, the system is unstable.
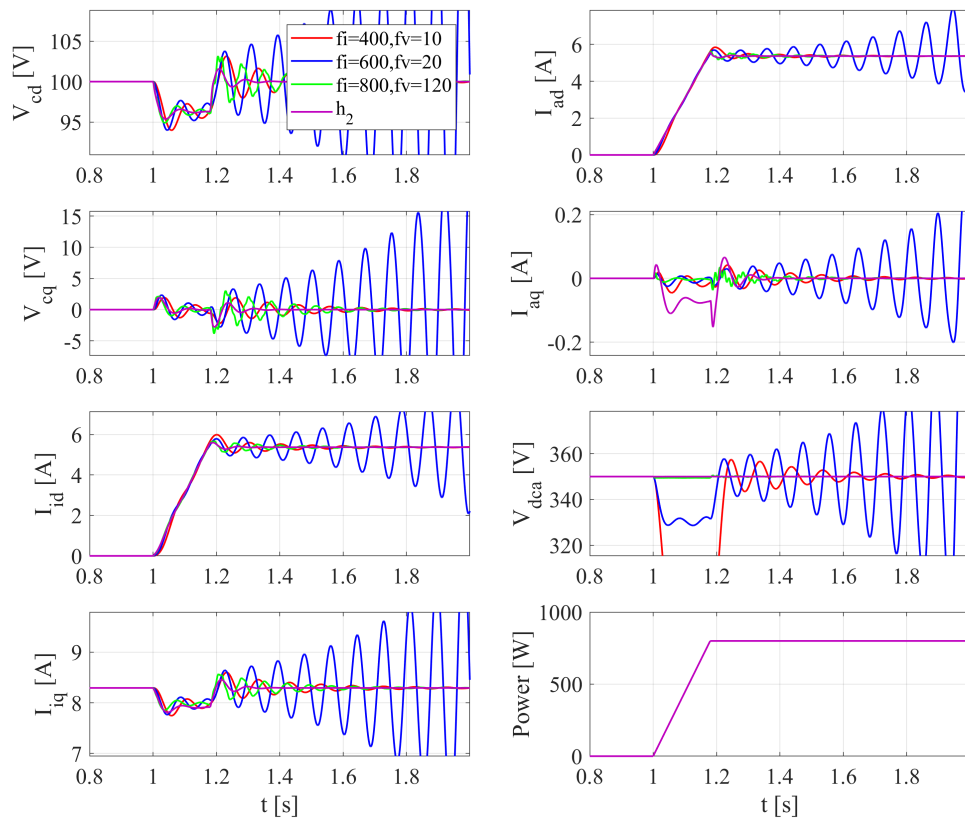
Figure 5.21: Time domain simulation waveforms when AFE uses low bandwidth PI controllers and an optimal H_2 controller

	Current Bandwidth (Hz)	Voltage Bandwidth (Hz)
f_i=400,f_v=10	221	7
f_i=600,f_v=20	357	14
f_i=800,f_v=120	497	85
f_i=1000,f_v=150	628	107
f_i=2000,f_v=300	1280	215
f_i=3000,f_v=450	1926	329
H_2	13.5	679

Table 5.2: Bandwidth of AFE with different f_i and f_v

This can be confirmed by the bode diagram of the d-d axis impedance of the VSI and AFE, as shown in Fig.5.22. In the figure, the impedance magnitude of both the VSI and AFE are plotted, together with their phase difference, from which the 180° crossover frequency of phase difference can be inspected. Because the magnitude of d-d axis impedance of AFE has a small down warping at frequency around 90Hz when $f_i = 600$ and $f_v = 20$, the impedance of AFE is smaller than that of VSI at that frequency, where exactly the 180° intersection in phase plot happens. Therefore, system instability occurred. In the Fig.5.23, the characteristic loci of the impedance ratio are plotted. As can be seen, one of the characteristic loci when $f_i = 600$ and $f_v = 20$ encircles the critical point $(-1, 0i)$ and signifies instability.
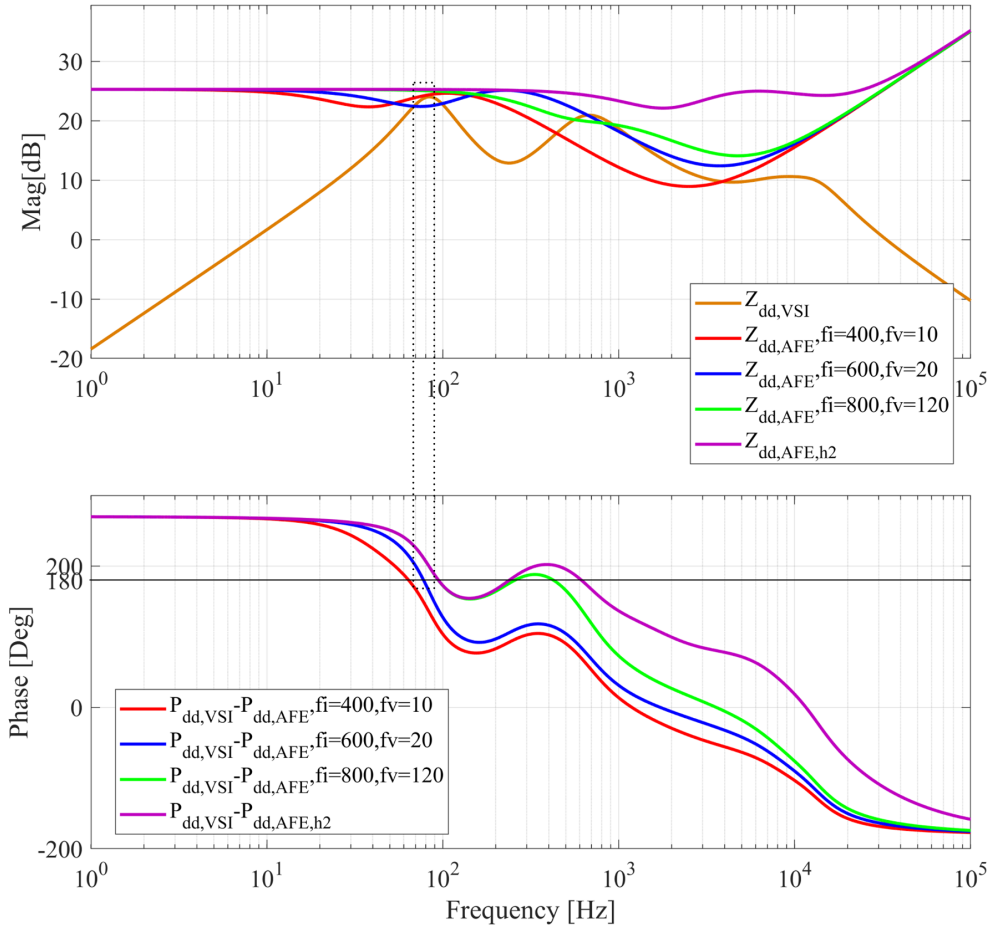
Figure 5.22: Bode diagram of impedance when AFE uses low bandwidth PI controllers and an optimal H_2 controller
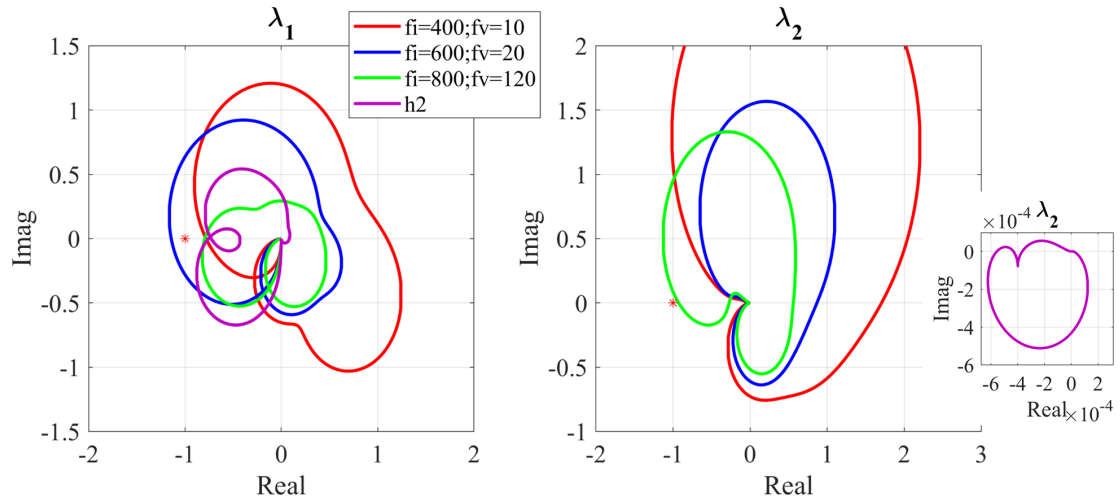
Figure 5.23: Characteristic loci of impedance ratio when AFE uses low bandwidth PI controllers and an optimal H_2 controller

Meanwhile, the case when AFE adopts an optimal H_2 controller is shown as well. As can be seen from the waveforms comparison, the H_2 controller is superior to the PI controllers as having fastest response and lowest overshoot during the transient. And the bode diagram of impedance ratio indicates that AFE's d-d axis impedance magnitude is always larger than that of VSI, which evinces a reliable stability.

When the bandwidth of AFE's PI controller is increased further, the impedance of AFE becomes bigger and the system is stable again, as shown in the case when $f_i = 800$ and $f_v = 120$ in the Fig.5.21.

If the f_i and f_v are increased even bigger, there will not be visible improvement in dynamic performance of the VSI-AFE system. In the Fig.5.24, three cases with even higher bandwidth PI controllers are shown. As can be seen, their time domain response are almost the same except slight improvement in I_{aq} and V_{dca} in terms of faster dynamics. Although the impedance magnitude is bigger, as shown in the Fig.5.25, the gain margin of these three cases are the same, as shown by the characteristic loci in the Fig.5.26.
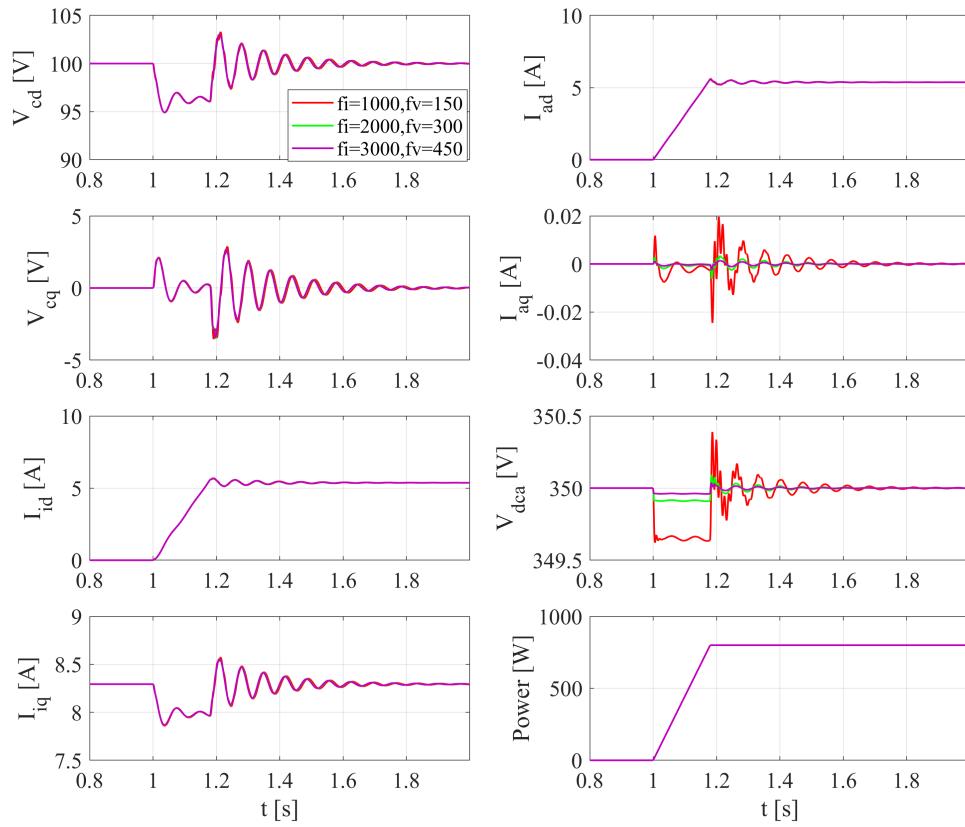
Figure 5.24: Time domain simulation waveforms when AFE uses high bandwidth PI controllers
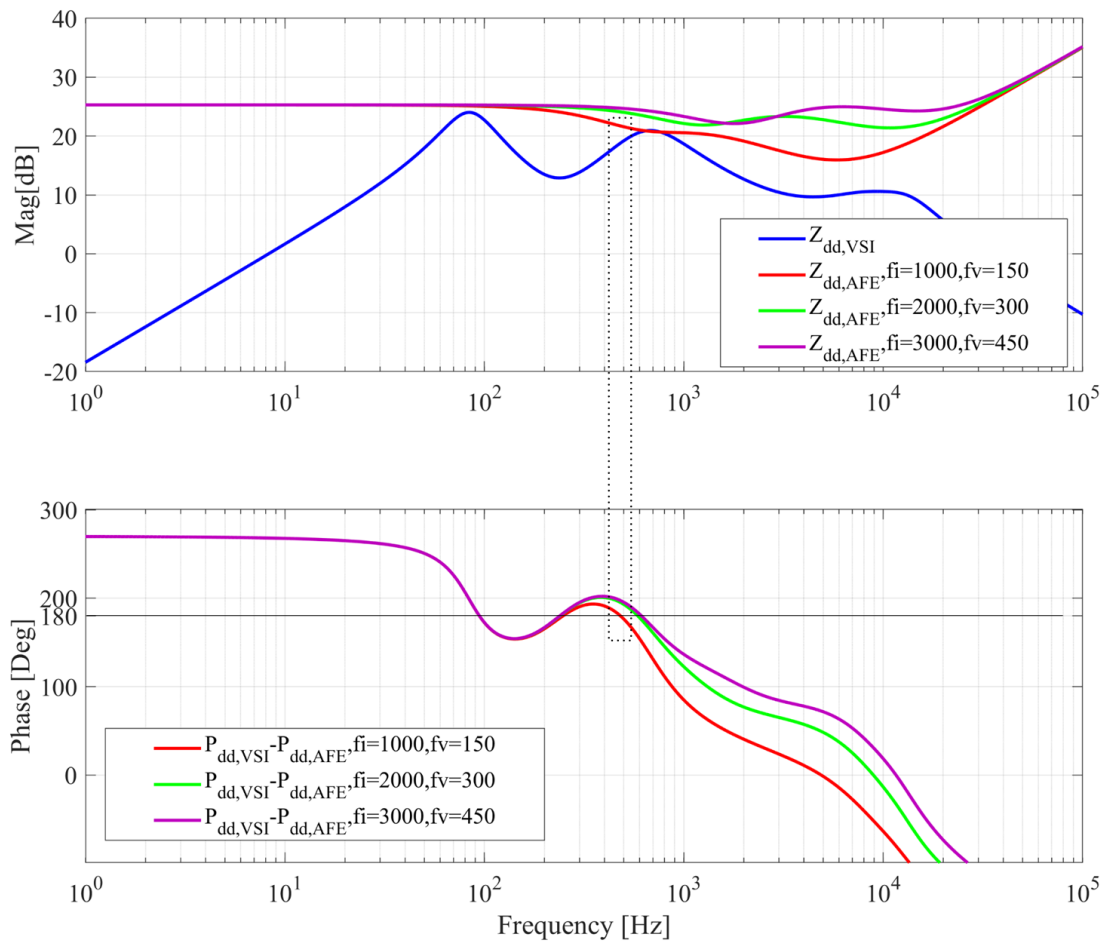
Figure 5.25: Bode diagram of impedance when AFE uses high bandwidth PI controllers
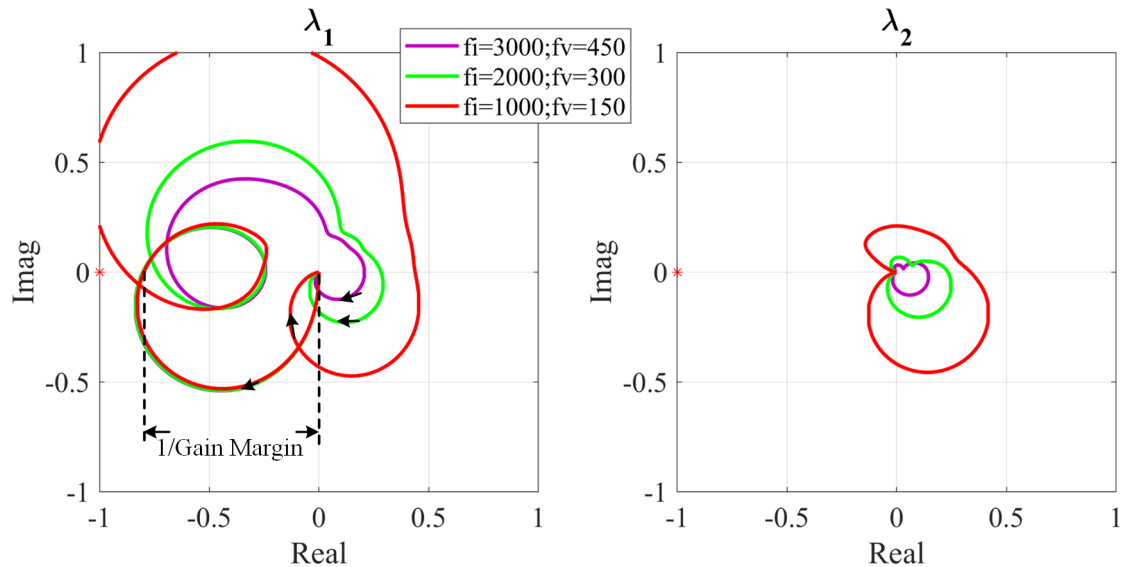
Figure 5.26: Characteristic loci of impedance ratio when AFE uses high bandwidth PI controllers

To sum up, when comparing the PI control method and the proposed optimal H_2 control design method, by applying them to the design of AFE and inspecting their dynamic performance, the author always elaborately tunes the PI controllers to their best performance by increasing their bandwidths, until no further improvement can be achieved in terms of response speed and overshoot. This is important for ensuring the fairness in comparing the two different control design method.

5.8 Conclusion

In this chapter, robustness of the proposed control design method against parameters drift was examined. At first, relationship between VSI LC filter capacitor C and VSI impedance was investigated. It was aimed to create a challenge for the control design of AFE by changing the C and shaping the VSI impedance. And then an optimal H_2 controller was compared with a PI controller in presence of difference C. The comparison confirmed advantage of the optimal control design method. Similar tests were also conducted to examine the impact of AFE DC-link capacitor C_a and power of CPL attached with AFE on the performance of optimal control design method. In addition, applicability of the optimal control design method in multi-converter network was investigated. At last, the relationship between bandwidths of PI controllers and optimal controllers and system stability was discussed. All the tests proved superiority of the optimal control design method over traditional PI method.

Chapter 6

Identification experiment design

As shown in the Sec.4.3.2, if grid model (emulated by a VSI in this research) is known and can be used in the control design of a local converter (i.e. the AFE in this research), overall dynamic performance of the interconnected grid-converter system can be significantly improved by the proposed optimal H_2 control design method. However, in practice, all the required information such as grid topologies and parameters are usually not available in commercial power converter-based grids that the to be designed converter will be integrated into. It prevents engineers from building nominal models of the grids. This enables identification techniques to be employed to identify a model of the unknown grid. And the identified model is intended to be utilized to establish a model of the whole system to be then used during controller synthesis.

In this chapter, the procedure to implement such identification experiments in this application is discussed in detail.

The mathematical technique of incorporating the identified closed loop model of grid into system global model is presented. And switching model simulation results of the VSI-AFE system when AFE adopts an optimal H_2 controller synthesized by such a global model is provided.

At the beginning, some preliminary knowledge about system identification theory and the prediction error method (PEM) is presented.

6.1 System identification and the prediction error method

In practice, system complexity, limited prior knowledge of the system, and incomplete of observed data prevent an exact mathematical description of the system. Consequently, system identification is considered as approximate modelling for a specific application on the basis of observed data collected in an identification experiment and prior system knowledge.

The idea of system identification is to estimate a best approximation of the input-output characteristic of the system, under a certain criterion. In general terms, an identification experiment is performed by exciting the system (using some sort of input signal such as a step, a sinusoid or a random sequence signal), observing its input and output over a time interval and fitting a parametric model of the process to the recorded input and output sequences. The first step is to select an appropriate candidate form of the model according to prior knowledge and intended utility of the model. Since the identified model will be integrated into a global state space model of the whole system, form of the to be identified model is fixed as state space models in this research. The only uncertainty is order of the to be identified state space model. As a second step some statistically based method is used to estimate the unknown parameters of the model (the coefficients in the state matrix, input and output matrix in this research). In practice, the estimations of parameters are often done iteratively. This means that a tentative order is chosen and the corresponding parameters are estimated. The model obtained is then tested to see whether it is an appropriate representation of the system. If this is not the case, some more complex model structures must be considered, its parameters estimated, the new model validated, etc.

In summary, the construction of a model from data involves three basic entities:

(1) A data set.

(2) A set of candidate models: a model structure.

(3) A rule by which candidate models can be assessed using the data, like the Least Square selection rule [136].

Flow chart of the procedure is given in Fig.6.1.

Consider a system in such a form,

$$A(z^{-1})y(k) = B(z^{-1})u(k) + \varepsilon(k) \tag{6.1}$$

where

$$A(z^{-1}) = 1 + a_1 z^{-1} + ... + a_{n_a} z^{-n_a} \tag{6.2}$$

$$B(z^{-1}) = 1 + b_1 z^{-1} + ... + a_{n_b} z^{-n_b} \tag{6.3}$$

In (6.1), the term $\varepsilon(k)$ denotes the equation error. (6.1) can be equivalently expressed as

$$y(k) = \varphi^T(k)\theta + \varepsilon(k) \tag{6.4}$$

where

$$\varphi^T(k) = (-y(k-1), ..., -y(k-n_a), u(k-1), ..., u(k-n_b)) \tag{6.5}$$

$$\theta = (a_1, ..., a_{n_a}, b_1, ..., b_{n_b})^T \tag{6.6}$$
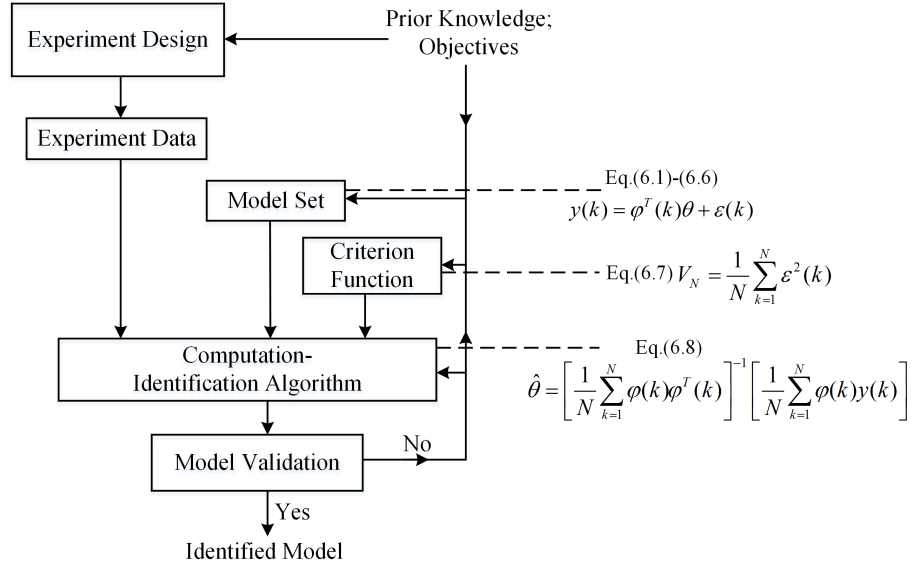
Figure 6.1: System identification loop

Consequently, it could be derived that the parameter vector which minimizes the sum of squared equation errors,

$$V_N = \frac{1}{N} \sum_{k=1}^{N} \varepsilon^2(k) \tag{6.7}$$

is given by [137]

$$\hat{\theta} = \left[\frac{1}{N} \sum_{k=1}^{N} \varphi(k)\varphi^T(k) \right]^{-1} \left[\frac{1}{N} \sum_{k=1}^{N} \varphi(k)y(k) \right] \tag{6.8}$$

This identification method is known as the least square (LS) method. The name 'equation error method' also appears in the literature. The reason is, of course, that $\varepsilon(k)$, whose sample variance is minimized, appears as an equation error in the model (6.1). (6.8) gives out an analytical solution for the estimation. However, the method has a crucial drawback. As in most cases, its result is not a consistent estimation. It means the estimation will not converge to the true value of parameters as N tends to infinity while consistency is a prerequisite in most cases of identifications.

To overcome the defect of LS method, the PEM is introduced [138]. A model obtained by identification can be used in many ways, depending on the purpose of modelling. In many applications the model is used for prediction. Note that this is often inherent when the model is to be used as a basis for control system synthesis. Most systems are stochastic, which means that the output at time $t = k$ cannot be determined exactly from data available at time $t = k - 1$. It is thus valuable to know at time $t = k - 1$ what the output of the process is likely to be at time $t = k$ in order to take an appropriate control action, i.e. to determine the input $u(k - 1)$.

It therefore makes sense to determine the model parameter vector θ so that the prediction error
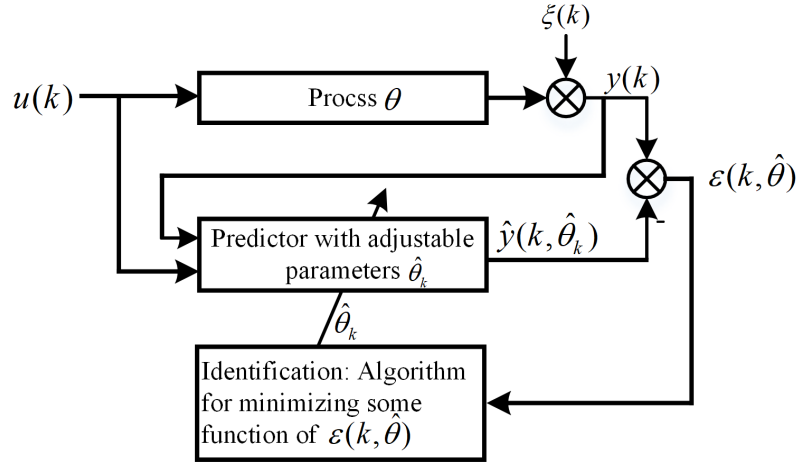
Figure 6.2: Block diagram of the prediction error method

$$\varepsilon(k, \theta) = y(k) - \hat{y}(k|k-1; \theta) \tag{6.9}$$

is small. $\hat{y}(k|k-1; \theta)$ denotes a prediction of $y(k)$ given the data up to and including time $t = k-1$, i.e. $y(k-1), u(k-1), y(k-2), u(k-2), ...$ and based on the model parameter vector θ. A block diagram illustrating the idea of PEM is shown in Fig.6.2.

To formalize this idea, consider a general model structure,

$$y(k) = G(z^{-1}; \theta)u(k) + H(z^{-1}; \theta)e(k) \tag{6.10}$$

$$Ee(t)e^{T}(s) = \Lambda(\theta)\delta_{t,s} \tag{6.11}$$

Assume that $G(0; \theta)=0$, i.e. that the model has at least one pure delay from input to output. As a general linear predictor, consider

$$\hat{y}(k|k-1; \theta) = L_1(z^{-1}; \theta)y(k) + L_2(z^{-1}; \theta)u(k) \tag{6.12}$$

which is a function of past data and the predictor filters $L_1(z^{-1}; \theta)$ and $L_2(z^{-1}; \theta)$ are constrained by

$$L_1(0; \theta) = 0; L_2(0; \theta) = 0 \tag{6.13}$$

The predictor (6.12) can be constructed in various ways for any give model (6.10). Once the model and the predictor are given, the prediction errors are computed as in (6.9). The parameter estimate $\hat{\theta}$ is then chosen to make the prediction errors $\varepsilon(1, \theta)$,.., $\varepsilon(N, \theta)$ small.

To define a prediction error method the user has to make the following choices:

(1) Choice of model structure. This concerns the parametrization of $G(z^{-1}; \theta)$, $H(z^{-1}; \theta)$ and $\Lambda(\theta)$ in (6.10) as functions of θ.

(2) Choice of predictor. The concerns the filters $L_1(z^{-1}; \theta)$ and $L_2(z^{-1}; \theta)$ once the model is specified.

(3) Choice of criterion. This concerns a scalar-valued function of all the prediction errors $\varepsilon(1, \theta)$,.., $\varepsilon(N, \theta)$, which will assess the performance of the predictor used; this criterion is to be minimized with respect to θ to choose the 'best' predictor in the class considered.

The predictor filters $L_1(z^{-1}; \theta)$ and $L_2(z^{-1}; \theta)$ can be in principle be chosen in many ways. The most common way it to let (6.12) be the optimal mean square predictor [137]. This means that the filters are chosen so that under the given model assumptions the prediction errors have as small a variance as possible. Hereafter, the derivation of such $L_1(z^{-1}; \theta)$ and $L_2(z^{-1}; \theta)$ will be presented. Consider the model shown in (6.10). Assume that $G(0; \theta) = 0$, $H(0; \theta) = I$ and that $H^{-1}(z^{-1}; \theta)$ and $H^{-1}(z^{-1}; \theta)G(z^{-1}; \theta)$ are asymptotically stable. Assume also that $u(k)$ and $e(s)$ are uncorrelated for $k < s$. This condition holds if either the system operates in open loop with disturbances uncorrelated with the input, or the input is determined by causal feedback.

The optimal predictor is easily found from the following calculations:

$$
\begin{aligned}
y(k) &= G(z^{-1}; \theta)u(k) + \big\{H(z^{-1}; \theta) - I\big\}e(k) + e(k) \\
&= \big[G(z^{-1}; \theta)u(k) + \big\{H(z^{-1}; \theta) - I\big\}H^{-1}(z^{-1}; \theta)\big\{y(k) - G(z^{-1}; \theta)u(k)\big\}\big] + e(k) \\
&= \big[H^{-1}(z^{-1}; \theta)G(z^{-1}; \theta)u(k) + \big\{I - H^{-1}(z^{-1}; \theta)\big\}y(k)\big] + e(k) \\
&\triangleq z(k) + e(k)
\end{aligned}
\tag{6.14}
$$

Note that $z(k)$ and $e(k)$ are uncorrelated. Let $y^*(k)$ be an arbitrary predictor of $y(k)$ based on data up to time $k - 1$. Then the following inequality holds for prediction error covariance matrix:

$$
\begin{aligned}
&E\big[y(k) - y^*(k)\big]\big[y(k) - y^*(k)\big]^T \\
&= E\big[z(k) + e(k) - y^*(k)\big]\big[z(k) + e(k) - y^*(k)\big]^T \\
&= E\big[z(k) - y^*(k)\big]\big[z(k) - y^*(k)\big]^T + \Lambda(\theta) \geqslant \Lambda(\theta)
\end{aligned}
\tag{6.15}
$$

Hence $z(k)$ is the optimal mean square predictor, and $e(k)$ the prediction error. This can be written as

$$
\begin{cases}
\hat{y}(k|k-1; \theta) = \big[H^{-1}(z^{-1}; \theta)G(z^{-1}; \theta)u(k) + \big\{I - H^{-1}(z^{-1}; \theta)\big\}y(k)\big] \\
\varepsilon(k, \theta) = e(k) = H^{-1}(z^{-1}; \theta)\big[y(k) - G(z^{-1}; \theta)u(k)\big]
\end{cases}
\tag{6.16}
$$

Note that the assumption $G(0; \theta) = 0$ means that the predictor $\hat{y}(k|k-1; \theta)$ depends only on previous inputs (i.e. $u(k-1), u(k-2), ...$) and not on $u(k)$. Similarly, since $H(0; \theta) = I$ and hence $H^{-1}(0; \theta) = I$, the predictor does not depend on $y(k)$ but only on former output values $y(k-1), y(k-2), ...$

Once the model and the predictor are given, the prediction errors are computed as (6.9). The parameter estimate $\hat{\theta}$ is then chosen to make the prediction errors $\varepsilon(1,\theta),...,\varepsilon(N,\theta)$ small.

In order to assess the performance of the predictor used, a scaler-valued function of all the prediction errors is defined and denoted as criterion function. The criterion which maps the sequence of prediction errors into a scalar can be chosen in many ways. Here the following class of criteria is adopted. Define the sample covariance matrix

$$R_N(\theta) = \frac{1}{N}\sum_{k=1}^{N}\varepsilon(k,\theta)\varepsilon^T(k,\theta) \tag{6.17}$$

where N denotes the number of data points. If the system has one output only then $\varepsilon(k,\theta)$ is a scalar and so is $R_N(\theta)$. In such a case $R_N(\theta)$ can be taken as a criterion to be minimized. In the multi-variable case, $R_N(\theta)$ is a positive definite matrix. Then the criterion

$$V_N(\theta) = h(R_N(\theta)) \tag{6.18}$$

is chosen, where $h(Q)$is a scalar-valued function defined on the set of positive definite matrices Q, which must satisfy certain conditions. $V_N(\theta)$ is frequently called a loss function. The requirement on the function $h(Q)$ is that it must be monotonically increasing.

In the special case where $\varepsilon(k,\theta)$ depends linearly on the θ, the minimization of $V_N(\theta)$ can be done analytically. In most cases the minimum of $V_N(\theta)$ cannot be found analytically. For such cases the minimization must be performed using a numerical search routine. A commonly used method is the Newton-Raphson algorithm.

$$\hat{\theta}(k+1) = \hat{\theta}(k) - \alpha(k)\big[V_N''(\hat{\theta}(k))\big]^{-1}V_N'(\hat{\theta}(k))^T \tag{6.19}$$

$\alpha(k)$ is the step size, typically taken as a positive decreasing function of k. The search goes iteratively until the increment of $V_N(\theta)$ in one step is smaller than a certain threshold and the $\hat{\theta}(k) =$ is thought to be a good estimation. Through model structure transformation, the above procedure could be used for state space model identification.

In this research, the numerical optimization of $V_N(\theta)$ and search of optimal estimation $\hat{\theta}$ is delivered by the Matlab 'System Identification Toolbox', which offers a convenient and reliable tool to implement the model identification.

6.2   Experiment design

To investigate effectiveness of the proposed optimal control design method, an experimental setup has been built, as shown in Fig.6.3. It is built in accordance with the schematics shown in Fig.3.1.

Passive components values and nominal reference values of major state variables are shown in Table. 4.1.
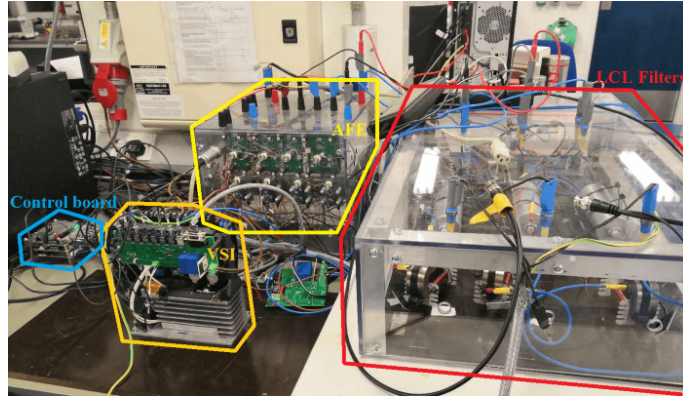
Figure 6.3: Experimental rig of the VSI-AFE system

In literatures [44–52], certain extra equipment besides the to be identified system is needed to generate excitations. However in this research, no extra cost on such specially designed hardware is needed for the identification of the VSI. The AFE itself will be utilized to generate the excitations when identifying the VSI at the PCC.

Although it is the VSI being identified in this research to obtain a model to represent the grid dynamic behaviour for the optimal H_2 control of AFE, the rig can also used for the identification of AFE. The identified model of AFE can be utilized to examine whether it is designed as expected and check the actual health condition of the VSI-AFE system based on impedance-based stability criterion. For example, when identifying the AFE, the VSI will not only supply power for the normal operation of AFE, but also act as an perturbation source. The voltage references of VSI then, denoted as $V_{cd_{ref}}^i$ and $V_{cq_{ref}}^i$, will be a combination of their nominal value and the random perturbation signals, as shown in the Fig.6.4. Here the PRBS is used due to its superiority in amplitude minimization, spectral optimization of the injected signal and ease of producing in digital control processor. The signal shifts between two levels and its first- and second-order characteristics (mean value and covariance function) are quite similar to those of a white noise process.

In theory, spectrum of the perturbations should be evenly distributed in the frequency range of interest and energy of the excitation needs to be rich enough throughout the whole frequency band. Based on prior knowledge of the converters, the frequency range of interest in identification is chosen as 0-3k Hz and generation frequency of the PRBS as 5kHz. As the perturbations may be filtered by the converter itself a filter is adopted here to enhance perturbations in high frequency range when identifying the VSI, just as shown in the Fig.6.5. Frequency spectrum of the perturbations
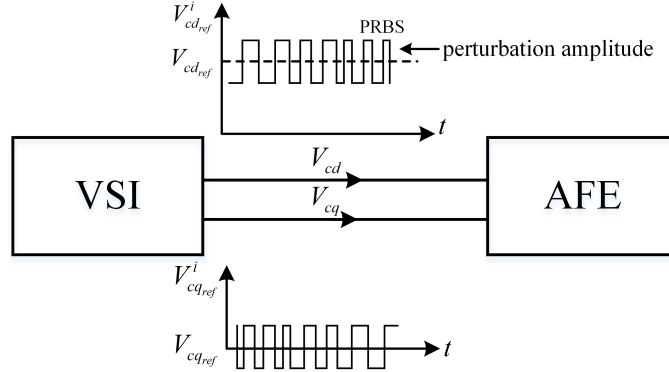
Figure 6.4: VSI's voltage reference $V^i_{cd_{ref}}$, $V^i_{cq_{ref}}$ in the model identification experiment of AFE

collected at the measurement point is a useful guidance to decide the passband when designing such filters. Alternatively, in [79], the perturbations are also injected directly into the duty cycle besides the input of current control loop, to circumvent the filtering impact of current and voltage control action within their bandwidths.
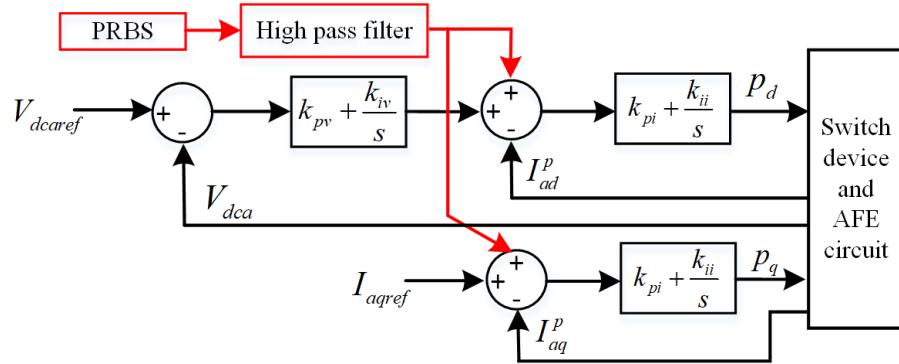
Figure 6.5: Scheme of PI AFE

It is also notable that amplitude of the perturbations should also be deliberately designed, aiming to generate harmonics of adequate energy and outstanding in the original noise, while keeping system states staying in the region where the linearised model used for control design is still valid. Therefore the amplitude needs to be kept as low as possible to guarantee normal system operate in the vicinity of its equilibrium point. In this study, 2V/2A peak-to-peak PRBS signals are determined as a result of trial and error. It is also important to remove mean from both the input and output data collected in the identification experiment to remove stationary component. The data is then passed to the PEM algorithm to estimate a model.

6.3 VSI Identification

When identifying a model of VSI, the AFE will be used to inject current perturbations into VSI terminals. The AFE, in addition to performing its original power conversion function, serves as a power amplifier for the injected PRBS. Along with the current perturbations, the VSI's voltage response will be collected as input data for identification algorithm. During the identification experiment, AFE is regulated with a traditional PI controller as shown in Fig.6.5, because the current perturbation injection points, namely the input of current loop, are explicit in the PI control. As for the H_2 control, an option is to inject the perturbations directly into the modulation indexes before duty cycle generations, which is a less precise way when adjusting the perturbation amplitude.

The PRBS is added to its current references and a high pass filter is probably also needed to enhance the high frequency perturbations, to counter its own filtering effect. Meanwhile, the AFE works with no load in the identification experiment to reduce the risk of instability when connected to the VSI.

Experimental data collected in the identification experiment is shown in Fig.6.6. The VSI-AFE system is normally working without load before 0.5s. The current perturbations is injected from t=0.5s and the injection lasts for one second. Four sets of data including perturbation currents I_{ad}^p, I_{ad}^p and VSI's response voltages V_{cd}^p and V_{cq}^p are collected in the PLL-dq frame from t=0.5 to t=1.5s. The data sampling rate is 20 kHz. Therefore a total of $2 * 10^4$ samples of data is recorded for each variable. A low pass filter with passband of 0-4k Hz is used to filter the data to exclude the impact of high frequency harmonics.
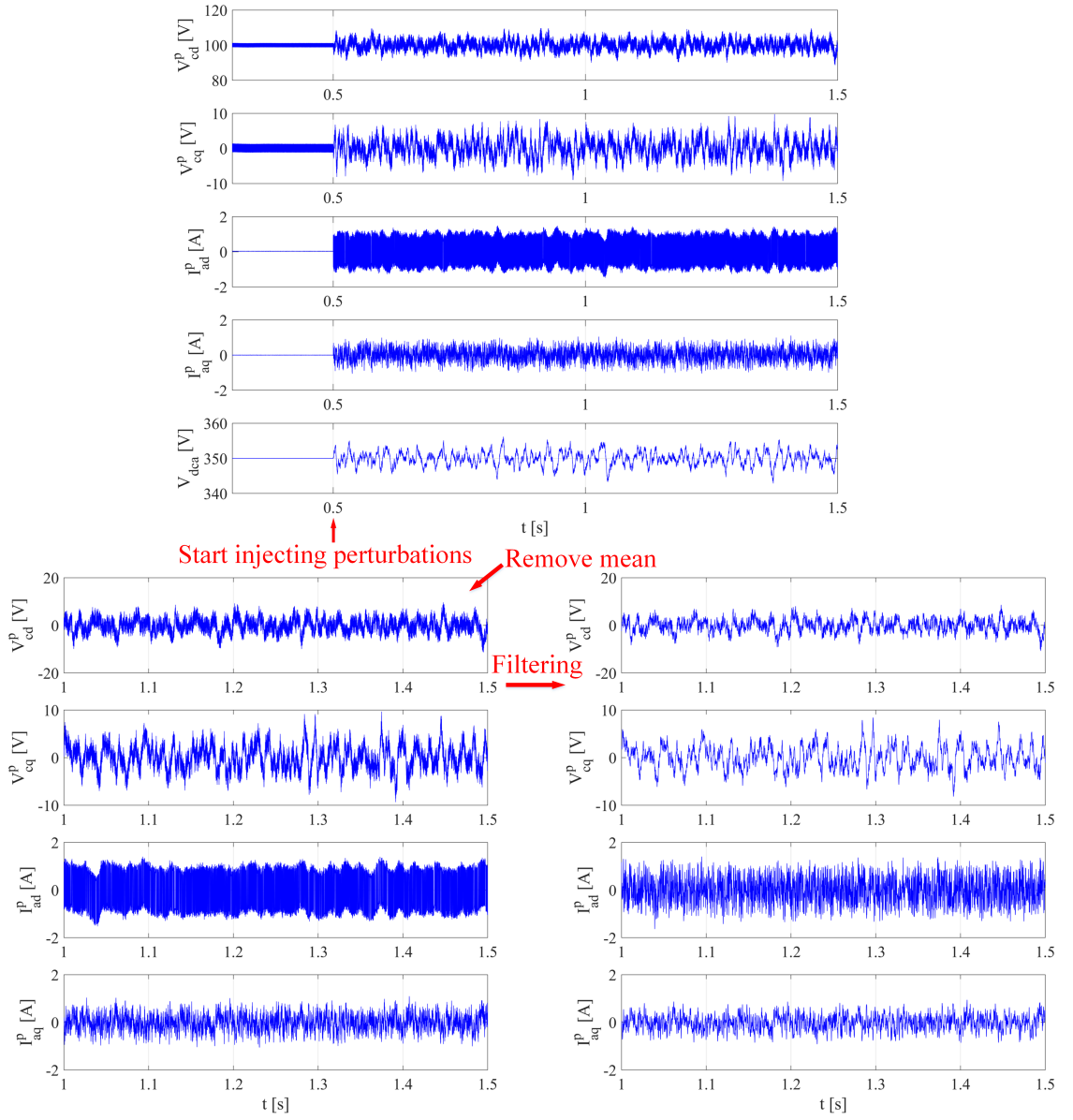
Figure 6.6: Process on the collected experimental data

By the use of PEM and Matlab Identification toolbox, a state space model can be obtained as (6.20) for the VSI.

$$\begin{cases} \dot{\tilde{x}}_{vsi} = \tilde{A}_{vsi}\tilde{x}_{vsi} + \tilde{B}_{vsi}\tilde{u}_{vsi} \\ \tilde{y}_{vsi} = \tilde{C}_{vsi}\tilde{x}_{vsi} \end{cases} \qquad (6.20)$$

where $\tilde{u}_{vsi} = [I_{ad} \quad I_{aq}]^T$ and $\tilde{y}_{vsi} = [V_{cd} \quad V_{cq}]^T$. Assume order of the identified model is m.

6.4 Optimal H_2 control design for AFE based on identified models of VSI

The optimal H_2 controllers for AFE shown above are synthesized by using the nominal closed loop models of grid/VSI. The models are developed by nominal values of VSI components and control parameters. However, such information is usually not available in practice and the existing power grids should be deemed as a black box. To address the problem, in this section, technique of using an identified model of the grid to replace its nominal model when building a system global model for control design is presented.

In the research, the grid that AFE is connected with is emulated by a VSI with PI control. A parametric model of the VSI is firstly required to be identified. Actually, existence of such a parametric model does not depend on topology, order or control scheme of the VSI.

Without loss of generality, assume the identified VSI model is shown in (6.20). Then a global model of VSI-AFE system could be built by merging the identified closed loop model of VSI (6.20) and open loop model of AFE (3.24) in a proper way. Similar to what has been done in the Sec.3.5.2, when merging the model of VSI and AFE together, the terms representing interactions i.e. I_{ad}, I_{aq} in (6.20), and V_{cd}^p, V_{cq}^p in (3.27) should be coordinated in a same reference frame.

Regarding to the VSI,

$$\dot{\tilde{x}}_{vsi} = \tilde{A}_{vsi}\tilde{x}_{vsi} + \tilde{B}_{vsi}\begin{bmatrix} i_{ad} \\ i_{aq} \end{bmatrix} = \tilde{A}_{vsi}\tilde{x}_{vsi} + \tilde{B}_{vsi}\begin{bmatrix} cos(\tilde{\theta}_e) & -sin(\tilde{\theta}_e) \\ sin(\tilde{\theta}_e) & cos(\tilde{\theta}_e) \end{bmatrix}\begin{bmatrix} i_{ad}^p \\ i_{aq}^p \end{bmatrix} \tag{6.21}$$

$$\dot{\tilde{x}}_{vsi} = \tilde{A}_{vsi}\tilde{x}_{vsi} + \tilde{B}_{vsi}\begin{bmatrix} 1 & -\tilde{\theta}_e \\ \tilde{\theta}_e & 1 \end{bmatrix}\begin{bmatrix} i_{ad}^p \\ i_{aq}^p \end{bmatrix} = \tilde{A}_{vsi}\tilde{x}_{vsi} + \tilde{B}_{vsi}\begin{bmatrix} i_{ad}^p \\ \tilde{\theta}_e I_{ad}^* + i_{aq}^p \end{bmatrix} \tag{6.22}$$

$$\dot{\tilde{x}}_{vsi} = \tilde{A}_{vsi}\tilde{x}_{vsi} + \tilde{B}_{vsi}\begin{bmatrix} i_{ad}^p \\ i_{aq}^p \end{bmatrix} + \tilde{B}_{vsi}\begin{bmatrix} 0 \\ I_{ad}^*\tilde{\theta}_e \end{bmatrix} \tag{6.23}$$

$$\dot{\tilde{x}}_{vsi} = \tilde{A}_{vsi}\tilde{x}_{vsi} + \tilde{B}_{vsi}\begin{bmatrix} i_{ad}^p \\ i_{aq}^p \end{bmatrix} + I_{ad}^*\tilde{B}_{vsi}\begin{bmatrix} 0 \\ 1 \end{bmatrix}\tilde{\theta}_e \tag{6.24}$$

According to (3.12d),

$$\dot{\tilde{x}}_{vsi} = \tilde{A}_{vsi}\tilde{x}_{vsi} + \tilde{B}_{vsi}C_{afe}x_{afe} + I_{ad}^*\tilde{B}_{vsi}\begin{bmatrix} 0 \\ 1 \end{bmatrix}\frac{v_{cq} - v_{cq}^p}{V_{cd}^*} \tag{6.25}$$

$$\dot{\tilde{x}}_{vsi} = \tilde{A}_{vsi}\tilde{x}_{vsi} + \tilde{B}_{vsi}C_{afe}x_{afe} + \frac{I_{ad}^*}{V_{cd}^*}\tilde{B}_{vsi}\begin{bmatrix} 0 \\ 1 \end{bmatrix}(v_{cq} - v_{cq}^p) \tag{6.26}$$

where

$$v_{cq} = \begin{bmatrix} 0 & 1 \end{bmatrix} \begin{bmatrix} v_{cd} \\ v_{cq} \end{bmatrix} = \begin{bmatrix} 0 & 1 \end{bmatrix} \tilde{C}_{vsi}\tilde{x}_{vsi} \tag{6.27}$$

Therefore,

$$\dot{\tilde{x}}_{vsi} = (\tilde{A}_{vsi} + \frac{I^*_{ad}}{V^*_{cd}}\tilde{B}_{vsi} \begin{bmatrix} 0 \\ 1 \end{bmatrix} \begin{bmatrix} 0 & 1 \end{bmatrix} \tilde{C}_{vsi})\tilde{x}_{vsi} + \tilde{B}_{vsi}C_{afe}x_{afe} - \frac{I^*_{ad}}{V^*_{cd}}\tilde{B}_{vsi} \begin{bmatrix} 0 \\ 1 \end{bmatrix} v^p_{cq} \tag{6.28}$$

Define $A'_{vsi} = (\tilde{A}_{vsi} + \frac{I^*_{ad}}{V^*_{cd}}\tilde{B}_{vsi} \begin{bmatrix} 0 \\ 1 \end{bmatrix} \begin{bmatrix} 0 & 1 \end{bmatrix} \tilde{C}_{vsi})$.

And the modified VSI's model is obtained as

$$\begin{cases} \dot{\tilde{x}}_{vsi} = A'_{vsi}\tilde{x}_{vsi} + \tilde{B}_{vsi}C_{afe}x_{afe} - \frac{I^*_{ad}}{V^*_{cd}}\tilde{B}_{vsi} \begin{bmatrix} 0 \\ 1 \end{bmatrix} v^p_{cq} \\ \\ \tilde{y}_{vsi} = \tilde{C}_{vsi}\tilde{x}_{vsi} \end{cases} \tag{6.29}$$

Regarding to the AFE, its open loop model in (3.24) is coped to here as

$$\dot{x}_{afe} = A_{afe}x_{afe} + B_{afe}u_{afe} + G_{afe}r_{afe} \tag{6.30}$$

where $r_{afe} = \begin{bmatrix} v^p_{cd} & v^p_{cq} \end{bmatrix}^T$.

$$\dot{x}_{afe} = A_{afe}x_{afe} + B_{afe}u_{afe} + G_{afe} \begin{bmatrix} v^p_{cd} \\ v^p_{cq} \end{bmatrix} \tag{6.31}$$

$$\dot{x}_{afe} = A_{afe}x_{afe} + B_{afe}u_{afe} + G_{afe} \begin{bmatrix} cos(\tilde{\theta}_e) & sin(\tilde{\theta}_e) \\ -sin(\tilde{\theta}_e) & cos(\tilde{\theta}_e) \end{bmatrix} \begin{bmatrix} v_{cd} \\ v_{cq} \end{bmatrix} \tag{6.32}$$

$$\dot{x}_{afe} = A_{afe}x_{afe} + B_{afe}u_{afe} + G_{afe} \begin{bmatrix} 1 & \tilde{\theta}_e \\ -\tilde{\theta}_e & 1 \end{bmatrix} \begin{bmatrix} V_{cd} \\ V_{cq} \end{bmatrix} \tag{6.33}$$

$$\dot{x}_{afe} = A_{afe}x_{afe} + B_{afe}u_{afe} + G_{afe} \begin{bmatrix} v_{cd} \\ v^p_{cq} \end{bmatrix} \tag{6.34}$$

$$\dot{x}_{afe} = A_{afe}x_{afe} + B_{afe}u_{afe} + G_{afe} \begin{bmatrix} 1 \\ 0 \end{bmatrix} v_{cd} + G_{afe} \begin{bmatrix} 0 \\ 1 \end{bmatrix} v^p_{cq} \tag{6.35}$$

And therefore the modified AFE's model is obtained as

$$\dot{x}_{afe} = A_{afe}x_{afe} + B_{afe}u_{afe} + G_{afe} \begin{bmatrix} 1 \\ 0 \end{bmatrix} \begin{bmatrix} 1 & 0 \end{bmatrix} \tilde{C}_{vsi}\tilde{x}_{vsi} + G_{afe} \begin{bmatrix} 0 \\ 1 \end{bmatrix} v^p_{cq} \tag{6.36}$$

Regarding to the PLL, its closed loop model (3.17) is coped to here as

$$
\begin{bmatrix} \dot{v}_{cq}^p \\ \dot{\omega}_i \end{bmatrix} = \begin{bmatrix} 0 & -V_{cd}^* \\ 0 & 0 \end{bmatrix} \begin{bmatrix} v_{cq}^p \\ \omega_i \end{bmatrix} + \begin{bmatrix} -V_{cd}^* & 0 \\ 0 & 1 \end{bmatrix} \begin{bmatrix} k_p^p & 0 \\ k_i^p & 0 \end{bmatrix} \begin{bmatrix} v_{cq}^p \\ \omega_i \end{bmatrix} + \begin{bmatrix} \dot{v}_{cq} \\ 0 \end{bmatrix} \tag{6.37}
$$

where

$$
\dot{v}_{cq} = \begin{bmatrix} 0 & 1 \end{bmatrix} \tilde{C}_{vsi} \dot{\tilde{x}}_{vsi} \tag{6.38}
$$

Combine (6.29)(6.36) and (6.37), the full model of the VSI-AFE system including PLL can be obtained as

$$
\begin{bmatrix} \dot{\tilde{x}}_{vsi} \\ \dot{x}_{afe} \\ \dot{v}_{cq}^p \\ \dot{\omega}_i \end{bmatrix} = \begin{bmatrix} A'_{vsi} & \tilde{B}_{vsi}C_{afe} & -\frac{I_{ad}^*}{V_{cd}^*}\tilde{B}_{vsi}\begin{bmatrix}0\\1\end{bmatrix} & 0 \\ G_{afe}\begin{bmatrix}1\\0\end{bmatrix}\begin{bmatrix}1 & 0\end{bmatrix}\tilde{C}_{vsi} & A_{afe} & G_{afe}\begin{bmatrix}0\\1\end{bmatrix} & 0 \\ \begin{bmatrix}0 & 1\end{bmatrix}\tilde{C}_{vsi}A'_{vsi} & \begin{bmatrix}0 & 1\end{bmatrix}\tilde{C}_{vsi}\tilde{B}_{vsi}C_{afe} & -\frac{I_{ad}^*}{V_{cd}^*}\begin{bmatrix}0 & 1\end{bmatrix}\tilde{C}_{vsi}\tilde{B}_{vsi}\begin{bmatrix}0\\1\end{bmatrix} & -V_{cd}^* \\ 0 & 0 & 0 & 0 \end{bmatrix} \begin{bmatrix} \tilde{x}_{vsi} \\ x_{afe} \\ v_{cq}^p \\ \omega_i \end{bmatrix}
$$

$$
+ \begin{bmatrix} 0 & 0 \\ B_{afe} & 0 \\ 0 & B^p \end{bmatrix} \begin{bmatrix} u_{afe} \\ x^p \end{bmatrix}
$$

$$
\tag{6.39}
$$

In addition, the structure of the control gains matrix is specified as shown in Fig.6.7.

$$
S = \begin{array}{c} \overbrace{\hspace{3cm}}^{m} \\ \begin{bmatrix} 0 & 0 & 0 & \dots & 0 & 0 & 0 & 0 & 0 & 0 & 0 & 0 & 0 \\ 0 & 0 & 0 & \dots & 0 & 0 & 0 & 0 & 0 & 0 & 0 & 0 & 0 \\ 0 & 0 & 0 & \dots & 0 & 0 & 1 & 1 & 1 & 1 & 1 & 0 & 0 \\ 0 & 0 & 0 & \dots & 0 & 0 & 1 & 1 & 1 & 1 & 1 & 0 & 0 \\ 0 & 0 & 0 & \dots & 0 & 0 & 0 & 0 & 0 & 0 & 0 & 1 & 0 \\ 0 & 0 & 0 & \dots & 0 & 0 & 0 & 0 & 0 & 0 & 0 & 1 & 0 \end{bmatrix} \end{array}
$$

Figure 6.7: Structure constraint imposed on the control gains matrix when synthesizing an optimal H_2 controller for AFE with the identified model of VSI

Then an optimal H_2 controller could be synthesized by the global model (6.39) and structured H_2 algorithm with a structure constraint shown in Fig.6.7. Time domain performance of the AFE's

optimal H_2 controller tuned with identified model of VSI is shown in Fig.6.8. As can be seen, the waveforms are very similar to those in the Fig.4.8. It demonstrates not only the effectiveness and advantages of the proposed control design method over standalone control design methods, in terms of faster dynamic performance and mitigating interactions, but also accuracy of the identified model of VSI.
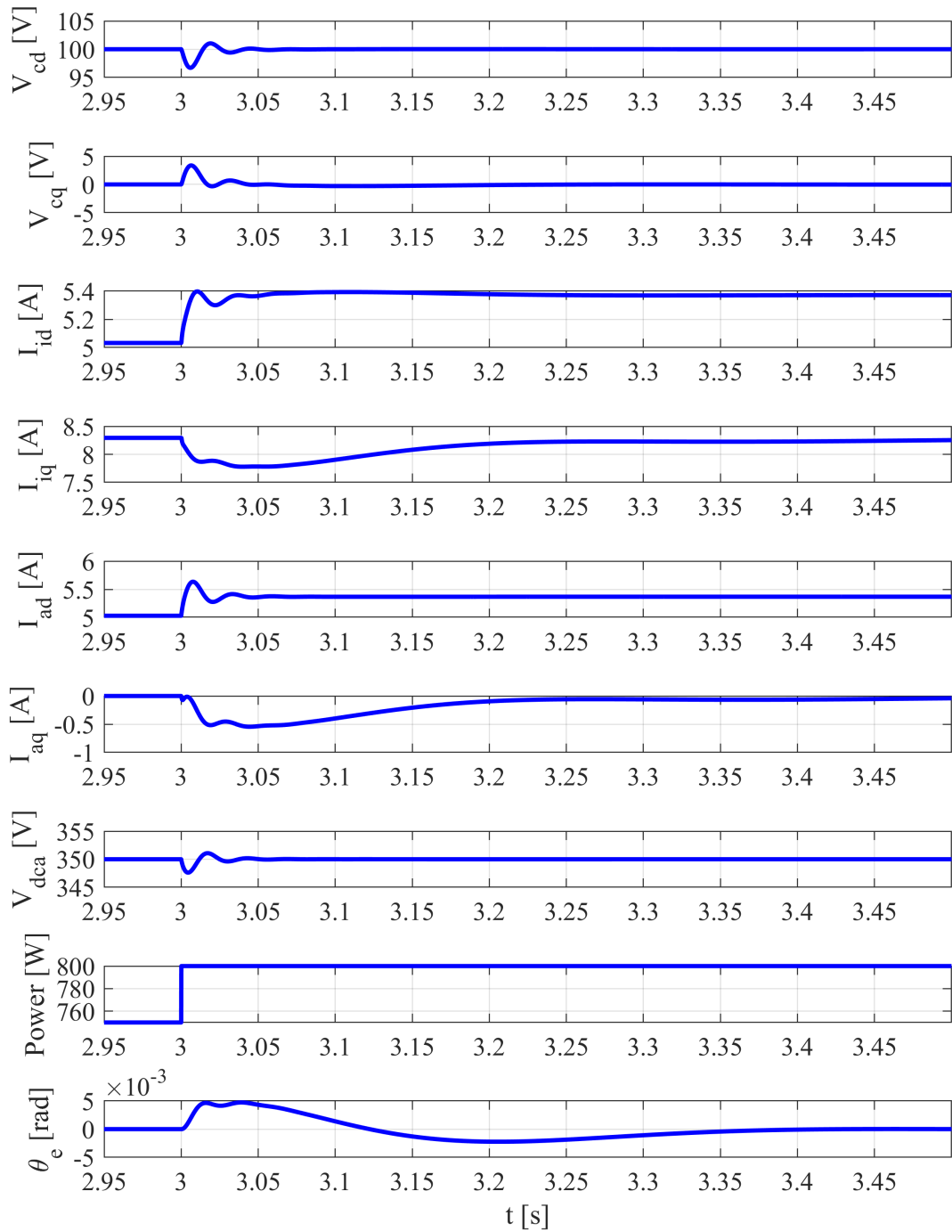
Figure 6.8: Switching model simulation results when the AFE adopts an optimal H_2 controller based on the identified model of VSI

The bode comparison between the identified model used here and the nominal model of the

VSI is shown in the Fig.6.9.
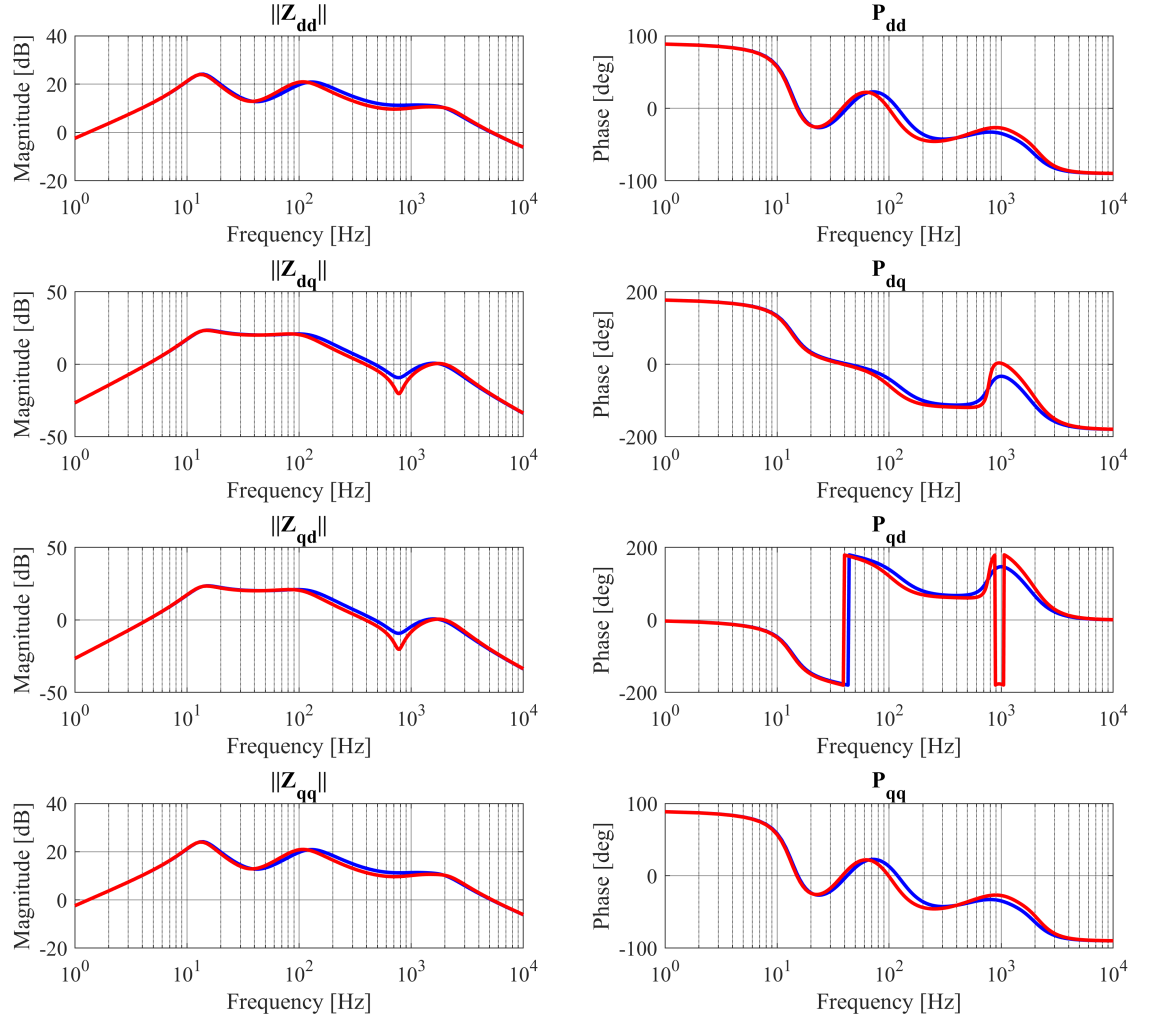
Figure 6.9: Bode diagram comparison between the identified model and nominal model of VSI

The Q and R matrices used for the optimal H_2 controller tuning are

$$Q = diag(0,...,0,0,0,1,10,1,1)$$
$$R = diag(1,1,0,0)$$

(6.40)

The resulting state feedback control gains matrix for AFE is

$$K_{AFE} = \begin{bmatrix} -0.0161 & -0.0349 & 0.0042 & 0.1463 & -2.7944 \\ 0.0248 & 0.0351 & 0.0092 & -0.1286 & -4.6374 \end{bmatrix}$$

(6.41)

The gains for PLL are

$$K_p^p = 0.225580 \quad K_i^p = 2.325406$$

(6.42)

6.5 Model order determination

An overparametrized model structure can lead to unnecessarily complicated computations for finding the parameter estimates and for using the estimated model, while an underparametrized model may be very inaccurate.

Generally speaking, the choice of model structure in practice is influenced greatly by the intended use of the model. A stabilizing regulator can often be based on a crude low order model, whereas more complex and detailed models are necessary if the model is aimed at giving physical insight into the process [137]. Since utility of the identified model is to tune a state feedback controller for a MIMO system (i.e. the AFE) based on the H_2 algorithm in this research, form of the to be identified model is fixed as state space models, instead of differential equations or any other types of nonparametric ones. Therefore, the 'model structure' here refers to the order of estimated model being requested.

Commonly, the model order is selected based on prior knowledge of the system and chosen through a trial and error process. In this research, as the structure of VSI is known, the preselected order is 8, in accordance with (3.50). For situations where there is no sufficient prior knowledge of the to be identified system, the subspace algorithm [139, 140] is adopted as it offers a useful tool to estimate the model order.
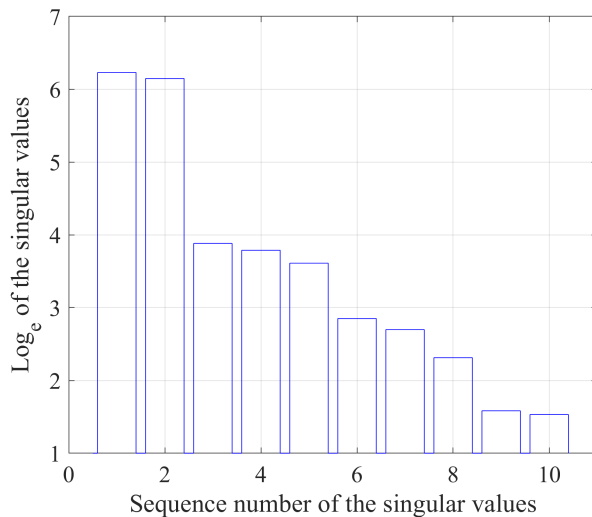
Figure 6.10: Model order selection according to the singular value of $\mathcal{O}$

In the subspace identification algorithm, singular values of a certain covariance matrix, i.e. the *oblique projection matrix* $\mathcal{O}$ (cf. B.3) that is constructed from the experimental data are computed [141, 142]. As shown in Fig.6.10, singular values of the $\mathcal{O}$ when identifying the VSI

are shown. The n'th singular value is a measure of how much the n'th component in the state vector contributes to the input-output behaviour of the model. The singular values are arranged in descending order. It means that as the sequence number n increases, the n'th state weigh less in describing the system behaviour. It is a trade-off between data fitting accuracy and model complexity. So a reasonable choice of order n (i.e. number of states used to describe the dynamic behavior of to be identified system) is one where the singular values to the right of n are far smaller compared to those to the left. According to the singular values shown in the Fig.6.10, 8 was chosen as the order of the to be identified model for VSI.

It is natural to doubt the utility of proposed optimal H_2 control method when applied in a converter-dense power grid, of which the actual model order could be huge. It would be quite a challenge to identify a model of such high order. Therefore, some simulations are performed to investigate the applicability of proposed optimal H_2 control design method in complex converter-dense grids.

Recall the multi-converter network discussed in the Sec.5.4 and shown in the Fig.5.10. Before designing an optimal H_2 controller based on the proposed method for the AFE2, it is requisite to identify a model for the VSI-AFE1 system. Let's consider how the order selection impacts performance of the optimal controller of AFE2 which will be synthesized based on the identified model. More important, how low the model order could reach when the identified model can be successfully used for the optimal H_2 control tuning of AFE2.

When comparing the PI control design method and the optimal H_2 control design method when they are applied in the control design of AFE2 in the Sec.5.5, nominal model of the VSI-AFE1 network was used to tune an optimal H_2 controller for the AFE2. The order of the nominal model is 14, including 8th order for the VSI and 6th order for the AFE1. Together with the 5th order of the to be designed AFE2, the order of the global model transferred to the H_2 algorithm is 19. As has been demonstrated in the Sec.5.5, the commercial tools used for the H_2 optimization has no problem in dealing with such high dimension systems.

Unlike the simulations there, here an identified model of VSI-AFE1 network is used to tune an optimal H_2 controller for the AFE2. In the Fig.6.11, singular values of the $\mathcal{O}$ built by the collected data in identification simulation are plotted.
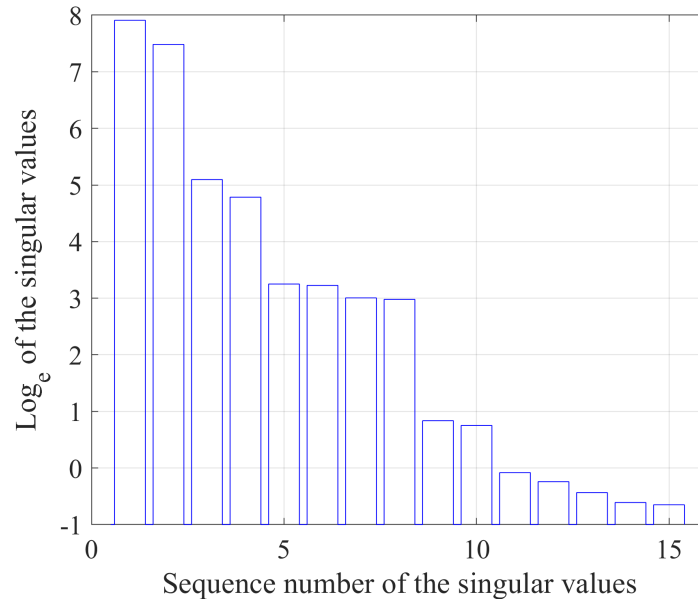
Figure 6.11: Order select according to the singular values of $\mathcal{O}$ in VSI-AFE1 system identification

Utilizing the collected data, different numbers were tried as the order of to be identified model of VSI-AFE1 network. Bode diagrams of those identified models of different orders are plotted in Fig.6.12 as well as the nominal model. Only d-d axis and q-q axis impedance magnitude are presented here. The discrepancy in low frequency is due to the fact that there was no adequate energy of perturbations injected in the low frequency range. Perturbations with more energy in low frequencies will make the whole system unstable as the VSI-AFE1 system is inherently close to be unstable .
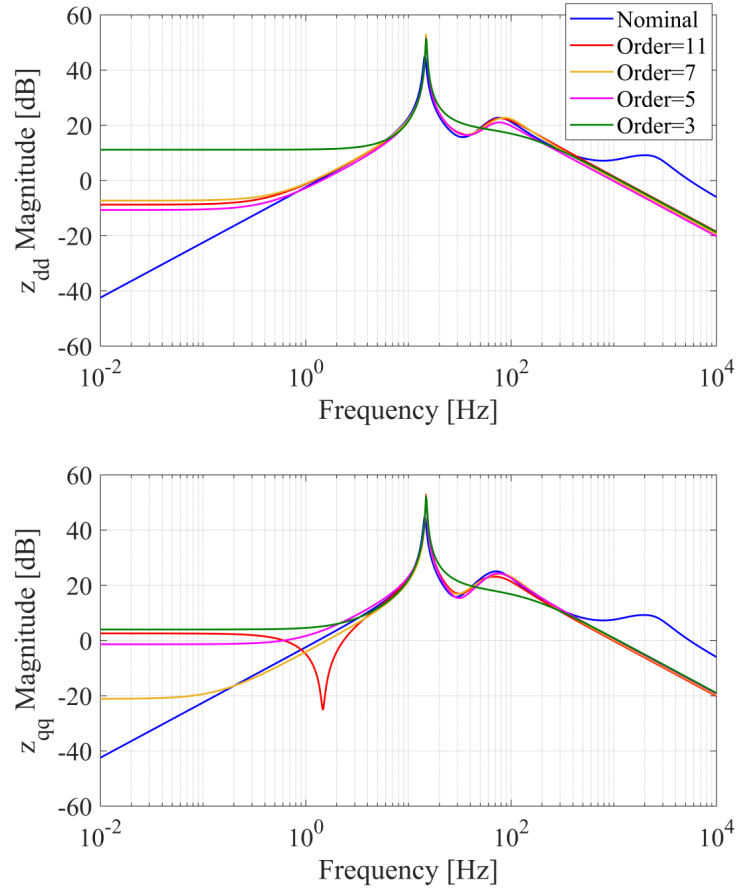
Figure 6.12: Bode diagrams of VSI-AFE1 system's nominal model and identified model of different orders

Then the identified models of different orders were used to tune optimal H_2 controllers for the AFE2. In the Fig.6.13, the VSI-AFE1-AFE2 system response waveforms obtained in the simulation when the AFE2 adopts those different optimal H_2 controllers are shown. Details of the waveforms in the transient are shown on the right. In this simulation, control scheme and parameters of the VSI and two AFEs are same with the simulations in Chapter 5. The load on AFE1 ramps up from 0 to its nominal value $P_1 = 800W$ at t=1s. Then the load of AFE2 is increased from 0 to $P_2 = 700W$ at t=3s.
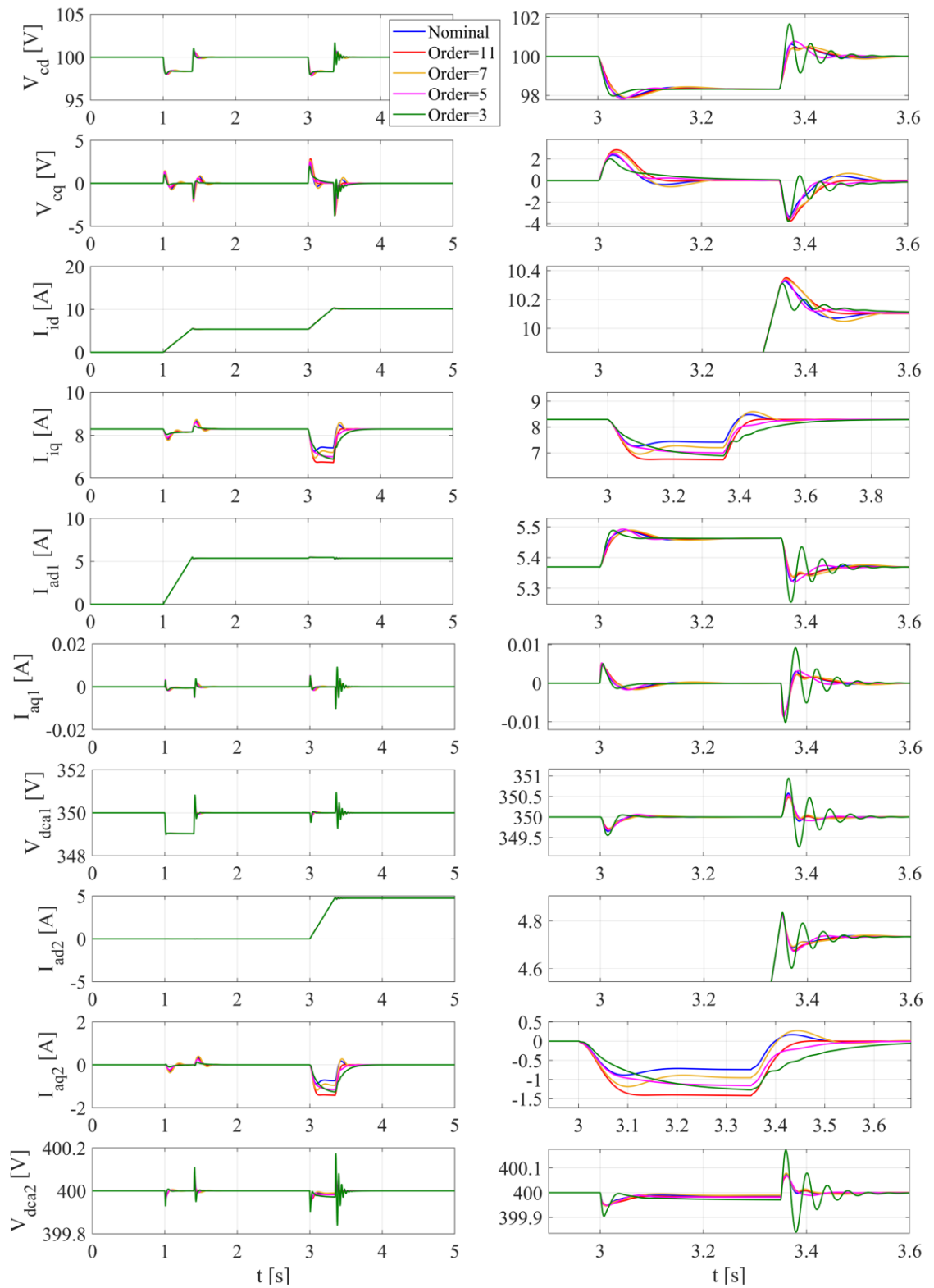
Figure 6.13: Waveforms of system response when AFE2's H_2 controller is tuned with VSI-AFE1 system's nominal model or identified model of different orders

According to the simulation results, except that the VSI-AFE1-AFE2 system exhibits oscillations in the transient when the AFE2 adopts a controller tuned by third order identified model of VSI-AFE1 network, all other cases work out satisfactory dynamic performance. Actually, 3 is the least acceptable order of VSI-AFE1's identified model. A second order identified model will not be able to find a stable controller for AFE2 when it is integrated to build the system global model.

Notably, the waveforms relating to the fifth order identified model is similar to those of the nominal model. The bode comparison between the fifth order identified model and the nominal model of the VSI-AFE1 system is shown in the Fig.6.14. And the optimal H_2 controller synthesized by the optimal control design method and the identified model is provided in (6.44).
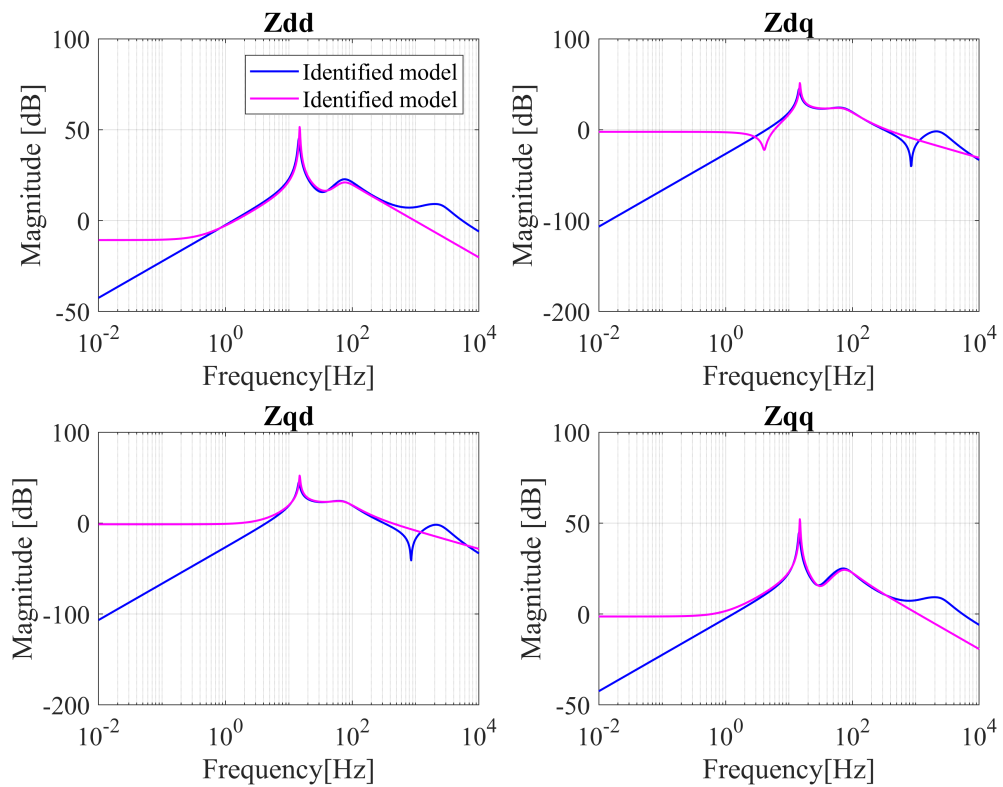
Figure 6.14: Bode diagram comparison between the 5th identified model and nominal model of VSI-AFE1 system

The Q and R matrices used for the optimal H_2 controller tuning are

$$Q = diag(0, ..., 0, 0, 0, 1, 10)$$
$$R = diag(1, 1)$$

(6.43)

The resulting state feedback control gains matrix for AFE2 is

$$K = \begin{bmatrix} 0.0037 & -0.0005 & 0.0149 & 0.0960 & -10.0451 \\ 0.0257 & 0.0393 & -0.0203 & -0.5466 & 11.3365 \end{bmatrix} \quad (6.44)$$

The simulation preliminarily proves that the proposed control design method could work well when applied in a complex power grid comprised of massive loads and sources. A relatively low order identified model of the grid is enough to tune a capable optimal H_2 controller for a local converter. This feature again confirms the effectiveness of optimal H_2 control design method.

6.6 Conclusion

In this chapter, the identification techniques in particular the prediction error method adopted in this research were described. The details of identification experiments were presented, including perturbation injection and data process. Most significantly, the mathematical way to build the system global model based on identified grid models is presented. The idea was demonstrated by a switching model simulation primarily. A critical point namely the model order determination in identification was also discussed.

Chapter 7

Experimental results

In this chapter, experimental results of the VSI-AFE system when the AFE adopts an optimal H_2 controller or a traditional PI controller are compared. The experimental results are inspected and analysed by time-domain response waveforms, pole map of system model, and characteristic loci. Advantages of the proposed optimal H_2 control design method are clearly proved.

7.1   Optimal control design for AFE

An overview of the optimal control design procedure for AFE that proposed in this thesis is presented in Fig.7.1. At first, the AFE is utilized as a current perturbation source to inject excitations into the grid (emulated by a VSI in the experimental rig) which the AFE will be attached with at the PCC. PRBS reference amplitude of the current perturbation injected into the VSI is $2A$. Then voltage and current responses are collected and passed to the PEM algorithm after process described in Sec.6.3. A state space model of the grid could then be estimated. It is combined with open loop model of the AFE to establish a global model for the whole VSI-AFE system. Based on this model and by the use of structured H_2 algorithm, an optimal state feedback controller for AFE can be synthesized and its execution does not require measurement of VSI's states.
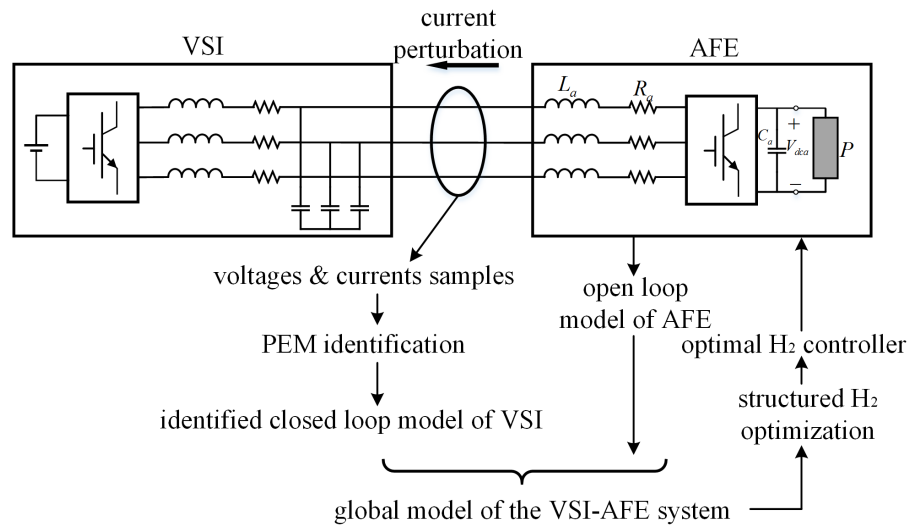
Figure 7.1: Optimal control design procedure of AFE

In the next, two cases of optimal control design experiments for AFE are conducted and anal-ysed. The VSI in these two cases is tuned to have different bandwidths and it means different grid conditions for the control design of AFE. Performance of the traditional PI control method and optimal H_2 control method under these two different conditions are compared.

7.1.1   Case 1, high bandwidth VSI

Model identification of VSI

Without loss of generality, traditional cascade PI control is employed for the VSI as shown in Fig.3.7. The tuning of control parameters in such applications is well documented in [126, 143, 144]. In the first case, the VSI is tuned to have a relatively high voltage bandwidth and its PI controller's parameters are shown in the Table.7.1. The resulting voltage bandwidth is 19.63 Hz. The corresponding $f_v = 80$ and $f_i = 800$. Switching frequency of the VSI is 10kHz.

Table 7.1: Parameters of VSI's PI controllers in case 1

	Voltage loop	Current loop
VSI	0.033+8.338/s	3.724+11622.446/s

AC grid generated by this VSI is then identified in procedure described in Sec.6.3. During the identification process, the PLL control loop is cut out. It is realized by forcing the PLL PI output to zero during the perturbation injection period, as shown in Fig.7.2.
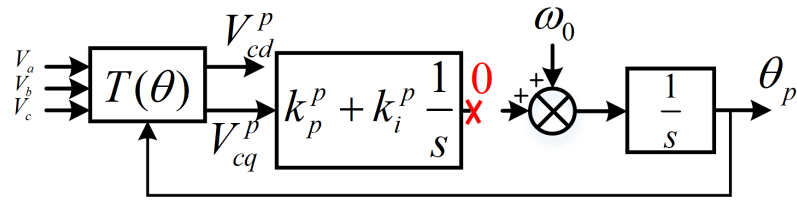
Figure 7.2: PLL control loop in identification experiment

In this way, the collected data for identification algorithm does not include PLL dynamics. Otherwise, the data will be a projection in PLL-dq frame. Instead, we want a VSI's model estimated in VSI-dq frame here.

As the perturbation injection only lasts 1 second in the experiment, the error of PLL output (i.e. the θ_e) accumulated in this period is relatively small and will not cause serious impact on the normal operation of AFE. A figure of the PLL error in the period of perturbation injection (lasts from 1.3s to 2.3s) in experiment is shown in Fig.7.3.
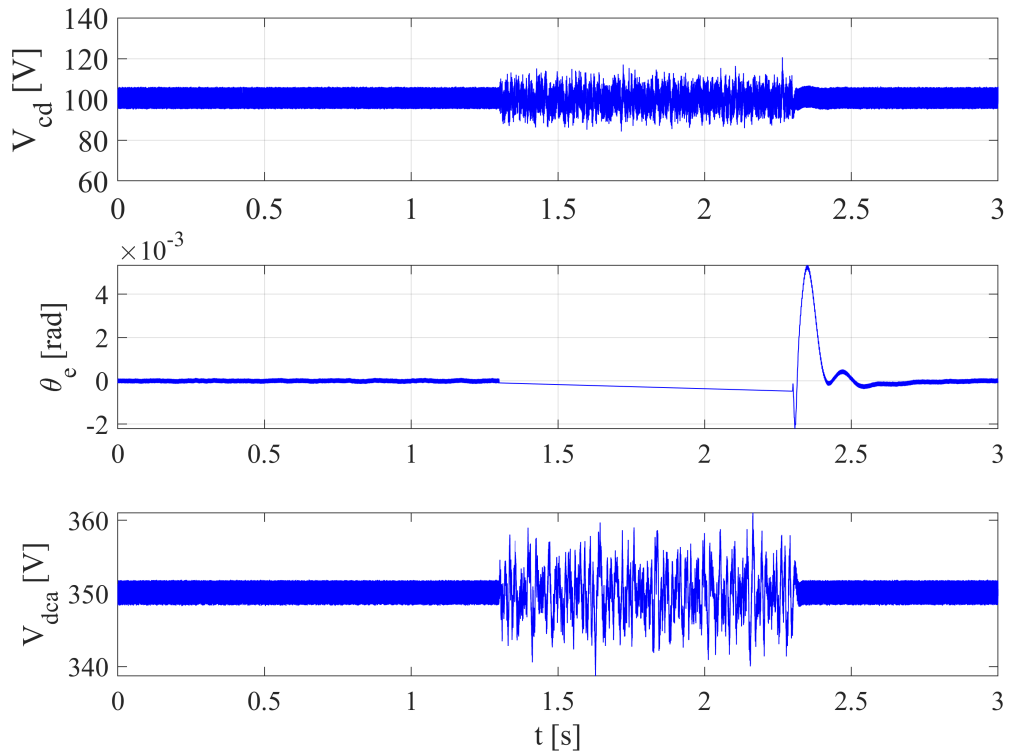
Figure 7.3: Waveforms of V_{cd}, PLL error θ_e and V_{dca} during perturbation injection period

After the current and voltage data was collected in the identification experiment, it is processed

to fit for estimation. Due to the nonlinearities from SPWM modulation, dead time in switching actions etc., harmonics at multiples of fundamental frequency, 400Hz here is present in the spectrum of sampled data, as shown in Fig.7.4. The fundamental frequency is selected according to the intended application of the proposed method in aircraft AC system. If these data is transferred to the PEM directly without proper process, many poles may be identified out at these frequencies. Therefore, a digital notching filter is integrated in the DSP program to filter those harmonics. A frequency spectrum of V_{cd} after notch filtering is plotted in blue in Fig.7.4.
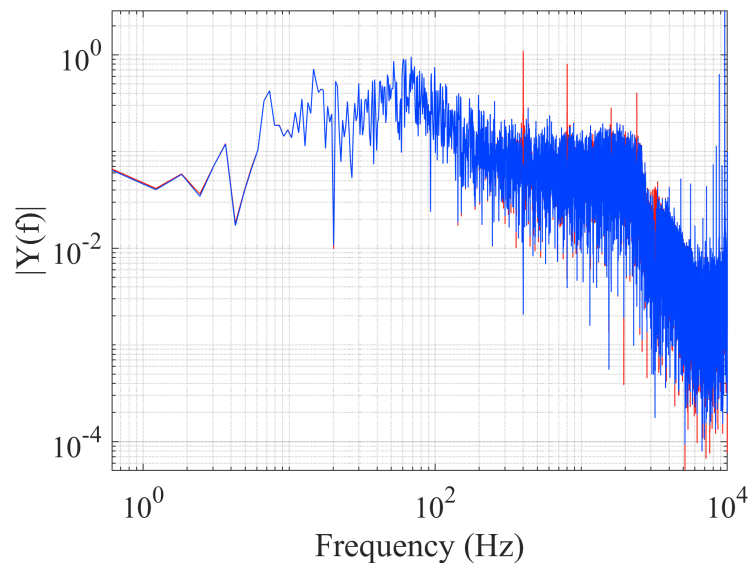
Figure 7.4: Spectrum of V_{cd} before (red) and after notch filtering (blue)

The identification of VSI is focused on the frequency range of 0 - 3kHz. Therefore, a low pass filter with a passband of 0 - 4kHz is adopted here as mentioned in the last chapter. Frequency spectrum of V_{cd} before and after the low pass filter is shown in Fig.7.5.
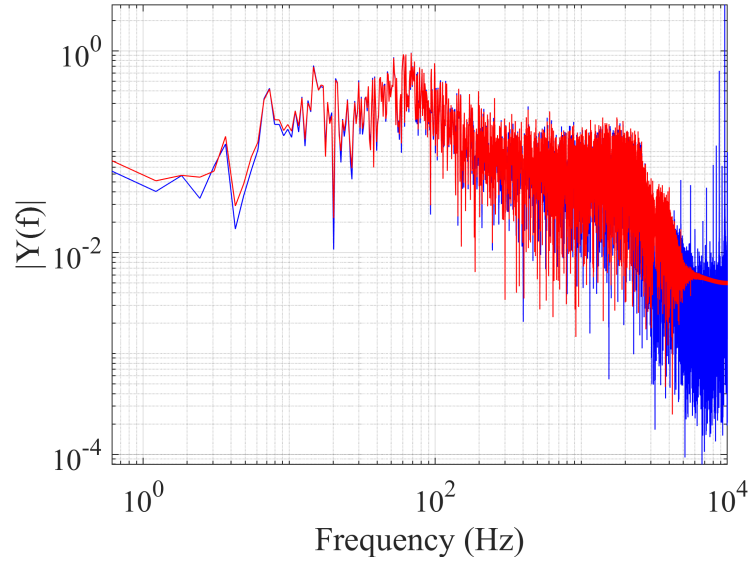
Figure 7.5: Frequency spectrum of V_{cd} before and after low pass filtering

Then the PEM is applied to estimate a state space model of VSI. The chosen model order is 8. Bode diagram of the identified model is shown in Fig.7.6. In this research, since the VSI is built by ourselves in lab, its passive components value and control parameters are known. Therefore a nominal model of VSI could be built. It is used to validate the identified model obtained in experiments by comparing them in a same bode diagram, as shown in Fig.7.6. As can be seen, a good match is achieved in the whole frequency range in d-d axis and q-q axis which proves high accuracy of the identified model.
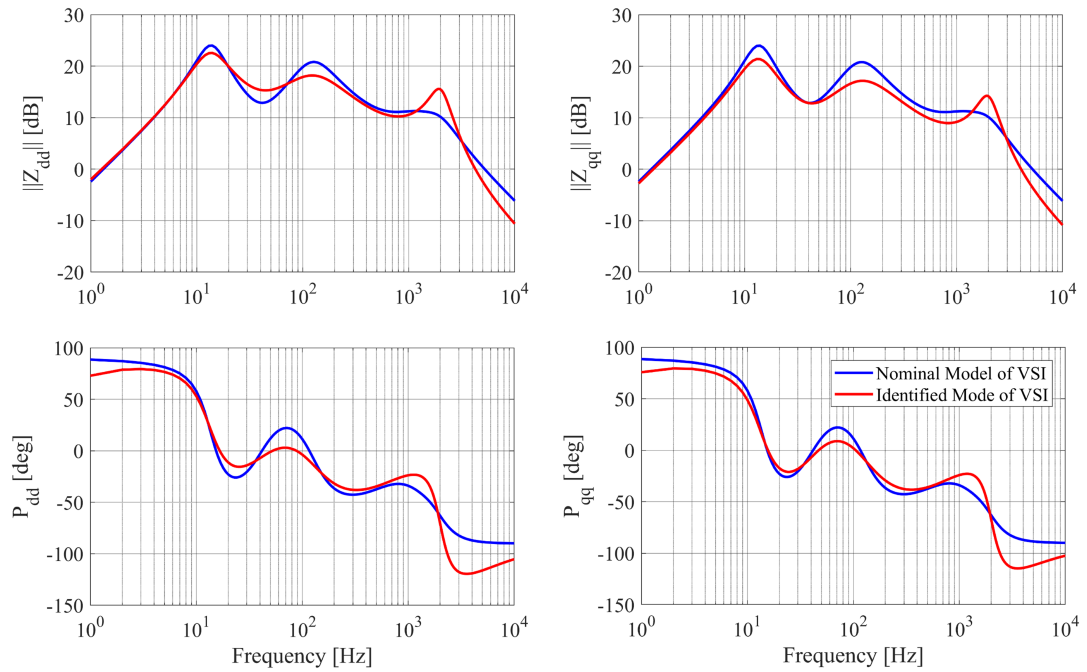
Figure 7.6: Bode diagram comparison of VSI's nominal model and identified model obtained in identification experiment in case 1

The assessment of identified model quality is typically about evaluating its capacity in predicting the output of being identified system. Therefore, another way of model validation is to compare predicted output of identified model and the measured data collected in identification experiment in time-domain when fed by same input. In Fig.7.7, the output voltage of VSI V_{cq} predicted by the identified model and V_{cq} collected and filtered in the identification experiment are plotted together. As can be seen, the two curves follow similar trajectory indicating that the identified model could be utilized in control system synthesis.
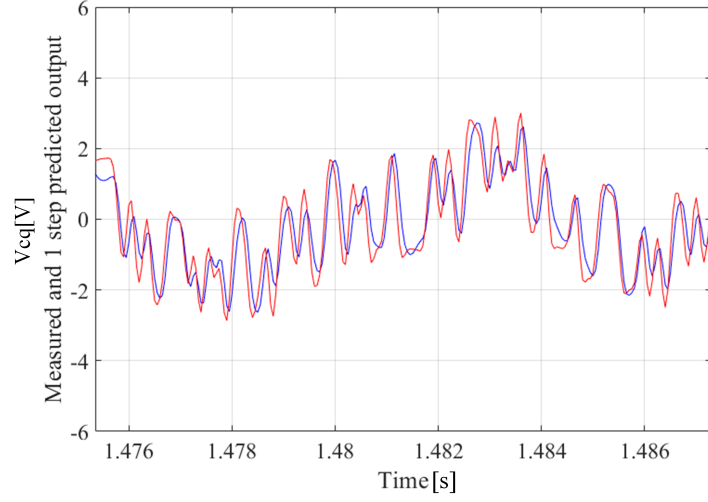
Figure 7.7: Comparison between V_{cq} obtained in experiment after filtering and 1 step predicted by the identified model

Optimal H_2 control with identified model of VSI

An optimal H_2 controller is then tuned for AFE by procedure described in Sec.6.4 based on the identified model of VSI. The weight on $w_{v_{dca}}$ in Q matrix (4.28) is tuned incrementally to its upper bound to achieve a high voltage bandwidth AFE controller, without losing anti-interference capability and introducing too much oscillations. The final choice of the Q, R matrices is shown in (7.1).

$$Q = diag(0, .., 0, 0, 0, 1, 10, 0, 2)$$
$$R = diag(2, 2, 0, 0)$$

(7.1)

The synthesized control parameters are shown below. Voltage bandwidth of the synthesized optimal H_2 controller is 280 Hz.

$$K_{AFE} = \begin{bmatrix} 0.0428 & -0.0129 & 0.0268 & 0.3955 & -25.0675 \\ 0.0124 & 0.0311 & -0.0031 & -1.0124 & -0.3196 \end{bmatrix}$$

(7.2)

$$k_p^p = 0.195; k_i^p = 1.956;$$

(7.3)
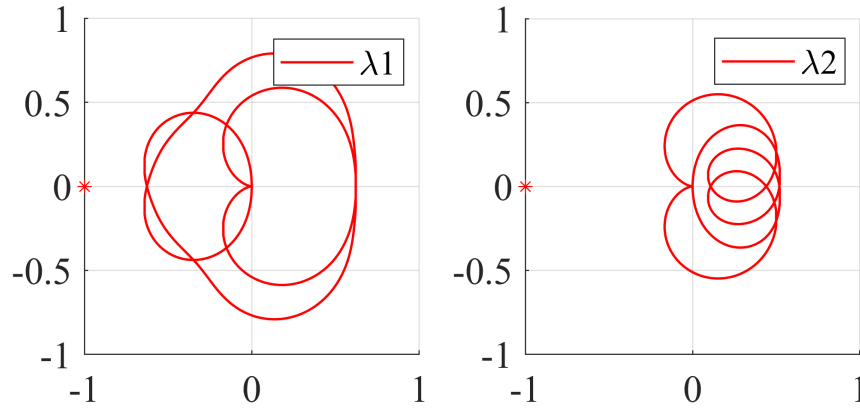
Figure 7.8: Characteristic loci of the VSI-AFE system when AFE uses the optimal H_2 controller based on identified model of VSI

Analytical impedance of the AFE with this H_2 controller can be derived by the equations in Sec.3.3.4. Based on the identified impedance model of VSI and AFE's analytical impedance model, characteristic loci of the impedance ratio from VSI to AFE can be computed. Characteristic loci of the VSI-AFE system when AFE uses the synthesized H_2 controller is plotted in Fig.7.8 and it is clear that the VSI-AFE system is guaranteed to be stable.

Fig.7.9 shows the VSI-AFE system response when a transient is created by ramping up the AFE DC-link CPL from zero to 0.6 kW from 0.1s to 0.18s. As can be noted from the figure, all quantities are regulated effectively to their reference values in a very short time without showing oscillatory behaviours due to interactions between the VSI and AFE. DC-link voltage peak variation is very small demonstrating a stiff DC bus for the load. Passive components values and nominal references in the experiments are shown in Table. 4.1. The negative value of I_{ad} in no load condition is thought as a result of poor calibration of current sensors.

Figure 7.9: Dynamic response waveforms of the VSI-AFE system under 0.6kW CPL loading when AFE adopts the optimal H_2 controller tuned with identified model of VSI

PI control

As a comparison, a PI controller (with a structure shown in Fig.3.8) is also tuned for AFE. The tuning has been performed increasing the DC-link voltage bandwidth aiming to obtain an as fast as possible PI controller. The inner current loop bandwidth is kept one order of magnitude bigger. The best tuned PI controller for AFE has a voltage bandwidth of 35 Hz. The corresponding $f_v = 50$ and $f_i = 800$. The resulting PI gains are reported in Table 7.2. Characteristic loci of the VSI-AFE system when AFE adopts this PI controller is shown in Fig.7.10.

Table 7.2: Parameters of the AFE PI controller in case 1

	Voltage loop	Current loop
AFE	0.0628+9.8696/s	-5.681-14780.719/s
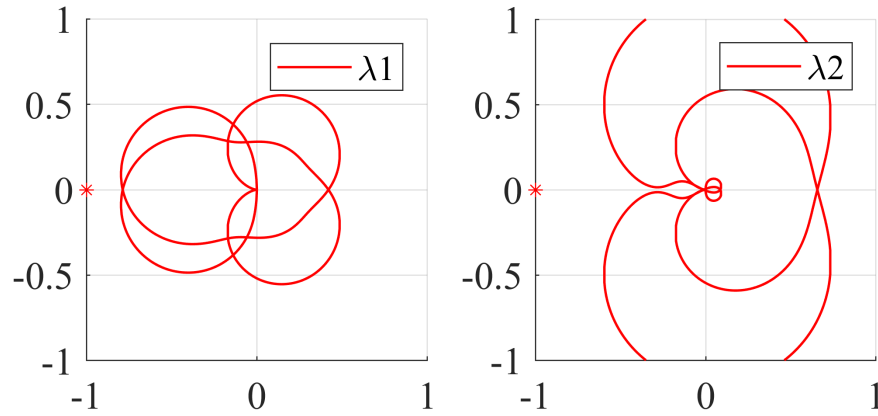
Figure 7.10: Characteristic loci of the VSI-AFE system when AFE uses the PI controller

The VSI-AFE system response to the same test described before when AFE adopts the PI controller is shown in Fig.7.11. As can be seen, the dynamic performance is inferior to the case when AFE uses the optimal H_2 controller, especially showing a bigger DC-link voltage drop in the transient. But generally speaking, performance of the PI controller in this case is still satisfactory.
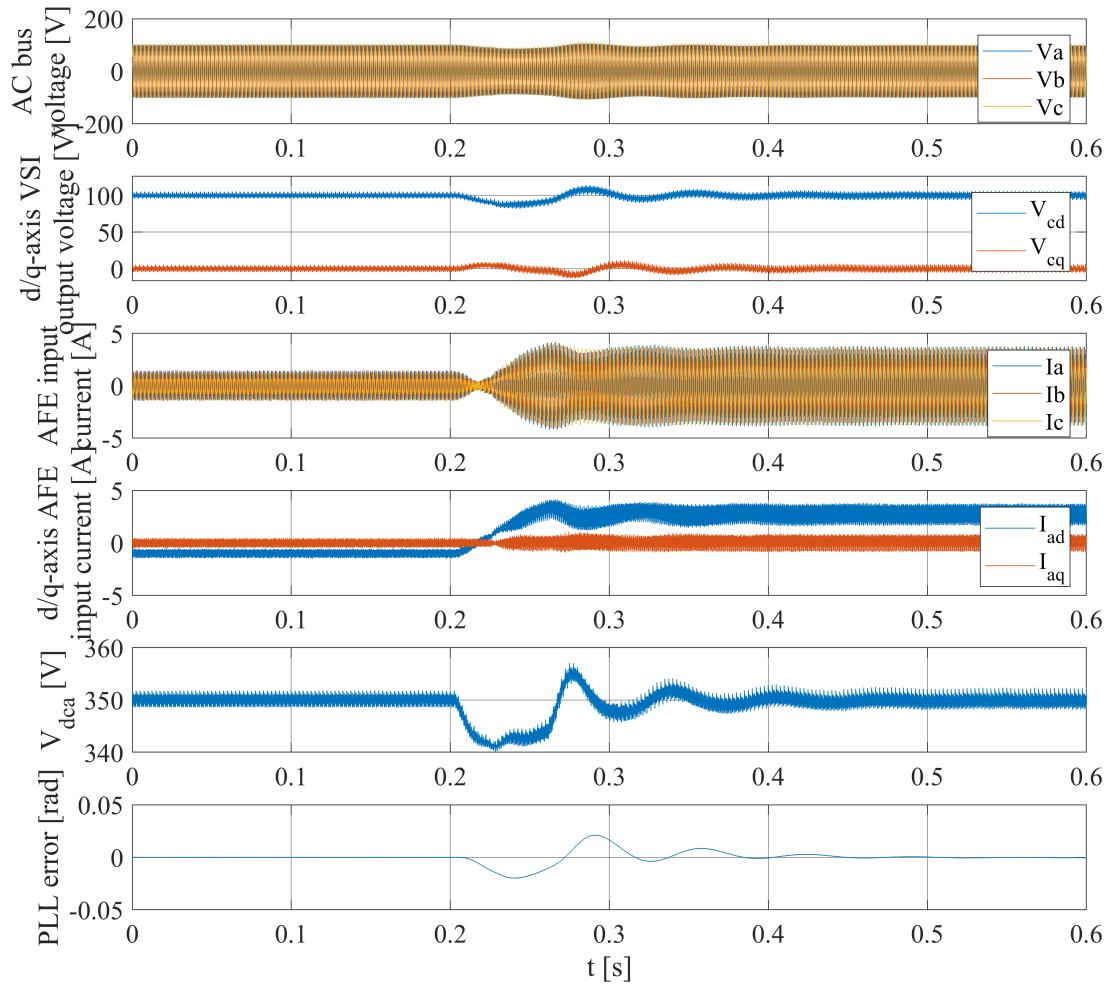
Figure 7.11: Dynamic response waveforms of the VSI-AFE system under 0.6kW CPL loading when AFE adopts the traditional PI controller

Superiority of the proposed optimal H_2 control method over the PI control can also be evinced by analysing closed-loop dominant poles of the VSI-AFE system model plotted in Fig.7.12 for both control approaches. When the PI method is used, dominant poles are at lower frequency compared to the H_2 controller demonstrating a lower bandwidth.
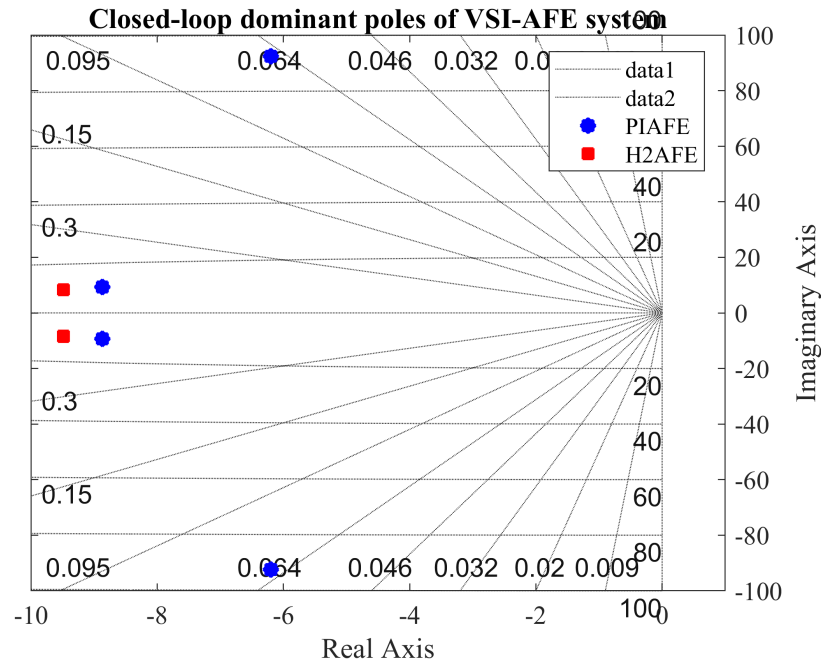
Figure 7.12: Locations of dominant poles of the VSI-AFE system when AFE adopts the traditional PI controller (blue aster), and the optimal H_2 controller tuned with identified model of VSI (red square)

Fig.7.13 shows the DC-link voltage waveforms recorded on the oscilloscope when AFE uses the two different controllers, i.e. the best-tuned PI controller and optimal H_2 controller respectively. It is obvious that with H_2 controller tuned by identified VSI model, the AFE generates a more stiff output voltage.
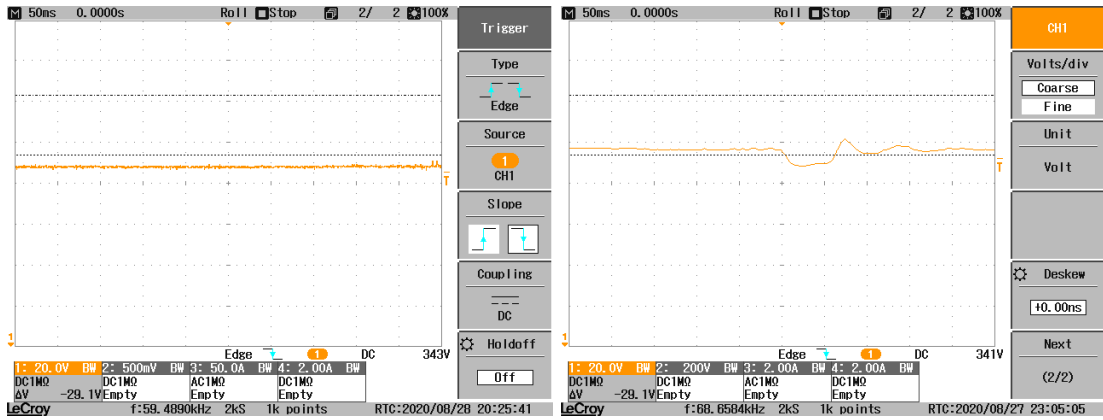
(a) H_2

(b) PI

Figure 7.13: DC-link voltage of AFE (a) optimal H_2 controller tuned with identified model of VSI (b) PI controller
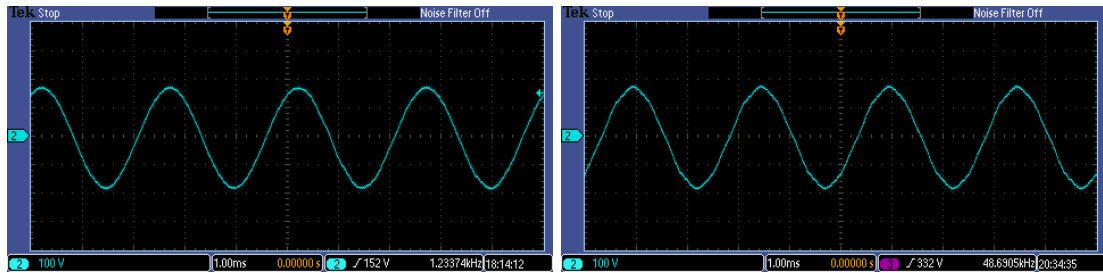
(a) H_2

(b) PI

Figure 7.14: Line-to-line grid voltage on scope — (a) optimal H_2 controller tuned with identified model of VSI (b) PI controller

In Fig.7.14, the AC grid line-to-line voltages in system steady state are shown. As can be seen, in the PI case, the voltage shows obvious distortion while the optimal H_2 controller case does not.

Optimal H_2 control with nominal model of VSI

To further validate the identification procedure, an additional test is performed. As the model of VSI is known in this study, another optimal H_2 controller has been tuned by replacing VSI's identified model with VSI's nominal closed loop model. Same weighting matrices Q and R have been used. Voltage bandwidth of the optimal H_2 controller achieved here is 264 Hz. And the controller gains are shown below.

$$K_{AFE} = \begin{bmatrix} -0.0073 & -0.0071 & 0.0107 & 0.0576 & -4.4043 \\ 0.0572 & 0.0409 & 0.0099 & -0.1521 & -3.6474 \end{bmatrix}$$ (7.4)

$$k_p^p = 0.1845; k_i^p = 1.8126;$$ (7.5)

Characteristic loci of the VSI-AFE system when AFE uses this optimal H_2 controller is shown in Fig.7.15.
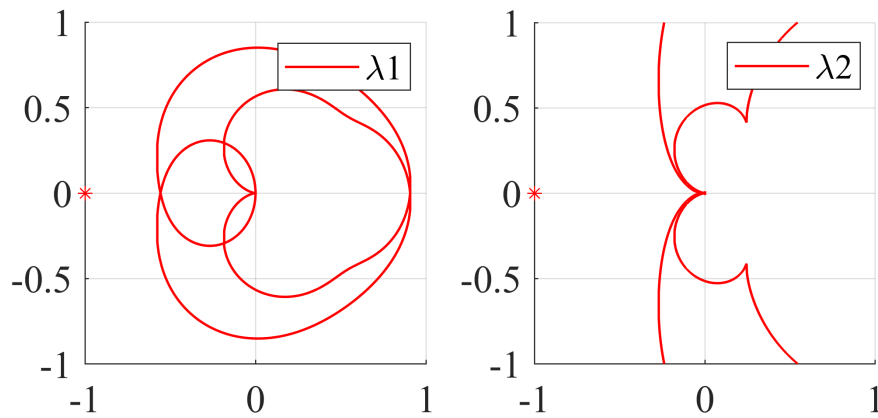
Figure 7.15: Characteristic loci of the VSI-AFE system when AFE uses the optimal H_2 controller based on nominal model of VSI

The system response to same test in this condition is reported in Fig.7.16. The transient time of I_{aq} is longer than the previous two cases due to a unsuccessful choice of Q. In the Q matrix, the weights relating to wI_{aq} should have been bigger to increase the response speed of I_{aq}.
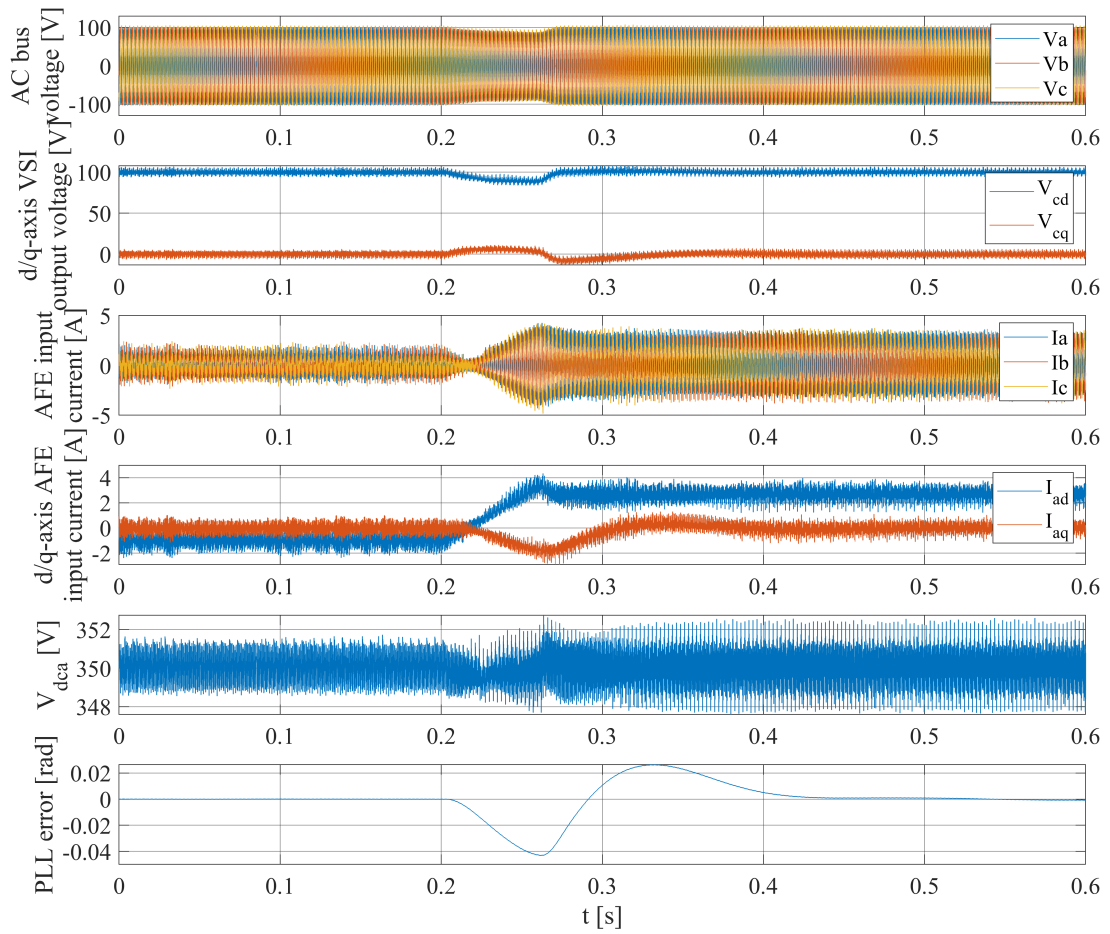
Figure 7.16: Dynamic response waveforms of the VSI-AFE system under 0.6kW CPL loading when AFE adopts the optimal H_2 controller tuned with nominal model of VSI

It can be noted that the performance is almost identical to that shown in Fig.7.9. It means a good match between identified model and nominal model of VSI and proved the reliability of identification experiment design. Both these two optimal H_2 controllers have a transient time about 0.08s whereas more than 0.2s of the traditional PI controller. The undershoot of AFE DC-link voltage also shows a great advantage, i.e. 0.005 p.u. of the optimal H_2 controllers contrasting with 0.03 p.u. of the PI controller.

7.1.2   Case 2, low bandwidth VSI

Model identification of VSI

To explore the capability of optimal H_2 control design method, the voltage bandwidth of VSI is decreased to 13.51 Hz in the second case. The corresponding PI parameters are shown in Table.7.3 and $f_i = 600$, $f_v = 60$. It means bigger output impedance of VSI, reduced stability margin of the VSI-AFE system, and a bigger challenge for AFE control design compared to the first case.

Table 7.3: Parameters of VSI's PI controllers in case 2

	Voltage loop	Current loop
VSI	0.0248+4.690/s	3.403+6537.626/s

Bode diagram of VSI's identified model in this cases is presented in Fig.7.17 together with that of VSI's nominal model. It proves the good accuracy of VSI's identified model in this case.
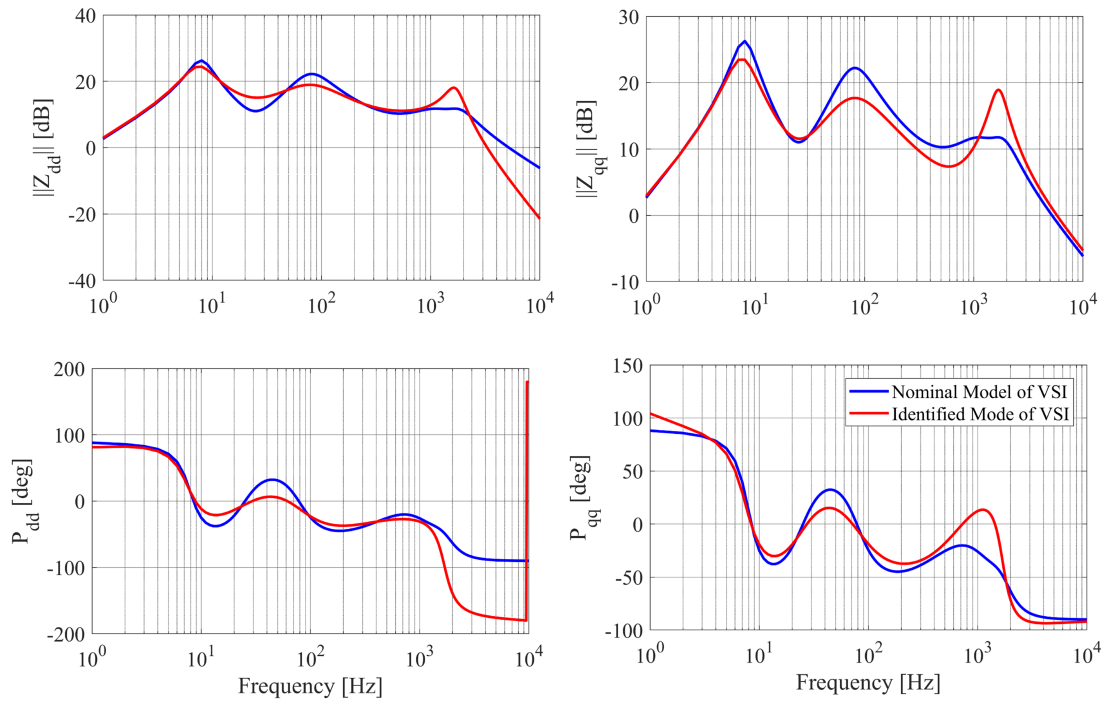
Figure 7.17: Bode diagram comparison of VSI's nominal model and identified model obtained in identification experiment when the VSI has a lower voltage bandwidth

Meanwhile, a bode diagram comparison of VSI's identified d-d axis impedance in these two cases is shown in Fig.7.18. The result is consistent with Fig.5.18, namely a smaller bandwidth means bigger impedance in the low frequency range.
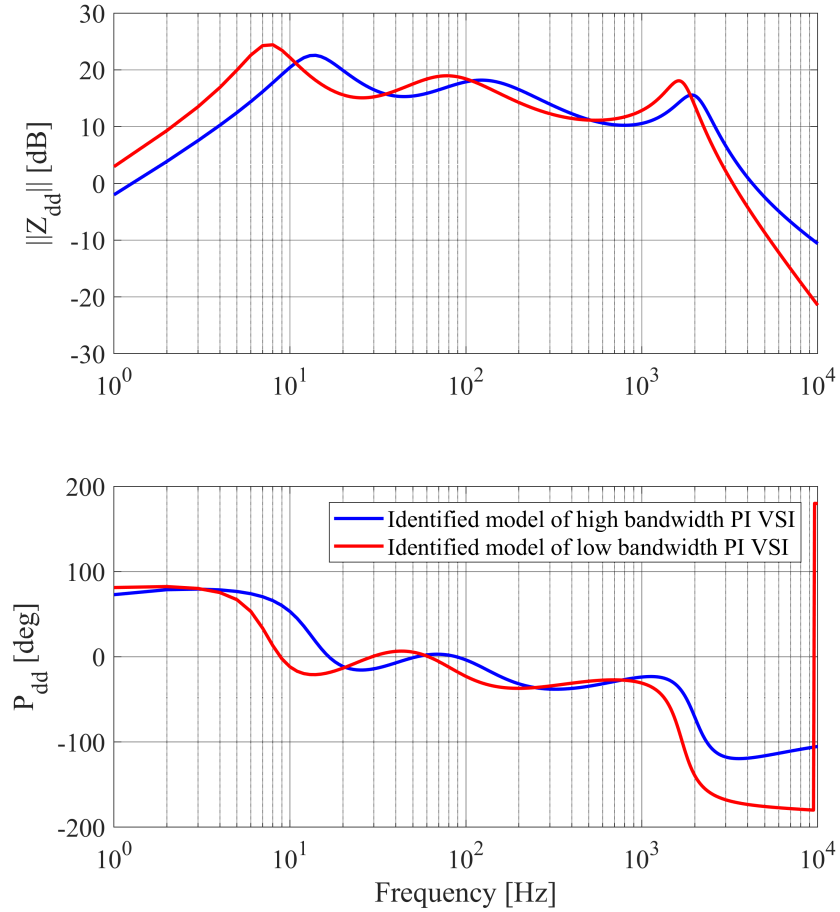
Figure 7.18: Bode diagram comparison of VSI's identified d-d axis impedance when VSI has different voltage bandwidths

To validate the identified model of VSI, VSI output voltage V_{cq} predicted by the identified model and measured in the experiment are compared in Fig.7.19. As can be seen, the trajectory corresponding to the identified model matches that of the measured output well, indicating the identified model could describe the real dynamic behaviour of VSI accurately.
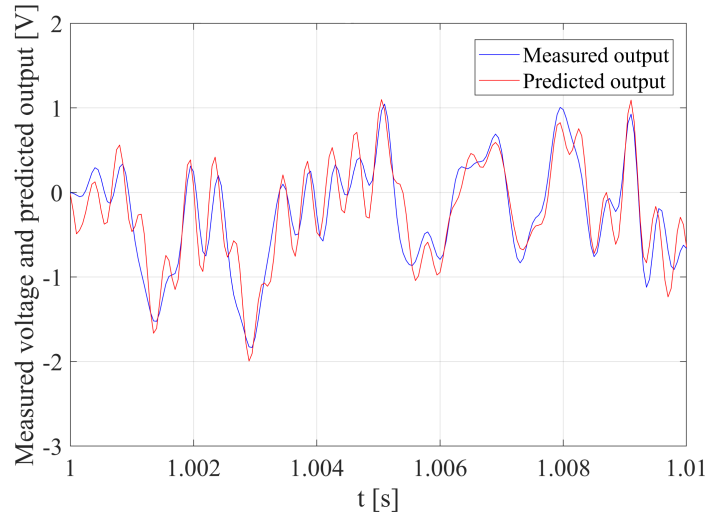
Figure 7.19: Comparison between q-axis voltage V_{cq} obtained in experiment after filtering and V_{cq} predicted by the identified model in case 2

Optimal H_2 control with identified model of VSI

In this case, the weighting matrices Q and R are still kept as the first case. The resulting optimal H_2 controller gains are presented below.

$$K_{AFE} = \begin{bmatrix} -0.0001 & -0.0176 & 0.0114 & 0.1587 & -11.3676 \\ 0.0306 & 0.0520 & 0.0050 & -0.3666 & -6.4587 \end{bmatrix} \tag{7.6}$$

$$k_p^p = 0.177; k_i^p = 1.484; \tag{7.7}$$

Characteristic loci of the VSI-AFE system when AFE uses the synthesized H_2 controller in this case is shown in Fig.7.20.

Figure 7.20: Characteristic loci of the VSI-AFE system when AFE uses the optimal H_2 controller based on identified model of VSI in case 2

Time-domain experimental results of the VSI-AFE system in the same test as before are shown below. As can be seen, although the d/q axis voltages exhibit a bigger deviation and transient compared to the first case, the overall performance is still satisfactory.
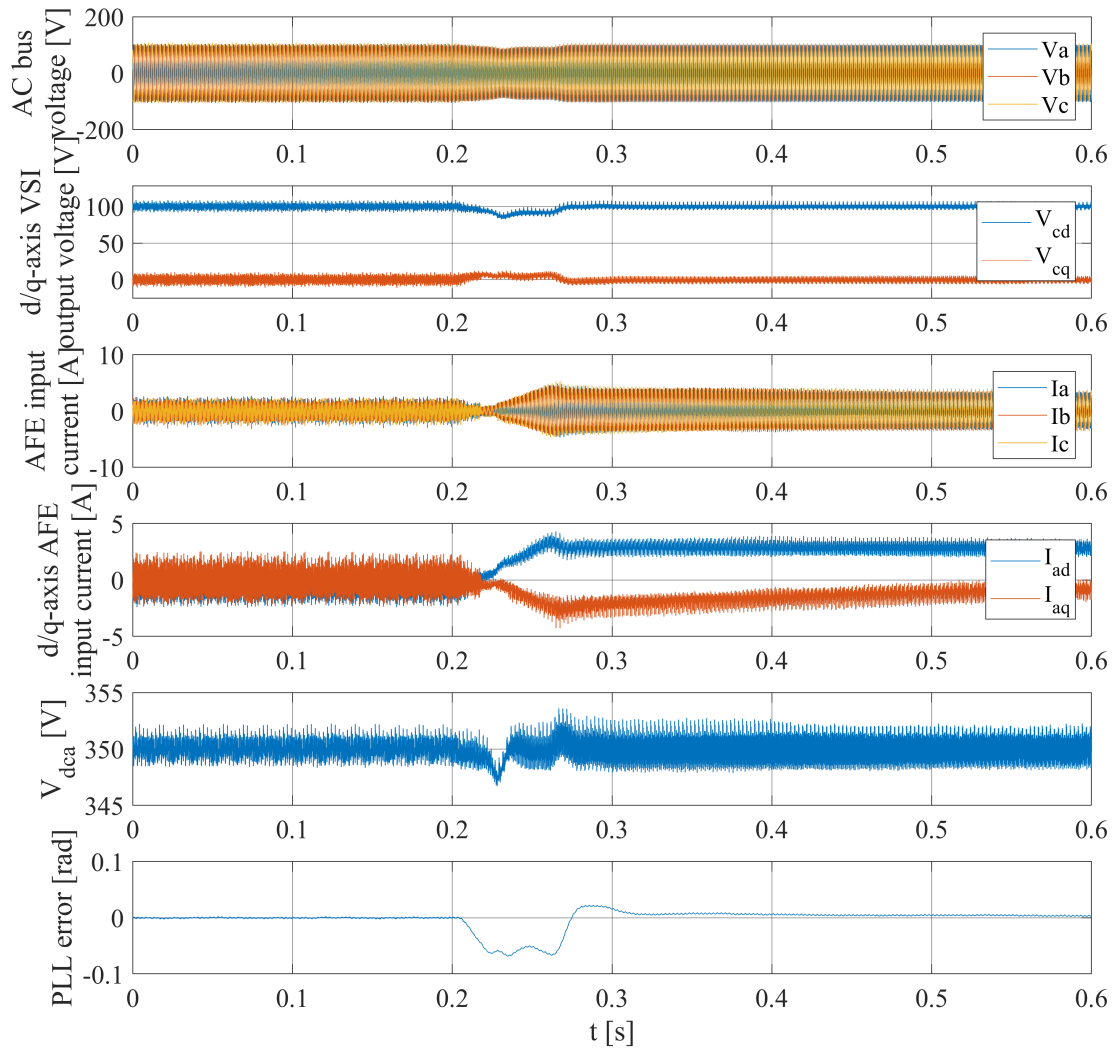
Figure 7.21: Dynamic response waveforms of the VSI-AFE system under 0.6kW CPL loading when AFE adopts the optimal H_2 controller tuned with identified model of VSI in case 2

PI control

Similarly, a PI controller is also tuned for AFE in this case. Parameters of the best-tuned PI controller are shown in the Table.7.4. $f_i = 700$ and $f_v = 35$. The voltage bandwidth obtained is only 26 Hz.

Table 7.4: Parameters of the PI controllers in case 2

	Voltage loop	Current loop
AFE	0.043982+4.836106/s	-4.945929-11316.488406/s

The characteristic loci in this case are plotted in Fig.7.22. As can be seen, the locus shown in

the left figure is close to encircling the critical point indicating insufficient stability margin.
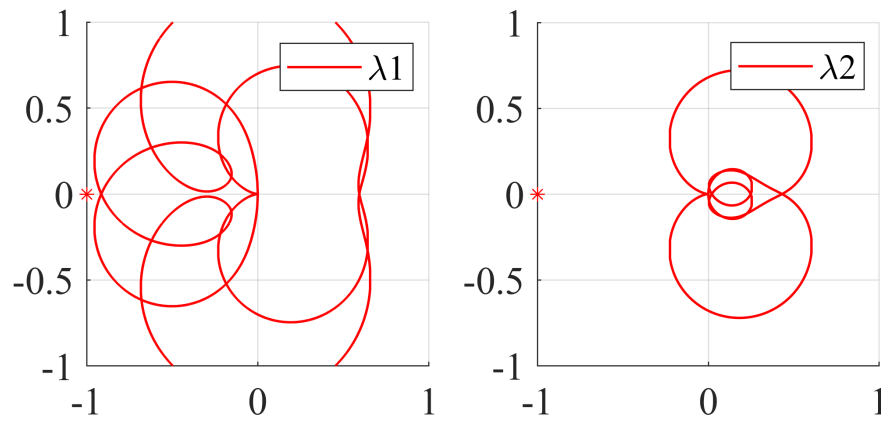
Figure 7.22: Characteristic loci of the VSI-AFE system when AFE uses the PI controller in case 2

Closed loop dominant poles of the VSI-AFE system model when AFE uses the optimal H_2 controller or the PI controller in this case are shown in Fig.7.23. It is clear that poles of H_2 controller are generally further from the imaginary axis and closer to the real axis indicating a faster performance and less oscillation in the transient when AFE adopts the optimal H_2 controller.
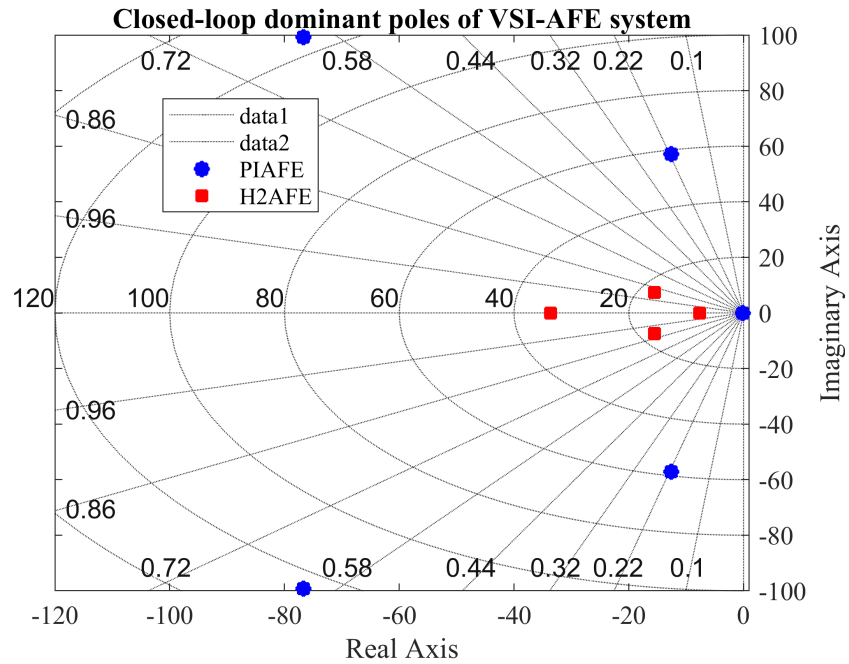
Figure 7.23: Locations of dominant poles of the VSI-AFE system when AFE adopts the traditional PI controller (blue aster), and the optimal H_2 controller tuned with identified model of VSI (red square)

Time-domain waveforms obtained in experiments when AFE adopts the traditional PI controller in this case are shown in Fig.7.24. As can be noted from the results, interactions between the VSI and AFE cause strong oscillatory behaviours on the AC grid. The modulation indexes were saturated by the oscillations at the beginning the transient. The DC-link voltage is also severely affected by showing a far bigger deviation from its reference and a longer settling time compared to the case when AFE adopts the optimal H_2 controller.
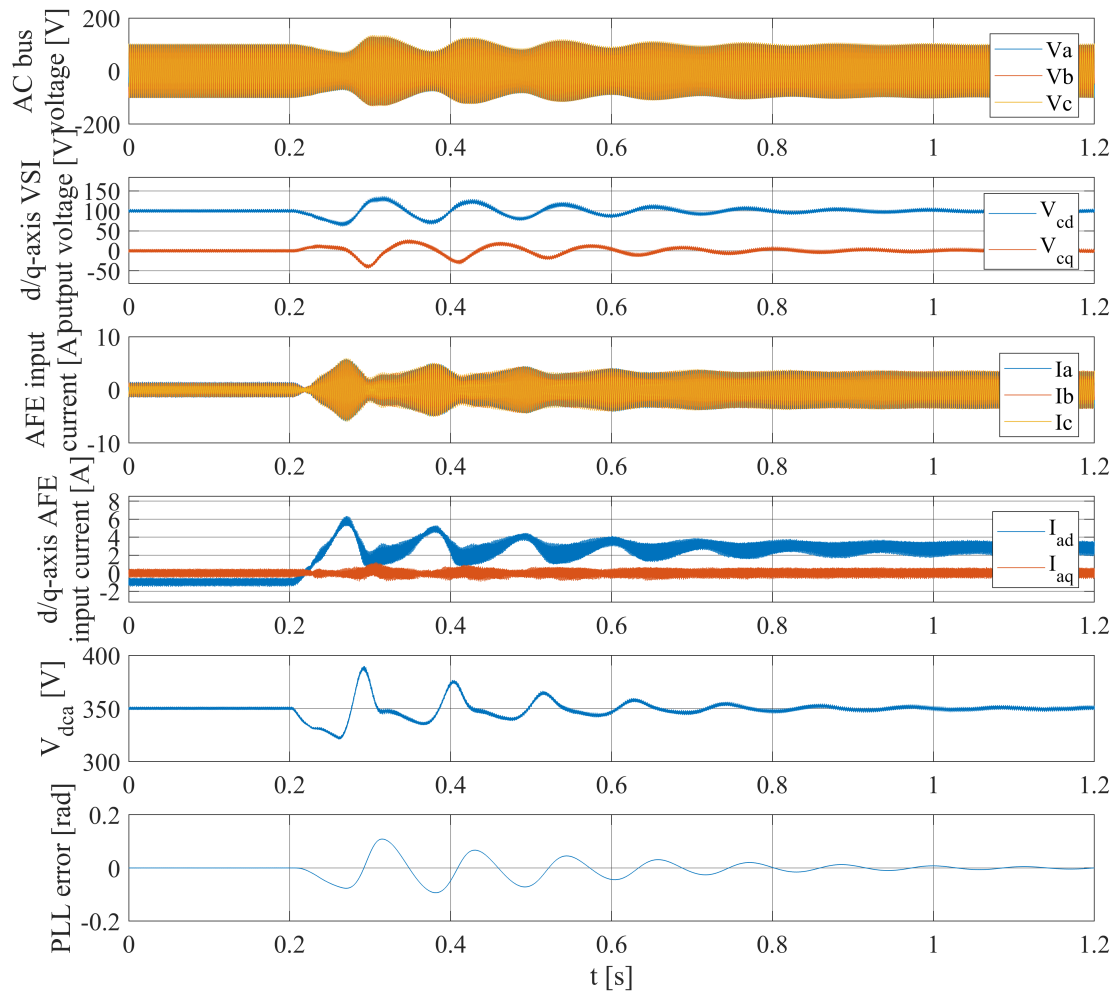
Figure 7.24: Dynamic response waveforms of the VSI-AFE system under 0.6kW CPL loading when AFE adopts the traditional PI controller in case 2

Comparison of AFE DC-link voltage undershoot in the transient when AFE uses the PI controller or optimal H_2 controller in this case is presented in Fig.7.25.
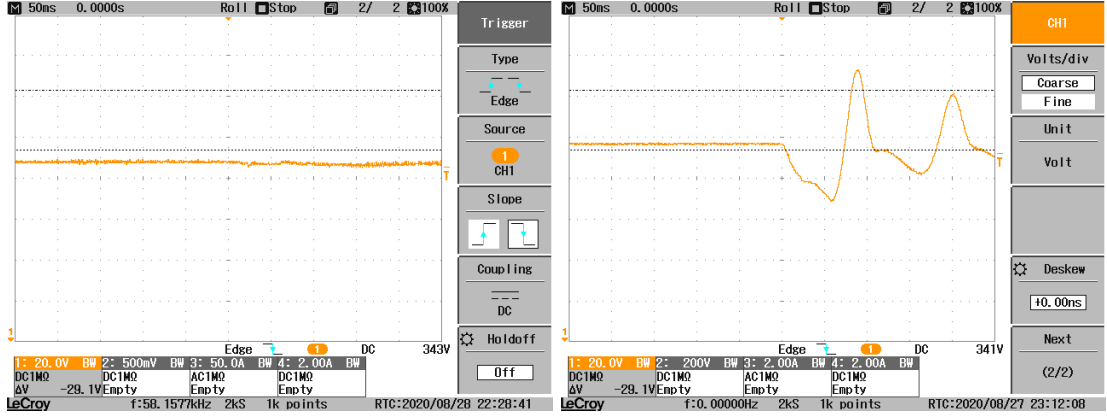
(a) H_2 (b) PI

Figure 7.25: DC-link voltage of AFE (a) optimal H_2 controller tuned with identified model of VSI (b) PI controller

In a conclusion, the optimal H_2 controller could still handle the load change well while the traditional PI controller could not in the second case. In the meantime, characteristic loci derived from impedance ratio matrix of the two subsystems show that the loci of optimal H_2 controller are further from the critical point $(-1, 0i)$ indicating a larger stability margin. The loci of PI case are too close to $(-1, 0i)$ and it is not sufficient to maintain stability under network disturbances. In all, optimal H_2 controllers considering identified grid feature are much better than PI controllers in mitigating subsystem interactions and extending stability margin of the whole grid.

Optimal H_2 control with nominal model of VSI

Similarly in this case, an optimal H_2 controller is tuned by replacing the identified model of VSI with its nominal model. The controller gains are shown below.

$$K_{AFE} = \begin{bmatrix} -0.0138 & -0.0246 & 0.0074 & 0.0903 & -4.1971 \\ 0.0404 & 0.0420 & 0.0090 & -0.1199 & -4.4944 \end{bmatrix} \tag{7.8}$$

$$k_p^p = 0.1771; k_i^p = 1.4848; \tag{7.9}$$

Characteristic loci and time-domain waveforms collected in experiments are shown below. It can be seen that the results are very similar to the case when AFE uses optimal H_2 controller tuned with identified model. The reliability of identification process is confirmed again.
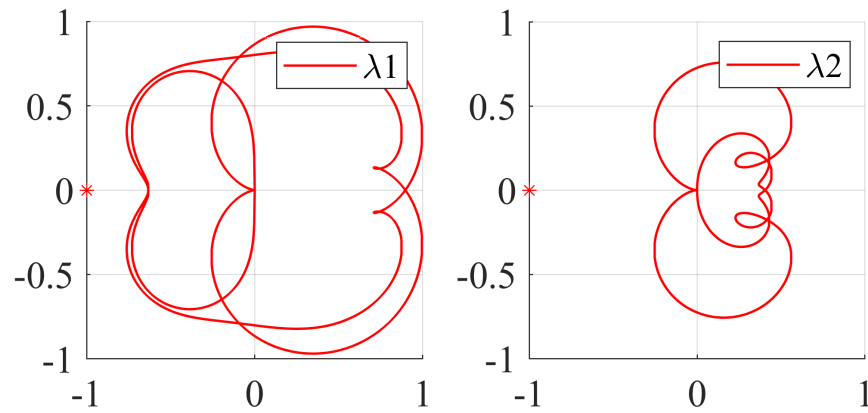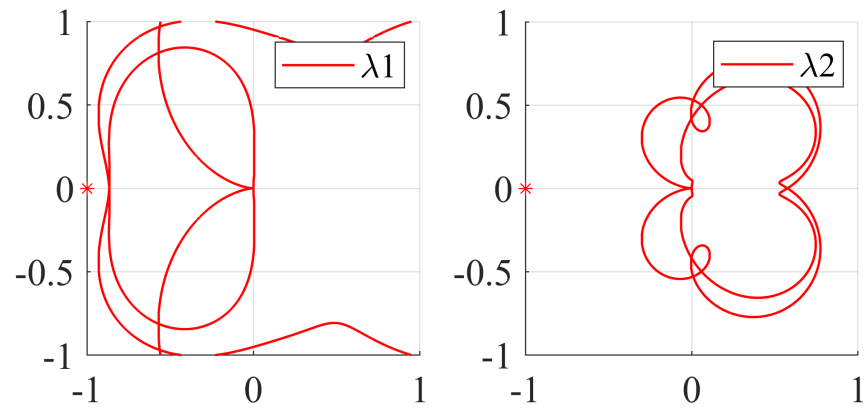
Figure 7.26: Characteristic loci of the VSI-AFE system when AFE uses the optimal H_2 controller based on nominal model of VSI in case 2
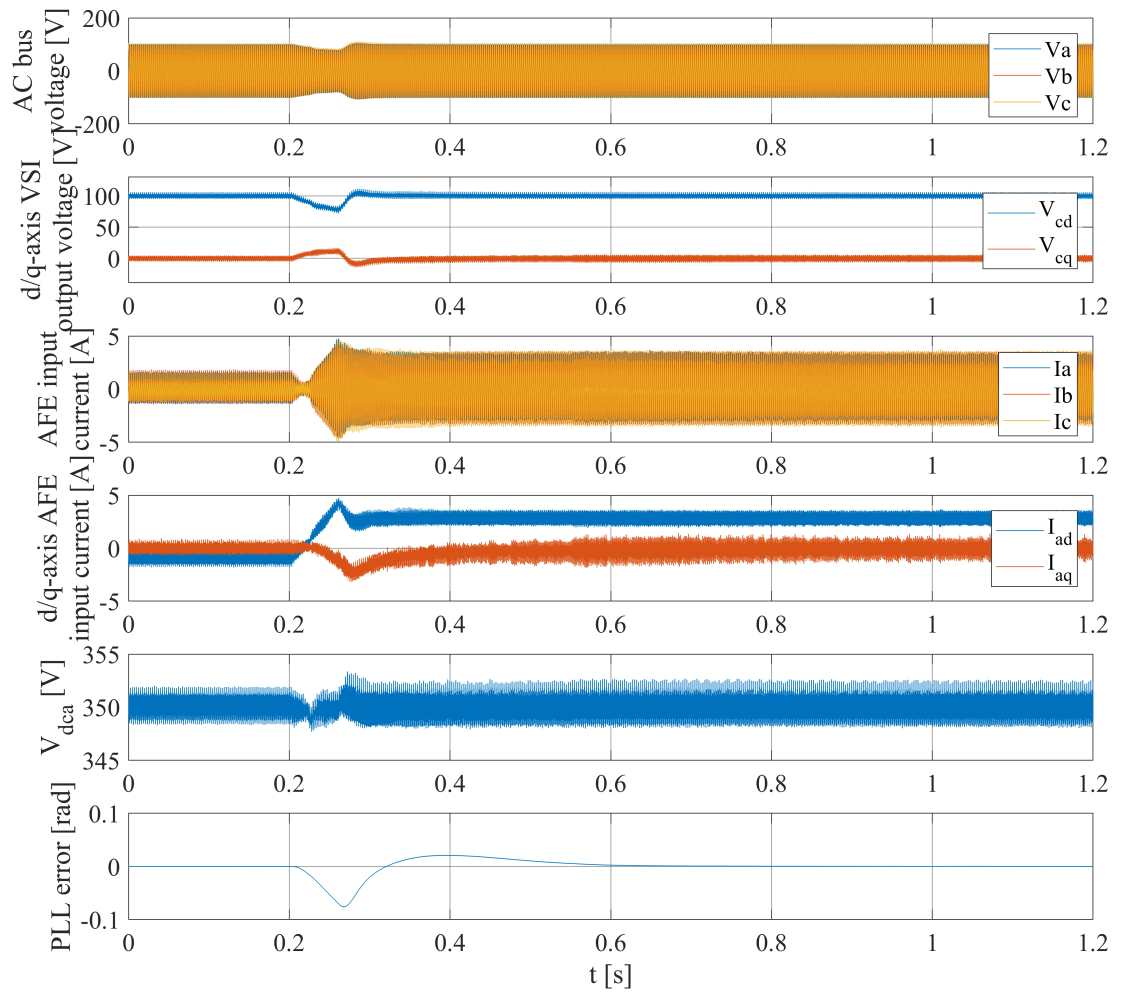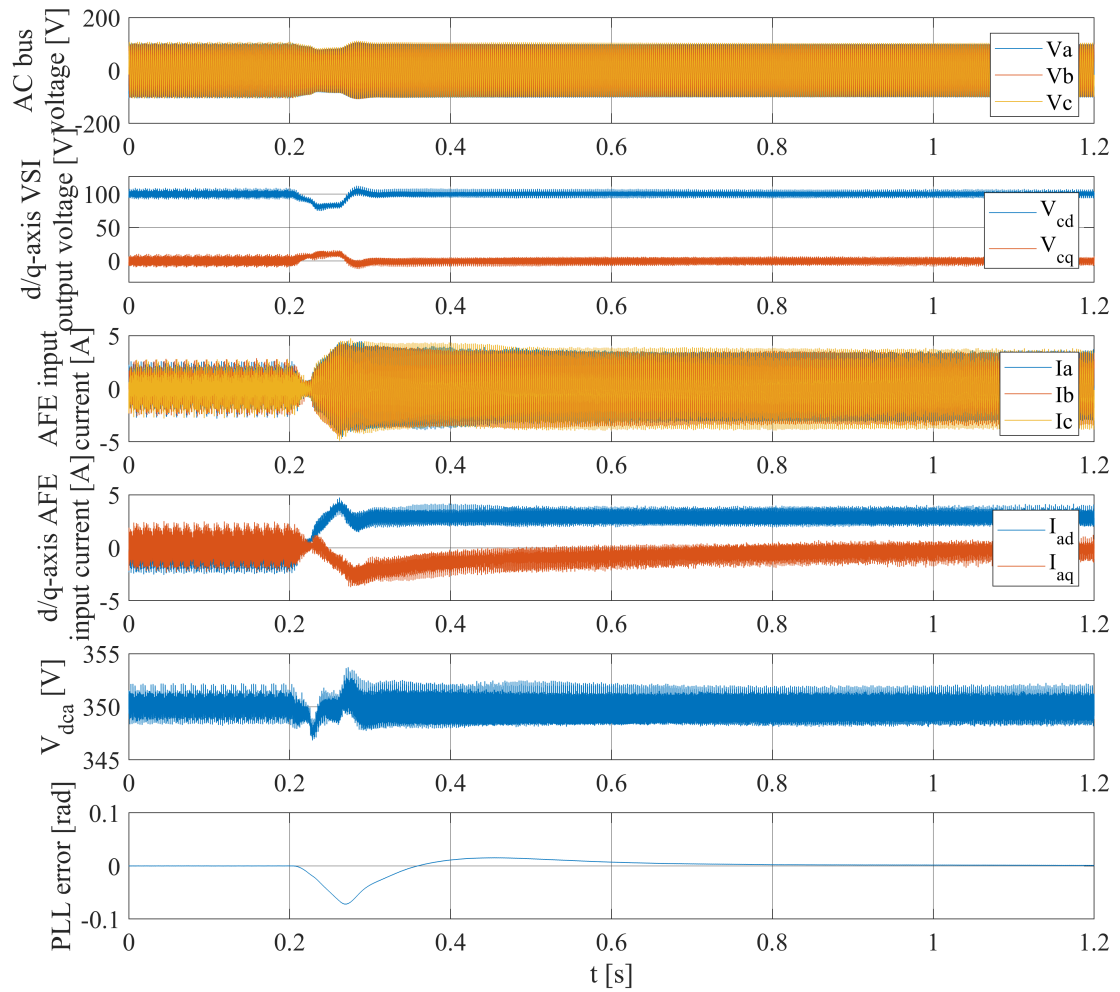
Figure 7.27: Dynamic response waveforms of the VSI-AFE system under 0.6kW CPL loading when AFE adopts the optimal H_2 controller tuned with nominal model of VSI in case 2

7.1.3   Order of VSI's identified model and system stability

In the above two cases, order of the VSI's identified model used for AFE controller tuning is 8. It is worth to investigate how low the order of identified model can reach when it can be successfully used in AFE's controller synthesize. Therefore, based on the same identification data collected in the first case, we try to reduce the order when estimating a desired model for VSI through the PEM algorithm. Three different numbers i.e. 4, 5 and 6 have been tried sequentially. Bode diagrams of these identified models together with the one obtained in first case which has a order of 8, are presented in Fig.7.28.
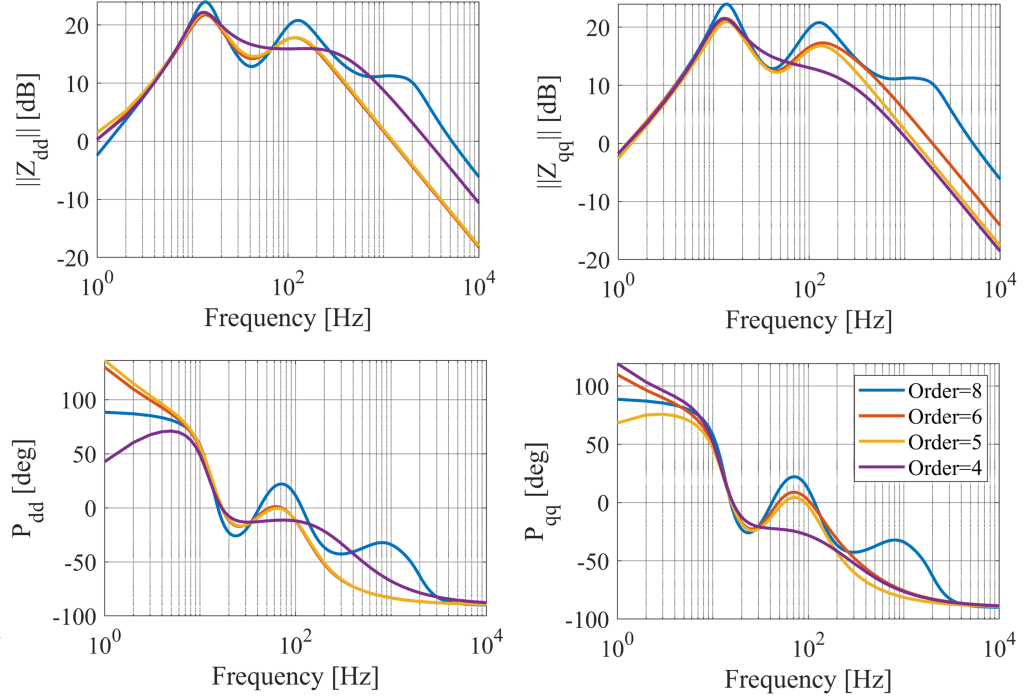
Figure 7.28: Bode diagram comparison of VSI's identified model of different orders

Then the 5th order identified model of VSI is tried to tune an optimal H_2 controller for AFE. The weighting matrices Q and R used and the controller gains obtained are presented below. The Q and R matrices here are different from those in previous cases because the previous choices of Q and R could not work out a stable controller when tuning with the 5th order identified model.

$$Q = diag(zeros(1,5), 0, 0, 0, 1, 1, 0, 2)$$
$$R = diag(5, 5, 0.2, 0.2)$$
(7.10)

$$K_{AFE} = \begin{bmatrix} 0.0120 & -0.0080 & 0.0146 & 0.2093 & -15.8348 \\ 0.0212 & 0.0311 & -0.0045 & -0.3618 & 1.3824 \end{bmatrix}$$
(7.11)

$$k_p^p = 1.1771; k_i^p = 9.4848;$$
(7.12)

Characteristic loci and time-domain performance of the VSI-AFE system when AFE uses the synthesized controller are shown below.
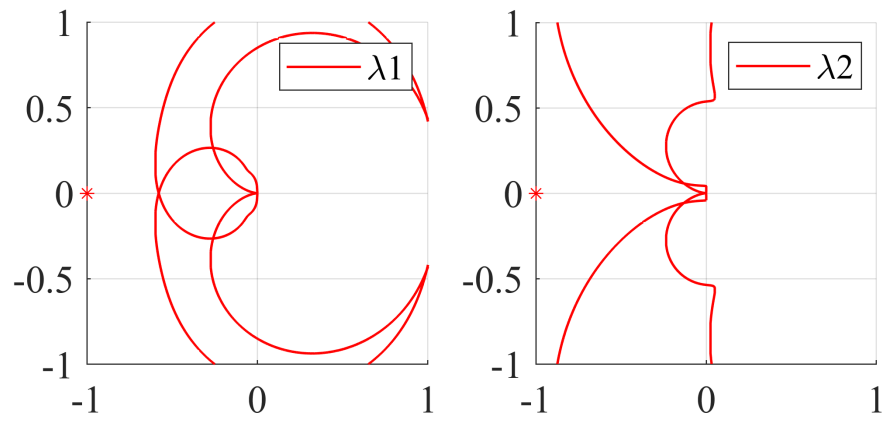
Figure 7.29: Characteristic loci of the VSI-AFE system when AFE's optimal H_2 controller is tuned with 5th order identified model of VSI
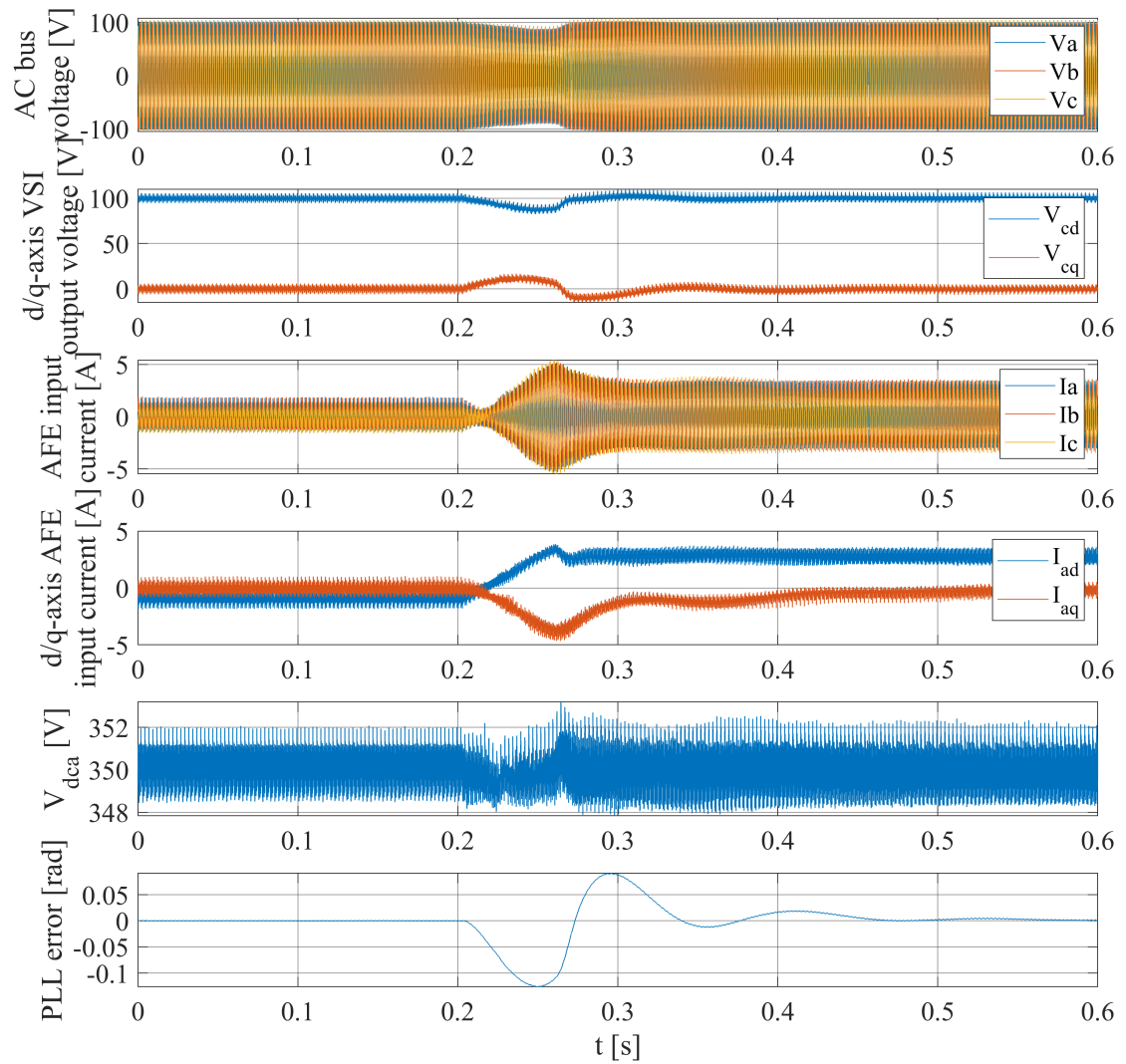
Figure 7.30: Dynamic response waveforms of the VSI-AFE system when AFE's optimal H_2 controller is tuned with 5th order identified model of VSI

As can be seen, there is no huge difference between waveforms when the optimal H_2 controllers are tuned with a 8th order or 5th order identified model of VSI. The lowest order of identified models that could be used for optimal control tuning is 5 according to experimental tests. Therefore the proposed control design method does not require a complex high order identification. A reasonably low order identification is enough to tune a capable H_2 controller.

7.2 The impact of VSI filter capacitor C

In this section, the relationship between VSI's filter capacitor C and its out impedance is investigated. The VSI impedance is identified when C of different values (there are 4 sets of capacitors here, i.e. $16\mu F$, $20\mu F$, $25\mu F$, $33\mu F$) is adopted in the LC filter. The identified d-d axis impedance of VSI obtained in the experiments in these 4 cases is plotted in a bode diagram as shown in Fig.7.31. Notably, the VSI's PI controller is fixed with parameters shown in the Table.7.1 in the comparisons.
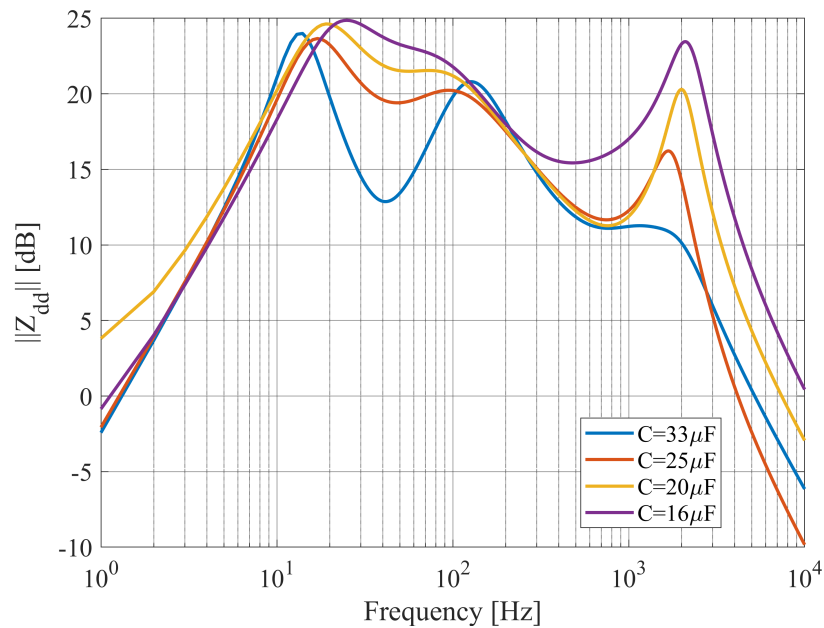
Figure 7.31: Bode diagram comparison of VSI's identified model when C is of different values

It is clear that the change of impedance shape is consistent with Fig.5.1, namely as the C decreases, the VSI's d-d axis impedance magnitude increases in the frequency range from 20 Hz to 100 Hz which means a bigger challenge for the control design of AFE.

In this section, a PI controller and an optimal H_2 controller tuned with identified model of VSI are synthesized for AFE when C is $20\mu F$. Time-domain performance of the VSI-AFE system in a transient when the AFE uses the PI controller and optimal H_2 controller are compared.

Even though great effort is made and different value is tried for f_i and f_v, it is impossible to find a PI controller can make the system stable. The gains of the PI controller in the comparison experiment are shown in Table.7.5.

The corresponding characteristic loci are shown below

Table 7.5: Parameters of the PI controllers

	Voltage loop	Current loop
AFE	0.050+6.316/s	-5.681-14780.719/s
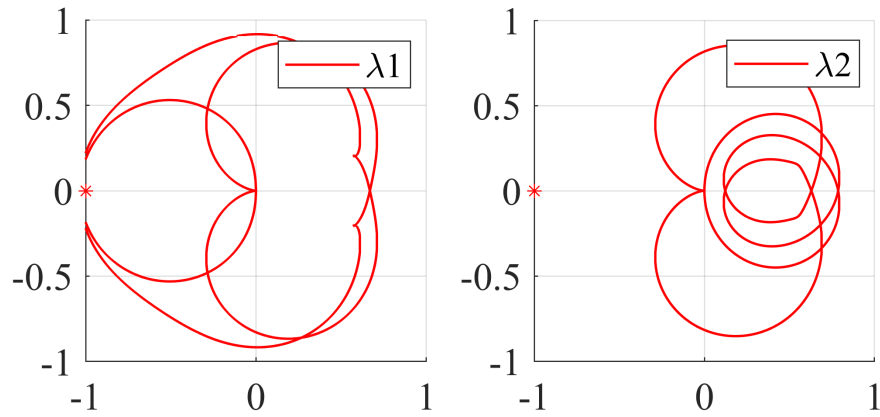
Figure 7.32: Characteristic loci of the impedance ratio between VSI and AFE when the AFE uses the PI controller and $C = 20\mu F$

As the characteristic loci encircled the critical point $(-1, 0i)$, the VSI-AFE system is unstable. Time-domain waveforms obtained in the load ramping test are
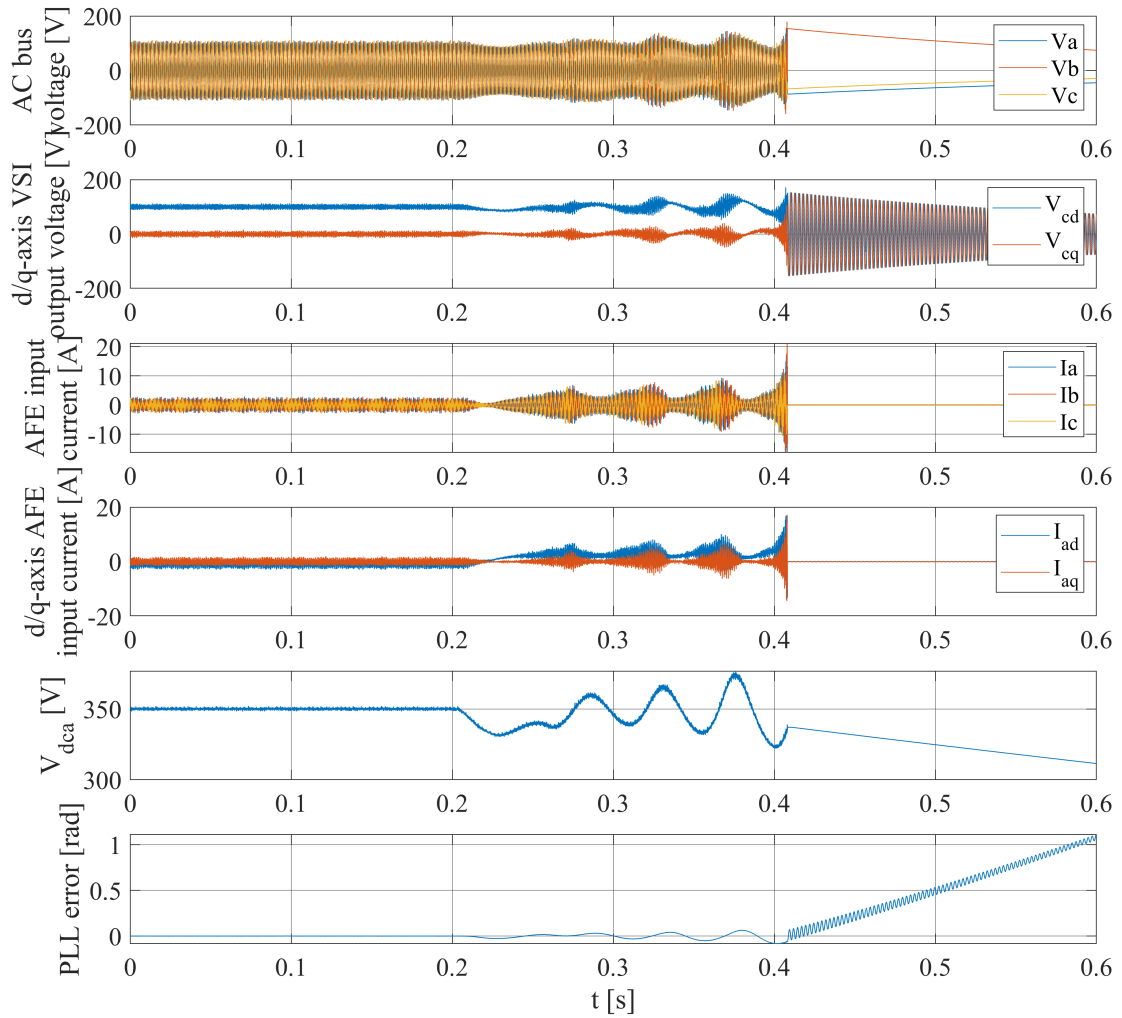
Figure 7.33: Dynamic response waveforms of the VSI-AFE system when the AFE uses the PI controller and C is $20\mu F$

Then an optimal H_2 controller is tuned with an identified model of the VSI. The gains of the controllers are

$$K_{AFE} = \begin{bmatrix} 0.029876 & 0.006151 & 0.016407 & 0.022116 & -8.976016 \\ 0.024451 & 0.025214 & -0.006036 & -0.628428 & 2.460846 \end{bmatrix} \quad (7.13)$$

Characteristic loci and time-domain performance of the VSI-AFE system when AFE uses this controller are shown below.
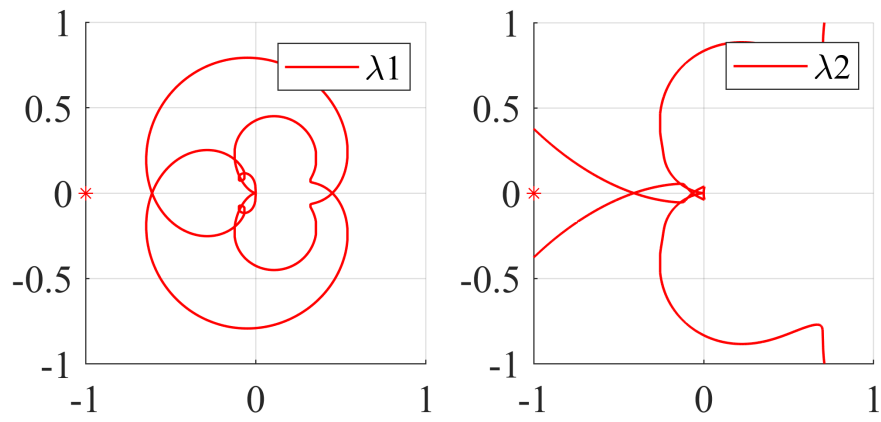
Figure 7.34: Characteristic loci of the VSI-AFE system when the AFE is tuned with identified model of VSI and C is $20\mu F$
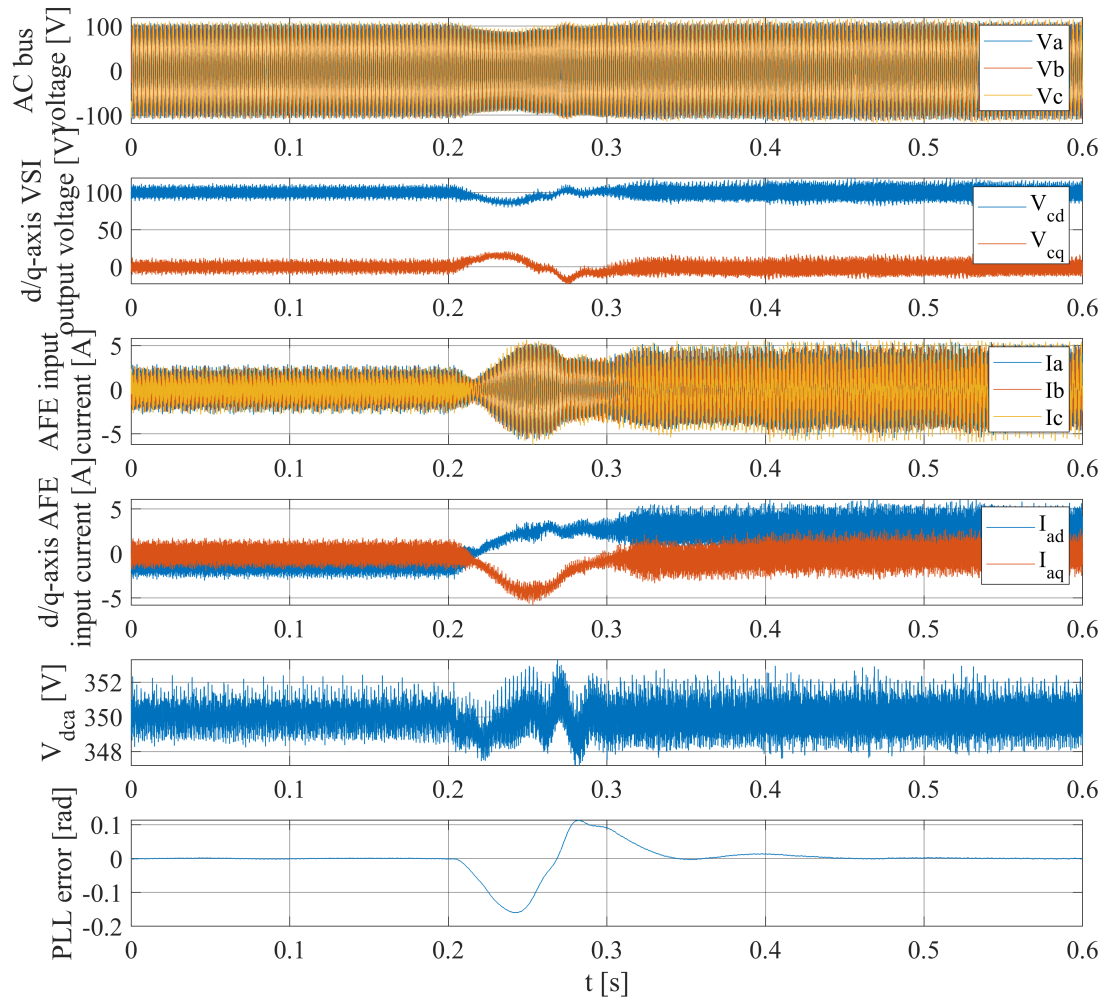
Figure 7.35: Dynamic response waveforms of the VSI-AFE system when the AFE is tuned with identified model of VSI and $C = 20\mu F$

Two conclusions can be reached by the above comparisons. At first, as the C decreases, the PI control design of AFE will be more and more difficult. However, it is not a big challenge for the optimal H_2 control design method. Secondly, for a specific C, the VSI-AFE system exhibits a far more better dynamic performance when the AFE uses an optimal H_2 controller compared to a PI controller, even if the PI controller is already tuned elaborately.

7.3   Impact of AFE CPL power on system stability

In this section, relationship between AFE's CPL power and VSI-AFE system stability is experimentally examined. In the experiment, the AFE's CPL steps up from $P = 0W$ to $P = 800W$,

with each step of $200W$. And waveforms of main variables of the VSI-AFE system are shown in Fig.7.36.
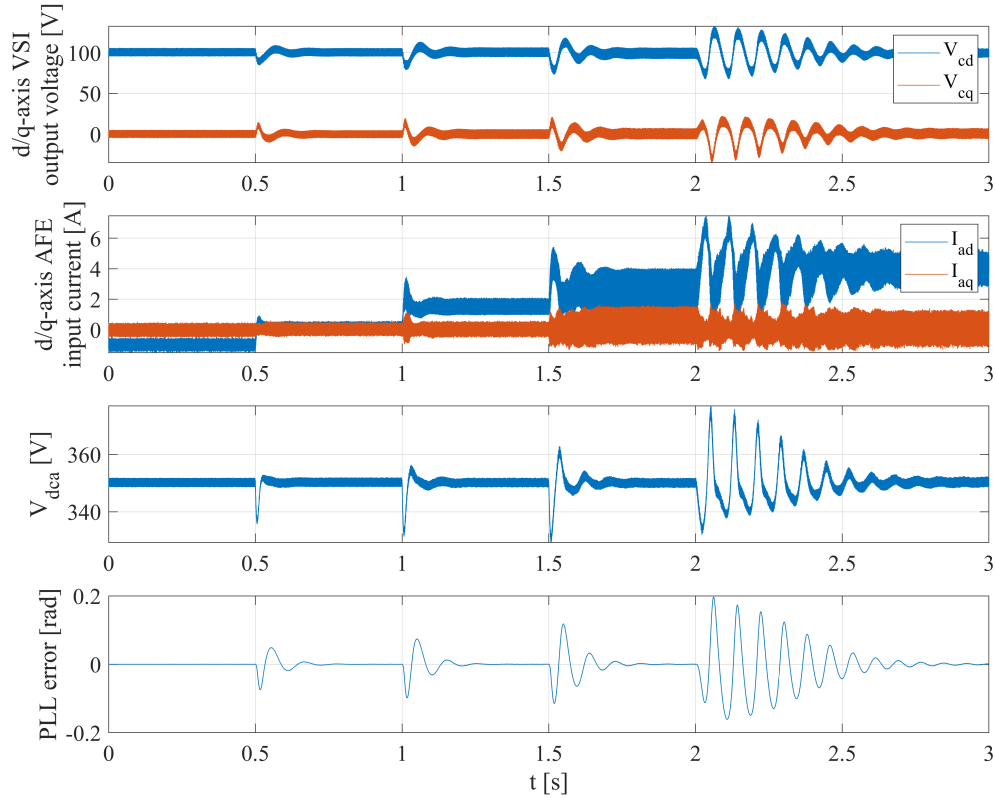
Figure 7.36: VSI-AFE system time-domain performance when increasing the power of AFE's CPL

As can be seen, the system starts with no load during the first 0.5s and the load steps up $200W$ every 0.5s. Transient oscillations caused by the power growth is bigger and bigger. When the power reaches $800W$, the system is critical stable. This is consistent with the conclusions reached in Sec.5.3 i.e. a bigger power of AFE's CPL will cause more risk of instability. The AFE uses a PI controller in this test.

In this chapter, the optimal H_2 control design method is experimentally compared with the tradition PI control method. Optimal H_2 controllers are tuned with the identified models of VSI under different grid conditions. And its advantages in terms of dynamic performance and stability margin over PI controllers are proved. Meanwhile, the impact of VSI's filter capacitor C and AFE's CPL power on the converter impedance and VSI-AFE system stability is also experimentally verified. Robustness of the proposed optimal H_2 control design method in these conditions is verified.

7.4   Conclusion

To verify the effectiveness of proposed control design method, a series of experiments were conducted and the results are presented in this chapter. The optimal H_2 control design method was firstly applied to an AFE. VSIs of high and low bandwidths were identified based on the methodology described in Chapter 6. Then the identified models of VSI were successfully used in the optimal H_2 tuning of AFE. Some experiments were also conducted to explore the lowest order when identifying VSI that could estimate a model to synthesize a stable controller for the AFE. In addition, the VSI LC filter capacitor C and power of CPL on AFE were changed in experiments to verify the analysis in Chapter 5. In all, the experiments included in this chapter has strongly demonstrate the effectiveness and advantages of the proposed control design method.

Chapter 8

Conclusion

Prior to this research, control design of power converters in AC grids was commonly implemented locally, with little and no consideration about dynamic characteristics of the grid. It usually leads to a conservative solution or even failure in weak grid conditions. This work proposed an optimal control design method for grid-connected active front-ends (AFEs), which could mitigate the AC bus interactions and optimize the dynamic performance of AFE while ensuring the system stability.

The approach employs impedance identification techniques to estimate a state space model of the grid. Then the identified model is combined with open loop model of the to be designed AFE, to build a global model of the grid-AFE system. In this way dynamic interactions between the grid and AFE are intrinsically kept in consideration in the control design.

Then a structured H_2 optimization algorithm is used to close the control loop by synthesizing a state feedback controller (denoted as 'optimal H_2 controller' in this thesis) for the AFE based on the global model. The structured H_2 algorithm could specify the structure of control gains matrix, hence the operation of AFE with the synthesized controller does not depend on measurement of inner states of the grid. The reference tracking and anti-interference capabilities are also guaranteed in the optimization process.

The proposed control design method is verified by a notional system which is comprised of a voltage source inverter (VSI) and an active front end (AFE). The AFE operates synchronously with the VSI through a phased locked loop (PLL) and feeds a constant power load. The impedance modelling of the two converters including PLL is discussed. The impact of PLL on the shape of AFE's admittance is analysed. Based on the derived impedance models and the impedance-based stability criterion, stability of the VSI-AFE system is assessed in different case studies.

Effectiveness and advantages of the optimal H_2 controllers are validated by simulations and experiments, in which the VSI is adopted to emulate the AC grid and supply power to the AFE.

Performance of the VSI-AFE system when the AFE adopts optimal H_2 controllers or traditional PI controllers are compared. The results clearly show the case relating to optimal H_2 controllers exhibits faster dynamic response and a far more stiff DC-link of the AFE.

Although the method is experimentally verified by a relatively simple prototype, its performance in multi-converter application is confirmed by simulations, which also demonstrates the superiority of proposed control design method. The proposed control design approach would offer a helpful tool for the design and integration of power converters in system assembling. In this research, for the proof of concept, the PI control method is here used to make a contrast with the proposed control design method, which is not the most sophisticated control algorithm. In the future, more advanced control design method such as MPC (model predictive control) and model reference control would be introduced to compare and examine whether the proposed control design method still exhibits some advantages in ensuring the system stability and good dynamic performance. In addition, the effectiveness of proposed control design in multi-converter applications is only confirmed by simulations, the corresponding results are worth to investigate after the hardware for building the complex system is available. In addition, it is also worth to explore the possibility of adapting the proposed method for online converter control design based on real-time grid impedance identification.

A limit in applications of the proposed control design method is the grid needs to be re-identified and optimal controller be re-tuned when the grid condition changes, especially for a weak grid. The re-identification and re-tune are necessary to ensure the optimal performance and system stability. But it is sure that the optimal H_2 controllers outperform the PI controllers regarding to the robustness against grid variation. Another concern in applications is that the proposed control design method depends on a numerical optimization process to synthesize controllers. The numerical optimization algorithm sometimes works out incapable solutions. Therefore, manual intervention to exclude those solutions is indispensable at the current stage.

Bibliography

[1] P. Wheeler, "Technology for the more and all electric aircraft of the future," in *2016 IEEE International Conference on Automatica (ICA-ACCA)*, IEEE, oct 2016.

[2] B. Rahrovi and M. Ehsani, "A review of the more electric aircraft power electronics," in *2019 IEEE Texas Power and Energy Conference (TPEC)*, IEEE, feb 2019.

[3] "Mil-std-704f, department of defense interface standard: Aircraft electric power characteristics."

[4] L. J. Petersen, "Next generation integrated power system: The backbone of the electric warship(hybrid electric drive: A near term opportunity)," in *2009 IEEE International Electric Machines and Drives Conference*, IEEE, may 2009.

[5] G. Sulligoi, A. Vicenzutti, and R. Menis, "All-electric ship design: From electrical propulsion to integrated electrical and electronic power systems," *IEEE Transactions on Transportation Electrification*, vol. 2, pp. 507–521, dec 2016.

[6] A. Azmy and I. Erlich, "Impact of distributed generation on the stability of electrical power systems," in *IEEE Power Engineering Society General Meeting, 2005*, IEEE, 2005.

[7] N. Hatziargyriou, H. Asano, R. Iravani, and C. Marnay, "Microgrids," *IEEE Power and Energy Magazine*, vol. 5, pp. 78–94, jul 2007.

[8] A. Ipakchi and F. Albuyeh, "Grid of the future," *IEEE Power and Energy Magazine*, vol. 7, pp. 52–62, mar 2009.

[9] G. Buticchi, S. Bozhko, M. Liserre, P. Wheeler, and K. Al-Haddad, "On-board microgrids for the more electric aircraft—technology review," *IEEE Transactions on Industrial Electronics*, vol. 66, pp. 5588–5599, jul 2019.

[10] Z. Bing, K. Karimi, and J. Sun, "Input impedance modeling and analysis of line-commutated rectifiers," *IEEE Transactions on Power Electronics*, vol. 24, pp. 2338–2346, oct 2009.

[11] J. Sun, "Impedance-based stability criterion for grid-connected inverters," *IEEE Transactions on Power Electronics*, vol. 26, pp. 3075–3078, nov 2011.

[12] M. Liserre, R. Teodorescu, and F. Blaabjerg, "Stability of photovoltaic and wind turbine grid-connected inverters for a large set of grid impedance values," *IEEE Transactions on Power Electronics*, vol. 21, pp. 263–272, jan 2006.

[13] B. Wen, D. Boroyevich, R. Burgos, P. Mattavelli, and Z. Shen, "Analysis of d-q small-signal impedance of grid-tied inverters," *IEEE Transactions on Power Electronics*, vol. 31, pp. 675–687, jan 2016.

[14] B. Wen, D. Boroyevich, R. Burgos, P. Mattavelli, and Z. Shen, "Small-signal stability analysis of three-phase AC systems in the presence of constant power loads based on measured d-q frame impedances," *IEEE Transactions on Power Electronics*, vol. 30, pp. 5952–5963, oct 2015.

[15] B. Wen, D. Boroyevich, R. Burgos, P. Mattavelli, and Z. Shen, "D-q impedance specification for balanced three-phase AC distributed power system," in *2015 IEEE Applied Power Electronics Conference and Exposition (APEC)*, IEEE, mar 2015.

[16] B. Wen, D. Boroyevich, R. Burgos, P. Mattavelli, and Z. Shen, "Inverse nyquist stability criterion for grid-tied inverters," *IEEE Transactions on Power Electronics*, vol. 32, pp. 1548–1556, feb 2017.

[17] M. Cespedes and J. Sun, "Renewable energy systems instability involving grid-parallel inverters," in *2009 Twenty-Fourth Annual IEEE Applied Power Electronics Conference and Exposition*, IEEE, feb 2009.

[18] J. Xie, Y. X. Feng, and N. Krap, "Network impedance measurements for three-phase high-voltage power systems," in *2010 Asia-Pacific Power and Energy Engineering Conference*, IEEE, 2010.

[19] A. A. A. Radwan and Y. A.-R. I. Mohamed, "Modeling, analysis, and stabilization of converter-fed AC microgrids with high penetration of converter-interfaced loads," *IEEE Transactions on Smart Grid*, vol. 3, pp. 1213–1225, sep 2012.

[20] K. M. Alawasa, Y. A.-R. I. Mohamed, and W. Xu, "Active mitigation of subsynchronous interactions between PWM voltage-source converters and power networks," *IEEE Transactions on Power Electronics*, vol. 29, pp. 121–134, jan 2014.

[21] W. Li, X. Ruan, D. Pan, and X. Wang, "Full-feedforward schemes of grid voltages for a three-phase lcl-type grid-connected inverter," *IEEE Transactions on Industrial Electronics*, vol. 60, pp. 2237–2250, jun 2013.

[22] M. Cespedes and J. Sun, "Impedance shaping of three-phase grid-parallel voltage-source converters," in *2012 Twenty-Seventh Annual IEEE Applied Power Electronics Conference and Exposition (APEC)*, IEEE, feb 2012.

[23] R. D. Middlebrook, "Input filter considerations in design and application of switching regulators," in *Computer Science*, 1976.

[24] J. Fang, X. Li, H. Li, and Y. Tang, "Stability improvement for three-phase grid-connected converters through impedance reshaping in quadrature-axis," *IEEE Transactions on Power Electronics*, vol. 33, pp. 8365–8375, oct 2018.

[25] R. Luhtala, T. Messo, T. Reinikka, J. Sihvo, T. Roinila, and M. Vilkko, "Adaptive control of grid-connected inverters based on real-time measurements of grid impedance: DQ-domain approach," in *2017 IEEE Energy Conversion Congress and Exposition (ECCE)*, IEEE, oct 2017.

[26] K. Areerak, S. V. Bozhko, G. M. Asher, L. D. Lillo, and D. W. P. Thomas, "Stability study for a hybrid ac-dc more-electric aircraft power system," *IEEE Transactions on Aerospace and Electronic Systems*, vol. 48, pp. 329–347, jan 2012.

[27] K.-N. Areerak, T. Wu, S. V. Bozhko, G. M. Asher, and D. W. P. Thomas, "Aircraft power system stability study including effect of voltage control and actuators dynamic," *IEEE Transactions on Aerospace and Electronic Systems*, vol. 47, no. 4, pp. 2574–2589, 2011.

[28] N. Bottrell, M. Prodanovic, and T. C. Green, "Dynamic stability of a microgrid with an active load," *IEEE Transactions on Power Electronics*, vol. 28, pp. 5107–5119, nov 2013.

[29] Q. Li, A. Formentini, A. Baraston, X. Zhang, P. Zanchetta, J. L. Schanen, and D. Boroyevich, "Taking into account interactions between converters in the design of aircraft power networks," in *2016 IEEE Energy Conversion Congress and Exposition (ECCE)*, IEEE, sep 2016.

[30] A. Emadi, "Modeling and analysis of multiconverter DC power electronic systems using the generalized state-space averaging method," *IEEE Transactions on Industrial Electronics*, vol. 51, pp. 661–668, jun 2004.

[31] A. Girgis and R. McManis, "Frequency domain techniques for modeling distribution or transmission networks using capacitor switching induced transients," *IEEE Transactions on Power Delivery*, vol. 4, pp. 1882–1890, jul 1989.

[32] F. Freijedo, J. Doval-Gandoy, O. Lopez, P. Fernandez-Comesana, and C. Martinez-Penalver, "A signal-processing adaptive algorithm for selective current harmonic cancellation in active power filters," *IEEE Transactions on Industrial Electronics*, vol. 56, pp. 2829–2840, aug 2009.

[33] L. Asiminoaei, R. Teodorescu, F. Blaabjerg, and U. Borup, "A new method of on-line grid impedance estimation for pv inverter," in *Nineteenth Annual IEEE Applied Power Electronics Conference and Exposition, 2004. APEC '04.*, IEEE, 2004.

[34] F. Alonge, F. DIppolito, and T. Cangemi, "Identification and robust control of dc dc converter hammerstein model," *IEEE Transactions on Power Electronics*, vol. 23, pp. 2990–3003, nov 2008.

[35] B. Miao, R. Zane, and D. Maksimovic, "System identification of power converters with digital control through cross-correlation methods," *IEEE Transactions on Power Electronics*, vol. 20, pp. 1093–1099, sep 2005.

[36] A. Barkley and E. Santi, "Online monitoring of network impedances using digital network analyzer techniques," in *2009 Twenty-Fourth Annual IEEE Applied Power Electronics Conference and Exposition*, IEEE, feb 2009.

[37] D. Martin, E. Santi, and A. Barkley, "Wide bandwidth system identification of AC system impedances by applying pertubations to an existing converter," in *2011 IEEE Energy Conversion Congress and Exposition*, IEEE, sep 2011.

[38] D. Martin, I. Nam, J. Siegers, and E. Santi, "Wide bandwidth three-phase impedance identification using existing power electronics inverter," in *2013 Twenty-Eighth Annual IEEE Applied Power Electronics Conference and Exposition (APEC)*, IEEE, mar 2013.

[39] A. Riccobono, S. K. A. Naqvi, A. Monti, T. Caldognetto, J. Siegers, and E. Santi, "Online wideband identification of single-phase AC power grid impedances using an existing grid-tied power electronic inverter," in *2015 IEEE 6th International Symposium on Power Electronics for Distributed Generation Systems (PEDG)*, IEEE, jun 2015.

[40] A. Riccobono, E. Liegmann, A. Monti, F. C. Dezza, J. Siegers, and E. Santi, "Online wideband identification of three-phase AC power grid impedances using an existing grid-tied power electronic inverter," in *2016 IEEE 17th Workshop on Control and Modeling for Power Electronics (COMPEL)*, IEEE, jun 2016.

[41] A. Riccobono, E. Liegmann, M. Pau, F. Ponci, and A. Monti, "Online parametric identification of power impedances to improve stability and accuracy of power hardware-in-the-loop simulations," *IEEE Transactions on Instrumentation and Measurement*, vol. 66, pp. 2247–2257, sep 2017.

[42] T. Roinila, T. Messo, and A. Aapro, "Impedance measurement of three phase systems in DQ-domain: Applying MIMO-identification techniques," in *2016 IEEE Energy Conversion Congress and Exposition (ECCE)*, IEEE, sep 2016.

[43] T. Roinila, M. Vilkko, and J. Sun, "Broadband methods for online grid impedance measurement," in *2013 IEEE Energy Conversion Congress and Exposition*, IEEE, sep 2013.

[44] J. Huang, K. A. Corzine, and M. Belkhayat, "Small-signal impedance measurement of power-electronics-based AC power systems using line-to-line current injection," *IEEE Transactions on Power Electronics*, vol. 24, pp. 445–455, feb 2009.

[45] M. Jaksic, Z. Shen, I. Cvetkovic, D. Boroyevich, R. Burgos, and P. Mattavelli, "Wide-bandwidth identification of small-signal dq impedances of ac power systems via single-phase series voltage injection," in *2015 17th European Conference on Power Electronics and Applications (EPE15 ECCE-Europe)*, IEEE, sep 2015.

[46] Z. Staroszczyk, "A method for real-time, wide-band identification of the source impedance in power systems," *IEEE Transactions on Instrumentation and Measurement*, vol. 54, pp. 377–385, feb 2005.

[47] R. Stiegler, J. Meyer, P. Schegner, and D. Chakravorty, "Measurement of network harmonic impedance in presence of electronic equipment," in *2015 IEEE International Workshop on Applied Measurements for Power Systems (AMPS)*, IEEE, sep 2015.

[48] L. Jessen and F. W. Fuchs, "Modeling of inverter output impedance for stability analysis in combination with measured grid impedances," in *2015 IEEE 6th International Symposium on Power Electronics for Distributed Generation Systems (PEDG)*, IEEE, jun 2015.

[49] L. Jessen, S. Gunter, F. W. Fuchs, M. Gottschalk, and H.-J. Hinrichs, "Measurement results and performance analysis of the grid impedance in different low voltage grids for a wide frequency band to support grid integration of renewables," in *2015 IEEE Energy Conversion Congress and Exposition (ECCE)*, IEEE, sep 2015.

[50] T. T. Do, M. Jordan, H. Langkowski, and D. Schulz, "Novel grid impedance measurement setups in electrical power systems," in *2016 IEEE International Workshop on Applied Measurements for Power Systems (AMPS)*, IEEE, sep 2016.

[51] M. Sumner, B. Palethorpe, D. Thomas, P. Zanchetta, and M. D. Piazza, "A technique for power supply harmonic impedance estimation using a controlled voltage disturbance," *IEEE Transactions on Power Electronics*, vol. 17, pp. 207–215, mar 2002.

[52] G. Francis, R. Burgos, D. Boroyevich, F. Wang, and K. Karimi, "An algorithm and implementation system for measuring impedance in the d-q domain," in *2011 IEEE Energy Conversion Congress and Exposition*, IEEE, sep 2011.

[53] M. Liserre, F. Blaabjerg, and R. Teodorescu, "Grid impedance estimation via excitation of lcl-filter resonance," *IEEE Transactions on Industry Applications*, vol. 43, no. 5, pp. 1401–1407, 2007.

[54] X. Sun, L. Wang, J. Chen, X. Li, and J. M. Guerrero, "Fundamental impedance identification method for grid-connected voltage source inverters," *IET Power Electronics*, vol. 7, pp. 1099–1105, may 2014.

[55] B. Cho and B. Choi, "Analysis and design of multi-stage distributed power systems," in *[Proceedings] Thirteenth International Telecommunications Energy Conference - INTELEC 91*, IEEE, 1991.

[56] K. J. Åström and B. Wittenmark, *Adaptive control.* Courier Corporation, 2013.

[57] S. Vesti, T. Suntio, J. A. Oliver, R. Prieto, and J. A. Cobos, "Impedance-based stability and transient-performance assessment applying maximum peak criteria," *IEEE Transactions on Power Electronics*, vol. 28, pp. 2099–2104, may 2013.

[58] M. Cespedes and J. Sun, "Adaptive control of grid-connected inverters based on online grid impedance measurements," *IEEE Transactions on Sustainable Energy*, vol. 5, pp. 516–523, apr 2014.

[59] B. Wen, D. Dong, D. Boroyevich, R. Burgos, P. Mattavelli, and Z. Shen, "Impedance-based analysis of grid-synchronization stability for three-phase paralleled converters," *IEEE Transactions on Power Electronics*, vol. 31, pp. 26–38, jan 2016.

[60] F. D. Freijedo, A. G. Yepes, Ó. López, A. Vidal, and J. Doval-Gandoy, "Three-phase PLLs with fast postfault retracking and steady-state rejection of voltage unbalance and harmonics by means of lead compensation," *IEEE Transactions on Power Electronics*, vol. 26, pp. 85–97, jan 2011.

[61] F. Blaabjerg, R. Teodorescu, M. Liserre, and A. Timbus, "Overview of control and grid synchronization for distributed power generation systems," *IEEE Transactions on Industrial Electronics*, vol. 53, pp. 1398–1409, oct 2006.

[62] W. Cao, Y. Ma, L. Yang, F. Wang, and L. M. Tolbert, "D–q impedance based stability analysis and parameter design of three-phase inverter-based AC power systems," *IEEE Transactions on Industrial Electronics*, vol. 64, pp. 6017–6028, jul 2017.

[63] A. G. J. MAcFARLANE and I. POSTLETHWAITE, "The generalized nyquist stability criterion and multivariable root loci," *International Journal of Control*, vol. 25, no. 1, pp. 81–127, 1977.

[64] X. Chen and J. Sun, "A study of renewable energy system harmonic resonance based on a DG test-bed," in *2011 Twenty-Sixth Annual IEEE Applied Power Electronics Conference and Exposition (APEC)*, IEEE, mar 2011.

[65] N. Hoffmann, F. W. Fuchs, and L. Asiminoaei, "Online grid-adaptive control and active-filter functionality of PWM-converters to mitigate voltage-unbalances and voltage-harmonics - a control concept based on grid-impedance measurement," in *2011 IEEE Energy Conversion Congress and Exposition*, IEEE, sep 2011.

[66] J. R. Massing, M. Stefanello, H. A. Grundling, and H. Pinheiro, "Adaptive current control for grid-connected converters with LCL filter," *IEEE Transactions on Industrial Electronics*, vol. 59, pp. 4681–4693, dec 2012.

[67] L. Asiminoaei, R. Teodorescu, F. Blaabjerg, and U. Borup, "A digital controlled PV-inverter with grid impedance estimation for ENS detection," *IEEE Transactions on Power Electronics*, vol. 20, pp. 1480–1490, nov 2005.

[68] M. Liserre, A. Pigazo, A. D. Aquila, and V. Moreno, "An anti-islanding method for single-phase inverters based on a grid voltage sensorless control," *IEEE Transactions on Industrial Electronics*, vol. 53, pp. 1418–1426, oct 2006.

[69] M. Sumner, A. Abusorrah, D. Thomas, and P. Zanchetta, "Real time parameter estimation for power quality control and intelligent protection of grid-connected power electronic converters," *IEEE Transactions on Smart Grid*, vol. 5, pp. 1602–1607, jul 2014.

[70] F. Wang, J. L. Duarte, M. A. M. Hendrix, and P. F. Ribeiro, "Modeling and analysis of grid harmonic distortion impact of aggregated DG inverters," *IEEE Transactions on Power Electronics*, vol. 26, pp. 786–797, mar 2011.

[71] Q. Dou, Z. Liu, J. Liu, and W. Bao, "A novel impedance measurement method for three-phase power electronic systems," in *2015 9th International Conference on Power Electronics and ECCE Asia (ICPE-ECCE Asia)*, IEEE, jun 2015.

[72] V. Valdivia, A. Lázaro, A. Barrado, P. Zumel, C. Fernández, and M. Sanz, "Impedance identification procedure of three-phase balanced voltage source inverters based on transient response measurements," *IEEE Transactions on Power Electronics*, vol. 26, pp. 3810–3816, dec 2011.

[73] N. Hoffmann and F. W. Fuchs, "Minimal invasive equivalent grid impedance estimation in inductive–resistive power networks using extended kalman filter," *IEEE Transactions on Power Electronics*, vol. 29, pp. 631–641, feb 2014.

[74] M. Nagpal, W. Xu, and J. Sawada, "Harmonic impedance measurement using three-phase transients," *IEEE Transactions on Power Delivery*, vol. 13, no. 1, pp. 272–277, 1998.

[75] Y. A. Familiant, J. Huang, K. A. Corzine, and M. Belkhayat, "New techniques for measuring impedance characteristics of three-phase AC power systems," *IEEE Transactions on Power Electronics*, vol. 24, pp. 1802–1810, jul 2009.

[76] P. Xiao, G. Venayagamoorthy, and K. Corzine, "A novel impedance measurement technique for power electronic systems," in *2007 IEEE Power Electronics Specialists Conference*, IEEE, 2007.

[77] Z. Staroszczyk and K. Mikolajuk, "Time-dependent power systems impedance-interpretation and measuring problems," in *IMTC/99. Proceedings of the 16th IEEE Instrumentation and Measurement Technology Conference (Cat. No.99CH36309)*, IEEE, 1999.

[78] P. E. Wellstead, "Non-parametric methods of system identification," *Automatica*, vol. 17, no. 1, pp. 55 – 69, 1981.

[79] A. Riccobono, M. Mirz, and A. Monti, "Noninvasive online parametric identification of three-phase AC power impedances to assess the stability of grid-tied power electronic inverters in LV networks," *IEEE Journal of Emerging and Selected Topics in Power Electronics*, vol. 6, pp. 629–647, jun 2018.

[80] M. Jordan, H. Langkowski, T. D. Thanh, and D. Schulz, "Frequency dependent grid-impedance determination with pulse-width-modulation-signals," in *2011 7th International Conference-Workshop Compatibility and Power Electronics (CPE)*, IEEE, jun 2011.

[81] M. Cespedes and J. Sun, "Online grid impedance identification for adaptive control of grid-connected inverters," in *2012 IEEE Energy Conversion Congress and Exposition (ECCE)*, IEEE, sep 2012.

[82] V. Braca and R. Petrella, "An improved method for grid impedance estimation by digital controlled PV inverters suitable for ENS detection," in *4th IET International Conference on Power Electronics, Machines and Drives (PEMD 2008)*, IEE, 2008.

[83] C. S. Burrus and T. Parks, *DFT/FFT and Convolution Algorithms - Theory and Implementation*. Wiley Interscience, 1985.

[84] K. Areerak, *Modelling and stability analysis of aircraft power systems*. PhD thesis, University of Nottingham, 2009.

[85] B. Wen, D. Boroyevich, R. Burgos, and P. Mattavelli, "Modeling the output impedance of three-phase uninterruptible power supply in d-q frame," in *2014 IEEE Energy Conversion Congress and Exposition (ECCE)*, IEEE, sep 2014.

[86] T. Roinila, T. Messo, T. Suntio, and M. Vilkko, "Pseudo-random sequences in dq-domain analysis of feedforward control in grid-connected inverters," *IFAC-PapersOnLine*, vol. 48, no. 28, pp. 1301 – 1306, 2015. 17th IFAC Symposium on System Identification SYSID 2015.

[87] T. Roinila, J. Huusari, and M. Vilkko, "On frequency-response measurements of power-electronic systems applying MIMO identification techniques," *IEEE Transactions on Industrial Electronics*, vol. 60, pp. 5270–5276, nov 2013.

[88] A. H. Tan, K. R. Godfrey, and H. A. Barker, "Identification of multi-input systems using simultaneous perturbation by pseudorandom input signals," *IET Control Theory & Applications*, vol. 9, pp. 2283–2292, oct 2015.

[89] T. Roinila, T. Messo, and E. Santi, "MIMO-identification techniques for rapid impedance-based stability assessment of three-phase systems in DQ domain," *IEEE Transactions on Power Electronics*, vol. 33, pp. 4015–4022, may 2018.

[90] A. Knop and F. W. Fuchs, "High frequency grid impedance analysis by current injection," in *2009 35th Annual Conference of IEEE Industrial Electronics*, IEEE, nov 2009.

[91] X. Yue, Z. Fang, F. Wang, Z. Zhang, and H. Shi, "A novel adaptive frequency injection method for power electronic system impedance measurement," *IEEE Transactions on Power Electronics*, vol. 29, pp. 6700–6711, dec 2014.

[92] J. Rhode, A. Kelley, and M. Baran, "Complete characterization of utilization-voltage power system impedance using wideband measurement," *IEEE Transactions on Industry Applications*, vol. 33, no. 6, pp. 1472–1479, 1997.

[93] J. van Rooijen and H. Vermeulen, "A perturbation source for in situ parameter estimation applications," in *Proceedings of IECON94 - 20th Annual Conference of IEEE Industrial Electronics*, IEEE, 1994.

[94] T. Roinila, M. Vilkko, and J. Sun, "Online grid impedance measurement using discrete-interval binary sequence injection," *IEEE Journal of Emerging and Selected Topics in Power Electronics*, vol. 2, pp. 985–993, dec 2014.

[95] T. REINIKKA, "Implementation of online impedance measurement setup for three phase grid-connected inverters," Master's thesis, Tampere university of technology, 2017.

[96] D. D. Rife and J. Vanderkooy, "Transfer-function measurement with maximum-length sequences," *J. Audio Eng. Soc*, vol. 37, no. 6, pp. 419–444, 1989.

[97] V. Thottuvelil and G. Verghese, "Simulation-based exploration of aliasing effects in PWM power converters," in *COMPEL.98. Record 6th Workshop on Computer in Power Electronics (Cat. No.98TH8358)*, IEEE.

[98] Wikipedia contributors, "Nyquist–shannon sampling theorem — Wikipedia, the free encyclopedia." `https://en.wikipedia.org/w/index.php?title=Nyquist%E2%80%93Shannon_sampling_theorem&oldid=954996359`, 2020. [Online; accessed 31-May-2020].

[99] W. contributors, "Spectral leakage — Wikipedia." `https://en.wikipedia.org/w/index.php?title=Spectral_leakage&oldid=926228869`, May 2019. Online; accessed 26-May-2020.

[100] R. P. . J. Schoukens, *System Identification: A Frequency Domain Approach*. Wiley-IEEE Press, 2001.

[101] K. Li, D. Dewar, A. Formentini, P. Zanchetta, and P. Wheeler, "Grid impedance identification and structured-h2 optimization based controller design of active front-end in embedded AC networks," in *2019 IEEE Energy Conversion Congress and Exposition (ECCE)*, IEEE, sep 2019.

[102] K. Li, D. Dewar, A. Formentini, P. Zanchetta, and P. Wheeler, "Optimized control design for power converters in power electronics embedded networks integrating grid model iden-

tification," in *2018 IEEE Industry Applications Society Annual Meeting (IAS)*, IEEE, sep 2018.

[103] B. Wen, *Stability analysis of three-phase AC power systems based on measured dq frame impedances*. PhD thesis, Virginia Polytechic Institute and State University, 2014.

[104] R. D. MIDDLEBROOK, "Measurement of loop gain in feedback systems," *International Journal of Electronics*, vol. 38, no. 4, pp. 485–512, 1975.

[105] M. Belkhayat, *stability criteria for ac power system with regulated loads*. PhD thesis, Purdue University, 1997.

[106] D. M. R. W. Erickson, *Fundamentals of Power Electronics,*. Kluwer Academic Publishers, 2001.

[107] M. Cespedes and J. Sun, "Impedance modeling and analysis of grid-connected voltage-source converters," *IEEE Transactions on Power Electronics*, vol. 29, pp. 1254–1261, mar 2014.

[108] M. Cespedes and J. Sun, "Three-phase impedance measurement for system stability analysis," in *2013 IEEE 14th Workshop on Control and Modeling for Power Electronics (COM-PEL)*, IEEE, jun 2013.

[109] J. Belletrutti and A. MacFarlane, "Characteristic loci techniques in multivariable-control-system design," *Proceedings of the Institution of Electrical Engineers*, vol. 118, no. 9, p. 1291, 1971.

[110] R. Burgos, D. Boroyevich, F. Wang, K. Karimi, and G. Francis, "On the ac stability of high power factor three-phase rectifiers," in *2010 IEEE Energy Conversion Congress and Exposition*, IEEE, sep 2010.

[111] B. Wen, R. Burgos, D. Boroyevich, P. Mattavelli, and Z. Shen, "Ac stability analysis and dq frame impedance specifications in power-electronics-based distributed power systems," *IEEE Journal of Emerging and Selected Topics in Power Electronics*, vol. 5, pp. 1455–1465, dec 2017.

[112] C. Wildrick, F. Lee, B. Cho, and B. Choi, "A method of defining the load impedance specification for a stable distributed power system," *IEEE Transactions on Power Electronics*, vol. 10, pp. 280–285, may 1995.

[113] S. Sudhoff, S. Glover, P. Lamm, D. Schmucker, and D. Delisle, "Admittance space stability analysis of power electronic systems," *IEEE Transactions on Aerospace and Electronic Systems*, vol. 36, no. 3, pp. 965–973, 2000.

[114] X. Feng, J. Liu, and F. Lee, "Impedance specifications for stable DC distributed power systems," *IEEE Transactions on Power Electronics*, vol. 17, pp. 157–162, mar 2002.

[115] V. R. Chowdhury and J. W. Kimball, "Control of a three-phase grid-connected inverter under non-ideal grid conditions with online parameter update," *IEEE Transactions on Energy Conversion*, vol. 34, pp. 1613–1622, sep 2019.

[116] R. Luhtala, T. Reinikka, H. Alenius, T. Roinila, and T. Messo, "Adaptive method for control tuning of grid-connected inverter based on grid measurements during start-up," in *2019 18th European Control Conference (ECC)*, IEEE, jun 2019.

[117] R. Luhtala, T. Messo, and T. Roinila, "Adaptive control of grid-voltage feedforward for grid-connected inverters based on real-time identification of grid impedance," in *2018 International Power Electronics Conference (IPEC-Niigata 2018 -ECCE Asia)*, IEEE, may 2018.

[118] S. Hiti, D. Boroyevich, and C. Cuadros, "Small-signal modeling and control of three-phase PWM converters," in *Proceedings of 1994 IEEE Industry Applications Society Annual Meeting*, IEEE.

[119] A. Yazdani and R. Iravani, *Voltage-sourced converters in power systems: modeling, control, and applications.* John Wiley & Sons, 2010.

[120] S. Ahmed, Z. Shen, P. Mattavelli, D. Boroyevich, and K. J. Karimi, "Small-signal model of voltage source inverter (VSI) and voltage source converter (VSC) considering the DeadTime effect and space vector modulation types," *IEEE Transactions on Power Electronics*, vol. 32, pp. 4145–4156, jun 2017.

[121] L. Harnefors, M. Bongiorno, and S. Lundberg, "Input-admittance calculation and shaping for controlled voltage-source converters," *IEEE Transactions on Industrial Electronics*, vol. 54, pp. 3323–3334, dec 2007.

[122] D. Dong, B. Wen, D. Boroyevich, P. Mattavelli, and Y. Xue, "Analysis of phase-locked loop low-frequency stability in three-phase grid-connected power converters considering impedance interactions," *IEEE Transactions on Industrial Electronics*, vol. 62, pp. 310–321, jan 2015.

[123] S.-K. Chung, "A phase tracking system for three phase utility interface inverters," *IEEE Transactions on Power Electronics*, vol. 15, pp. 431–438, may 2000.

[124] J. Sun, "Small-signal methods for AC distributed power systems–a review," *IEEE Transactions on Power Electronics*, vol. 24, pp. 2545–2554, nov 2009.

[125] D. Dewar, A. Formentini, and P. Zanchetta, "Automated and scalable optimal control of three-phase embedded power grids including PLL," in *2017 IEEE Energy Conversion Congress and Exposition (ECCE)*, IEEE, oct 2017.

[126] D. Dewar, K. Li, A. Formentini, P. Zanchetta, and P. Wheeler, "Performance analysis of h2 optimally controlled three-phase grids," in *2018 IEEE Energy Conversion Congress and Exposition (ECCE)*, IEEE, sep 2018.

[127] B. Wen, D. Boroyevich, P. Mattavelli, Z. Shen, and R. Burgos, "Influence of phase-locked loop on input admittance of three-phase voltage-source converters," in *2013 Twenty-Eighth Annual IEEE Applied Power Electronics Conference and Exposition (APEC)*, IEEE, mar 2013.

[128] S. Skogestad and I. Postlethwaite, *Multivariable feedback control: analysis and design*, vol. 2. Wiley New York, 2007.

[129] J. B. Burl, *Linear optimal control: H (2) and H (Infinity) methods*. Addison-Wesley Longman Publishing Co., Inc., 1998.

[130] H. Kwakernaak, "H2—optimization-theory and applications to robust control design," *IFAC Proceedings Volumes*, vol. 33, no. 14, pp. 437–448, 2000.

[131] G. R. G. da Silva, A. S. Bazanella, C. Lorenzini, and L. Campestrini, "Data-driven LQR control design," *IEEE Control Systems Letters*, vol. 3, pp. 180–185, jan 2019.

[132] M. M. S. Gumussoy, D. Henrion and M. Overton., "Multiobjective robust control with hifoo 2.0," in *Proceedings of the IFAC Symposium on Robust Control Design, Haifa*, 2009.

[133] S. G. D. Arzelier, G. Deaconu and D. Henrion., "H2 for hifoo," in *International Conference on Control and Optimization with Industrial Applications*, 2011.

[134] D. A. Michael Overton, Didier Henrion. https://cs.nyu.edu/overton/software/hifoo/.

[135] F. Lin, M. Fardad, and M. R. Jovanovic, "Augmented lagrangian approach to design of structured optimal state feedback gains," *IEEE Transactions on Automatic Control*, vol. 56, pp. 2923–2929, dec 2011.

[136] L. Ljung, *System identification, theory for the user*. Prentice-Hall, 1999.

[137] T. Soderstrom and P. Stoica, *System Identification.* Prentice Hall, 1989.

[138] K. Keesman, *System Identification: An Introduction.* Springer London, 2011.

[139] X. Luo, G. Zhou, and B. Cao, "Constrained applied predictive control based on closed-loop subspace identification," in *2016 International Conference on Integrated Circuits and Microsystems (ICICM)*, IEEE, nov 2016.

[140] P. Van Overschee and B. De Moor, *Subspace identification for linear systems: Theory—Implementation—Applications.* Springer Science & Business Media, 2012.

[141] A. G. Costa, J. L. B. Maldonado, F. A. Romero, J. C. Sanmartin, M. Valarezo, and H. Castillo, "N4sid method applied to obtain a discrete-time linear state space system as a mathematical model of a jaw crusher prototype," in *2017 CHILEAN Conference on Electrical, Electronics Engineering, Information and Communication Technologies (CHILECON)*, IEEE, oct 2017.

[142] M. Viberg, "Subspace-based state-space system identification," *Circuits, Systems, and Signal Processing*, vol. 21, pp. 23–37, jan 2002.

[143] J. Dannehl, C. Wessels, and F. Fuchs, "Limitations of voltage-oriented pi current control of grid-connected pwm rectifiers with lcl filters," *IEEE Transactions on Industrial Electronics*, vol. 56, pp. 380–388, feb 2009.

[144] J. Alvarez-Ramirez, I. Cervantes, G. Espinosa-Perez, P. Maya, and A. Morales, "A stable design of PI control for DC-DC converters with an RHS zero," *IEEE Transactions on Circuits and Systems I: Fundamental Theory and Applications*, vol. 48, no. 1, pp. 103–106, 2001.

Appendix A

A.1 Transformation Conventions

Consider the space phasor

$$\vec{f}(t) = \frac{2}{3}[e^{j0}f_a(t) + e^{j\frac{2\pi}{3}}f_b(t) + e^{j\frac{4\pi}{3}}f_c(t)] \tag{A.1}$$

where $f_a + f_b + f_c = 0$. $\vec{f}(t)$ can be decomposed into its real and imaginary components as

$$\vec{f}(t) = f_\alpha(t) + jf_\beta(t) \tag{A.2}$$

where f_α and f_β are referred to as $\alpha-$ and $\beta-$axis components of $\vec{f}(t)$, respectively. Substituting for $\vec{f}(t)$ from (A.2) in (A.1) and equating the corresponding real and imaginary parts of both sides of the resultant, we deduce

$$\begin{bmatrix} f_\alpha(t) \\ f_\beta(t) \end{bmatrix} = \frac{2}{3}C \begin{bmatrix} f_a(t) \\ f_b(t) \\ f_c(t) \end{bmatrix} \tag{A.3}$$

where

$$C = \begin{bmatrix} 1 & -\frac{1}{2} & -\frac{1}{2} \\ 0 & \frac{\sqrt{3}}{2} & -\frac{\sqrt{3}}{2} \end{bmatrix} \tag{A.4}$$

f_{abc} can also be expressed in terms of $f_{\alpha\beta}$ as

$$f_a(t) = Re\left\{[f_\alpha(t) + jf_\beta(t)]e^{-j0}\right\} = f_\alpha(t) \tag{A.5a}$$

$$f_b(t) = Re\left\{[f_\alpha(t) + jf_\beta(t)]e^{-j\frac{2\pi}{3}}\right\} = -\frac{1}{2}f_\alpha(t) + \frac{\sqrt{3}}{2}f_\beta(t) \tag{A.5b}$$

$$f_c(t) = Re\left\{[f_\alpha(t) + jf_\beta(t)]e^{-j\frac{4\pi}{3}}\right\} = -\frac{1}{2}f_\alpha(t) - \frac{\sqrt{3}}{2}f_\beta(t) \tag{A.5c}$$

Equation (A.5) can written in the following matrix form:

$$\begin{bmatrix} f_a(t) \\ f_b(t) \\ f_c(t) \end{bmatrix} = \begin{bmatrix} 1 & 0 \\ -\frac{1}{2} & \frac{\sqrt{3}}{2} \\ -\frac{1}{2} & -\frac{\sqrt{3}}{2} \end{bmatrix} \begin{bmatrix} f_\alpha(t) \\ f_\beta(t) \end{bmatrix} = \boldsymbol{C}^T \begin{bmatrix} f_\alpha(t) \\ f_\beta(t) \end{bmatrix} \tag{A.6}$$

Equation (A.3) and(A.6) introduce the matrix transformations from the abc-frame to the $\alpha\beta$ frame, and vice versa, respectively. One can conclude that $f_\alpha(t)$ and $f_\beta(t)$ are the projection of $\vec{f}(t)$ on te real axis and the imaginary axis, respectively. Thus we rename the real and the imaginary axes to α-axis and β-axis, respectively, as shown in Fig.A.1.
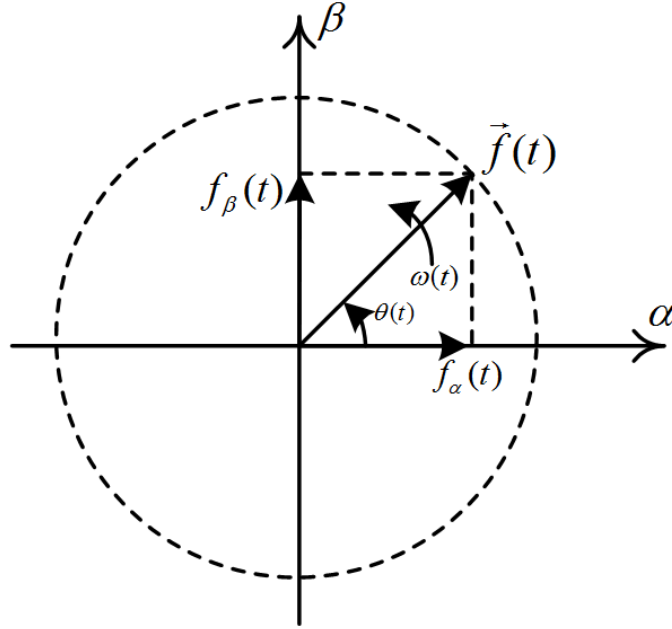
Figure A.1: The $\alpha\beta$-frame components of a space phasor

For the space phasor $\vec{f} = f_\alpha + jf_\beta$, the $\alpha\beta-$ to $dq-$frame transformation is defined by

$$f_d + jf_q = (f_\alpha + jf_\beta)e^{-j\varepsilon(t)} \tag{A.7}$$

which is equivalent to a phase shift in $\vec{f}(t)$ by the angle $-\varepsilon(t)$. The $dq-$ to $\alpha\beta-$frame can be obtained by multiplying both sides of (A.7) by $e^{j\varepsilon(t)}$. Thus,

$$f_\alpha + jf_\beta = (f_d + jf_q)e^{j\varepsilon(t)} \tag{A.8}$$

To highlight the usefulness of the transformation given by (A.7), assume that $\vec{f}$ has the following general form:

$$\vec{f}(t) = f_\alpha + jf_\beta = \hat{f}(t)e^{j[\theta_0 + \int \omega(\tau)d\tau]} \tag{A.9}$$

where $\omega(t)$ is the (time-varying) frequency and θ_0 is the initial phase angle of the three-phase signal corresponding to $\vec{f}(t)$. If $\varepsilon(t)$ is chosen as

$$\varepsilon(t) = \varepsilon_0 + \int \omega(\tau)d\tau \tag{A.10}$$

which is stationary and, therefore, the constituent of its corresponding three-phase signal are DC quantities. Note that $\theta(t)$ and $\varepsilon(t)$ are not necessarily equal, but $d\theta(t)/dt = d\varepsilon(t)/dt$ must be ensured.

To be better describe the dq-frame transformation, let us rewrite (A.8) as

$$\vec{f} = f_d(1 + 0j)e^{j\varepsilon(t)} + f_q(0 + 1j)e^{j\varepsilon(t)} \tag{A.11}$$

An interpretation of (A.11) is that the vector $\vec{f}$ is represented by its components, that is, f_d and f_q, in an orthogonal coordinate system whose axes are along the unit vectors $(1 + 0j)e^{j\varepsilon(t)}$ and $(0 + 1j)e^{j\varepsilon(t)}$. In turn, $(1 + 0j)$ and $(0 + 1j)$ are the unit vectors along the $\alpha-$axis and the $\beta-$axis of the $\alpha\beta-$frame, respectively. Therefore, as illustrated in Fig.A.2, one can consider $\vec{f}$ as a vector represented by the components f_d and f_q in a coordinate system that is rotated by $\varepsilon(t)$ with respect to the $\alpha\beta-$frame. We refer to this rotated coordinate system as $dq-$frame. For the reason above, the $dq-$frame is also known as rotating reference frame, in the technical literature. Usually, the rotational speed of the $dq-$frame is selected to be equal to that of $\vec{f}$.
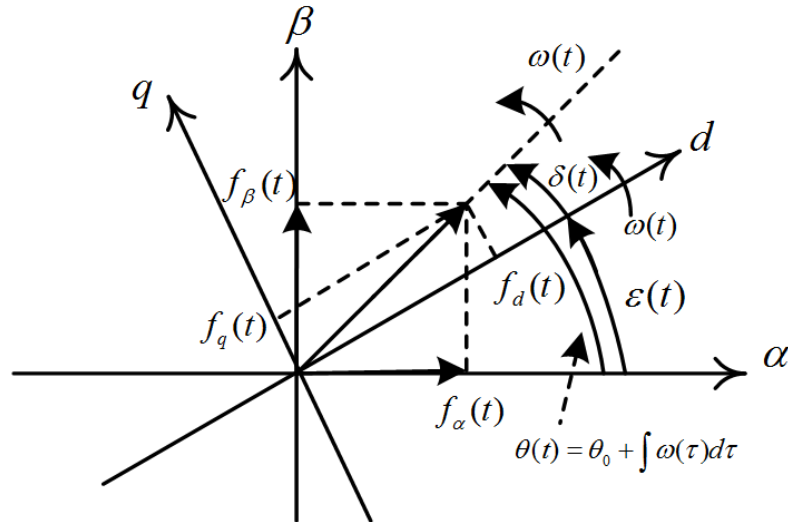
Figure A.2: $\alpha\beta-$ and $dq-$frame coordinate systems

Based on the Euler's identity $e^{j(*)} = cos(*) + jsin(*)$, (A.7) can be written as

$$\begin{bmatrix} f_d(t) \\ f_q(t) \end{bmatrix} = \boldsymbol{R}[\varepsilon(t)] \begin{bmatrix} f_\alpha(t) \\ f_\beta(t) \end{bmatrix} \tag{A.12}$$

where

$$\boldsymbol{R} = \begin{bmatrix} cos\varepsilon(t) & sin\varepsilon(t) \\ -sin\varepsilon(t) & cos\varepsilon(t) \end{bmatrix} \tag{A.13}$$

Similarly, the $dq-$ to $\alpha\beta-$ frame transformation (A.8) can be rewritten as

$$\begin{bmatrix} f_\alpha(t) \\ f_\beta(t) \end{bmatrix} = \boldsymbol{R}^{-1}[\varepsilon(t)] \begin{bmatrix} f_d(t) \\ f_q(t) \end{bmatrix} = \boldsymbol{R}[-\varepsilon(t)] \begin{bmatrix} f_d(t) \\ f_q(t) \end{bmatrix} \tag{A.14}$$

where

$$\boldsymbol{R}^{-1}[\varepsilon(t)] = \boldsymbol{R}[-\varepsilon(t)] \begin{bmatrix} cos\varepsilon(t) & -sin\varepsilon(t) \\ sin\varepsilon(t) & cos\varepsilon(t) \end{bmatrix} \tag{A.15}$$

It can also be verified that

$$\boldsymbol{R}^{-1}[\varepsilon(t)] = \boldsymbol{R}^T[\varepsilon(t)] \tag{A.16}$$

A direct transformation from the $abc-$frame to the $dq-$frame can be obtained by substitution of $[f_\alpha \quad f_\beta]^T$ from (A.3) in (A.14), as

$$\begin{bmatrix} f_d(t) \\ f_q(t) \end{bmatrix} = \frac{2}{3}\boldsymbol{T}[\varepsilon(t)] \begin{bmatrix} f_a(t) \\ f_b(t) \\ f_c(t) \end{bmatrix} \tag{A.17}$$

where

$$\boldsymbol{T}[\varepsilon(t)] = \boldsymbol{R}[\varepsilon(t)]\boldsymbol{C} = \begin{bmatrix} cos[\varepsilon(t)] & cos[\varepsilon(t) - \frac{2\pi}{3}] & cos[\varepsilon(t) - \frac{4\pi}{3}] \\ sin[\varepsilon(t)] & sin[\varepsilon(t) - \frac{2\pi}{3}] & sin[\varepsilon(t) - \frac{4\pi}{3}] \end{bmatrix} \tag{A.18}$$

Similarly, a direct transformation from the $dq-$frame to the $abc-$frame can be obtained by substituting for $[f_\alpha \quad f_\beta]^T$ from (A.16) in (A.6), as

$$\begin{bmatrix} f_a(t) \\ f_b(t) \\ f_c(t) \end{bmatrix} = \boldsymbol{T}[\varepsilon(t)]^T \begin{bmatrix} f_d(t) \\ f_q(t) \end{bmatrix} \tag{A.19}$$

where

$$\boldsymbol{T}[\varepsilon(t)]^T = \boldsymbol{C}^T\boldsymbol{R}[-\varepsilon(t)] = \begin{bmatrix} cos[\varepsilon(t)] & sin[\varepsilon(t)] \\ cos[\varepsilon(t) - \frac{2\pi}{3}] & sin[\varepsilon(t) - \frac{2\pi}{3}] \\ cos[\varepsilon(t) - \frac{4\pi}{3}] & sin[\varepsilon(t) - \frac{4\pi}{3}] \end{bmatrix} \tag{A.20}$$

When we derive the expressions for the instantaneous real- and reactive-power in terms of dq-frame variables, we substitute for $\vec{v}(t) = (v_d + jv_q)e^{j\varepsilon(t)}$ and $\vec{i}^*(t) = (i_d - ji_q)e^{-j\varepsilon(t)}$ in

$$P(t) = Re\left\{\frac{3}{2}\vec{v}(t)\vec{i}^*(t)\right\} \tag{A.21}$$

and

$$S(t) = P(t) + jQ(t) = \frac{3}{2}\vec{v}(t)\vec{i}^*(t) \tag{A.22}$$

we deduce

$$P(t) = \frac{3}{2}[v_d(t)i_d(t) + v_q(t)i_q(t)] \tag{A.23}$$

and

$$Q(t) = \frac{3}{2}[-v_d(t)i_q(t) + v_q(t)i_d(t)] \tag{A.24}$$

A.2 Notations

SYMBOLS

I_{ad} d-axis current on the AC bus viewed in VSI-dq frame

I_{ad}^p d-axis current on the AC bus viewed in PLL-dq frame

i_{ad} small variation of I_{ad}

i_{ad}^p small variation of I_{ad}^p

I_{ad}^* equilibrium value of d-axis current on the AC bus

I_{aq} q-axis current on the AC bus viewed in VSI-dq frame

I_{aq}^p q-axis current on the AC bus viewed in PLL-dq frame

i_{aq} small variation of I_{aq}

i_{aq}^p small variation of I_{aq}^p

I_{aq}^* equilibrium value of q-axis current on the AC bus

I_{id} d-axis current of VSI LC fiter inductor

i_{id} small variation of I_{id}

I_{iq} q-axis current of VSI LC fiter inductor

i_{iq} small variation of I_{iq}

m_d d-axis control input modulation index for VSI

m_q q-axis control input modulation index for VSI

p_d d-axis control input modulation index for AFE

p_q q-axis control input modulation index for AFE

V_{cd} d-axis voltage on the AC bus viewed in VSI-dq frame

V_{cd}^p d-axis voltage on the AC bus viewed in PLL-dq frame

v_{cd} small variation of V_{cd}

v_{cd}^p small variation of V_{cd}^p

V_{cd}^* equilibrium value of the d-axis voltage

V_{cq} q-axis voltage on the AC bus viewed in VSI-dq frame

V_{cq}^p q-axis voltage on the AC bus viewed in PLL-dq frame

v_{cq} small variation of V_{cq}

v_{cq}^p small variation of V_{cq}^p

V_{cq}^* equilibrium value of the q-axis voltage

$W_{v_{dca}}$ integral error of V_{dca}

$w_{v_{dca}}$ small variation of $W_{v_{dca}}$

$W_{i_{aq}}$ integral error of I_{aq}

$w_{i_{aq}}$ small variation of $W_{i_{aq}}$

k_p^p proportional gain of PLL's internal PI

k_i^p integral gain of PLL's internal PI

k_{pv} proportional gain of voltage regulator in a PI controller

k_{pi} proportional gain of current regulator in a PI controller

k_{iv} integral gain of voltage regulator in a PI controller

k_{ii} integral gain of current regulator in a PI controller

θ_e difference between PLL output and real phase angle

$\tilde{\theta}_e$ small variation of θ_e

θ_g	real phase angle generated by the VSI
θ_p	PLL's estimated phase angle
i_D^g	instant d-axis current in grid-dq frame when AFE does not include a PLL
i_Q^g	instant q-axis current in grid-dq frame when AFE does not include a PLL
v_D^g	instant d-axis voltage in grid-dq frame when AFE does not include a PLL
v_Q^g	instant q-axis voltage in grid-dq frame when AFE does not include a PLL
i_D^{gp}	instant d-axis current in grid-dq frame when AFE includes a PLL
i_Q^{gp}	instant q-axis current in grid-dq frame when AFE includes a PLL
v_D^{gp}	instant d-axis voltage in grid-dq frame when AFE includes a PLL
v_Q^{gp}	instant q-axis voltage in grid-dq frame when AFE includes a PLL
i_D^p	instant d-axis current in PLL-dq frame when AFE includes a PLL
i_Q^p	instant q-axis current in PLL-dq frame when AFE includes a PLL
v_D^p	instant d-axis voltage in PLL-dq frame when AFE includes a PLL
v_Q^p	instant q-axis voltage in PLL-dq frame when AFE includes a PLL
V_D	equals with the d-axis voltage equilibrium value V_{cd}^*
V_Q	equals with the q-axis voltage equilibrium value 0
v_d^p	small variation of v_D^p
v_q^p	small variation of v_Q^p

A.3 Acronyms

VSI	Voltage source inverter
AFE	Active front-end
PLL	Phase locked-loop
PCC	Point of common coupling
PEM	Prediction error method

CPL   Constant power load

RL   Resistive load

MIMO   Multi-input multi-output

PI   Proportion-integral

PI-SRF   Proportion-integral synchronous reference frame

Appendix B

B.1 SISO system closed loop stability

As noted above the stability of a linear system is equivalent to the system having no poles in the closed right-half plane (RHP). Here, we first derive some preliminary results involving the determinant of the return difference operator $I + L$. Consider the feedback system shown in Fig.3.17, where $L(s)$ is the loop transfer function matrix. Stability of the open-loop system is determined by the poles of $L(s)$. If $L(s)$ has a state-space realization $\begin{bmatrix} A_{ol} & B_{ol} \\ C_{ol} & D_{ol} \end{bmatrix}$, that is

$$L(s) = C_{ol}(sI - Aol)^{-1}B_{ol} + Dol \tag{B.1}$$

then the poles of $L(s)$ are the roots of the open loop characteristic polynomial

$$\phi_{ol}(s) = det(sI - Aol) \tag{B.2}$$

Then the stability of the closed-loop system is equivalent to the stability of $S(s) = (1+L(s))^{-1}$. The state matrix of $S(s)$ if given by (assuming $L(s)$ is well posed, i.e. $D_{ol} + I$ is invertible)

$$A_{cl} = A_{ol} - B_{ol}(I + D_{ol})^{-1}C_{ol} \tag{B.3}$$

This equation may be derived by writing down the state space equations for the transfer function from r to y in Fig.3.17,

$$\dot{x} = A_{ol}x + B_{ol}(r - y) \tag{B.4}$$

$$y = C_{ol}x + D_{ol}(r - y) \tag{B.5}$$

and using (B.5) to eliminate y from (B.4). The closed loop characteristic polynomial is thus given by

$$\phi_{cl}(s) \triangleq det(sI - A_{cl}) = det(sI - A_{ol} + B_{ol}(I + D_{ol})^{-1}C_{ol}) \tag{B.6}$$

According to the **Schur's formula** for determinant of a partitioned matrix,

$$det \begin{bmatrix} A_{11} & A_{12} \\ A_{21} & A_{22} \end{bmatrix} = det(A_{11}) \cdot det(A_{22} - A_{21}A_{11}^{-1}A_{12})$$

$$= det(A_{22}) \cdot det(A_{11} - A_{12}A_{22}^{-1}A_{21}) \tag{B.7}$$

where it is assumed that A_{11} and/or A_{22} are non-singular. Proof: Note that A has the following decomposition if A_{11} is non-singular:

$$\begin{bmatrix} A_{11} & A_{12} \\ A_{21} & A_{22} \end{bmatrix} = \begin{bmatrix} I & 0 \\ A_{21}A_{11}^{-1} & I \end{bmatrix} \begin{bmatrix} A_{11} & 0 \\ 0 & X \end{bmatrix} \begin{bmatrix} I & A_{11}^{-1}A_{12} \\ 0 & I \end{bmatrix} \tag{B.8}$$

where $X = A_{22} - A_{21}A_{11}^{-1}A_{12}$. The first part of (B.7) is proved by noting that

$$det(A_1 A_2) = det(A_2 A_1) = det A_1 \cdot det A_2 \tag{B.9}$$

If we define $A_{11} = I + D_{ol}, A_{12} = -C_{ol}, A_{21} = B_{ol}, A_{22} = sI - A_{ol}$, then

$$det \begin{bmatrix} A_{11} & A_{12} \\ A_{21} & A_{22} \end{bmatrix} = det(A_{11}) \cdot det(A_{22} - A_{21}A_{11}^{-1}A_{12})$$

$$= det(I + D_{ol}) \cdot det(sI - A_{ol} + B_{ol}(I + D_{ol})^{-1}C_{ol}$$

$$= det(I + D_{ol}) \cdot \phi_{cl}(s) \tag{B.10}$$

$$= det(A_{22}) \cdot det(A_{11} - A_{12}A_{22}^{-1}A_{21})$$

$$= det(sI - A_{ol}) \cdot det(I + D_{ol} + C_{ol}(sI - A_{ol})^{-1}B_{ol})$$

$$= \phi_{ol}(s) \cdot det(I + L(s))$$

Therefore,

$$det(I + L(s)) = \frac{\phi_{cl}(s)}{\phi_{ol}(s)}c \tag{B.11}$$

where $c = det(I + D_{ol})$.

B.2   Matrices in the impedance model of PI AFE

$$
A_{afe}^{cl} =
\begin{bmatrix}
-\frac{R_a}{L_a} & \omega & 0 & 0 & -\frac{1}{L_a} & 0 & -I_{ad}^*\omega & 0 \\
-\omega & -\frac{R_a}{L_a} & 0 & 0 & 0 & -\frac{1}{L_a} & \frac{1}{L_a}(I_{ad}^*R_a - V_{cd}^*) - k_p^p I_{ad}^* V_{cd}^* & I_{ad}^* \\
\frac{3U_d^*}{2C_a V_{dca}^*} & \frac{3U_q^*}{2C_a V_{dca}^*} & \lambda_1 & 0 & \frac{3I_{ad}^*}{2C_a V_{dca}^*} & 0 & -\frac{3I_{ad}^* U_q^*}{2C_a V_{dca}^*} & 0 \\
-\lambda_4 & -\lambda_3 & -k_{iv} - k_{pv}\lambda_1 & 0 & -\lambda_5 & 0 & \lambda_2 & 0 \\
k_{pi}(\frac{R_a}{L_a} - \lambda_4) - k_{ii} & -k_{pi}(\omega + \lambda_3) & -k_{pi}(k_{iv} + k_{pv}\lambda_1) & k_{ii} & k_{pi}(\frac{1}{L_a} - \lambda_5) & 0 & k_{pi}(I_{ad}^*\omega + \lambda_2) & 0 \\
k_{pi}\omega & k_{pi}\frac{R_a}{L_a} - k_{ii} & 0 & 0 & 0 & k_{pi}\frac{1}{L_a} & \frac{k_{pi}}{L_a}(V_{cd}^* - I_{ad}^*R_a) + I_{ad}^* k_{ii} & 0 \\
0 & 0 & 0 & 0 & 0 & 0 & -k_p^p V_{cd}^* & 1 \\
0 & 0 & 0 & 0 & 0 & 0 & -k_i^p V_{cd}^* & 0
\end{bmatrix}
\tag{B.12}
$$

$$G_{afe}^{cl} = \begin{bmatrix} \frac{1}{L_a} & 0 \\ 0 & \frac{1}{L_a} + k_p^p I_{ad}^* \\ 0 & 0 \\ 0 & 0 \\ -\frac{k_{pi}}{L_a} & 0 \\ 0 & -\frac{k_{pi}}{L_a} \\ 0 & k_p^p \\ 0 & k_i^p \end{bmatrix} \tag{B.13}$$

$$\lambda_1 = \frac{P}{C_a V_{dca}^2} - \frac{3 I_{ad}^* U_d^*}{2 C_a V_{dca}^{*2}} \tag{B.14}$$

$$\lambda_2 = \frac{3 k_{pv} I_{ad}^* U_q^*}{2 C_a V_{dca}^*} \tag{B.15}$$

$$\lambda_3 = \frac{3 k_{pv} U_q^*}{2 C_a V_{dca}^*} \tag{B.16}$$

$$\lambda_4 = \frac{3 k_{pv} U_d^*}{2 C_a V_{dca}^*} \tag{B.17}$$

$$\lambda_5 = \frac{3 k_{pv} I_{ad}^*}{2 C_a V_{dca}^*} \tag{B.18}$$

$$C_{afe}^{cl} = \begin{bmatrix} 1 & 0 & 0 & 0 & 0 & 0 & 0 & 0 \\ 0 & 1 & 0 & 0 & 0 & 0 & 0 & 0 \end{bmatrix} \tag{B.19}$$

B.3 Model order estimate by the use of Hankel matrix

Block Hankel matrices play an important role in subspace identification algorithms. These matrices can be easily constructed from the given input-output data. Input block Hankel matrices are defined as:

The number of block rows i is a user-defined index which is large enough i.e. it should at least be larger than the maximum $order^2$ of the system one wants to identify. Note that, since each block row contains m (number of inputs) rows, the matrix $U_{0|2i-1}$ consists of $2mi$ rows.

The number of columns j is typically equal to $s - 2i + 1$, which implies that all given data samples are used. s is the number of measurements.

The subscripts of $U_{0|2i-1}$, $U_{0|i-1}$, $U_{i|2i-1}$ denote the subscript of the first and last element of the first column in the block Hankel matrix. The subscript "p" stands for "past" and the subscript "f" for "future".

The output block Hankel matrices $Y_{0|2i-1}$, Y_p, Y_f are defined in a similar way. The block Hankel matrices consisting of inputs and outputs is defined as $W_{0|i-1}$:

$$W_{0|i-1} \triangleq \left(\frac{U_{0|i-1}}{Y_{0|i-1}} \right) = \left(\frac{U_p}{Y_p} \right) = W_p$$

And $\mathcal{O}$ is defined as the oblique projection [140]:

$$\mathcal{O} = Y_f /_{U_f} W_p \tag{B.20}$$

By the use of singular value decomposition:

$$W_1 \mathcal{O} W_2 = \begin{bmatrix} U_1 & U_2 \end{bmatrix} \begin{bmatrix} S_1 & 0 \\ 0 & 0 \end{bmatrix} \begin{bmatrix} V_1^T & V_2^T \end{bmatrix} = U_1 S_1 V_1^T \tag{B.21}$$

The order of the system is equal to the number of singular values in the above equation different from zero.

Appendix C

C.1 MATLAB code for impedance calculation

```matlab
%% System Equilibrium Value Calculation
syms Iido Iiqo Vdo Vqo Iado Udo Uqo
[Iidn,Iiqn,Vdn,Vqn,Iadn,Udn,Uqn]...
=solve([1/C*Iido-1/C*Iado==0,...
        -w*Vcd+1/C*Iiqo==0,...
        -R/L*Iido-1/L*Vcd+w*Iiqo+Vdo/L==0,...
        -w*Iido-R/L*Iiqo+Vqo/L==0, ...
        -Ra/La*Iado-Udo/La+Vcd/La==0,...
        -w*Iado-Uqo/La==0,...
        3/4/Ca*(2*Udo/Vdca*Iado)-Power/Vdca/Ca==0],[Iido,Iiqo,Vdo,
            Vqo,Iado,Udo,Uqo]);
%Pick the rational value from the two sets of solutions
Iade = double(Iadn(2)); %Equilibrium for Iad. If the Iade is not a
    rational number, then replace Iade with Iadn(1)
Iide = double(Iidn(2)); %Equilibrium for Iid
Iiqe = double(Iiqn(2)); %Equilibrium for Iiq
Vde = double(Vdn(2)); %Equilibrium for Ud
Vqe = double(Vqn(2)); %Equilibrium for Uq
Ude = double(Udn(2)); %Equilibrium for Ud
Uqe = double(Uqn(2)); %Equilibrium for Uq
pde = 2*Ude/Vdca; %Equilibrium for pd
pqe = 2*Uqe/Vdca; %Equilibrium for pq
Equilibrium = [Iide,Iiqe,Vde,Vqe,Iade,Ude,Uqe,pde,pqe];
```

```matlab
1  %% Impedance of AFE including PLL using PI controllers
2  syms Iadw Iaqw Vdcaw VXw Udw Uqw Vcdw Vcqw Thetaew Xw Vdca_ref
      Iaq_ref
3  Iadpllw = Iadw;
4  Iaqpllw = -Thetaew*Iadw + Iaqw;
5
6  Vcdpllw = Vcdw;
7  vcqpllw = -Thetaew*Vcdw+Vcqw;
8
9  Thetaew_DIF = -Kp_PLL*Vcd*Thetaew + Kp_PLL*Vcqw + Xw;%Differential
      equations of AFE including PLL
10 XwDIF = - Ki_PLL*Vcd*Thetaew + Ki_PLL*Vcqw;
11
12 Vdcaw_DIF = 3/4/Ca*(2*Udw/Vdcaw*Iadpllw+2*Uqw/Vdcaw*Iaqpllw)-Power/
      Vdcaw/Ca;
13 VXw_DIF = Kpv_AFE*(0-Vdcaw_DIF)+Kiv_AFE*(Vdca_ref-Vdcaw);
14
15 Iad_DIF = -Ra/La*Iadpllw+w*Iaqpllw-Udw/La+Vcdpllw/La;
16 Iaq_DIF = -Ra/La*Iaqpllw-w*Iadpllw-Uqw/La+vcqpllw/La + Thetaew_DIF*
      Iade;
17 Iadpllw_DIF = -Ra/La*Iadpllw+w*Iaqpllw-Udw/La+Vcdpllw/La;
18 Iaqpllw_DIF = -Ra/La*Iaqpllw-w*Iadpllw-Uqw/La+vcqpllw/La;
19
20 Udw_DIF = Kpi_AFE*(VXw_DIF-Iadpllw_DIF)+Kii_AFE*(VXw-Iadpllw);
21 Uqw_DIF = Kpi_AFE*(0-Iaqpllw_DIF)+Kii_AFE*(Iaq_ref-Iaqpllw);
22
23 F = [Iad_DIF Iaq_DIF Vdcaw_DIF VXw_DIF Udw_DIF Uqw_DIF Thetaew_DIF
      XwDIF];
24 v = [Iadw Iaqw Vdcaw VXw Udw Uqw Thetaew Xw Vcdw Vcqw];
25 J = jacobian(F,v);
26 p = [Iade,0,Vdca,Iade,Ude,Uqe,0,0,Vcd,0];
27 a = subs(J,v,p);
28 AA = double(a);
29
30 AAFE = AA(:,1:8);
```

```matlab
31 BAFE = AA(:,9:10);%Vcd Vcq
32 CAFE = [1 0 0 0 0 0 0 0;0 1 0 0 0 0 0 0];%%Iad Iaq
33 G_AFEPI = ss(AAFE,BAFE,CAFE, []);
34
35 Z_AFEPI = inv(G_AFEPI);%Transform from admittance to impedance
36 TFZ_AFEPI = tf(Z_AFEPI);
37 Zdd_AFEPI = TFZ_AFEPI(1,1);
38 Zdq_AFEPI = TFZ_AFEPI(1,2);
39 Zqd_AFEPI = TFZ_AFEPI(2,1);
40 Zqq_AFEPI = TFZ_AFEPI(2,2);
41 % Impedance of AFE using H2 Controllers
42 Aafe = [-Ra/La w -Equilibrium(6)/2/La 0 0;
43         -w -Ra/La -Equilibrium(7)/2/La 0 0;
44         3*Equilibrium(6)/4/Ca 3*Equilibrium(7)/4/Ca Power/Ca/(Vdca
            ^2) 0 0;
45         0 -1 0 0 0;
46         0 0 -1 0 0];
47 B2afe = [-Vdca/2/La 0;
48         0 -Vdca/2/La;
49         3*Equilibrium(3)/4/Ca 0;
50         0 0;
51         0 0];
52 B1afe = [1/La 0;
53         0 1/La;
54         0 0;
55         0 0;
56         0 0];%Input Maxtrix for Vcd and Vcq
57 Cafe = [1 0 0 0 0;
58         0 1 0 0 0];%Output Maxtrix for Iad and Iaq
59 G_AFEH2 = ss(Aafe+B2afe*Kx_AFE,B1afe,Cafe, []);%Kx_AFE is the h2
     Control Gain
60 Z_AFEH2 = inv(G_AFEH2);
61 TFZ_AFEH2 = tf(Z_AFEH2);
62 Zdd_AFEH2= TFZ_AFEH2(1,1);
63 Zdq_AFEH2= TFZ_AFEH2(1,2);
```

```
64  Zqd_AFEH2= TFZ_AFEH2(2,1);
65  Zqq_AFEH2= TFZ_AFEH2(2,2);
```

C.2 MATLAB code for characteristic loci plot

```matlab
1   %Characteristic Loci
2   wx=logspace(-10,10,1e6);
3   [a1PI,bPI]=nyquist(ZddVSI*YddAFE+ZdqVSI*YqdAFE,wx);%Impedance ratio
        at each frequency
4   [cPI,dPI]=nyquist(ZddVSI*YdqAFE+ZdqVSI*YqqAFE,wx);
5   [ePI,fPI]=nyquist(ZqdVSI*YddAFE+ZqqVSI*YqdAFE,wx);
6   [gPI,hPI]=nyquist(ZqdVSI*YdqAFE+ZqqVSI*YqqAFE,wx);
7   a1PI=squeeze(a1PI);bPI=squeeze(bPI);
8   cPI=squeeze(cPI);dPI=squeeze(dPI);
9   ePI=squeeze(ePI);fPI=squeeze(fPI);
10  gPI=squeeze(gPI);hPI=squeeze(hPI);
11  xPI=zeros(1e6,2);xxPI=zeros(1e6,1);
12  yyPI=zeros(1e6,1);
13
14  flag=1;
15  %Eigen value of the 2 by 2 impedance ratio matrix
16  xPI(1,:)=eig([a1PI(1)+bPI(1)*1i cPI(1)+dPI(1)*1i;ePI(1)+fPI(1)*1i
        gPI(1)+hPI(1)*1i]);
17  xxPI(1)=xPI(1,1);
18  yyPI(1)=xPI(1,2);
19
20  for j=2:1:1e6
21  xPI(j,:)=eig([a1PI(j)+bPI(j)*1i cPI(j)+dPI(j)*1i;ePI(j)+fPI(j)*1i
        gPI(j)+hPI(j)*1i]);
22      if flag
23          xxPI(j)=xPI(j,1);
24          yyPI(j)=xPI(j,2);
25      else
26          yyPI(j)=xPI(j,1);
27          xxPI(j)=xPI(j,2);
```

```matlab
28    end
29    if abs(xxPI(j)-xxPI(j-1))>abs(yyPI(j)-xxPI(j-1))
30        %Fix eigen value entries be swapped by Matlab
31        flag=~flag;
32        xxxxx=xxPI(j);
33        xxPI(j)=yyPI(j);
34        yyPI(j)=xxxxx;
35    end
36 end
37
38 figure
39 subplot(1,2,1)%Locus 1
40 axis([-1 1 -1 1]);
41 axis square;
42 plot(xxPI,'r');
43 hold on
44 plot(-1,0,'r*');%Critical Point
45 grid
46
47 subplot(1,2,2)%Locus 2
48 axis([-1 1 -1 1]);
49 axis square;
50 plot(yyPI,'r');
51 hold on
52 plot(-1,0,'r*');
53 grid
```

C.3   MATLAB code for optimal H_2 controller synthesize

```matlab
1 %Tuning h2 controller for AFE including PLL based on the identfied
      model
2 %of VSI
3 A_VSI_IDENT = ss8.A; %Identified model of VSI, state matrix
4 B_VSI_IDENT = ss8.B; %Input matrix
5 C_VSI_IDENT = ss8.C; %Output matrix
```

```
6  order = size(A_VSI_IDENT ,1);%Oder of the identified VSI model

7

8  A_AFE = [-Ra/La w -pde/2/La 0 0;
9          -w -Ra/La -pqe/2/La 0 0;
10         3*pde/4/Ca 3*pqe/4/Ca Power/Ca/(Vdca^2) 0 0;
11         0 -1 0 0 0;
12         0 0 -1 0 0];
13 C_AFE = [1 0 0 0 0;
14         0 1 0 0 0];
15 G_AFE = [1/La 0;
16          0 1/La;
17          0 0;
18          0 0;
19          0 0];

20

21 AVSIX = A_VSI_IDENT - Iade/Vcd*B_VSI_IDENT*[0;1]*[0 1]*C_VSI_IDENT;
22 %In the identified model , the Iad and Iaq flow into VSI , but in the
       system model , the Iad and Iaq flow out of VSI
23 A=[AVSIX -B_VSI_IDENT*C_AFE -Iade/Vcd*B_VSI_IDENT*[0;1] zeros(order
       ,1);
24    G_AFE*[1;0]*[1 0]*C_VSI_IDENT A_AFE G_AFE*[0;1] zeros(5,1);
25    [0 1]*C_VSI_IDENT*AVSIX [0 1]*C_VSI_IDENT*B_VSI_IDENT*C_AFE -
          Iade/Vcd*[0 1]*C_VSI_IDENT*B_VSI_IDENT*[0;1] -Vcd;
26    zeros(1,order+7)];

27

28 B2AFE=[-Vdca/2/La 0 0 0;
29        0 -Vdca/2/La 0 0;
30        3*Iade/4/Ca 0 0 0;
31        0 0 0 0;
32        0 0 0 0;
33        0 0 -Vcd 0;
34        0 0 0 1];

35

36 B2=[zeros(order ,4);
37         B2AFE];
```

```
38
39  B1=eye(order+7);
40
41  Q = diag([zeros(1,order) 0 0 0 3 30 0 3]);
42  RR = diag([1 1 0.1 0.1]);
43
44  C1=[Q;zeros(4,order+7)];
45  D11=zeros(order+7+4,order+7);
46  D12=[zeros(order+7,4);RR];
47  C2=eye(order+7);
48  D21=zeros(order+7,order+7);
49  D22=zeros(order+7,4);
50
51  options.prtlevel = 0;
52  options.nrand = 30;
53  P1.A = A;
54  P1.B1 = B1;
55  P1.B2 = B2;
56  P1.C1 = C1;
57  P1.C2 = C2;
58  P1.D11 = D11;
59  P1.D12 = D12;
60  P1.D21 = D21;
61  P1.D22 = D22;
62
63  options.struct.d = [zeros(1,order) 1 1 1 1 1 0 0;
64                      zeros(1,order) 1 1 1 1 1 0 0;
65                      zeros(1,order) 0 0 0 0 0 1 0;
66                      zeros(1,order) 0 0 0 0 0 1 0];
67
68  K = hifoo(P1, 't', options);
69  K_hifoo = K.d;
70  Kx_AFE = K_hifoo(1:2,order+1:order+5)
71
72  K_s_AFE=Kx_AFE(1:2,1:3);
```

```
73  K_s_error_AFE=Kx_AFE(1:2,4:5);

74

75  Kp_PLL=K_hifoo(3,order+6)

76  Ki_PLL=K_hifoo(4,order+6)
```